

---

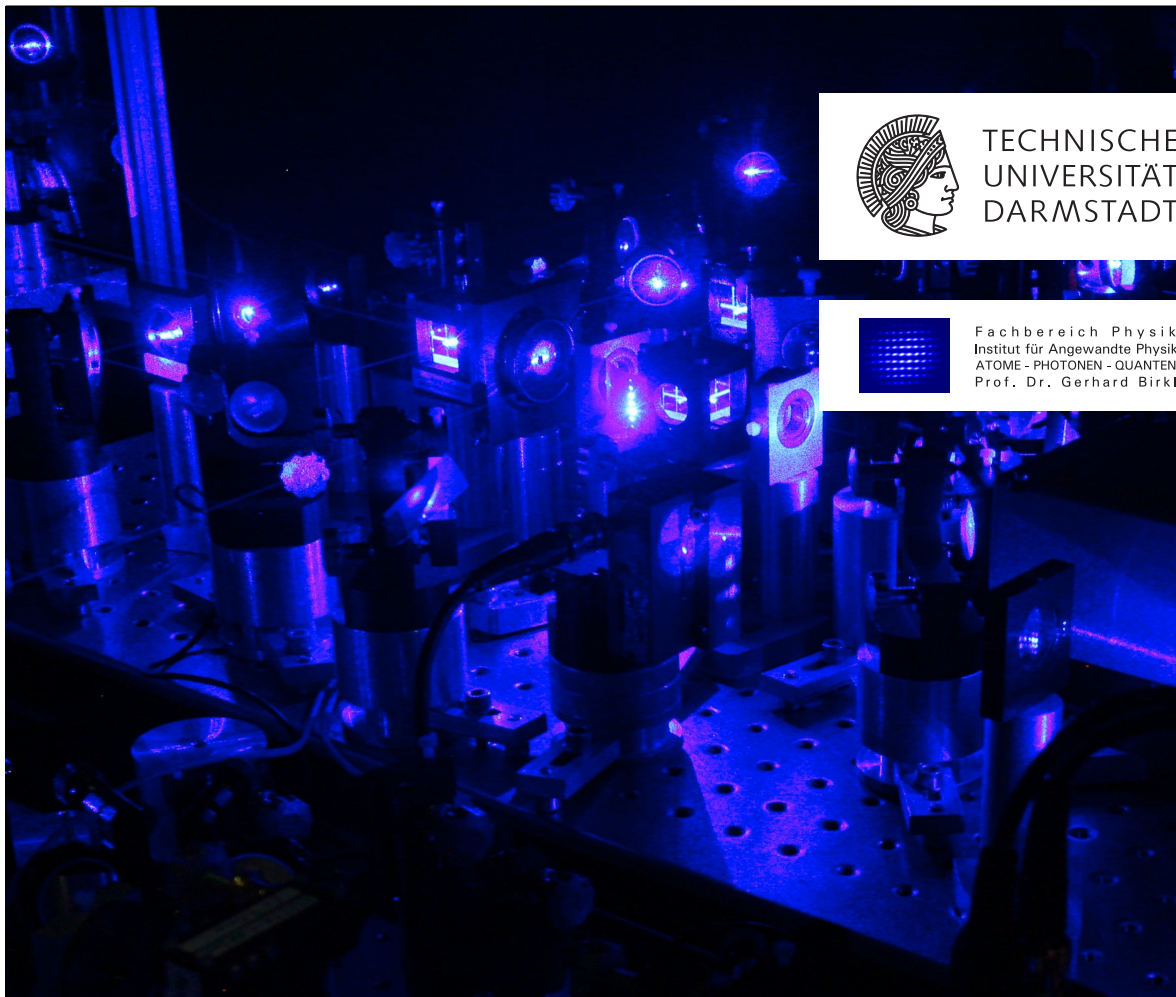
# Laser Spectroscopic Investigation of Exotic States in Noble Gases

---

**Laserspektroskopische Untersuchungen von exotischen Zuständen in  
Edelgasatomen**

Zur Erlangung des Grades eines Doktors der Naturwissenschaften (Dr. rer. nat.)  
genehmigte Dissertation von Alexander Martin, M.Sc. aus Darmstadt  
Tag der Einreichung: 07.02.2017, Tag der Prüfung: 26.04.2017  
2017 — Darmstadt — D 17

1. Gutachten: Prof. Dr. Gerhard Birkl
2. Gutachten: Prof. Dr. Thomas Walther



Laser Spectroscopic Investigation of Exotic States in Noble Gases  
Laserspektroskopische Untersuchungen von exotischen Zuständen in Edelgasatomen

Genehmigte Dissertation von Alexander Martin, M.Sc. aus Darmstadt

1. Gutachten: Prof. Dr. Gerhard Birkel
2. Gutachten: Prof. Dr. Thomas Walther

Tag der Einreichung: 07.02.2017

Tag der Prüfung: 26.04.2017

Darmstadt – D 17

Bitte zitieren Sie dieses Dokument als:

URN: urn:nbn:de:tuda-tuprints-66662

URL: <http://tuprints.ulb.tu-darmstadt.de/6666>

Dieses Dokument wird bereitgestellt von tuprints,

E-Publishing-Service der TU Darmstadt

<http://tuprints.ulb.tu-darmstadt.de>

[tuprints@ulb.tu-darmstadt.de](mailto:tuprints@ulb.tu-darmstadt.de)



Die Veröffentlichung steht unter folgender Creative Commons Lizenz:

Namensnennung – Keine kommerzielle Nutzung – Keine Bearbeitung 4.0 International

<http://creativecommons.org/licenses/by-nc-nd/4.0/>

---

# Abstract

The focus of this thesis lies on exotic states of noble gases, in particular metastable neon ( $\text{Ne}^*$ ) and boron-like argon ions ( $\text{Ar}^{13+}$ ): the former shows extraordinary collisional properties due to its high internal energy compared to its low kinetic energy. On the other hand, highly charged ions, such as  $\text{Ar}^{13+}$ , can be used to verify quantum electrodynamics with extremely high accuracy by determining their magnetic moments. These extraordinary atomic states can be probed with methods of laser spectroscopy and allow for deep insights of timely physical question.

The magnetic moment of bound electrons in  $\text{Ar}^{13+}$  shall be determined by the energy-splitting of the Zeeman sublevels of the fine structure transition  $^2P_{1/2} - ^2P_{3/2}$  at a wavelength of 441 nm in the magnetic field of a Penning trap. For this, the transition is measured by means of microwave and fluorescence laser spectroscopy. The first part of this thesis presents the laser system for the spectroscopy of  $\text{Ar}^{13+}$  and tellurium  $^{130}\text{Te}_2$ . Using a polarization stabilization scheme, a single-mode diode laser with a high long-term stability of up to two days has been developed. Using a Doppler-free  $^{130}\text{Te}_2$ -spectroscopy, six lines close to the expected  $\text{Ar}^{13+}$  transitions have been characterized with an absolute frequency accuracy of 2.2 MHz. A first characterization of the  $\text{Ar}^{13+}$  fluorescence spectroscopy has been conducted with a dark-measurement without ions. During this process, the measured background signal was reduced by three orders of magnitude by optimizing the setup. Thus, a reliable laser system is provided for experiments with ions, as planned for the near future.

The second part of this thesis investigates the two-body collisional interactions of ultra-cold  $\text{Ne}^*$  atoms. Inelastic collisions of  $\text{Ne}^*$  atoms leads to losses due to Penning and associative ionization. The efficient detection of the ions produced by these processes allows for determining the collision rate. For the investigations, a laser-cooled atom cloud is prepared in a magnetic trap at 350  $\mu\text{K}$ . The measurement of the inelastic collision rate in a regime between 20  $\mu\text{K}$  and 350  $\mu\text{K}$  confirms the theoretical predicted temperature-independent rate for  $^{20}\text{Ne}$  and  $^{22}\text{Ne}$  of mixtures of the Zeeman sublevels  $m_j = +2$  and  $m_j = +1$ . Furthermore, the dependence of the collision rate on external magnetic fields has been measured. For fields up to 120 G, a suppression by a factor of 5.6 for  $^{22}\text{Ne}$  has been proved. Additionally, the so called  $\delta$ -kick cooling, a method for manipulating the phase-space density of cold atom clouds, was implemented by using the magnetic trap. This allowed for a variation of the velocity distribution of the cloud over a range, which corresponds to an effective temperature between 10  $\mu\text{K}$  and 460  $\mu\text{K}$ .



---

# Zusammenfassung

Der Fokus dieser Arbeit liegt auf exotischen Zuständen von Edelgasatomen, insbesondere metastabilem Neon ( $\text{Ne}^*$ ) und Bor-ähnlichen Argonionen ( $\text{Ar}^{13+}$ ): Während ersteres durch seine hohe interne Energie im Vergleich zur niedrigen kinetischen Energie außergewöhnliche Stoßeigenschaften aufzeigt, lässt sich durch Bestimmung des magnetischen Moments gebundener Elektronen in hoch geladenen Ionen, wie  $\text{Ar}^{13+}$ , die Quantenelektrodynamik präzise überprüfen. Diese extremen Zustände von Atomen können mit Methoden der Laserspektroskopie untersucht werden und erlauben tiefe Einblicke in aktuelle physikalische Fragestellungen.

Das magnetische Moment gebundener Elektronen in  $\text{Ar}^{13+}$  soll über die im Magnetfeld einer Penningfalle energetisch-aufgespaltenen Zeeman-Unterstufen des optischen Feinstrukturübergangs  $^2P_{1/2} - ^2P_{3/2}$  bei 441 nm bestimmt werden. Hierzu wird der Übergang mittels Mikrowellen- und Fluoreszenz-Laserspektroskopie untersucht. Diese Arbeit beschäftigt sich im ersten Teil mit der Entwicklung eines Lasersystems für die Spektroskopie von  $\text{Ar}^{13+}$  und Tellur  $^{130}\text{Te}_2$ . Unter Verwendung einer Polarisationsstabilisierung wurde ein einfrequenter Diodenlaser mit einer hohen Langzeitstabilität von bis zu zwei Tagen entwickelt. Mit einer Doppler-freien  $^{130}\text{Te}_2$ -Spektroskopie wurden sechs Linien in der Nähe der  $\text{Ar}^{13+}$ -Übergänge mit einer absoluten Frequenzgenauigkeit von 2,2 MHz bestimmt. Eine erste Charakterisierung der Fluoreszenzspektroskopie von  $\text{Ar}^{13+}$  in der Penningfalle wurde mit Dunkelmessungen ohne Ionen durchgeführt. Das dabei auftretende Untergrundsignal konnte durch Optimierungen des Aufbaus um drei Größenordnungen reduziert werden. Damit steht das Lasersystem für Experimente an Ionen bereit.

Der zweite Teil dieser Arbeit untersucht die Zweikörper-Stoßwechselwirkung ultrakalter  $\text{Ne}^*$ -Atome. Bei inelastischen Stößen zwischen  $\text{Ne}^*$ -Atomen kommt es zum Teilchenverlust durch Penning- oder assoziativer Ionisation. Der effiziente Nachweis der dabei entstehenden Ionen erlaubt die Bestimmung der Stoßrate. Zur Untersuchung dieser Prozesse wird eine Atomwolke durch Laserkühlung in einer Magnetfalle bei 350  $\mu\text{K}$  präpariert. Die Bestimmung der inelastischen Stoßrate in Abhängigkeit der relativen Kollisionsenergie im Bereich zwischen 20  $\mu\text{K}$  und 350  $\mu\text{K}$  bestätigt die theoretisch vorhergesagte, temperaturunabhängige Rate für  $^{20}\text{Ne}$  und  $^{22}\text{Ne}$  in Mischungen der Zeeman-Unterstufen  $m_j = +2$  und  $m_j = +1$ . Des Weiteren wurde der Einfluss externer Magnetfelder auf die Stoßrate gemessen. Hier wurde bei Feldern bis 120 G eine Unterdrückung der Stoßrate um einen Faktor 5,6 für  $^{22}\text{Ne}$  nachgewiesen. Außerdem wurde die sogenannte  $\delta$ -Stoßkühlung, eine Methode zur Manipulation des Phasenraumvolumens kalter Atomwolken, mit Hilfe der Magnetfalle realisiert. Damit ließ sich die Impulsverteilung der Wolke über einen Bereich variieren, welcher einer effektiven Temperatur von 10  $\mu\text{K}$  und 460  $\mu\text{K}$  entspricht.



---

---

# Contents

<b>1</b>	<b>Introduction</b>	<b>1</b>
<b>2</b>	<b>Preparation and Detection of Boron-like Ar<sup>13+</sup></b>	<b>5</b>
2.1	Properties of Boron-like Argon Ions . . . . .	6
2.2	Preparation and Trapping of Ions . . . . .	8
2.3	Laser System . . . . .	10
2.3.1	Master Laser . . . . .	12
2.3.2	Spectroscopy Laser . . . . .	24
2.3.3	Transfer Cavity . . . . .	25
2.3.4	Tellurium Spectroscopy . . . . .	26
2.4	Towards Laser Spectroscopy of Ar <sup>13+</sup> . . . . .	27
2.4.1	Optical Excitation and Detection Setup . . . . .	27
2.4.2	Experimental Control Scheme and Data Recording System . . .	32
2.4.3	Background Signal Analysis . . . . .	34
<b>3</b>	<b>Tellurium Spectroscopy</b>	<b>43</b>
3.1	Refractive Index of Air . . . . .	43
3.2	Continuous Frequency Stabilization Scheme . . . . .	45
3.2.1	High Resolution Frequency Scan over Several Gigahertz . . . . .	48
3.3	Frequency Determination of Important Lamb dips . . . . .	50
3.4	Absolute Frequency Determination with the Te <sub>2</sub> -Spectrum . . . . .	55
3.5	Long Term Characterization of the Laser System . . . . .	58
3.5.1	Air Pressure Dependence of the Spectroscopy-Laser Frequency .	58
3.5.2	Long Term Frequency Stability of the Laser System . . . . .	60
3.6	Conclusion . . . . .	62
<b>4</b>	<b>Preparation and Detection of Laser Cooled Metastable Neon Atoms</b>	<b>65</b>
4.1	Properties of Metastable Neon . . . . .	65
4.2	Measurement Setup . . . . .	67
4.2.1	Creation and Transport of Metastable Neon Atoms . . . . .	68
4.2.2	Magneto-Optical and Magnetic Trap . . . . .	68
4.3	Detection . . . . .	70
4.3.1	Optical Detection . . . . .	70
4.3.2	Single Atom Detection . . . . .	72

<b>5</b>	<b>Dynamics of a Cold Atom Cloud</b>	<b>75</b>
5.1	Density Distribution in a Harmonic Potential . . . . .	75
5.1.1	Velocity Distribution . . . . .	76
5.1.2	Position Distribution . . . . .	77
5.2	Free Expansion of an Atom Cloud and Reduction of Collision Energy .	78
5.2.1	Local Velocity Distribution . . . . .	81
5.3	Dynamics of an Atom Cloud in a Harmonic Potential . . . . .	82
5.4	General Dynamics of an Atom Cloud after $\delta$ -Kick Cooling . . . . .	84
5.4.1	Phase Space Density Discussion . . . . .	89
5.5	Implementation of $\delta$ -Kick Cooling with Ne* atoms . . . . .	89
5.5.1	Preparation and Measurement . . . . .	90
5.5.2	Influence of the Primary Expansion Time $t_{\text{pre}}$ . . . . .	90
5.5.3	Influence of the $\delta$ -Kick Cooling Length . . . . .	94
5.5.4	Cloud Dynamic during $\delta$ -Kick Cooling . . . . .	100
5.6	Conclusion . . . . .	104
<b>6</b>	<b>Magnetic Field Dependence of Ionizing Collisions of Ne*</b>	<b>105</b>
6.1	Measurement Evaluation . . . . .	105
6.2	Ionizing Collisions for spin polarized Ne* in $^3P_2, m_J = +2$ . . . . .	108
6.3	Comparison of Ionizing Collisions between spin polarized Ne* in $m_J =$ +2 and $m_J = -2$ . . . . .	110
6.4	Conclusion . . . . .	113
<b>7</b>	<b>Temperature Dependence of Ionizing Collisions of Ne*</b>	<b>115</b>
7.1	Measurement Evaluation . . . . .	115
7.2	Temperature Depending Ionizing Collisions of Spin Polarized Neon . .	117
7.3	Temperature Dependent Ionizing Collisions of Neon Spin Mixtures . .	120
7.4	Conclusion . . . . .	125
<b>8</b>	<b>Summary and Outlook</b>	<b>127</b>
<b>A</b>	<b>Tellurium Spectrum</b>	<b>I</b>
<b>B</b>	<b>List of Publications</b>	<b>XI</b>
	<b>Bibliography</b>	<b>XIII</b>

---

# 1 Introduction

The first observations of spectral lines in the solar spectrum at the beginning of the 19<sup>th</sup> century by Wollaston and Fraunhofer [1, 2] lead to the development of models for the inner structure of atoms and molecules, such as the Bohr model, and resulted in the theory of modern quantum mechanics. With the development of lasers [3–5], the achievable resolution in atom spectroscopy increased by more than nine orders of magnitude: whereas modern optical spectrum analysers reach a resolution of  $10^{-7}$  [6], current laser spectroscopy yields resolutions in the sub-Hz regime with relative accuracy of  $3.8 \times 10^{-16}$  [7]. The availability of strong coherent light sources led to methods for cooling of charged [8, 9] and neutral atoms [10, 11] and also allowed for trapping of neutral atoms [12–14]. These methods are excellent tools to test quantum electrodynamics (QED) [15–17] with high accuracy and to study the interaction of laser-cooled atoms. This thesis describes two aspects how laser spectroscopy of exotic states of noble gases leads to new insights of these two timely physical questions: boron-like argon ( $\text{Ar}^{13+}$ ) is a good first candidate for the new ARTEMIS Penning trap which allows for high precision tests of QED, whereas metastable neon ( $\text{Ne}^*$ ) is highly sensitive to collision interactions, such as inelastic two-body collisions.

QED describes the interaction of light and matter in the context of relativistic quantum mechanics. A good choice for QED tests under exceptional conditions are highly charged ions (HCI), since the high fields of up to  $10^{18} \text{ V m}^{-1}$  in the vicinity of the nucleus for example change the energy difference between atom levels, the lifetimes of excited states, and the magnetic moments  $\mu$  of the atom shell. Experimentally determined quantities include the fine-structure and hyperfine-structure splitting, the Lamb-shift, and the Landé  $g$ -factor [18, 19]. In this thesis, the Landé factor (gyromagnetic factor or  $g$ -factor) is of specific interest. The  $g$ -factor is a dimensionless quantity and connects the spin  $S$  to the magnetic moment  $\mu$ :

$$\mu = g \frac{\mu_B S}{\hbar},$$

with Planck's constant  $\hbar$  and the Bohr magneton  $\mu_B$ . This  $g$ -factor can be calculated with high accuracy in the framework of QED and its determination is the goal of various high precision measurements. For example, the most precise measurement for the  $g$ -factor was performed with a free electron in a Penning trap and yielded a relative uncertainty of  $10^{-13}$ , whereas the relative accuracy of theoretical predictions is good to a few parts per billion. These high resolutions in both theory and experiment lead to the currently most precise value for the mass of the electron [20].

For calculations of the Landé  $g$ -factor of bound electrons in an atom shell, additional bound-state QED effects, arising from the inter-electronic interactions [21],

---

must be considered. Due to the Coulomb interaction, the size of electronic shell shrinks with the degree of ionization [22]. Therefore, measurements of the magnetic moments in HCIs are sensitive to these inter-electronic QED contributions. These measurements of the  $g$ -factor of bound electrons are performed by spectroscopy of the atomic transitions which yields the magnetic moments. Since the imbalance between the charge of the nucleus and the atom shell shifts the wavelength of fine-structure and hyper-fine-structure transitions in HCI to the optical regime, the measurements are based on laser spectroscopy of these levels.

The ARTEMIS experiment is designed for the spectroscopy of HCIs and is situated at HITRAP at the GSI Helmholtzzentrum für Schwerionenforschung and FAIR. It consists of a Penning trap, which stores ions with electric and magnetic fields. It is currently being commissioned and a connection to the accelerator facility is planned. A good first candidate for spectroscopy is boron-like argon ( $\text{Ar}^{13+}$ ), since the ions can be created from a neutral gas with an electron beam in a part of the trap dedicated to ion creation. In  $\text{Ar}^{13+}$ , the fine-structure transition between the states  $[(1s)^2(2s)^22p]^2 P_{1/2} - ^2 P_{3/2}$  has a transition wavelength of 441 nm. The large magnetic field of  $B \approx 7\text{T}$  in the Artemis Penning trap leads to an energy splitting of the Zeeman sub-levels of 65 GHz for the ground state  $^2P_{1/2}$  and 130 GHz for the excited state  $^2P_{3/2}$ . This level scheme allows for a double resonance spectroscopy with microwaves and laser light to determine the bound-electron  $g$ -factor of both states [23].

The second part of this thesis investigates two-body collisions of metastable neon. In general, the collisional interaction of neutral atoms can be studied under well-controlled conditions as they are provided by laser cooling and trapping. External environmental influences are negligible due to the ultra-high vacuum conditions in the experiments. In atom clouds with several  $10^8$  atoms, temperatures of less than one millikelvin can be created and the density of the trapped atom clouds can be manipulated, which allows for tuning of the relative collision energies of two interacting atoms. For the preparation and storage of the atom clouds, magneto-optical traps (MOT) and magnetic traps are often used [11].

The first trapping experiments used sodium [10,24], but a variety of atomic species can be trapped today in magneto-optical traps [25–28], even molecules have been captured [29]. Rather exotic atom species are excited metastable rare gases ( $\text{Rg}^*$ ). Their closed ground-state shell structure results in an excitation energy for the first excited state of more than half of the ionization energy ( $\approx 10\text{eV}$ ). Since this large energy difference is not suitable for laser cooling and the lifetime of the first excited state is rather long with a few seconds, the first excited state is used as the new effective ground state in experiments. This leads to a system with high internal energy and simultaneously low kinetic energies (below 1 mK or  $\approx 10^{-7}\text{eV}$ ).

The collisional interactions of metastable noble gases differ significantly from collisions of alkali atoms. The high internal energy allows for inelastic collisions resulting in ionizing processes. Two different processes occur: In the Penning ionization (PI), the collision between two  $\text{Rg}^*$  atoms generates an atom in the ground state (Rg), an

ionized atom ( $Rg^+$ ), and an electron, whereas the associative ionization (AI) yields an ionized dimer ( $2Rg^+$ ) and a free electron. These loss processes prevent further cooling of the atom cloud and sufficient increase of the spatial density towards a quantum degenerate gas, but allow for an easy observation of the collision rate due to high-efficient single-ion detection. Despite these collisional losses, a quantum degenerated Bose-Einstein condensate could be realized with  $He^*$  by means of spin polarization of the ensemble [30]. In the case of  $He^*$ , spin polarization leads to collision suppression by a factor of  $\approx 10^4$  due to spin selection rules [31,32]. However, no suppression could be observed for heavier spin-polarized rare gases such as  $Ar^*$ ,  $Kr^*$  or  $Xe^*$ . In between  $^{20}Ne^*$  and  $^{22}Ne^*$ , which is the second noble gas in the periodic table, a suppression of 38(16) and 7(5) has been measured [33]. This intermediate behaviour makes neon an interesting candidate for further investigations. In this neon experiment, the atoms are stored in a magnetic trap and laser-cooled to about 350  $\mu$ K. The typical cloud size is between  $1 \times 10^8$  to  $2 \times 10^8$  atoms. For the detection of the ionization rate, a micro-channel plate is available.

In this thesis, investigations of two exotic states of rare gases, boron-like argon and metastable neon, will be presented. Laser cooling and the high detection efficiency of  $Ne^*$  are used to obtain the temperature dependence of inelastic  $Ne^*-Ne^*$  collisions in different spin states. The results of collisions with an externally applied magnetic field will also be presented. Aiming towards the spectroscopy of  $Ar^{13+}$ , the results of the laser system developed in this thesis and the characterization of a Doppler-free tellurium spectroscopy will be shown. The presented high-precision frequency measurements of a variety of tellurium lines close to the  $Ar^{13+}$  fine-structure transition can be used for an absolute wavelength determination.

This thesis is organized in six main parts:

**Chapter 2** summarizes atomic properties of boron-like argon ions and introduces the ARTEMIS experiment. One focus lies on the laser spectroscopy of  $Ar^{13+}$ , which includes the laser system and the optical excitation and detection setup. Therefore, a characterization of the spectroscopy without ions serves as a first test of the complete system.

**Chapter 3** describes the frequency stabilization of the laser system and the absolute frequency determination of selected  $^{130}Te_2$  transitions close to the expected position of the  $Ar^{13+}$  fine-structure transitions in the magnetic field of  $B \approx 7$  T of the ARTEMIS Penning trap. The results and the given instructions allows for further characterizations of transition frequencies with the Doppler-free tellurium spectroscopy.

**Chapter 4** summarizes the atomic properties of  $Ne^*$  and the setup for trapping and laser cooling of atoms in the neon experiment.

**Chapter 5** introduces the so called  $\delta$ -kick cooling, which allows for an efficient manipulation of the phase-space distribution of laser-cooled atom clouds. A theoretical description is developed and tested in the experiment with the magnetic trap.

**Chapter 6** discusses the measurement and results of rate coefficients for ionizing collisions of  $Ne^*$  atoms in dependence of magnetic fields up to 122.5 G for the Zeeman sublevels  $m_j = +2$  and  $m_j = -2$ .

---

**Chapter 7** presents rate coefficients for ionizing collisions of  $\text{Ne}^*$  atoms in dependence of the temperature. The evaluation covers a range of 20  $\mu\text{K}$  to 300  $\mu\text{K}$  and the spin mixtures of the Zeeman sublevels  $m_J = +2$  and  $m_J = +1$ .  
**Chapter 8** concludes this thesis with a summary and an outlook.

---

## 2 Preparation and Detection of Boron-like Ar<sup>13+</sup>

In modern atomic physics, laser-spectroscopical investigations of highly charged ions are conducted in accelerator rings [34, 35] and traps [36–38]. The advantage of accelerators are the availability of any elements with arbitrary charge states, whereas the advantage of traps are the long storage and observation times of up to one year [39] and the low Doppler broadening due to temperatures of typically between 300 K and 4 K but even down to millikelvin [37] which allows for high-resolution spectroscopy.

Highly charged ions are typically produced in electron-beam ion sources (EBIS) with ionizing collisions of electrons. Breeding of charge states up to hydrogen-like and bare uranium is possible [40] and also fluorescence spectroscopy can be done in the EBIS at high kinetic energies of hundreds of eV. However, efficient laser spectroscopy requires ion clouds with a lower Doppler broadening. This can be done by transporting the cloud to an ion trap and consecutive cooling. Typical cooling methods in traps are resistive cooling by coupling the ion motion to a resonator at the temperature of liquid helium (4 K), buffer gas cooling due to thermalizing collisions, or sympathetic cooling with another laser-cooled ion species.

The ARTEMIS Penning trap can produce ions with an integrated ion source and consists of two parts: an ion creation section and a highly harmonic spectroscopy trap. A cold valve allows for the loading of rare gases in the creation section, where charge states of up to helium-like Ar<sup>16+</sup> can be reached. A future upgrade will give access to even higher charged ions from the HITRAP facility and from the GSI accelerator facility. The resistive cooling of the ions in the trap is done via the coupling of the axial motion with an electrical resonator at cryogenic temperatures of about 4 K. Resonators also allow for the detection of the different ion species via the mass-to-charge ratio dependence of oscillation frequency.

For the laser and microwave spectroscopy of the fine-structure transition of Ar<sup>13+</sup>, the ARTEMIS Penning trap has a cylindrical structure which allows for optical access in axial direction [41]. The laser light generation for the spectroscopy is facilitated by the recent development of blue semiconductor lasers [42–44] which make compact laser setups possible. External cavity diode lasers (ECDLs) with these diodes are used in the laser system which will be presented in detail in this chapter.

At the beginning of this chapter, the properties of boron-like Ar<sup>13+</sup> will be summarized. The experimental setup of the Penning trap is discussed in detail in the thesis of D. v. Lindenfels [45]. Therefore, only an overview will be given in this chapter with the focus on the optical excitation and detection setup. The chapter finishes

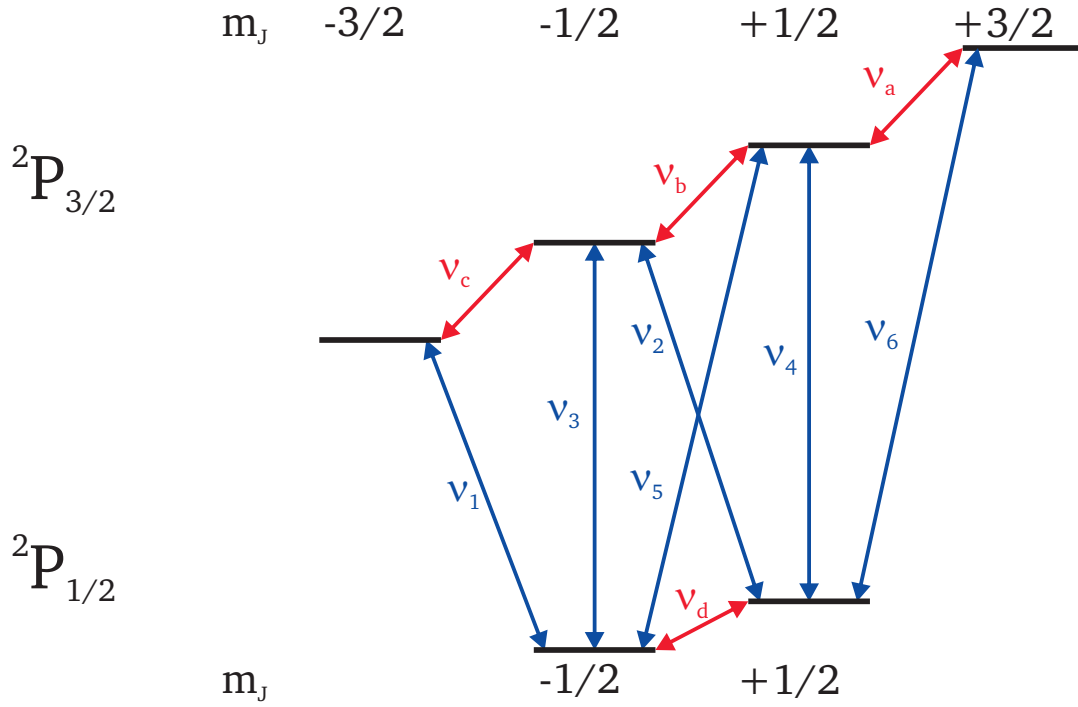


**Figure 2.1:** Fine-structure transitions of  $\text{Ar}^{13+}$  including the Zeeman splitting. The optical transitions are shown in blue and the microwave transitions in red. The transition frequency of  $\nu_a$ ,  $\nu_b$ , and  $\nu_c$  is about 130 GHz and the frequency of  $\nu_d$  is about 65 GHz. The optical transitions have a wavelength of about 441 nm.

with a characterization of the excitation and detection setup for laser spectroscopy in the Penning trap.

## 2.1 Properties of Boron-like Argon Ions

Argon is a rare gas and has three stable isotopes  $^{36}\text{Ar}$ ,  $^{38}\text{Ar}$ , and  $^{40}\text{Ar}$  with relative natural abundances in mole fractions of 0.3336(21)%, 0.0629(7)%, and 99.6035(25)% [46]. All these isotopes are bosonic and have no nuclear spin. The laser spectroscopy is done with Boron-like argon ( $\text{Ar}^{13+}$ ) which has five electrons in the shells  $(1s)^2(2s)^22p$  which form the ground state  $^2P_{1/2}$  and the first excited state  $^2P_{3/2}$ .

The energy splitting of the magnetic-dipole fine-structure transitions in hydrogen-like ions is proportional to the fourth order of the nuclear charge  $Z^4$  [47, 48]. The scaling is similar for few-electron systems and leads for the magnetic dipole transition  $^2P_{1/2} - ^2P_{3/2}$  in  $\text{Ar}^{13+}$  to a splitting of 2.8 eV. This corresponds to a wavelength of 441.25575(17) nm [49] which is in the blue part of the visible spectrum. Since the magnetic-dipole transition is forbidden, the excited state  $^2P_{3/2}$  has a large lifetime of 9.573(6) ms [36] and thus a natural linewidth of  $\Gamma \approx 2\pi \times 16.63(1)$  Hz.

The laser spectroscopy of  $\text{Ar}^{13+}$  is conducted in a Penning trap with a magnetic field of  $B_0 = 7.003 \text{ T}$ . This leads to a splitting of the ground and excited states due to the Zeeman effect (Fig. 2.1). Because of the strong field, higher orders of the Zeeman effect must be considered which can be evaluated within perturbation theory [23] and yield the energy shift

$$E(B) = E_0 + \Delta E_1(B) + \Delta E_2(B) + \Delta E_3(B) \text{ with} \quad (2.1)$$

$$\Delta E_1(B) = g_J m_J \mu_B B \text{ and} \quad (2.2)$$

$$\Delta E_2(B) = g_J^{(2)} m_J \frac{(\mu_B B)^2}{m c_0^2} \text{ and} \quad (2.3)$$

$$\Delta E_3(B) = g_J^{(3)} m_J \frac{(\mu_B B)^3}{(m c_0^2)^2}, \quad (2.4)$$

where  $E_n(B)$  denotes the  $n$ th order of the Zeeman effect,  $E_0$  is the energy of the unperturbed state in absence of a magnetic field,  $g_J$  is the Landé  $g$ -factor in first order,  $g_J^{(n)}$  is the Landé  $g$ -factor in  $n$ th order,  $m_J$  is the Zeeman sublevel,  $m$  is the atom mass, and  $c_0$  is the speed of light. The ground state  $^2P_{1/2}$  has a calculated Landé  $g$ -factor of  $g_{1/2} = 0.663\,647(1)$  and the excited state has a  $g$ -factor of  $g_{3/2} = 1.332\,285(3)$  [50]. This leads to an energy splitting between the sub levels in first order of  $\approx 65 \text{ GHz}$  for the ground state and  $\approx 130 \text{ GHz}$  for the excited state. The second order leads to corrections of a few MHz and the third order only to a few hundreds of Hz (exact values in table 2.2 in [45] and table 2 in [23]). This yields six different optical transitions which are denoted with increasing frequency from  $\nu_1$  to  $\nu_6$ . The total shifts and the resulting wavelengths are shown schematically in figure 2.1 and given in table 2.1. The transitions  $\nu_3$  and  $\nu_4$  emit linear polarized light perpendicular to the magnetic field in radial direction, while the other optical transitions emit circular polarized light mainly in axial direction. Since the excitation and detection is done in axial direction, only four transitions can be used in this experiment.

Transition	Frequency shift in MHz	Wavelength in nm	Axial excitation
$\nu_1$	-163 280	441.362	×
$\nu_2$	-97 769	441.319	×
$\nu_3$	-32 749	441.277	
$\nu_4$	32 761	441.234	
$\nu_5$	97 781	441.192	×
$\nu_6$	163 286	441.150	×

**Table 2.1:** Optical fine-structure transitions of  $\text{Ar}^{13+}$ . The frequency shift includes the corrections of the first and second order Zeeman-shift.

---

## 2.2 Preparation and Trapping of Ions

---

The preparation, storage, and spectroscopy of boron-like  $\text{Ar}^{13+}$ -ions in the ARTEMIS experiment are done in a cylindrical Penning trap. This section gives a brief overview of the experimental setup. A detailed description can be found in the thesis of D. v. Lindenfels [45].

A Penning trap uses static electric and magnetic fields for the storage of ions. A homogeneous magnetic field  $B$ , which defines the axial direction, leads to a radial confinement due to the Lorentz force, which forces charged particles on a cyclotron trajectory. The axial trapping is done with an electric quadrupole field. The combination of the fields yields an oscillatory motion with three characteristic oscillation frequencies: The axial oscillation due to the electric field is given by

$$\omega_z = \sqrt{\frac{qU_0}{md^2}} \quad (2.5)$$

with the particle charge  $q$ , the trapping potential  $U_0$ , the particle mass  $m$ , and the characteristic trap dimension  $d$  [51]. The radial motion oscillates with the reduced cyclotron frequency  $\omega_+$  and the magnetron drift frequency  $\omega_-$  which are given by

$$\omega_+ = \frac{\omega_c}{2} + \sqrt{\left(\frac{\omega_c}{2}\right)^2 - \frac{\omega_z^2}{2}} \quad \text{and} \quad (2.6)$$

$$\omega_- = \frac{\omega_c}{2} - \sqrt{\left(\frac{\omega_c}{2}\right)^2 - \frac{\omega_z^2}{2}}, \quad (2.7)$$

where  $\omega_c$  is the unperturbed cyclotron frequency which would result due to the magnetic field in absence of the electric field. It is given by  $\omega_c = \frac{q}{m}B$ . In an ideal Penning trap with an electric quadrupole field and a homogeneous magnetic field, the invariance theorem  $\omega_c^2 = \omega_+^2 + \omega_-^2 + \omega_z^2$  yields a quadratic dependence of the four frequencies. Thus, the design of the Penning trap in the experiment includes compensation electrodes for fine tuning of the spectroscopy trap.

The magnetic field of up to 7.003 T for the ARTEMIS Penning trap is produced by a superconducting magnet (Fig. 2.2 a)). Its coils are cooled with liquid helium in a thermally isolated and with liquid nitrogen cooled tank. The cylindrical electrode setup is situated in a vertical bore at room temperature (Fig. 4.5 in [45] and Fig. 2.2 b)). The electrode design with several cylindrical electrodes allows for a variety of electric field configurations. The complete trap setup is cooled down with a cold head to around 4 K.

The spectroscopy trap is formed by 6 electrodes at the upper end of the setup. They are designed to produce a harmonic potential in axial direction. The top electrode consists of a BK7 glass substrate with an indium-tin-oxide coating. This allows for optical access to the centre of the spectroscopy trap from the top. One electrode is split in two segments. With these segments, the cyclotron motion of the ion cloud can

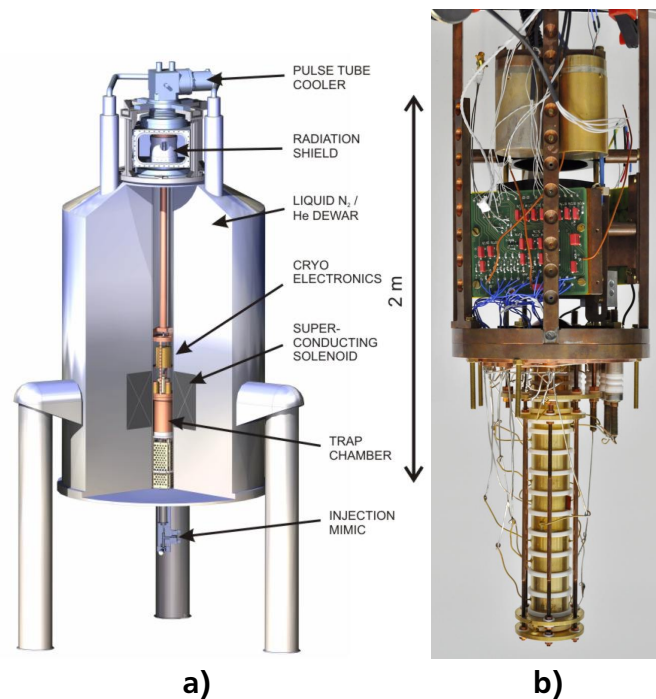


**Figure 2.2:** a) Drawing of the complete cryogenic setup in the magnet [45]. b) Image of the Penning trap with detection electronics. The trap is the gold-coated electrode structure in the lower half.

either be radially excited with an irradiated radio-frequency (RF) signal or the radial motion can be measured. Another electrode is split in four segments which allows for forming the ion cloud between a cigar shape and an oblate shape by applying a rotating-wall technique [52].

The creation trap is placed at the lower end of the setup and is based on a mechanically compensated design [53] for a harmonic potential. This part of the trap is used to superimpose ions and neutral gas with an electron beam. Due to collisions with the electrons, the gas is ionized and the charge state of the ions increases. The final charge state distribution depends on the electron-beam current, the electric field, and the breeding time (Sec. 5.4 in [45]). The electron beam is produced at the bottom of the setup utilizing a tip shaped cathode. A high voltage applied leads to an emission of electrons.

The argon gas is injected from a gas bottle. The pressure is reduced with several metering valves and the gas inlet is controlled with a shut-off valve and a cryogenic ultra-high-vacuum (UHV) valve. The last valve is attached to the Penning trap setup from below and consists of a meandering pattern bore in a copper block. Due to collisions, all incoming gas freezes on the walls. Thermal heating by an electric current through a resistor opens the valve for a short time and allows the argon to enter the creation trap.

---

After breeding the ions, they can be cooled and transported into the spectroscopy trap. The transport is done using an electrode-voltage sequence, which moves the axial trap centre upwards. Typical kinetic energies after ion breeding are on the order of a few hundred eV which corresponds to a temperature of several million kelvins. For cooling, an axial resonator at cryogenic temperatures is used as a thermal bath and is connected with the endcap electrode of the creation trap. This yields a coupling of the axial motion of the ions to the resonator via the induced image charges, thus cooling the ions down to 4 K.

The electronic detection of the ions is also realized by the axial resonator. A spectrum analyser in zero-span mode at the resonance frequency measures the signal amplitude, which is amplified with a cryogenic low-noise amplifier. Since the oscillation frequency of the ions depends on the charge-to-mass ration  $q/m$  and the trap depth  $U_0$  (Eq. (2.5)), the trap depth can be tuned in order to scan over all ion species in the trap (Chap. 5 in [45]). The in radial direction reduced cyclotron motion can be measured like the axial oscillation using a cyclotron resonator and the split ring-electrode.

---

## 2.3 Laser System

---

The laser spectroscopy of the fine-structure transition of  $\text{Ar}^{13+}$  requires a frequency stabilized laser at 441 nm which can be tuned over several gigahertz with sub-megahertz resolution. This stabilization is achieved with a secondary laser system. The full system consists of two lasers, the spectroscopy laser at 441 nm and a master laser at 452.756 nm, a transfer cavity, and a Doppler-free tellurium spectroscopy (Fig. 2.3).

The light of the master laser is split in two beams with a polarizing beam splitter (PBS). One beam is overlapped with the spectroscopy light for the tellurium spectroscopy using a second PBS. The other beam is used for the transfer cavity. To have a good beam quality in the cavity, the light is coupled into a 2 m polarization-maintaining single-mode fibre (P3-405BPM-FC-2 by Thorlabs). A fraction of about 1 mW of the spectroscopy-laser light is frequency shifted using a double-pass acousto-optic modulator (AOM) setup and coupled into a second fibre for the transfer cavity. The adjustment uses the negative first order of the diffracted beam after the AOM, which yields a negative frequency shift. The main beam can be switched with a PBS between the 27 m fibre to the Penning trap for the  $\text{Ar}^{13+}$  spectroscopy or the tellurium spectroscopy. For the latter spectroscopy, the beam is overlapped with the master laser light at the PBS. The light for the  $\text{Ar}^{13+}$  spectroscopy can be switched with a shutter. With a beam sampler and a photodiode in front of the fibre, the exact shutter timings are monitored. The AOM in front of the fibre is optional and can be used for an intensity stabilization of the light.

A stabilization chain allows for the controlled tuning of the spectroscopy-laser frequency. Therefore, the master laser is locked to a Lamb dip of the tellurium spectrum. The length of the transfer cavity is fixed with the stabilization of a longitudinal cavity

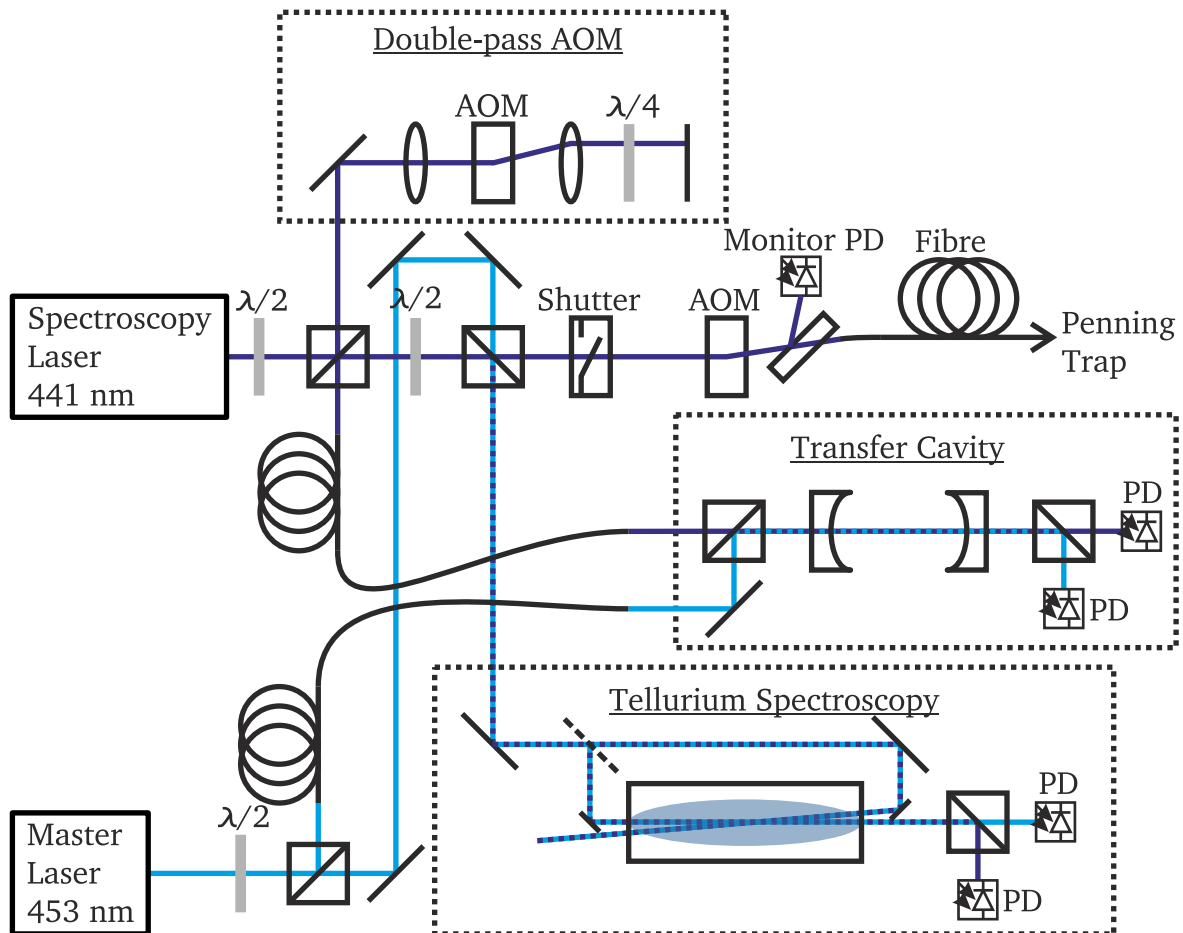


**Figure 2.3:** Setup of the laser system. The light from the master laser is split in two parts with a polarizing beam splitter (PBS), one for the tellurium spectroscopy and one for transfer resonator. A fraction of about 1 mW of the spectroscopy laser light is frequency shifted with the double-pass AOM and coupled into the fibre for the transfer resonator. The main beam can be split between the fibre to the Penning trap for the  $\text{Ar}^{13+}$  spectroscopy and the tellurium spectroscopy. For the latter, the beam is overlapped with the master laser light.

---

mode to the master-laser frequency while the spectroscopy laser is locked to another cavity mode via the double-pass AOM setup which allows for a fine tuning of the frequency. A detailed description of the locking scheme to cover the complete frequency range of the fine-structure transition of  $\text{Ar}^{13+}$  is given in chapter 3.

This section gives an overview of the different components of the laser system which was set up in the framework of this thesis.

---

### 2.3.1 Master Laser

---

The master laser is the heart of the stabilization scheme. It is frequency-stabilized to the tellurium spectroscopy and is used to keep the length and thus the free spectral range of the transfer cavity constant. The laser is a new-developed external-cavity diode laser (ECDL) based on an interference filter design. In this chapter the setup will be discussed and characterized. An important part will be the intra-cavity polarization lock, which increases the long-term stability of the laser to a stable operation over several days. The laser setup was developed together with Patrick Baus and a detailed description can be found in his master's thesis [54]. This chapter is based in large parts on a paper published during this thesis [55].

---

#### Setup of the Master Laser

---

The laser setup depicted in figure 2.4 is a variation of the design of Baillard et al. [56] in the form introduced by Thompson and Scholten in [57]. The light from the laser diode (LD) is collimated by a lens (L1) with 3.1 mm focal length. The external resonator consists of a silver coated mirror (M) (reflectivity  $R_M = 99\%$ ) and lens L2 ( $f = 18.4\text{mm}$ ) in a cat's eye configuration. The resonator has a total geometrical length of 59 mm. For adjustment of the resonator length, the mirror is glued to a piezoelectric ring-actuator with a length-change coefficient of approximately 100 nm/V. For outcoupling of the laser light, a polarization-dependent beam splitter cube (BS) is used in combination with a quarter-wave plate (QWP1). The BS has a transmittance of  $T_p \approx 90\%$  ( $10\%$ ) for p-polarized (s-polarized) light. Depending on the rotation angle of QWP1, the back-reflectivity of the combination of BS, QWP1, and M can be varied between  $T_p \cdot R_M \cdot T_s \approx 9\%$  and  $T_p \cdot R_M \cdot T_p \approx 80\%$ . The laser diode must therefore be mounted with its polarization axis in the p-plane of the BS. Two bandpass filters (F1 and F2) provide the wavelength selection. The laser uses interference filters (Semrock Laser-Line LL01-458) with a centre wavelength of 457.9 nm and a measured full width at half maximum (FWHM) of 1.6 nm at normal incidence. The filters are mounted on a rotary stage for easy tuning of the transmission wavelength. If required, a non-zero relative angle ( $\theta_1 \neq \theta_2$ ) allows for the modification of the effective spectral transmission characteristics.

The central element for improved long-term stability of this laser setup is the additional intra-cavity lock based on the Hänsch-Couillaud locking scheme [58] using

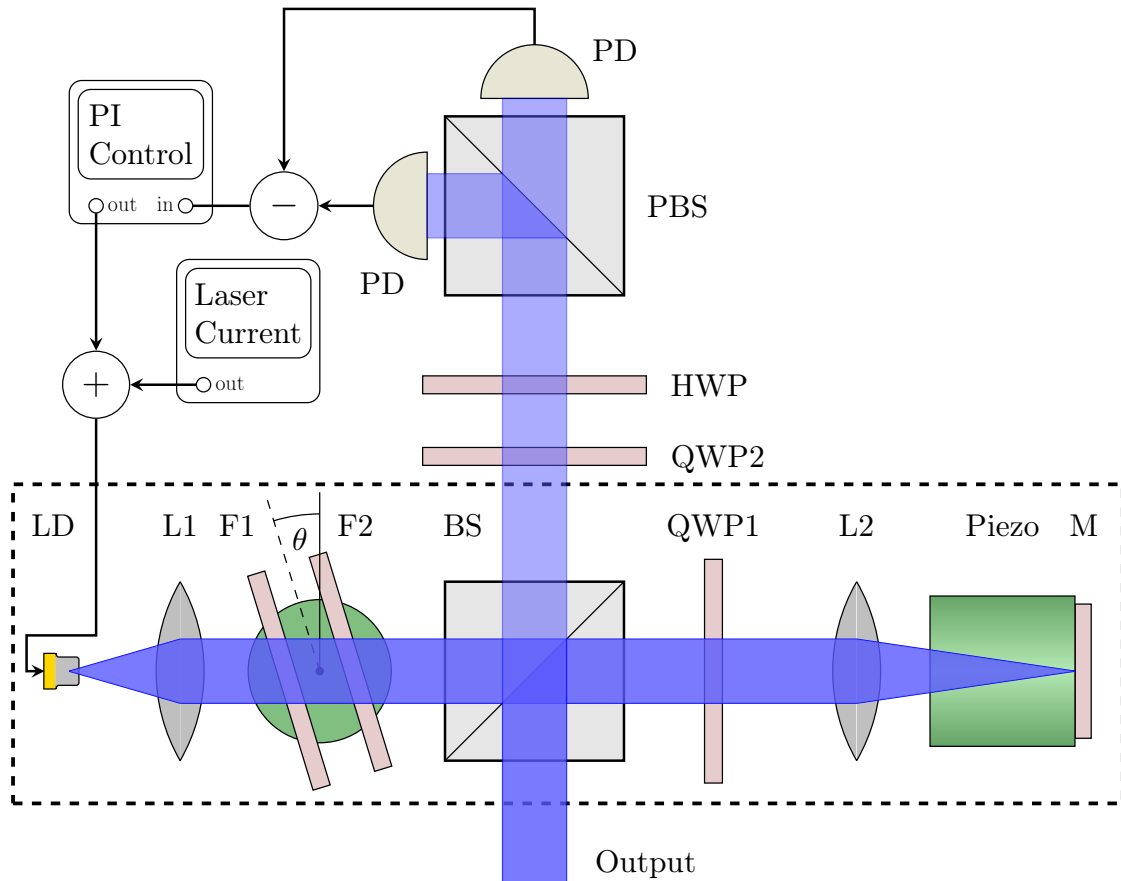


**Figure 2.4:** Schematic setup of the external-cavity diode laser (ECDL) based on figure 2 from [54]. The laser light is coupled out to the bottom. The external resonator consists of the laser diode (LD) and the mirror (M) in cat's eye configuration. The reflectivity can be adjusted by rotating the  $\lambda/4$ -plate (QWP1). The two interference filters (F1 and F2) are mounted on a rotary stage for easy wavelength tuning. The intra-cavity lock uses the upwards out-coupled light and consists of the two subtracting photo diodes (PD) and the polarizing beam splitter (PBS). With the  $\lambda/2$ -plate (HWP) and the  $\lambda/4$ -plate (QWP2) in front of the polarizing beam splitter the amplitude of the error signal can be maximized. The external resonator has a total geometrical length of 59 mm from laser diodes back facet to Mirror M.

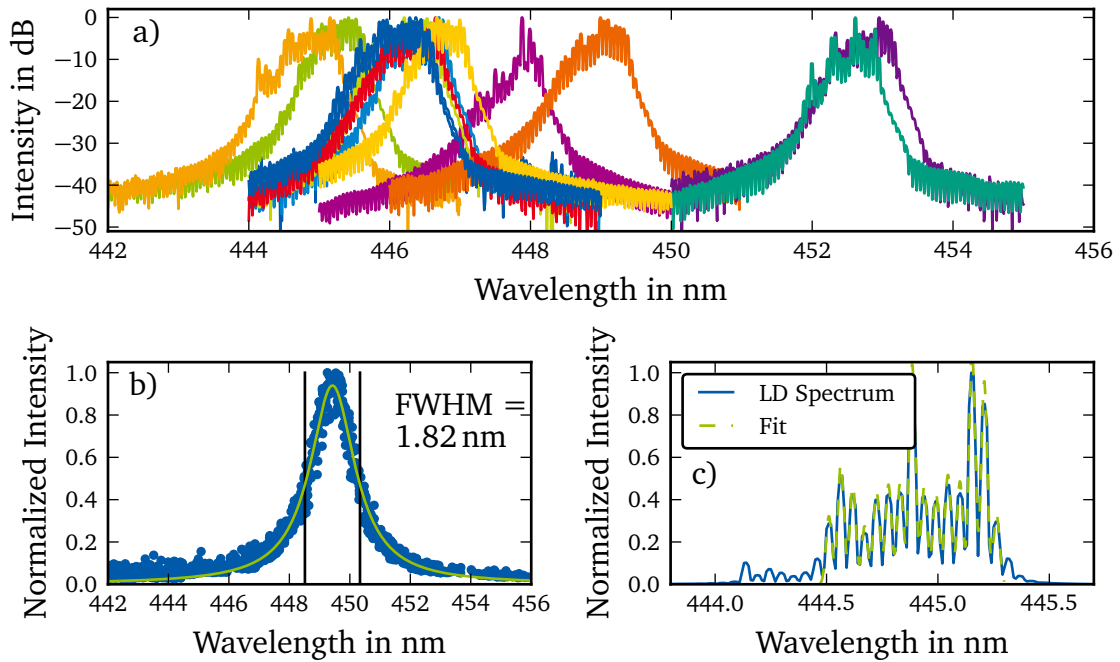


**Figure 2.5:** a) Spectra of twelve laser diodes PL-450B by OSRAM above the laser threshold measured in [54] with a current of 60 mA. b) Free running laser diode below the laser threshold. c) Close up view of the spectrum of a free running laser diode above the laser threshold from a). The internal mode separation of 0.0537(3) nm can be seen.

the fact, that a mismatch between the internal modes of the laser diode gain medium and the external resonator modes changes the state of polarization of the light in the external resonator. Following the implementation of Führer et al. [59], the second output beam produced by the beam splitter BS is used for generation of the respective error signal: The ratio between p- and s-polarization in the external resonator is measured by subtracting the photo-diode signals after the external-cavity polarizing beam splitter (PBS) (Fig. 2.4). With QWP2 and a half-wave plate (HWP), the signal-to-noise ratio of the error signal can be maximized. A proportional-integral (PI) controller locks the internal to the external resonator modes by regulating the laser current.

---

### Characterization of the Laser Diode

---

The ECDL setup uses the laser diode PL-450B by OSRAM [60]. It has an optical output power of 80 mW in a wavelength range from 440 nm to 460 nm and is a single-transverse-mode semiconductor laser. With an optical spectrum analyser (AQ6373 by YOKOGAWA) the spectra of twelve different free running laser diodes were measured from different batches by P Baus in [54] (Fig. 2.5 a)). All diodes were measured with a current of 60 mA. The wavelength for lasing ranges from 445.15 nm to 452.95 nm

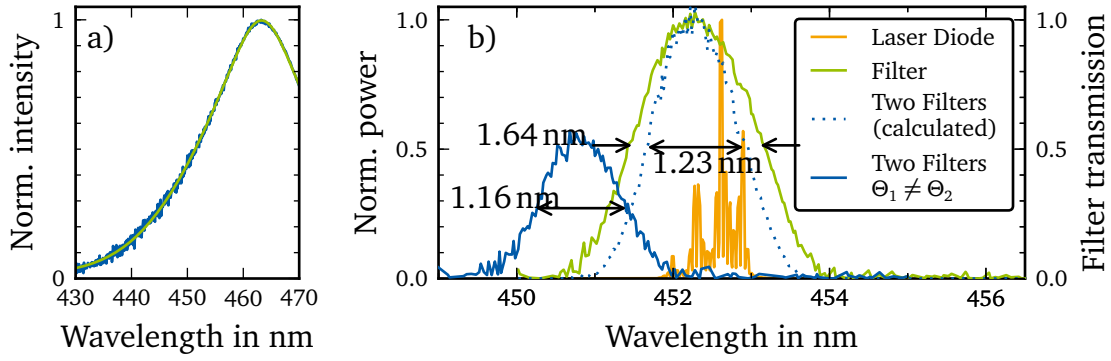


**Figure 2.6:** a) Spectrum of the LED used as light source. The centre wavelength at 463.3 nm and the FWHM of 23.8 nm are well suited for the filter characterization. b) Comparison of the emission spectrum of a free running laser diode (red) with filter transmission curves: (green) measured transmittance of one interference filter at 20°, (dotted blue) calculated transmittance of two parallel filters at 20° in series, and (yellow) two filters in series at  $\approx 23^\circ$  with a slight relative tilt ( $\theta_1 \neq \theta_2$ ).

with a mean value of 447.66 nm. Figure 2.5 b) shows the spectrum of a laser diode below the laser threshold. A fit yields a full width at half maximum (FWHM) of 1.82(2) nm, which is much smaller than the 20 nm width of typical infrared diodes [61]. Due to the narrow spontaneous-emission spectrum, a pre-selection for the desired wavelength is necessary. In addition, the wavelength shift with temperature of 0.06 nm/K for InGaN [62] is about five times smaller than for InGaAs. The peak structure of the spectrum of a free running LD (Fig. 2.5 c)) is the result of the internal resonator formed by the front and the back facet. The internal mode separation of

$$\Delta\lambda = 0.0537(3) \text{ nm or} \quad (2.8)$$

$$\Delta\nu = \frac{c_0}{\lambda_0} \cdot \Delta\lambda = 81.4(4) \text{ GHz} \quad (2.9)$$

can be clearly seen in the spectrum (Fig. 2.5 c)). This is in good agreement with the calculated spacing of  $\Delta\nu = \frac{c_0}{2 \cdot nL} = 94 \text{ GHz}$  with the length of the laser diode  $L = 600 \mu\text{m}$  [63] and the refractive index of 2.67 [62].

### Filter Characterization

For the laser, two identical laser line filters LL01-458-12.5 by Semrock are used. The data sheet specifies a central transmission wavelength of 457.9 nm and a spectral width of 1.7 nm to 3.2 nm. The transmission wavelength can be tuned by rotating the filter by an angle  $\theta$  leading to a shorter centre wavelength of

$$\lambda = \lambda_0 \sqrt{1 - \left(\frac{\sin \theta}{n}\right)^2}, \quad (2.10)$$

---

with the transmission wavelength at normal incident  $\lambda_0$ , the effective refractive index  $n$  of the filter, and the incident angle  $\theta$  as shown in figure 2.4.

With a small setup and the optical spectrum analyser, the filter has been characterized. The test setup used a blue ultra-bright LED as broadband light source, which was mounted at one end of a Thorlabs cage system. A rough collimation was achieved with a  $f = 50$  mm lens. The filter sat in a rotatable mount in front of the fibre coupler for the analyser. Figure 2.6 a) shows the background measurement for the calibration. The spectrum is fitted with a Voigt profile and has a FWHM of 23.8 nm and the maximum intensity at 463.3 nm. This is well suited for the filter characterization, which are depicted in figures 2.6 b) and 2.7 a). In the second figure, the filter transmission at different angles of incidence is depicted. The transmittance profile has Gaussian wings with a flattop at low angles, also implemented is the fit function of the transmittance profiles. With increasing angles, the centre wavelength shifts towards shorter wavelength. Also, the transmittance profile changes from a flattop to a Gaussian shaped and the absolute transmittance decreases. The quantitative results are shown in the figures 2.7 b) to e). Figure b) shows the centre wavelength over the angle together with the fit function using equation (2.10). The fit yields a centre wavelength of  $\lambda_0 = 458.3(1)$  nm and an effective refractive index of  $n_{\text{eff}} = 2.08(1)$ , which are in good agreement with the specification of  $n_{\text{eff}} = 1.98$  and  $\lambda = 457.9$  nm. The maximum transmittance, shown in c), stays above 95 % up to an angle of  $20^\circ$ . While the shape of the filter changes significantly with large angles, the full width at half maximum (FWHM) shows variations between 1.7 nm and 2.1 nm (Fig. 2.7 d)). A slight decrease of the FWHM from  $0^\circ$  to  $20^\circ$  is noticeable, but for higher angles it rises rapidly. The flattop width shown in figure e) shrinks almost in the same manner as the edge steepness, which is measured with the 10 %-to-90 % width, grows. This explains the minor variations in the FWHM up to an angle of  $20^\circ$ .

A comparison of the filters with the free running laser diode is shown in figure 2.6 b). The filter width is larger than the full emission spectrum of the laser diode and corresponds to the combined spectral width of more than 30 internal cavity modes. These are significantly more modes than in the ECDL setup of [57] in the infrared. Their setup uses an interference filter and laser diode combination, in which only five internal cavity modes fit into the transmission band of the filter. In their case, utilizing the edges of the gain profile of the diode allows for a stabilization of the laser wavelength. The smaller mode spacing – and the fact that the edges of the filters are not as steep as in the infrared – contribute significantly to the difficulty of achieving stable single-frequency operation of blue diode lasers. At the targeted wavelength of operation of 452.756 nm, the filter ( $\theta \approx 20^\circ$ ) has a FWHM = 1.64 nm, an edge steepness of 1.01 nm (10%-to-90% value), and a peak transmittance of  $\approx 98\%$  (Fig. 2.7). To improve the filter performance, two filters were mounted in series. This decreased the FWHM to 1.23 nm (Fig. 2.6 b)) and improved the edge steepness to 0.80 nm without significant loss in transmittance.

A simple model can be used to determine the behaviour of two filters, which are tilted against each other. Therefore, the fit of the flattop Gaussian under normal

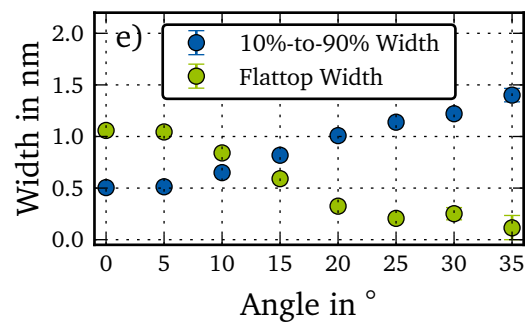
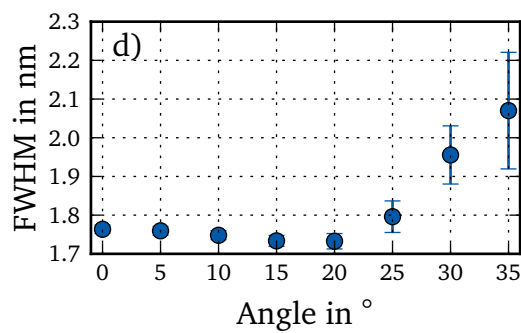
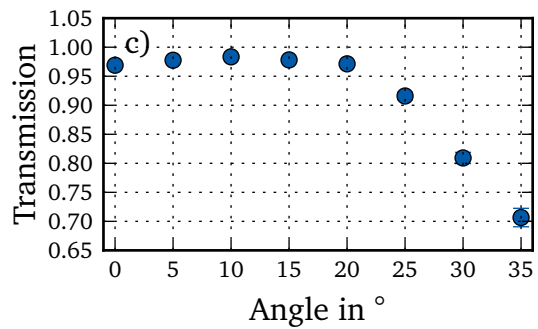
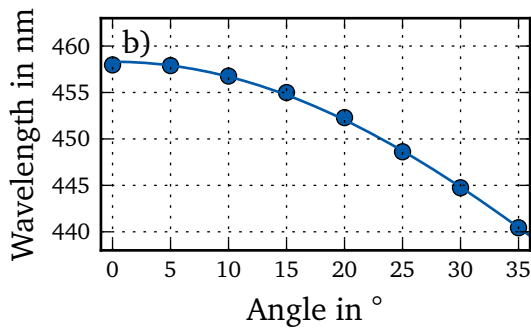
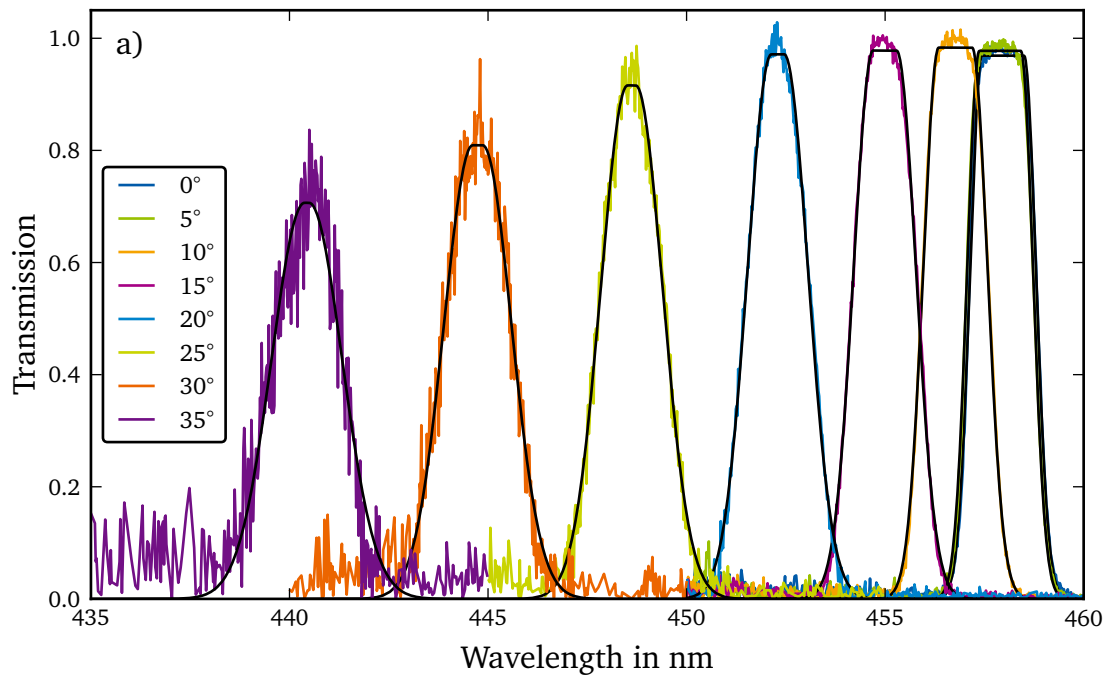


**Figure 2.7:** a) Filter transmission at different angles of incident of the light. The profiles are fitted with flattop Gaussian. b) to e) Results for the various fit parameters for different filter angles.

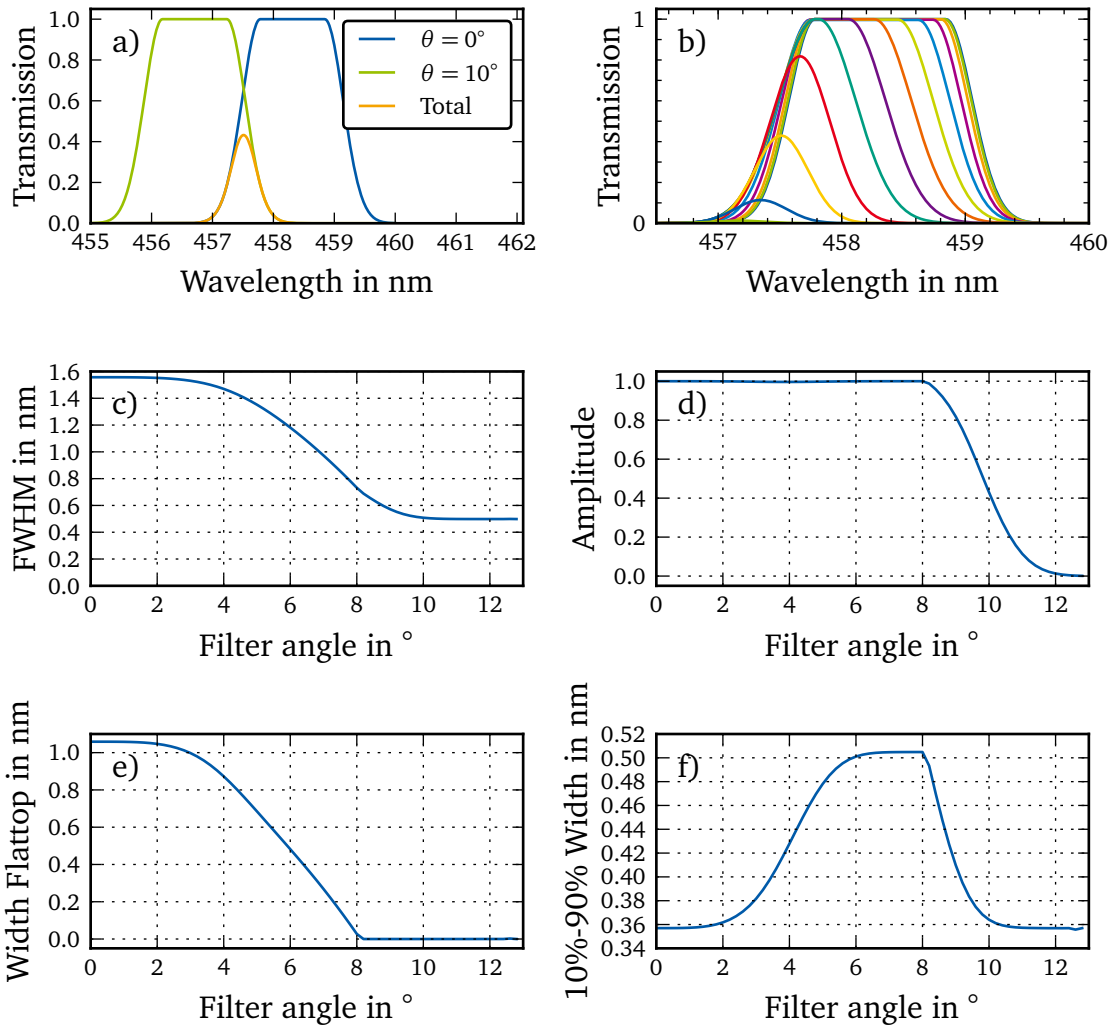


**Figure 2.8:** a) Transmittance of two combined filters. The first filter is aligned for normal incidence while the second filter can be tilted by an angle  $\theta$ . b) Combined transmittance for different tilting angles  $\theta$  of the second filter beginning from  $0^\circ$  in  $1^\circ$  steps up to  $12^\circ$ . c), d), e), and f) Full width at half maximum (FWHM), maximum amplitude, width of the flattop, and edge steepness in 10-to-90% width of the combined transmittance.

light incidence  $T_{F1}(\lambda)$  but with a maximum transmittance of unity is used. The second filter transmission  $T_{F2}(\lambda)$  is simulated by adjusting only the centre wavelength for different tilting angles  $\theta_2$  by using equation (2.10) (Fig. 2.8 a)). The total transmittance of the combined filter can be obtained by multiplying both profiles,  $T_{\text{Total}}(\lambda) = T_{F1}(\lambda) \times T_{F2}(\lambda)$ . The total transmittance for variations of the filter angle  $\theta_2$  are depicted in Fig. 2.8 b). The results in c) to f) show, that the FWHM and the flattop width decrease with higher tilting angles, while the amplitude remains constant up to  $8^\circ$ . The edge steepness (10%-to-90% width) is minimum for parallel alignment ( $\theta_2 = 0^\circ$ ) or at high angles above  $10^\circ$ . As for the large angles the maximum transmittance decreases rapidly (Fig. d)), the sharpest edge steepness is achieved in the aligned case.

This simple model is a good approximation for tilting angles smaller than  $\theta_2 \lesssim 15^\circ$ . It demonstrates the possibility to decrease the FWHM and to change the profile to a more Gaussian shape. In the case of high angles of incidence  $\theta_1, \theta_2 > 15^\circ$  for both filters, the shape is almost Gaussian and a relative angle between the filters of  $\theta_1 \neq \theta_2$  only leads to a decrease of the total transmittance but does not change the width or the edge steepness. Because of this, the filters are adjusted in parallel in the final setup at a total angle of  $\theta_1 = \theta_2 \approx 20^\circ$  for the wavelength of 452.756 nm.

---

### Laser Characterization

---

For the determination of the optimum feedback of the external resonator of the ECDL, the intra-cavity beam splitter BS was replaced by a polarization beam splitter (PBS) giving an effective cavity mirror with adjustable reflectivity and constant polarization (Fig. 2.4): By rotating QWP1, the overall reflectivity of the combination of PBS, QWP1, and mirror M could be changed. For a reflectivity  $R > 45\%$ , the stability of the laser significantly decreased. The best stability could be achieved between 10% and 20% reflectivity depending on the targeted internal laser mode. A maximum output power of 17 mW was reached at a wavelength of 454 nm. Since this configuration has not the intra-cavity polarization lock, all further measurements were performed with the ECDL in the original setup described above (Fig. 2.4) with a beam splitter BS. To receive a complete picture, the ECDL setup from Baillard et al. [56] with one filter and a 15% back reflecting mirror for feedback and outcoupling was tested. Here, an output power of up to 22 mW was achieved, but single-frequency operation was limited to a duration of one hour typically. More details are provided in [54].

To further characterize the setup, the wavelength and the output power of the double-filter ECDL ( $\theta \approx 20^\circ$ ) were measured as a function of the diode injection current (Fig. 2.9). The wavelength was measured with a commercial wavemeter (WaveMaster by Coherent) and the optical output power with a calibrated photo diode. The digital remote control of the laser diode current was realized with a new development of the current driver based on the proposal of Erickson et al. [64]. It has a maximum output power of 130 mA and a step size of approximately  $2 \mu\text{A}$ . With increasing current, the wavelength and the output power increase. The laser

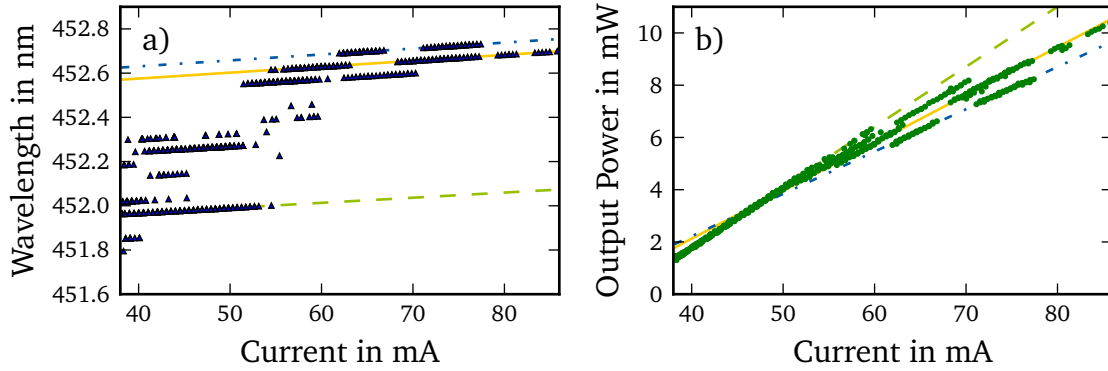


**Figure 2.9:** Characteristics of the ECDL. The laser output power and the wavelength rise with increasing current. The three example lines are fits to different internal modes of the laser diode. Wavelength and output power for each mode increase linearly.

diode current was changed in steps of  $21 \mu\text{A}$ . Data was only recorded when the wavemeter confirmed single mode operation of the laser. Below  $38 \text{ mA}$  and above  $86 \text{ mA}$  no stable operation was achieved. Following the internal modes (indicated by linear fits with specific colors in Fig. 2.9 b)), the output power rises linearly with the applied current, with different slopes for different modes. The slopes vary between  $240 \mu\text{W}/\text{mA}$  and  $360 \mu\text{W}/\text{mA}$ . More than  $10 \text{ mW}$  of output power could be achieved at  $86 \text{ mA}$  injection current. The slope of the wavelength shift for all laser modes is approximately  $2.59(4) \text{ pm}/\text{mA}$ .

With rising current, additional jumps in the wavelength of  $0.05 \text{ nm}$  towards longer wavelengths occur. The step size agrees with the internal mode spacing of the laser diode. Due to the broad filter transmission compared to the internal mode spacing, the wavelength can be tuned over a wide range of  $0.8 \text{ nm}$  without changing the angle  $\theta$  of the filters. The stability is best at high currents: Here, the laser medium favours emission at higher wavelengths, whereas the edge of the filters suppresses internal modes with even larger wavelengths. The measurement also shows a current range of only several tens of  $\mu\text{A}$  for stable operation at a given laser mode before the next mode hop occurs. This is an additional reason to use the digital current driver which allows a current-variation in steps of  $2 \mu\text{A}$ .

---

## Mode Selection

---

The output wavelength of the laser is influenced by different gain and loss factors [57]: The transmittance of the internal cavity formed by the facets of the laser diode  $T_{\text{LD}}$ , the external cavity  $T_{\text{Cavity}}$ , the two filters  $T_{\text{F}} = T_{\text{F1}} \times T_{\text{F2}}$ , and the gain profile of the laser diode  $G_{\text{LD}}$ . This leads to the total transmission function

$$T_{\text{total}} = G_{\text{LD}} T_{\text{LD}} T_{\text{F}} T_{\text{Cavity}} \cdot \quad (2.11)$$

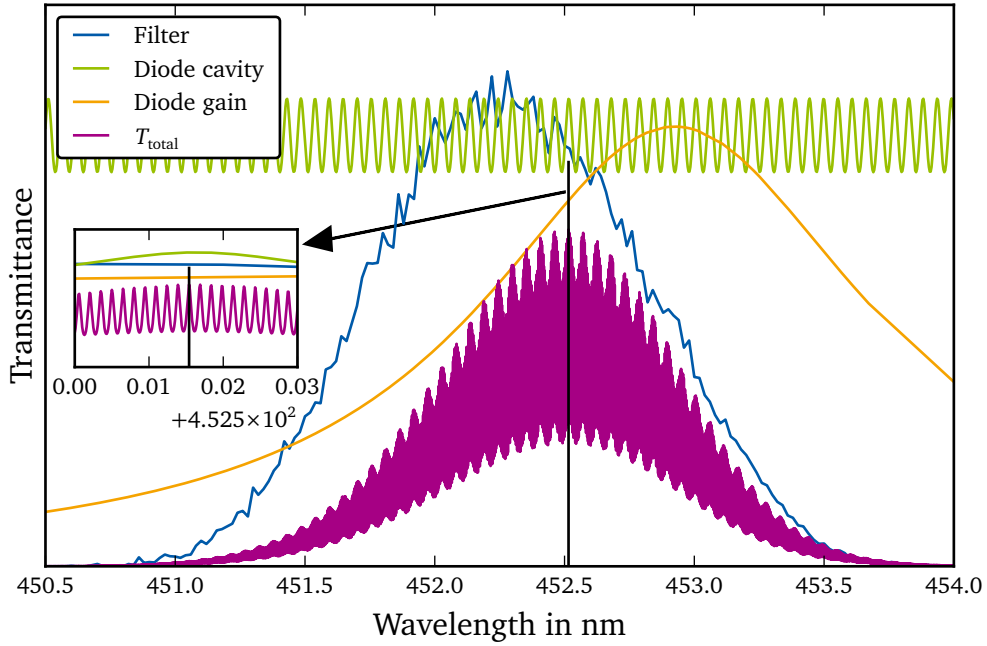


**Figure 2.10:** Model for the different frequency dependent parameters for the mode selection adopted from [57]. The laser favours emission at the strongest transmittance. The position is indicated with a black vertical line. The mode structure of the external resonator cannot be resolved in the full figure, but it can be estimated from the total transmittance  $T_{\text{total}}$  in the inset.

The gain profile is given by the diode spectrum below the laser threshold (Fig. 2.5 b)). The centre wavelength of the profile can be freely selected in a small range, since it is shifted by a change of the injection current or the temperature. The transmittance of the internal resonator can be calculated with the Airy function

$$T_{\text{LD}} = \frac{1}{1 + F \sin^2(\delta/2)}, \quad (2.12)$$

where  $F = 4r_1r_2/(1 - r_1r_2)^2$  is the coefficient of finesse and  $\delta = (2\pi/\lambda)2nl \cos(\theta)$  is the phase difference. The phase difference depends on the refractive index of the medium  $n$ , the geometrical length of the resonator  $l$ , and the incident angle of the beam  $\theta = 0$ . The blue laser diode PL450-B has a length of  $600 \mu\text{m}$  and a refractive index of  $n = 2.67$ . This leads to the previously mentioned mode separation of  $81 \text{ GHz}$  ( $54 \text{ pm}$ ) and a reflectance of  $r_1 = r_2 = 0.2$ . This is less than the typical parameters for infrared diodes of  $125 \text{ GHz}$  and  $r_1 = r_2 = 0.3$  [57]. The transmittance of the external cavity can also be obtained with the Airy function (2.12) with the appropriate parameters. The resonator has a geometrical length of  $59 \text{ mm}$  which yields an optical length of  $69 \text{ mm}$  and a mode spacing of  $2.2 \text{ GHz}$ . The centre wavelength of the transmittance of the filters under an incident angle  $\theta$  can be calculated with equation (2.10).

---

The total transmittance together with each separate component is shown in figure 2.10. The envelope of the total transmittance is limited by the filter and the gain profile. The internal resonator of the laser diode yields a small oscillation amplitude due to the low reflectance of 20%. The external cavity modes are shown in the inset of the figure. It shows the region around the strongest transmittance.

The output wavelength will most likely settle on one of the strongest transmittance peaks. The dense mode structure compared to the filter width is one reason for the difficulties in achieving stable single-mode operation. Small disturbances, like temperature or current drifts, are sufficient to cause a mode hop. On the other side, the wavelength can be tuned without rotating the filter simply by adjusting the injection current or the diode temperature.

---

### Frequency Stability

---

Due to the broad transmission spectrum of the utilized interference filters compared to the laser diode mode spacing, the frequency stability of the ECDL is strongly dependent on the external cavity configuration. With the original setup described in [56] and a single filter, single-frequency operation could be sustained for one hour only. Switching to the two-filter configuration described in section 2.3.1, in which no intra-cavity locking applied was applied, the duration of single-frequency operation was extended to several hours. The laser remained sensitive to small disturbances. These can lead to a misalignment between internal and external resonator, which causes mode jumps. A significant improvement of the long-term stability was achieved by adding the intra-cavity polarization locking scheme described earlier. For a characterization of the long-term stability, the laser was frequency-stabilized via Doppler-free saturation spectroscopy to  $^{130}\text{Te}_2$  which has a dense line spectrum in the blue wavelength region [65]. The stabilization on a Lamb-dip of tellurium uses a second lock-in servo loop, which generates the derivative of the Lamb-dip via a 40 kHz modulation of the laser current. This modulation is faster than the feedback bandwidths of both lock-in servo loops. The dispersion signal from the spectroscopy is fed to a second PI controller which adjusts the length of the ECDL cavity with a piezo voltage and the laser diode current.

For a long-term measurement of the frequency stability, the error signal of the tellurium lock and the piezo voltage for stabilizing the ECDL cavity length were recorded in intervals of five second. For each interval, the signals were averaged over 100 samples to reduce the noise. In order to determine the influence of the laboratory conditions, room temperature, ambient air pressure, and humidity were recorded every five minutes. Figures 2.11 a), b), and c) show a respective measurement over a duration of two days. The laser stays locked over the full duration and thus demonstrates excellent long-term stability. The piezo voltage shows a strong correlation with air pressure, superimposed by a small negative piezo voltage drift, starting after the first half of the measurement time. The room temperature of 21.5 °C was stable to better than 0.5 K and the relative humidity always stayed between 40%

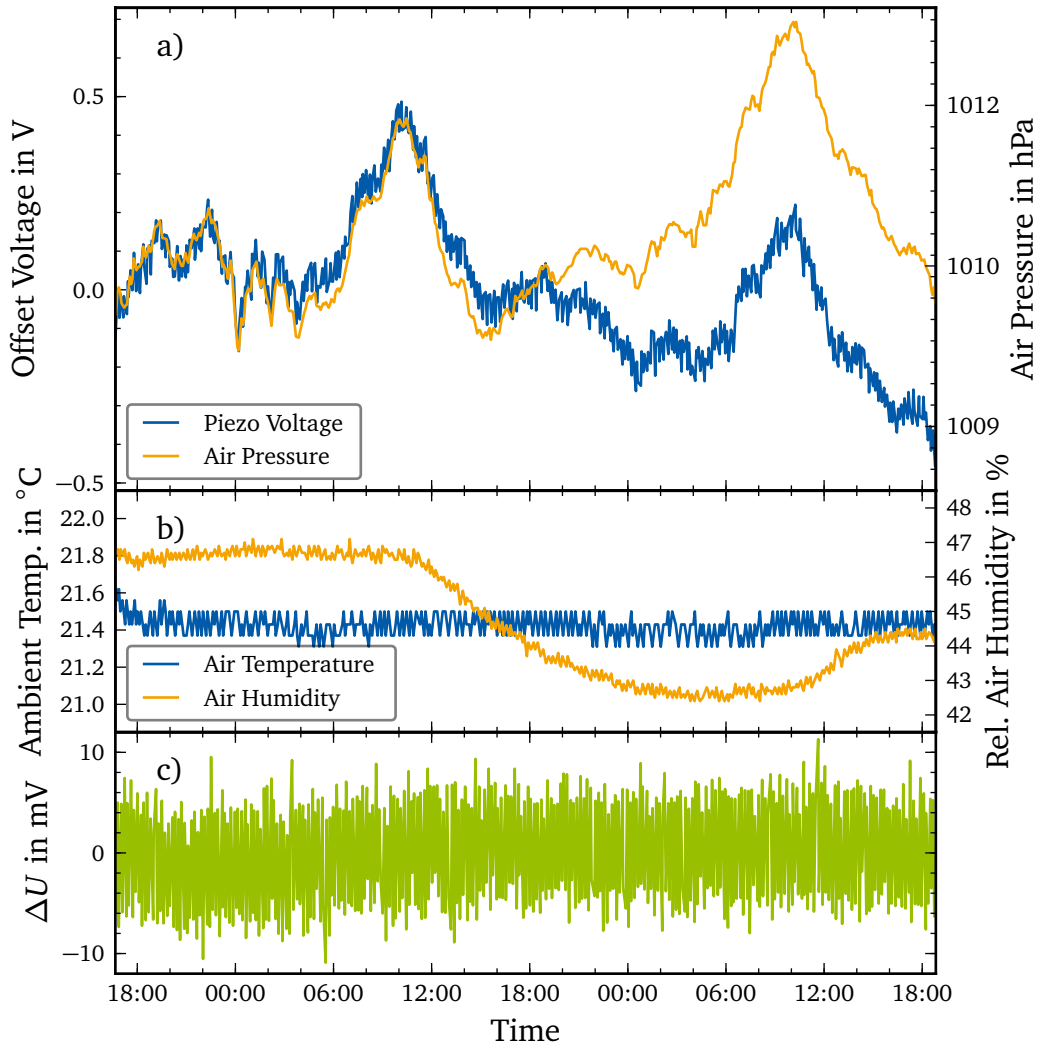


**Figure 2.11:** a) Long-term stability of the laser recorded over a period of two days. The laser is stabilized to a Doppler-free tellurium line. The applied offset voltage of the ring piezo compensates the length change of the external resonator predominantly caused by air pressure variations. b) Temperature and air humidity variations. c) The corresponding error signal of the tellurium stabilization loop demonstrates the stable laser operation over the full measurement period.

---

and 50 %. The absolute variation of the piezo voltage does not exceed 1 V which corresponds to an upper bound for the change of the cavity length of 100 nm. Figure 2.11 c) confirms that the laser stayed in lock during the full measurement time. The in-loop deviation of the error signal is symmetric around the setpoint of 0 V with a mean excursion of only a few mV. An out-of-lock event would show a large discontinuous jump of several tens of mV.

---

### 2.3.2 Spectroscopy Laser

---

The spectroscopy laser, a DL 100 pro by Toptica, is an ECDL using a back-reflecting grating. It has a maximum output power of 16 mW after the optical isolator at a current of 66.6 mA. This is sufficient for the stabilization to the transfer resonator and the spectroscopy of tellurium or  $\text{Ar}^{13+}$ . By rotating the grating manually a coarse tuning range between 439.4 to 445.8 nm can be achieved. This covers the complete frequency range of the expected fine-structure transitions of  $\text{Ar}^{13+}$ .

The output beam of the laser has an elliptical profile with an aspect ratio of 3.14. A Keplerian cylinder-lens telescope using lenses with focal lengths of 4 mm and 12.7 mm generates a spherical profile and increases the in-coupling efficiency into a fibre by 45 % compared to the efficiency without the telescope.

The laser is frequency stabilized via the double-pass AOM setup (Fig. 2.3) to a longitudinal mode of the transfer cavity. To do so, the current of the laser diode is modulated with a frequency of 25 kHz with the proportional–integral–derivative controller (PID controller) DigiLock 110 by Toptica. The PID controller has a built-in lock-in amplifier which generates the dispersion signal of the transmitted laser light of the transfer cavity. This dispersion signal is used to control the piezo voltage and the injection current of the laser diode in a feed forward circuit with the PID. In principle, the current modulation could also be applied to the AOM for the stabilization on the transfer cavity. However, this would not allow for the simultaneous observation of the tellurium Lamb dips which is used in the actual setup.

The mode-hop-free tuning range of up to 50 GHz is too small for driving multiple  $\text{Ar}^{13+}$  transitions, which have a frequency splitting of 65 GHz due to the magnetic field of  $B \approx 7\text{ T}$ , with an automatized routine. The effective tuning range in the experiment is further decreased by the frequency stabilization on the transfer resonator: An acceptable dispersion signal can only be achieved in a small current range of the complete single-mode operation region and is always next to the threshold for a mode hop. This limits the stable tuning range to around 10 GHz in practice.

---

### 2.3.3 Transfer Cavity

---

The purpose of the transfer resonator is the frequency stabilization of a slave laser, in this case the spectroscopy laser, to a master laser. The resonance condition is given by

$$\nu = \frac{Nc_0}{2nl_{\text{geom}}}, \quad (2.13)$$

with the geometrical distance between the two mirrors  $l_{\text{geom}}$ , the refractive index of the medium in the resonator  $n$ , the speed of light  $c_0$ , and the longitudinal mode  $N$ . The formula yields equidistant resonance frequencies over the complete spectrum, which can be used for frequency stabilization. This is an advantage compared to an atom or a molecular spectroscopy, that may have frequency regions without suitable transitions.

The transfer cavity consists of two plano-concave mirrors with a radius of curvature of  $r = 75$  mm. The mirrors are silver coated with an additional  $\text{MgF}_2$  coating and have a reflectivity of 93 % at a wavelength of 441 nm. This yields a finesse of  $F = \pi(r_1 r_2)^{1/4} (1 - (r_1 r_2)^{1/2}) \approx 43$  (58 at a wavelength of 480 nm). The cavity is based on a design of C. Siegel [66]. The mirrors are attached to an outer and an inner cylinder. They are bolted together via a fine-pitch thread, which allows for a length adjustment. One of the mirror is mounted on a pair of piezo ring-actuators for length adjustment of several tenth of  $\mu\text{m}$ . Their nested configuration compensates temperature drifts.

The control of the cavity length is achieved via two positive high-voltages (HV) of up to 1250 V (negative voltages damage the actuators) in an opposing scheme. Therefore, the control voltage-signal is split in two, whereby one is inverted. An offset of half of the maximum voltage is added to both signals. These split signals are fed into two HV amplifiers, which drive the ring piezo actuators.

The design is optimized for an optional operation in vacuum. All inner volumes are connected to the outside via pressure-compensation holes and virtual leakages due to thread holes were avoided. Additionally, connections are provided for temperature stabilization via thermal connections. The current version is used in air and the temperature is stabilized with a thermoelectric cooler and a passive heatsink on top of the resonator.

The cavity has a total length of  $l = 71$  mm and a free spectral range (FSR) of 2111 MHz (Chap. 3). These properties yield a stability parameter of  $g = 1 - l/r = 0.05$  and therefore stable operation, since stable operation is possible for  $0 \leq g^2 \leq 1$  (Chap. 5 in [67]). It is almost a confocal configuration, where the length equals the radius of curvature. The adjustment is optimized for the lowest eigenmode  $\text{TEM}_{00}$ . This corresponds to a Gaussian beam shape in the resonator, where the incoming and reflected beam overlap. The waist of the Gaussian beam in the centre of the cavity is  $\approx 73$   $\mu\text{m}$ . To meet this condition, the beams from the master and the spectroscopy laser must be adjusted with lenses. Gaussian optics and ABCD matrix analysis are

---

used to calculate the optimal distances between the respective optical components. A clean initial condition for the beams is reached by using single-mode polarization-maintaining fibres for both lasers to transport the light to the cavity setup. The lenses of the outcouplers have a focal length of  $f = 7.5$  mm. The overlap with orthogonal polarization is done with a polarizing beam splitter (PBS). A lens with a focal length of 150 mm in a distance of 46 cm to the centre of the cavity and 34 cm after the outcoupler lens focuses the overlapped beams into the cavity. The splitting of the beams after the cavity is done with a second PBS and separate photodiodes monitor the transmitted power.

---

### 2.3.4 Tellurium Spectroscopy

---

The  $^{130}\text{Te}_2$  spectroscopy serves two purposes in this experiment: It is used for the frequency stabilization of the master laser and it serves as an absolute frequency reference for the spectroscopy of the fine-structure transition of  $\text{Ar}^{13+}$ . Tellurium is a good choice due to various transitions over the full visible wavelength range, especially in the blue, which are also well documented in a tellurium atlas by Cariou and Luc published in 1980. They measured a Doppler-broadened spectrum in a wavelength range between 420 nm and 540 nm with a resolution of around 1 GHz [65, 68, 69]. Reference lines with a relative uncertainty of  $10^{-9}$  were measured in [70–77]. The reference lines measured by Scholl et al. [77] have an absolute uncertainty of 1 MHz and are used in chapter 3 to determine the wavelength of tellurium lines next to the  $\text{Ar}^{13+}$  transitions.

The setup of the Doppler-free spectroscopy is similar to the one by S. Albrecht shown in [75]. A probe beam passing through the tellurium cell is overlapped with a counter propagating saturation beam (Fig. 2.3). This allows for the detection of the Doppler-free Lamb dips (detailed explanations can be found in [78]).

The  $^{130}\text{Te}_2$ -cell by Ophos Instruments [79] has a length of 100 mm and a diameter of 25 mm. Since tellurium is solid at room temperature, it must be heated for a sufficiently high optical density. A temperature of 502 K has been chosen in this experiment, which is the same temperature Scholl et al. used. This temperature corresponds to a vapour pressure of 91 Pa [80]. For heating, the cell is situated in a cylindrical oven with open ends for the optical access. To increase the temperature stability, fireclay stones and aluminium foil at the ends seal the oven except for small holes for the spectroscopy beams. This suppresses air convection and unnecessary heating of the surrounding optics.

Probe and saturation beams for the spectroscopy are produced from the incoming laser beam by an N-BK7 glass plate used as a beam splitter (Fig. 2.3). The reflectivity of  $\approx 4\%$  is sufficient for the probe beam. The overlap with the saturation beam is achieved with mirrors which leads to a small relative angle of around  $0.1^\circ$ . For the tellurium spectroscopy, laser powers of several mW are sufficient to resolve the Lamb dips.

---

The spectroscopy can be used with two independent lasers at the same time. Both laser beams of orthogonal polarization are overlapped with a polarizing beam splitter (PBS) before entering the spectroscopy. With a second PBS, the probe beams are separated after the tellurium cell to detect each individual laser beam with photodiodes. The advantage of this method is an easier adjustment: It is sufficient to adjust the spectroscopy with one laser and then to overlap the second beam. Typically, the second beam only requires minor adjustment for optimal signals.

In the experiment, the lock-in technique is used to generate the dispersion signal of the Lamb dips. This yields a higher signal-to-noise ratio and allows for the frequency stabilization on the  $^{130}\text{Te}_2$  Lamb dips. The required modulation of the laser beams is done via a current modulation of the laser diodes of the master and spectroscopy laser.

Since the master and the spectroscopy lasers have a large wavelength separation with 453 and 441 nm, an upgrade for a second spectroscopy laser could be done easily with additional edge filters. Therefore, the additional laser light could be overlapped with the beam of the master laser by using the same linear polarization. Since the polarization of the new and the existing spectroscopy laser would be orthogonal, the separation of the similar wavelengths could be reached with the PBS.

---

## 2.4 Towards Laser Spectroscopy of $\text{Ar}^{13+}$

---

The cylindrical design of the Penning trap allows for optical axial access from the top. Since the Penning trap is in cryogenic vacuum with magnetic fields of several tesla, the optical detector cannot be mounted directly above the Penning trap. Therefore, an optical setup with passive optical components and fibres is used for the laser excitation and the fluorescence light collection. The detection of the fluorescence photons is accomplished outside of the experiment with a channeltron photo-multiplier (CPM).

The CPM has a TTL-logic output which is connected to the measurement computer and single-photon events are recorded time-resolved to calculate histograms of time-dependent signal rates.

For the spectroscopy of the  $\text{Ar}^{13+}$  fine-structure transition, a repeating measurement cycle has been implemented: The ions are excited with the light of the spectroscopy laser for 50 ms and the fluorescence light is recorded for another 150 ms. During the detection, the laser light must be blocked completely since the stray light is several orders of magnitude stronger than the expected fluorescence signal.

---

### 2.4.1 Optical Excitation and Detection Setup

---

The optical excitation of the  $\text{Ar}^{13+}$  ions and the collection of the fluorescence light are combined in one optical setup (Fig. 2.12 a), b), and c)). The setup is placed in the cryogenic vacuum on top of the spectroscopy trap. A vacuum quartz window and the

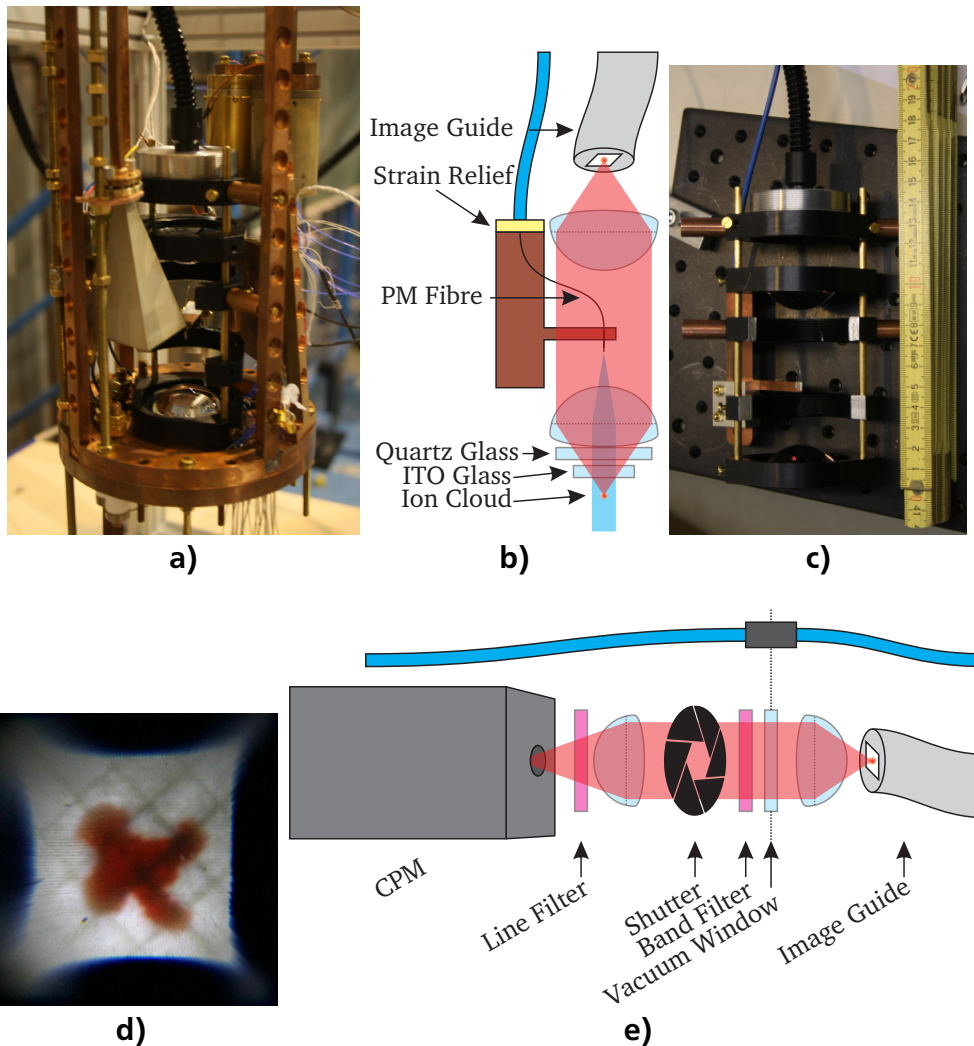


**Figure 2.12:** a) Image of the optical setup for the ion excitation and fluorescence collection, mounted in the vacuum setup. b) and c) Schematic and image of the optical setup. The lower lens collimates the laser light (blue) and the fluorescence light (red) from the ions. The upper lens focuses the fluorescence light onto the image guide. d) Image of a test sheet at the position of the ion cloud seen through the image guide and the collection setup shown in b). The sheet has a 5 mm chequerboard pattern. The trap centre is marked with a red cross. e) Schematic of the detection setup for single-photon counting. The light from the image guide is focused with two lenses onto the channeltron photo multiplier (CPM). A shutter between the lenses protects the CPM from stray light during the optical excitation. Two filters narrow down the detectable spectrum to suppress the background signal.

---

top electrode of the Penning trap which is a glass substrate with a conductive coating of indium tin oxide (ITO) allows for the optical access to the trap centre. All parts are cooled to about 4 K and are in a magnetic field of several tesla. To withstand these temperatures and not influence the magnetic field, the materials used must be carefully chosen. Therefore, all mountings are made of aluminium, brass, or copper. These materials are not magnetic and have no effect on the magnetic field.

The laser light is transmitted using a 2 m single-mode polarization maintaining fibre (P3-405BPM-FC-2 from Thorlabs) which has FC-APC connectors and is specified for a wavelength range of 400 to 680 nm. The top end of the fibre is connected to a vacuum feed through (CF16-SM633-FCAPC-1 by Vacom). The fibre connector at the lower end is cut off and the bare fibre tip is glued to a copper arm and points toward the spectroscopy trap (Fig. 2.12 b)). The emitted cone of light has a half-angle of  $7^\circ$  due to the numerical aperture of the fibre of 0.12. The light is collimated by an aspheric condenser lens ACL4532-A from Thorlabs with a focal length of 32 mm and a numerical aperture (NA) of 0.612. This collimated beam illuminates the ion cloud.

The same condenser lens for the laser beam collimation also collimates the fluorescence light emitted from the ions. This fluorescence beam is then focused by a second lens (also ACL4532-A) onto the end of the image guide (IG-154-72 by SCHOTT) (Fig. 2.12 d)). From there, the light is transported to the detection setup. The image guide has an active area of  $4\text{ mm} \times 4\text{ mm}$  and consists of  $72 \times 72$  fibres with an NA of 0.63. Its transmittance is approximately 40 % at 450 nm.

To have a collimated beam in between the two lenses has the advantage that apertures in the path only lower the image contrast and block evenly distributed light, but do not produce shadows in the image of the ion cloud. Therefore, the copper arm, which can be seen as a partial beam block, is, with a thickness of 1 mm, as small as possible and only the bare fibre tip is glued to its end. Thus, the fluorescence light is only attenuated minimally. This can be seen in figure 2.12 d) which shows a picture taken through the image guide. The adjustment of the optical setup has been checked through the image guide with a chequerboard paper at the location of the Penning-trap centre. The centre itself is marked with a red cross. In the image, the copper arm with the fibre or a shadow cannot be seen which is an indication for a proper alignment.

The coarse collimation of the laser beam has been based on comparing the beam size at several distances from the condenser lens. To check the adjustment, images of the beam were taken with an EOS 40D camera by Canon which has a sufficiently large CMOS sensor with  $22.2\text{ mm} \times 14.8\text{ mm}$  (Fig. 2.13 a) and b)). The evaluation of the images yields a Gaussian shaped beam with an additional small peak at the centre. The FWHM at a distance of 53 mm is  $3.711(6)\text{ mm}$  and  $3.860(6)\text{ mm}$  in the short and the long axes. After the adjustment, the beam displayed only minor divergence (Fig. 2.13 c)). The beam size can be derived from an ABCD matrix analysis, which uses the measured slope to determine the misalignment of the focus length between fibre tip and condenser lens. The calculation yields a distance of 30.4 mm instead of the nominal focal length of  $f = 32\text{ mm}$ . This misalignment is sufficiently low since

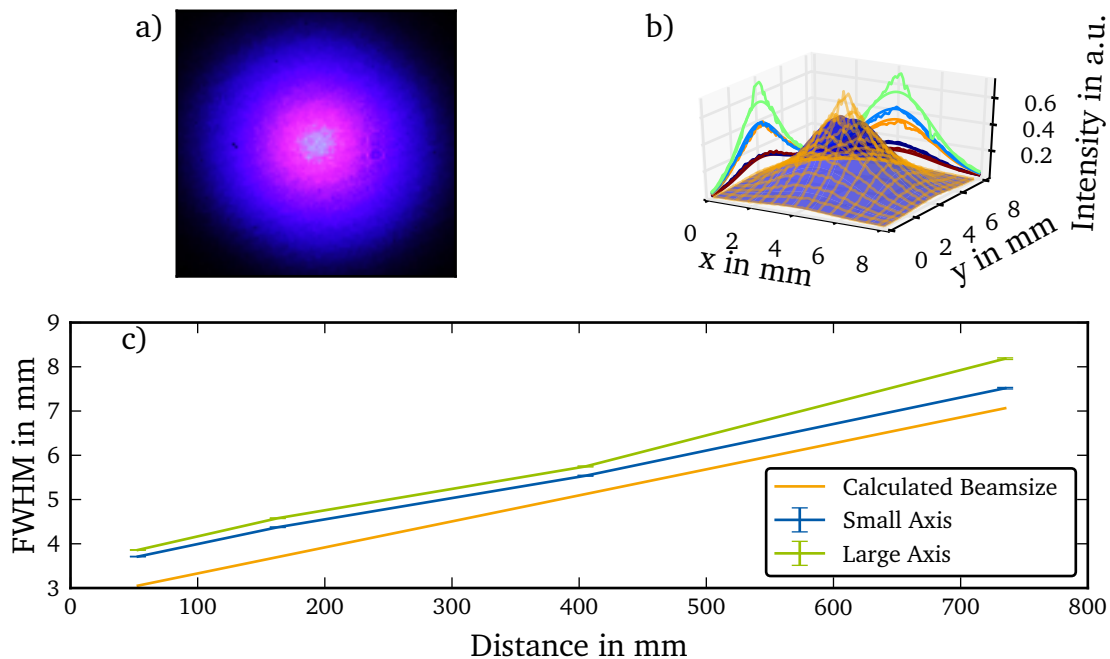


**Figure 2.13:** a) Image of the collimated laser beam at a distance of 53 mm after the fibre and the collimation lens. b) Intensity distribution of the beam shown in a). The profile deviates significantly from Gaussian shape in the centre. c) Beam width (FWHM) over distance. The beam is slightly diverging. The slope indicates a misalignment of 1.6 mm of the fibre end from the focal position of the collimation lens.

the ion cloud is in an optical distance of approximately 35 mm from the condenser lens. The calculated beam diameter at the trap centre is approximately 3.7 mm. This is in the same range as the expected ion cloud diameter of about 3 mm. An advantage of the large beam diameter is the insensitivity to misalignments of the illuminated area at the trap centre. This is important since the materials shrink in the cryogenic vacuum and later adjustments in the evacuated setup are not possible.

The fluorescence detection is achieved with a photosensitive single-photon electron multiplier (CPM = channeltron photo-multiplier, MP 984 by EXCELITAS). The detection setup collimates the fluorescence light leaving the image guide with an aspheric lens (ACL2520-A by Thorlabs,  $f = 20$  mm) before the vacuum window (Fig. 2.12 e)). On the outside, a second lens (ACL2520-A) focuses the fluorescence beam on the CPM. Between the two lenses, the vacuum window, a dielectric band filter (FB440-10 by Thorlabs), and a C-mount shutter are included. In front of the CPM an additional line filter (LL01-442-12.5 by Semrock) is inserted. The filters reduce the background fluorescence light discussed in the following sections. While the band filter is used to block the visible spectrum except a 10 nm band at 440 nm, the line filter with a FWHM of 1.7 nm and a centre wavelength of 441 nm narrows the optical transmittance. The line filter cannot be used without the band filter, since it is trans-

parent in the red optical spectrum. The C-mount shutter blocks the stray light of the laser beam during the excitation of the  $\text{Ar}^{13+}$  ions. This is necessary, as otherwise the CPM would degrade due to an overexposure with laser light. The complete detection setup is mounted in a system of C-mount tubes between the optical components. These tubes block stray light coming from the laboratory. A further reduction of stray light has been achieved with a flexible bellows around the complete setup between the vacuum flange and the CPM. This reduces the stray light from the laboratory to a single detected background event per second.

---

### Fluorescence Signal Estimation

---

Weighted solid angle (fract. of $4\pi$ )	0.08
Transmittance through 2 vacuum windows	each 0.9
Transmittance through endcap electrode	0.75
Transmittance through 4 AR-coated lenses	each 0.99
Transmittance through image guide	0.5
Detector quantum efficiency	0.17
Transmittance through Filter LL01-442-12.5	0.95
Transmittance through Filter FL441.6-10	0.75
Total detection efficiency	0.003

**Table 2.2:** Overview of transmittance and efficiencies of the parts of the fluorescence setup based on table 4.7 in [45] with updated values.

To decide whether one background event per second is sufficiently low, a comparison with the expected signal rate from the  $\text{Ar}^{13+}$  fluorescence can be done. This estimation has been already done in section 4.10 and is shown in table 4.7 in [45]. Due to the optimization, an updated version is shown in table 2.2. Assuming  $10^5$  excited ions in the Penning trap, this leads in the first 10 ms to 100 observed events. However, the number of fluoresce ions is decreased by the total excitation efficiency. This depends on the saturation intensity of the transition and the laser light intensity. The saturation intensity is given by

$$I_0 = \frac{\pi h c_0 \Gamma}{3 \lambda^3} \approx 2.5 \times 10^{-4} \text{ W/m}^2,$$

where  $h$  is Planck's constant,  $c_0$  is the speed of light in vacuum,  $\Gamma = 2\pi \times 16.6 \text{ Hz}$  is the transition width, and  $\lambda = 441 \text{ nm}$  is the transition wavelength. The diameter of the laser beam at the trap centre is about 3.7 mm. Thus, the saturation intensity is reached with a total power of approximately  $P \approx 5.5 \text{ nW}$ . For the excitation of the ions, laser power of around 1 mW is available in the cryogenic setup, which leads to an intensity of  $I = 1.8 \times 10^5 \times I_0$ . Therefore, it can be expected that every ion in the

---

ground state is immediately excited and half of the ions are in the excited state after excitation period. For a worst case assumption, the Doppler broadening of about  $2\pi \times 150$  MHz must be compared the homogeneous-broadened transition width [78]  $\Gamma_S = \Gamma(1 + I/I_0)^{1/2} \approx 2\pi \times 7$  kHz. The ratio  $150 \text{ MHz}/7 \text{ kHz} \approx 2 \times 10^4$  is still smaller than the saturation factor  $I/I_0 \approx 1.8 \times 10^5$ . In this case, half of the ions can be still expected in the excited state. This worst case assumption leads for  $10^5$  ions to about 50 observed events in 10 ms, which corresponds to a mean signal rate of  $5 \times 10^3 \text{ s}^{-1}$ . Thus, the expected signal is much stronger than the background signal of the stray light.

---

## 2.4.2 Experimental Control Scheme and Data Recording System

---

A dedicated computer controls the measurement sequence and records the data. The control program on the computer is written in LabView and is able to perform a complete frequency scan over a predefined range with the spectroscopy laser. A typical fluorescence measurement cycle consists of three steps: setting the laser to the desired frequency, programming and starting the excitation and detection cycle, and finally the recording of the fluorescence data.

The frequency of the spectroscopy laser can be fine-tuned with an RF synthesizer, which drives the double-pass AOM and is connected to the computer control of the laser system. The coarse tuning is done by re-locking the transfer cavity to different longitudinal modes of the master laser wavelength (Sec. 3.2). For this, the PI controller of the transfer cavity can be programmed through the computer. It is possible to start and pause the stabilization and to lock the cavity on the next higher or lower longitudinal mode. The spectroscopy laser is stabilized with the DigiLock 110, which also allows for remote control. The computer puts the stabilization on “hold” during the re-locking of the transfer cavity.

The program flow is as follows: The LabView program on the control computer in the first step sends the new RF frequency for the AOM and, if necessary, the new cavity mode to a slave LabView program running on the computer for the laser system. After the new settings are applied, the slave program sends a confirmation since the required time for the re-locking of the transfer resonator can vary over several hundreds of ms.

A delay generator which controls the excitation and detection cycle is programmed after the new frequency is set. Three channels of the delay generator are used for the cycle measurement (Fig. 2.14). The laser shutter (Fig. 2.3) is controlled by channel A and the C-mount shutter (Fig. 2.12 e)) by channel C. The laser shutter is normally open, which means a logical 0 (in TTL standard 0V) results in an open shutter. Since the delay generator sets the outputs to 0V at the end of the cycle, the laser shutter would be open after the measurement is finished. To prevent a continuous illumination and for laser safety reason channel B is used to generate an envelope for the measurement. A logic circuit makes sure, that the shutter opens only during the

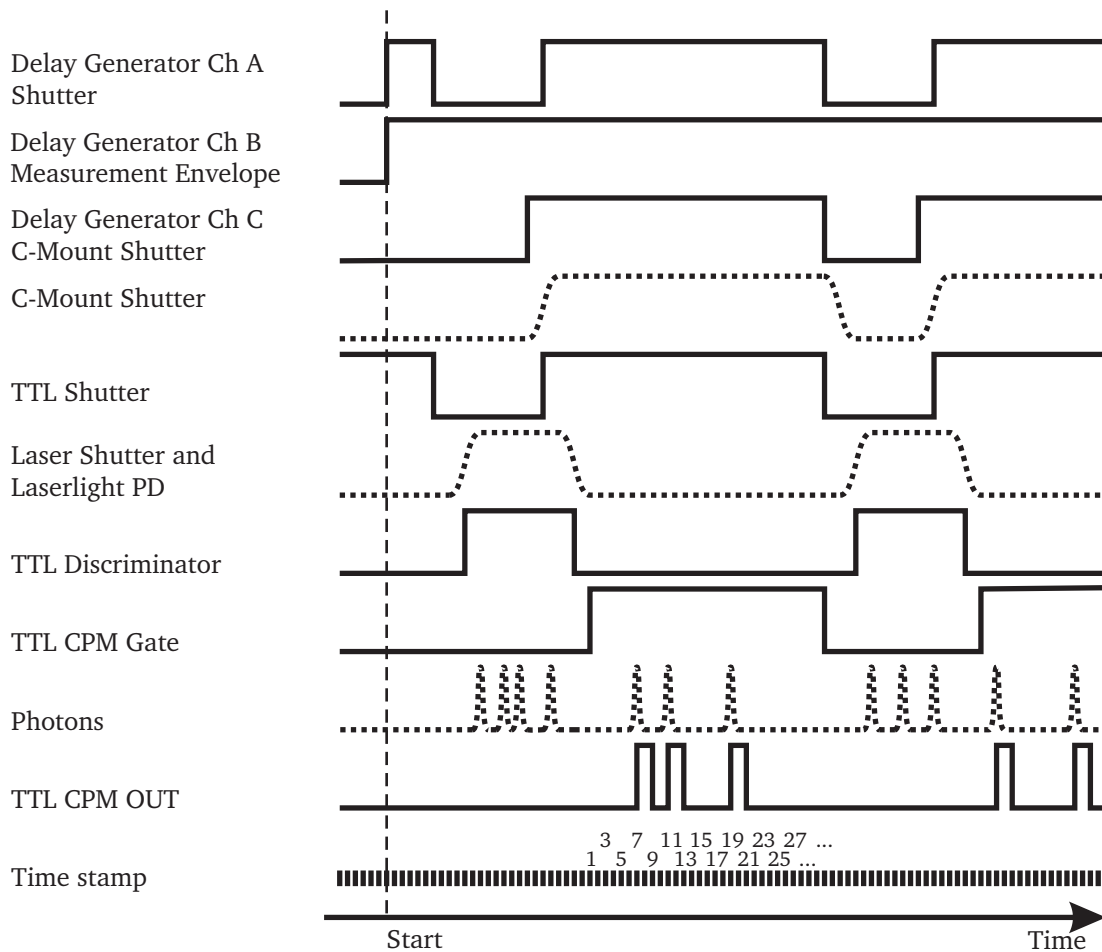


**Figure 2.14:** Timing diagram of the  $\text{Ar}^{13+}$  spectroscopy experiment control. The solid lines indicate electric signals.

measurement cycle with the Boolean calculation  $\text{TTL}_{\text{Shutter}} = (\text{Ch A}) \vee \overline{(\text{Ch C})}$  (TTL Shutter in Fig. 2.14).

Channel B is programmed to be constantly high during the measurement time (Fig. 2.14). After a short delay to channel B (named “Anfang delay” in the LabView software, typically 20 ms), channel A starts with the pulse sequence in burst mode. The output then changes periodically between low, which opens the laser shutter for a small time (typically 50 ms), and high (typically 150 ms, LabView option “Chan width”). The number of bursts “Chan Burst #” and the period “Sys Period” can be selected in the software. Channel C for the C-mount shutter is programmed with the same parameters as channel A, but with a negative opening delay (“Start Delay after Laser Shutter”, typically  $-18$  ms), so that the C-mount shutter is completely open when the the laser shutter closes. After the pulse sequence is finished the envelope of channel B is set to low after an additional small delay (“Ende Delay”) of typically 30 ms.

---

During the pulse sequence, the photons detected by the CPM are recorded time-resolved with a data acquisition card (NI PCI-6602 by National Instruments). This card has eight 32 bit counters with an update rate of 80 MHz. This corresponds to a time resolution of 12.5 ns. Each event is directly written into the memory (RAM) of the computer via direct memory access (DMA). The CPM output (TTL CPM OUT in Fig. 2.14) is connected to Gate0 (PFI38). The recording starts with a trigger signal (TTL CPM Gate in Fig. 2.14) at pin PFI37. This trigger comes from a discriminator circuit, which measures whether the shutter is open or closed with a beam sampler and a photodiode after the laser shutter (Fig. 2.3). When the laser power drops below a certain threshold the discriminator output yields a logic 1 after a delay of 400  $\mu$ s. The delay ensures that the trigger signal always comes after the complete blocking of the spectroscopy laser. The trigger signal is used to start the measurement and to protect the CPM. This protection is done using a build-in electronic shutter, which decreases the high voltage of the photo-multiplier tube within a few hundreds of nanoseconds and stops therefore the amplification of photo-electrons in the multiplier stage. The laser shutter has a jitter of several tenths of microseconds and a delay of several hundreds of microseconds. To consider these delays for the measurements, the trigger signal of the discriminator circuit attached to the monitor photo diode (TTL CPM Gate in Fig. 2.14) is recorded along with counter 1 by connecting it to Gate1 (PFI34). This counter is also started by PFI37.

The data acquisition card together with the LabView program records the time differences between two events in nanoseconds and saves them in two files, one for the single events of the CPM and the other for the trigger timings of the discriminator shutter (TTL CPM Gate). For the first event, the time since the start is also saved. Thus all data from a complete measurement cycle are stored in these two files.

---

## Data Evaluation of the Fluorescence Signal

---

The fluorescence evaluation uses the detected single events from the CPM and the closing times of the laser shutter. Besides the information of the total counts, which only requires the single event data, a time resolved evaluation of the signal rate is of interest to measure the decay time of the Ar<sup>13+</sup> transitions. Therefore, the closing time of the last shutter is subtracted from the absolute time stamps of the single fluorescence events. This yields the event times relative to the switch-off time of the spectroscopy laser. These event times are used to calculate histograms which show the time depending signal rate (Fig. 2.15 a)). The histograms are then normalized by the number of cycles, which allows for better comparison.

---

### 2.4.3 Background Signal Analysis

---

An important step towards the laser spectroscopy of Ar<sup>13+</sup> is the testing and characterization of the complete excitation and detection system. This can be done to a

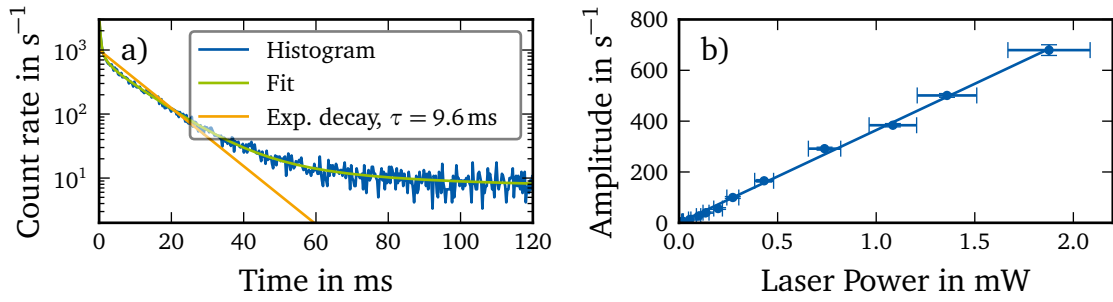


**Figure 2.15:** a) Fluorescence signal of a background measurement. A histogram is calculated from the timings of the single events relative to the switch-off times of the spectroscopy laser light. The fit consists of four exponential decays and an offset. The red curve shows an exponential decay with a time constant corresponding to the expected lifetime of the excited  $\text{Ar}^{13+}$  state. b) Dependence of the background signal strength on the laser power. Therefore, background signals were measured and fitted as shown in a). The amplitude of the exponential decay close to  $\approx 10$  ms from the fits is plotted.

high degree without ions in the spectroscopy trap. The test includes the communication of the two control computers, the synchronization of the laser system with the detection system, and the data evaluation.

The system was tested with 4.17 mW of laser power of the spectroscopy laser coupled into a 27 m fibre at a wavelength of around 441.15 nm close to the highest transition frequency  $\nu_6$  of the Zeeman sub-level transitions of  $\text{Ar}^{13+}$ . Approximately 45% or 1.9 mW of the measured laser power is available at the trap centre due to losses in the fibre and couplers. Two measurements with 2000 cycles were recorded. Each cycle consists of an excitation with laser light for 50 ms and a single-event detection for 150 ms. A safety margin of about 1 ms after the excitation and before the detection were used to protect the CPM. The data evaluation yields a decaying fluorescence signal (Fig. 2.15 a)). For the histogram, a bin width of 0.3 ms is used. A fit of a function consisting of four exponential decays plus offset gives the four decay constants 0.31(3) ms, 1.5(3) ms, 10.5(7) ms, and 37(6) ms with the amplitudes  $2700(200) \text{ s}^{-1}$ ,  $410(70) \text{ s}^{-1}$ ,  $670(40) \text{ s}^{-1}$ , and  $22(4) \text{ s}^{-1}$ . The offset is  $7(4) \text{ s}^{-1}$ . Due to the safety margin of 1 ms between excitation and detection, fluorescence decays with much smaller decay constants than  $\approx 1$  ms cannot be measured.

The second-largest decay time of 10.5(7) ms is next to the expected decay time of 9.6 ms of the excited state of  $\text{Ar}^{13+}$  (red curve in Fig. 2.15 a)). This could interfere with the laser spectroscopy of  $\text{Ar}^{13+}$ . Therefore, this fluorescence background signal must be examined more closely. One of its properties is the scaling with laser power. For the measurement of the scaling behaviour, the power was varied between 32  $\mu\text{W}$  and 4.17 mW, which corresponds to a power at the trap centre be-

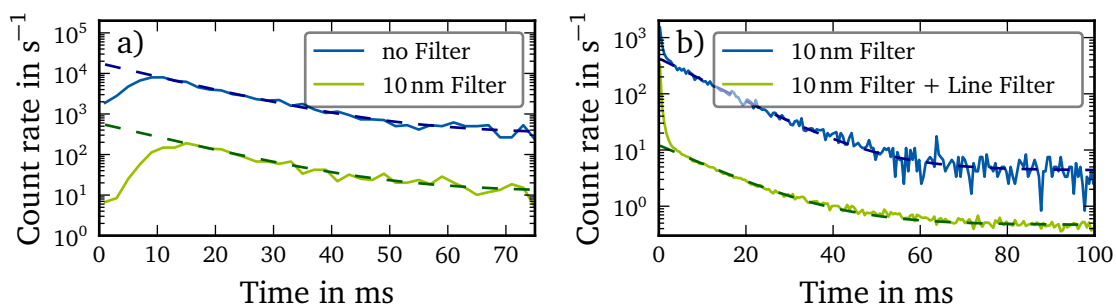


**Figure 2.16:** a) Background fluorescence signal with and without an FL441.6-10 10 nm filter by Thorlabs. b) Background fluorescence signal with and without a laser line filter LL01-442-12.5 by Semrock. The darker and dashed lines are exponential fits.

tween  $14 \mu\text{W}$  and  $1.9 \text{ mW}$ . For the evaluation of the signal rates, a function of four exponential decays is fitted again. The amplitude of the decay constant closest to  $9.6 \text{ ms}$  is shown in figure 2.15 b). As can be seen, the amplitude scales linearly with the laser power with a slope of  $162(2) \text{ mW}^{-1} \text{ s}^{-1}$ .

Another important property is the spectrum of the fluorescence background. Since no spectrometer with a single photon sensitivity was available, two dielectric filters, a band filter with a width of  $10 \text{ nm}$  (FL441.6-10 by Thorlabs) and a line filter with  $1.7 \text{ nm}$  (LL01-442-12.5 by Semrock), were used to narrow down the spectrum (Fig. 2.12 e)). The previous background measurements were already done with these filters, but for the characterization, a measurement without any filter and a measurement using only the  $10 \text{ nm}$  band filter were added.

The measurement without any filter yields a high signal rate with amplitudes over  $1 \times 10^4 \text{ s}^{-1}$ . To prevent damage to the CPM, the laser power was reduced and the C mount shutter in front of the CPM opened only after the laser was blocked. Thus, the shutter starts to open at the beginning of the fluorescence observation which leads to an increasing signal rate during the first  $10 \text{ ms}$  (Fig. 2.16 a)). For comparison with and without the filter a single exponential decay with a time constant of  $12.7 \text{ ms}$  is fitted between  $15$  and  $90 \text{ ms}$  to the histograms, which have a bin width of  $2 \text{ ms}$ . The amplitude obtained from the fit decreases from  $17652$  to  $574 \text{ s}^{-1}$  with the band filter which corresponds to a suppression factor of  $31$ .

In the second measurement series the line filter LL01-442-12.5 was inserted in addition to the  $10 \text{ nm}$  filter (Fig. 2.12 e)). The amplitude of the fitted exponential decay drops from  $424$  to  $11.7 \text{ s}^{-1}$  with the line filter, whereas the time constant increases from  $11.1 \text{ ms}$  to  $12.4 \text{ ms}$  with the additional filter. Therefore it suppresses the background fluorescence by a factor of  $36$ . The fast decay in the first  $2 \text{ ms}$ , which can be seen in the first few milliseconds (Fig. 2.16 b)), was excluded from the fit. This fast decay is probably another fluorescence decay from a material in the spectroscopy setup. It can be ignored by starting the evaluation at  $t > 5 \text{ ms}$ .

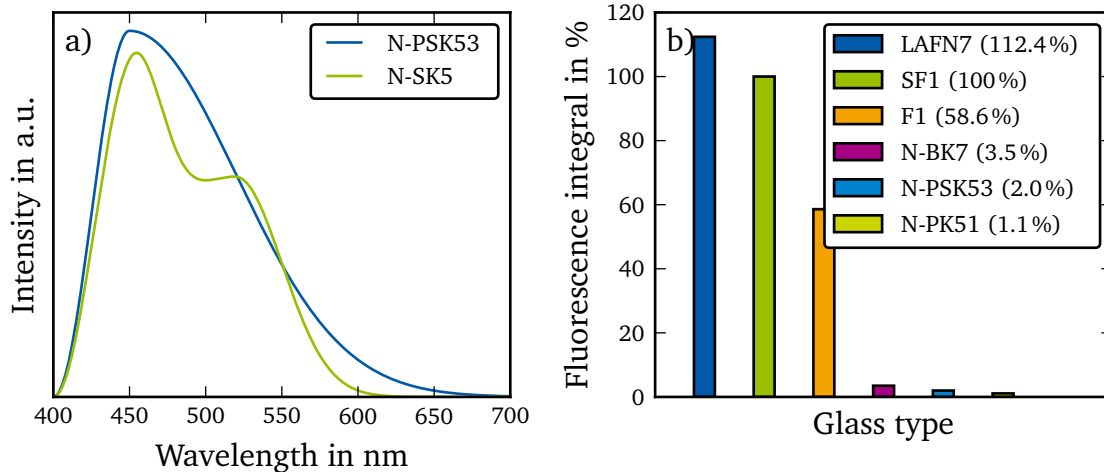


**Figure 2.17:** a) Qualitative emission spectra of low fluorescent optical glasses using an excitation wavelength of 365 nm and a cut off filter (KV 418). b) Typical fluorescence data normalized to SF1 using an excitation wavelength of 365 nm. Based on figures 5a and 5b from [81].

Both filters together attenuate the background by a factor of  $31 \times 36 = 1116 \approx 10^3$ . This indicates a broad fluorescence spectrum of the background signal. A measurement with the master laser at the longer wavelength of 452.756 nm and both filters yield no exponential decaying background signal. Only a constant background signal, due to external stray light from the laboratory, could be measured. Since the laser wavelength is blocked by both filters, this measurement is an indication that the decaying fluorescence background has spectral components at the excitation wavelength and a broad red-detuned spectrum. Noticeable is the fact that the shape of the histogram is not significantly affected significantly by the optical filters. Especially the interesting time constants around 10 ms are still observable.

---

### Fluorescence Signals of Different Materials

---

The fluorescence background signal has the temporal structure of a multi-exponential decay with at least four different decay times between 0.3 and 40 ms as discussed in the previous section. These long times compared to the short lifetimes of nanoseconds to microseconds of typical optical transitions in atoms and molecules indicates phosphorescence of the illuminated materials in the optical excitation and detection setup and the trap, especially the glass used. For phosphorescence, the excited molecules do not decay directly back into the ground state, but through one or several lower states, where only forbidden transitions are allowed. They have significantly longer lifetimes and the emitted photons have the same or a longer wavelength than the excitation light. This corresponds to the observation, that no fluorescence decay has been seen by excitation with longer wavelength at 452.756 nm of the master

---

laser. This wavelength is blocked by both filters. Since the exact origin of the background signal and therefore the exact emission process is unknown, it is not necessary to discriminate between phosphorescence and fluorescence in the further discussion and only the latter term will be used.

The background fluorescence signal is probably caused by a material in the optical excitation and detection setup. For a further suppression, a measurement of the material used has been performed.

A modified optical setup was necessary for a fast access to switch between different materials. Therefore, the optical preparation and fluorescence collection setup which sits in the cryogenic vacuum was placed in a test stand at room temperature. This test stand consists of standard CF vacuum parts, like bellows, chambers and flanges, made out of stainless steel to shield against stray light. For the measurement, the excitation and collection setup was a precursor of the current one shown in Fig. 2.12 b) and c). The precursor setup is discussed in detail in the thesis of von Lindenfels [45]. The main difference to the current one is the lens mountings, which were made of PEEK-cylinders instead of an aluminium cage system, and the incoupling of the laser light. In the old design, the fibre was attached to the outside of the mounting and the laser light beam was formed with an aspherical lens. The overlap of the laser light with the optical axis of the old setup was done with two prism glued to an aluminium arm.

Various materials were placed in front of the optical setup and were roughly fixed in place with aluminium foil. The laser power in front of the 27 m fibre was 1.7 mW, the laser was free running at approximately 441 nm, and the line filter (LL01-458-12.5) was removed to increase the signal rate by a factor of 14. The measurement was similar to the previous section: Illumination for 50 ms and fluorescence detection for 150 ms with 10 to 2000 repetitions. Again, a safety margin after the excitation and before the detection of 1 ms was used to prevent the detector from stray light of the laser. For the analysis, typical materials used in the cryogenic vacuum were chosen. These are aluminium, PEEK, polytetrafluoroethylene best known as Teflon, and a quartz window, which is the same material used for the optical access to the spectroscopy trap (Fig. 2.12 b)). Additionally, two different adhesives were tested, Armstrong A12 and low temperature varnish LTV SCBltv01. The adhesives were applied to microscope glass slides.

The results are shown in Fig. 2.18 and in table 2.3. The histograms of the fluorescence have a binwidth of 0.3 ms. The fits are based on an exponential decaying fluorescence rate  $\dot{N} = a \cdot e^{-t/\tau} + b$  with the amplitude  $a$ , the decay time  $\tau$  and an offset  $b$ . The fluorescence rate has a fast decay in the first 2 ms, therefore only the time interval between 2 and 120 ms were fitted. The absolute counts in Fig. 2.18 b) were calculated by integrating the fit function over the observation interval from 0 to 150 ms. The uncertainty of the amplitude and the total count number is approximately 30%. This uncertainty was obtained by repeating the measurement with the Armstrong A12 and the aluminium and is caused by variations in the positioning in front of the excitation setup. The uncertainties from the fits are significantly smaller

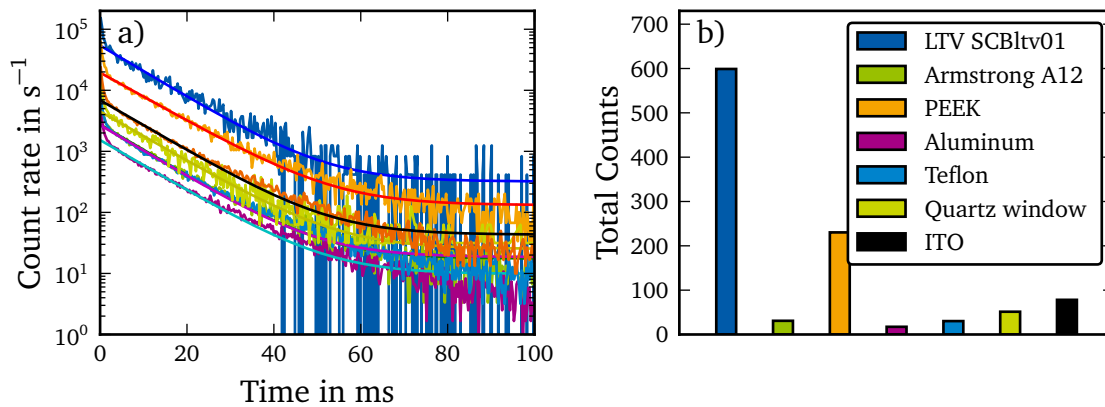


**Figure 2.18:** Evaluation of the fluorescence signal of different materials. a) Fluorescence histograms and fits after the laser light is switched off. The binwidth is 0.3 ms and the count rate is normalized by dividing the counts per bin through the binwidth. The exponential decay constants varies between 8 and 11 ms. b) Total counts calculated from the fits by integrating over one observation cycle from 0 to 150 ms. The uncertainties are about 30 %.

and can be neglected. The decay time varies in a small range between 8 and 11 ms, but the total counts and the amplitude spread over more than a factor 30. PEEK and the low temperature adhesive LTV produce the strongest fluorescence which was one of the main reasons to redesign the optical excitation and collection setup. The new setup (Fig. 2.12 c)) consists of an aluminium cage system instead of a PEEK mount and no adhesives are used.

A further reduced test stand using only a blue LED in a vacuum flange and the detection setup (Fig. 2.12 e)) without the image guide and the optical excitation setup still yields a weak decaying fluorescence signal with a time constant of 10.6 ms. This is an indication that the glass optics also fluoresce.

This assumption is reinforced by measurements presented by SCHOTT in [81]. With a fluorescence spectrometer consisting of a Czerny-Turner Double monochromator and a photomultiplier, the fluorescence spectra of different optical glasses were measured (Fig. 2.17 a) and b)). The excitation was done using light with a wavelength of 365 nm. All glass types have a strong fluorescence peak at 435 nm. Most optical elements in the optical setup are made out of N-BK 7. This type of glass shows only a weak fluorescence compared to other substrates (Fig. 2.17 b) and Fig. 5b in [81]).

---

## Conclusion

---

The fluorescence spectroscopy for the  $Ar^{13+}$  fine-structure transition was tested and characterized in a background measurement without ions. The obtained background

Material	Amplitude in $s^{-1}$	Time constant in ms	Total counts per cycle
Aluminum	1521	10.4	17
ITO coated BK7	6844	10.5	78
Quartz window	4473	10.6	51
Teflon	2673	10.3	30
PEEK	19323	10.9	230
Armstrong A12	2741	10.3	31
LTV SCBltv01	53867	10.2	599
LTV SCBltv01 <sup>1)</sup>	513 / 38 <sup>2)</sup>	9.0 / 7.9 <sup>2)</sup>	5.7 / 0.4 <sup>2)</sup>

**Table 2.3:** Fluorescence signal evaluation of different materials. The total counts per detection cycle and the amplitude are derived from exponential fits to the fluorescence histograms. The PEEK and the low temperature varnish show the strongest fluorescence, while teflon, aluminium, and armstrong A12 are only weakly fluorescing. Notes: 1) Only a small amount of LTV on a glass substrate were used. 2) Measurement with the narrow line filter (LL01-458-12.5) by Semrock. The other measurements were made without this filter to increase the statistics and measurement speed. The filter suppresses the signal by a factor of 14.

signal yields a temporal decay similar to the expected lifetime of the excited  $Ar^{13+}$  state. This signal interferes with the  $Ar^{13+}$  spectroscopy and has been therefore suppressed with two filters by three orders of magnitude. For further reduction, the fluorescence of the materials used in the spectroscopy were measured in a test setup. The results were used to optimize the optical setup for the excitation and fluorescence collection.

A result of the material characterization is the strong fluorescence of low temperature varnish and PEEK. The measurements with the reduced setup excludes the image guide and the single-mode fibre as the source of the residual fluorescence. Thus, the origin of the residual fluorescence are probably the glass substrates of the used optics such as the vacuum window, the lenses, and the filters. An additional indication for the fluorescence of the glass are the spectral measurements by Schott [81].

A further reduction of the background signal could be done with an additional narrowband filter. Alternatively, the existing line filter could be rotated by  $8^\circ$ . This shifts the edge of the transmittance range to shorter wavelength next to the expected  $Ar^{13+}$ -transition.

Another option to handle the background signal is the implementation of a camera instead of the single-photon detector. This allows to discriminate the regions of the background fluorescence from the expected ion fluorescence. This can be done with standard image processing of the recorded fluorescence images such as subtracting a dark image (without any laser excitation) and dividing by a white image (with laser light but no ions in the trap).

---

Considering the estimated signal rate of up to  $5 \times 10^3 \text{ s}^{-1}$  of the  $\text{Ar}^{13+}$  fluorescence (page 31), the current optimized setup is sufficient for the spectroscopy.



---

## 3 Tellurium Spectroscopy

The optical fine-structure transitions of  $\text{Ar}^{13+}$  can be found in a range between 441.150 nm and 441.360 nm. The six transitions are equally spaced by 65 GHz due to the Zeeman-shift in the magnetic field of the Penning trap. Thus, the laser spectroscopy requires a laser system, which can be stabilized at arbitrary frequencies in this range. The necessary accuracy depends on the transition width. In the ARTEMIS Penning trap, the natural linewidth  $\Gamma = 2\pi \times 16.6 \text{ s}^{-1}$  is surpassed by the Doppler broadening at 4 K, causing a full width at half maximum of 150 MHz. As the Doppler broadening limits the achievable resolution, an overall absolute accuracy of around 10 MHz is sufficient for the laser spectroscopy at this stage

Molecular spectroscopy of  $^{130}\text{Te}_2$  is an optimal choice as a reference: It has a variety of transitions in the blue wavelength region, some of which are mapped in the tellurium atlas of Cariou and Luc [65]. Unfortunately, their setup was only able to measure the Doppler-broadened spectrum. Thus, the resolution is limited to several 10 MHz to 100 MHz and a constant offset of around 60 MHz was found in [70, 76]. Additionally, the distance between those lines can be up to several  $10^{10}$  Hz. These limitations make a re-evaluation of the tellurium spectrum in the region of interest necessary. Scholl et al. [77] also characterized several lines, but using a Doppler-free spectroscopy with an absolute accuracy of 1 MHz. These results will be used in this chapter to determine the absolute frequency of selected Lamb dips close to the expected  $\text{Ar}^{13+}$ -transitions with respect to the Zeeman splitting in the Penning trap. Furthermore, the continuous frequency stabilization and the long-term frequency stability of the laser system will be discussed.

---

### 3.1 Refractive Index of Air

---

A central element of the laser system is the transfer resonator (Fig. 2.3). As it is not evacuated but situated in air, the accuracy of the frequency stabilisation and scan methods depend on the dispersion in air. Due to the large wavelength difference between the master (452.756 nm) and the spectroscopy laser (441.150 nm to 441.360 nm) it has a significant influence on the frequency stability of the transfer cavity.

The refractive index of air does not only depend on the wavelength, but also on temperature and pressure. A much smaller influence can be attributed to the humidity and the carbon dioxide concentration. These quantities were measured and fitted to phenomenological equations by Edlén [82]. A revised version was published in 1993 by Birch and Downs [83]. Besides a higher accuracy and a correction for higher carbon dioxide levels, they also expressed all values in SI units.

Not considering the temperature and pressure dependence, the dispersion in air is given by

$$n(\sigma) = 1 + \left( 8343.05 + \frac{2406294}{130 - (\sigma/\mu\text{m}^{-1})^2} + \frac{15999}{38.9 - (\sigma/\mu\text{m}^{-1})^2} \right) \times 10^8, \quad (3.1)$$

with the vacuum wavenumber  $\sigma$ . It is the reciprocal wavelength in vacuum,  $\sigma = 1/\lambda$ .

The main contributions to the variation of the refractivity are the temperature  $T_C$  and the pressure  $p$ . They yield the correction term

$$n(\sigma, T_C, p) = 1 + \frac{(n(\sigma) - 1)p/\text{Pa}}{96095.43} \frac{1 + 10^{-8} (0.601 - 0.00972 T_C/^\circ\text{C}) p/\text{Pa}}{1 + 0.0036610 T/^\circ\text{C}}. \quad (3.2)$$

The temperature  $T_C$  is given in  $^\circ\text{C}$ . The equation is valid between 15 and 30  $^\circ\text{C}$  and between 933 and 1067 hPa with a deviation in  $n$  not larger than  $1 \times 10^{-8}$ .

The humidity, or rather the water vapour pressure  $p_w$  in air, has a much smaller influence given by

$$n(\sigma, T_C, p, p_w) = n(\sigma, T_C, p) - p_w/\text{Pa} \left( 3.7345 - 0.0401 (\sigma/\mu\text{m}^{-1})^2 \right) 10^{-10}. \quad (3.3)$$

Most commercially available sensors measures relative humidity  $\varphi \leq 1$  instead of the vapour pressure. A conversion can be done using

$$p_w = \varphi p_{w,\text{sat}}, \quad (3.4)$$

with the temperature-dependent water vapour pressure of saturated air

$$p_{w,\text{sat}} = 611.2 e^{\frac{17.62 T_C/^\circ\text{C}}{243.12 + T_C/^\circ\text{C}}}. \quad (3.5)$$

The temperature  $T_C$  is again given in  $^\circ\text{C}$ .

The air pressure, the temperature, and the relative humidity are measured in the laboratory every five minutes and can be used to calculate the refractive index of air at this time. This is needed in the next sections to determine the optical length  $l_{\text{opt}}$  of the transfer cavity, which depends both on the geometrical length  $l_{\text{geom}}$  and the refractive index. The environmental conditions in the laboratory are stable with a temperature of 21.4(2)  $^\circ\text{C}$  and a relative humidity between 40 and 50% (Fig. 2.11 b)). The transfer cavity is temperature stabilized to 19.8  $^\circ\text{C}$ . Additionally, the air convection is limited by a closed cavity case with only small holes for pressure compensation. Thus, the humidity in the resonator only changes due to slow diffusion and a constant relative humidity of  $\varphi = 0.4 \pm 0.1$  can be assumed. Because of this, only the measured air pressure is used in the next sections to calculate the refractive index. Temperature and humidity are fixed to the given constant values. All calculations in this section use the full refractive index  $n(\sigma, T_C, p, p_w)$ . To improve the readability, the notation is simplified to  $n_{\text{ML}}$ ,  $n_{\text{SL}}$ , and  $n_\lambda$  for the refractivity at the master laser (ML) wavelength, the spectroscopy laser (SL) wavelength, and the wavelength  $\lambda$  with the current air pressure. If an equation has multiple refractivities, an additional index  $i$  is used to indicate different measurement times, e.g.  $n_{\text{ML},i}$ . This is important for time depending drifts of the air pressure.

---

## 3.2 Continuous Frequency Stabilization Scheme

---

The stabilization scheme of the laser system will be discussed in this section. It can be divided into three parts, a coarse frequency stabilization, a scheme which allows smaller frequency steps of around 60 MHz, and a continuous fine-tuning with a sub-MHz resolution.

The selection of the desired Zeeman transition which are separated by 65 GHz must be done manually by rotating the back-reflecting grating of the external cavity of the spectroscopy laser. Since the mode hop free tuning range with the laser current and piezo ring actuator voltage, which are accessible via a software interface on the laboratory computer, is only a few tens of GHz.

After setting the spectroscopy laser to the desired frequency, it can be stabilized using the three schemes mentioned above. First, it can be locked on the longitudinal modes of the transfer cavity. This allows for coarse locking in discrete frequency intervals of the free spectral range of 2111.45 MHz (Sec. 3.3, p. 54). The length, and with it the longitudinal modes of the transfer resonator, are stabilized to the master laser wavelength, which uses the tellurium spectroscopy for its stabilization.

However, a fine-tuning method is needed to cover the range in between. Therefore, different methods were tested and presented in detail by F. Vollrath in [84]: One idea was a sideband modulation of the spectroscopy laser. A radio frequency (RF) of several hundreds of MHz is modulated on the laser diode current with a bias tee. This produces sidebands around the centre wavelength of the laser. With the spectroscopy laser, sidebands between 290 MHz and 400 MHz can be achieved. Using both upper and lower sideband together, a scan range of around 10 % of the FSR is achievable by locking the laser to one of them. A disadvantage of this method is the loss of laser power in the central laser mode into the sidebands and an instability of the single frequency mode operation with increasing RF modulation. Because of this and the limited scan range, the method was discarded. The same arguments apply for the modulation of the master laser: No stable single frequency mode could be established with the RF modulation. Another option to tune the laser frequency is the use of an acousto-optic modulator (AOM) to stabilize the spectroscopy laser wavelength on the transfer resonator. This method was finally implemented. The AOM has a centre frequency of 125 MHz and approximately 1 mW of the spectroscopy laser main beam is sufficient for the stabilization. To increase the scan range, the AOM is used in a double pass configuration. This also solves the issue of unwanted beam pointing, which inhibits efficient coupling into a fibre. A scan range of 70 to 210 MHz could be achieved. This corresponds to a frequency range of the laser light of  $2 \times 140 \text{ MHz} = 280 \text{ MHz}$  due to the double pass configuration. This is in the same order as the sideband modulation, but has the advantage that the stability of the single mode operation isn't decreased. The use of the minus-first order of the AOM leads to a positive frequency shift of the main beam for the  $\text{Ar}^{13+}$ - and tellurium-spectroscopy.

However, a scan over the tellurium spectrum with the double-pass AOM only covers a small part of the FSR of the transfer cavity (Fig. 3.1 a) and b)). To increase the fine

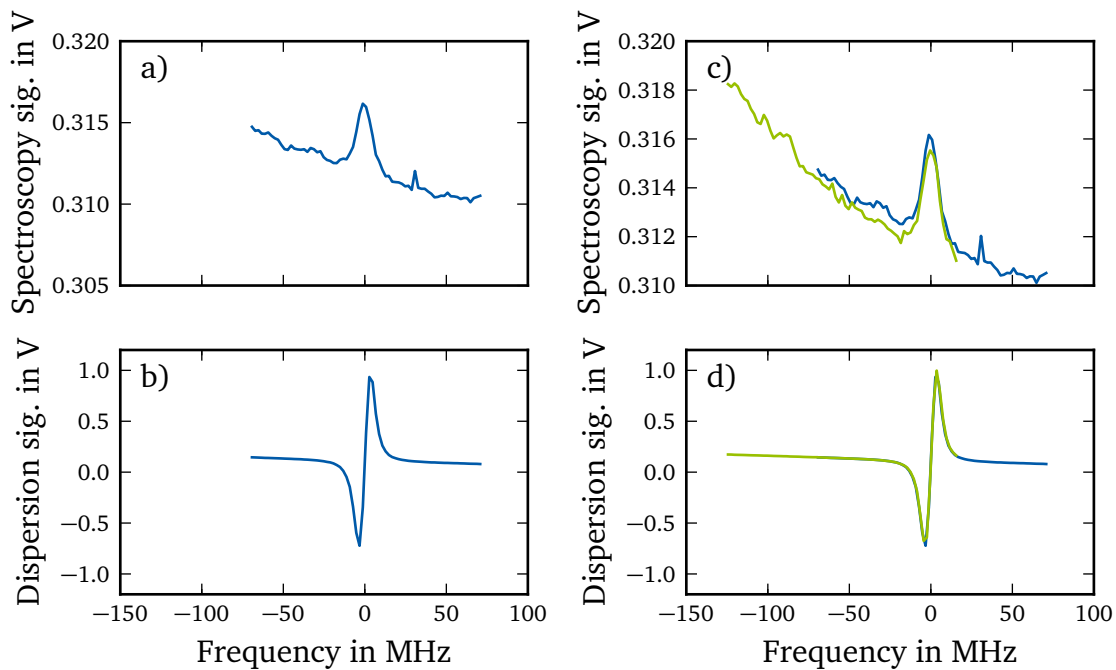


**Figure 3.1:** Scan over  $\text{Te}_2$ -spectrum with the double-pass AOM around a Lamb dip at 441.156 nm. a) and b) show the photodiode signal, which corresponds to the transmission of the spectroscopy, and the dispersion signal. c) and d) Additional frequency-shifted scan based on locking to the next longitudinal resonator mode at the master and spectroscopy laser wavelength.

tuning range of the laser frequency to the full FSR two methods were investigated. The first option to increase the scan range, which was discarded, is a stabilization of the master laser to different tellurium Lamb dips [84]. This causes small changes (only fractions of the wavelength) of the transfer resonator length, which is stabilized on the maser laser wavelength. Together with the double-pass AOM the complete FSR can be covered with enough Lamb dips. The disadvantage of this method is the manual locking to another Lamb dip, which is hard to automatize.

A better option is the usage of a cavity mode jump technique. Here, the master laser is always locked to the same Lamb dip and the transfer resonator is stabilized to different longitudinal cavity modes. This is done by changing the resonator length with the piezoelectric ring actuator. A change of one cavity mode at the master laser wavelength leads also to one mode jump at the spectroscopy laser wavelength plus a small frequency offset due to the wavelength difference (Fig. 3.2). These offsets are smaller than the scan range of the double-pass AOM. Thus, the complete FSR can be covered with multiple jumps.

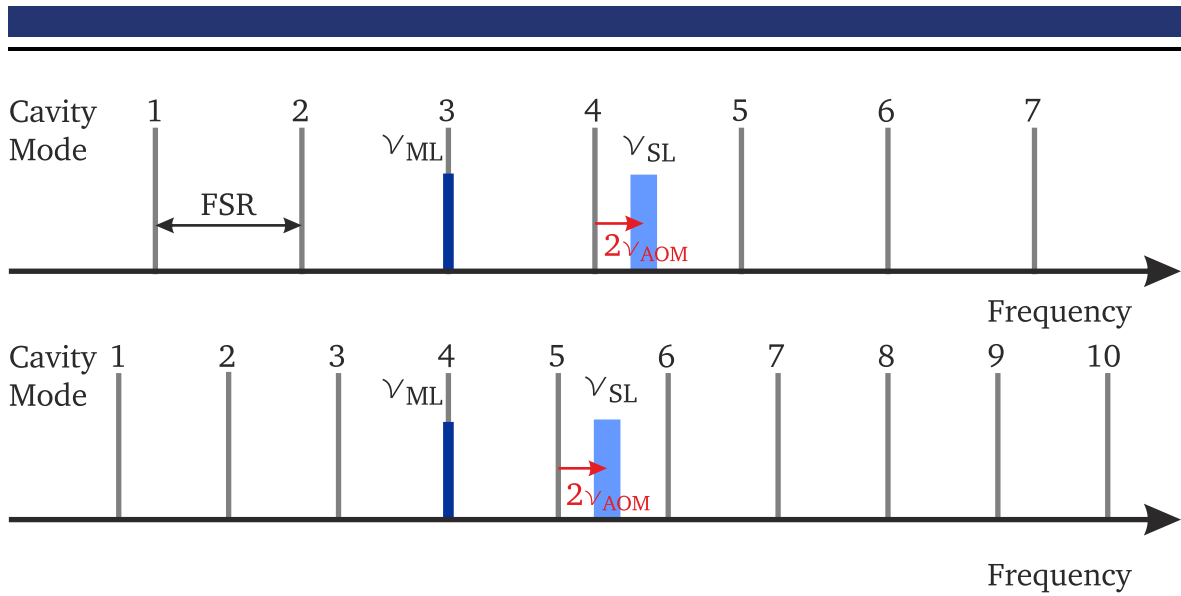


**Figure 3.2:** Cavity mode jump scheme. In the top graph the cavity is stabilized at the master laser frequency (indicated in dark blue) on the third cavity mode. The spectroscopy laser (light blue) is locked on the fourth mode via the double pass AOM, while the centre wavelength is shifted by twice the RF frequency (red arrow), which drives the AOM, to a higher frequency. The bottom graph shows the cavity stabilized on the 4th mode, while the slaver laser is on the 5th mode. The centre wavelength of the spectroscopy laser is shifted by a frequency offset and the FSR of the cavity is smaller due to the length change of the cavity.

The calculation of the frequency offset due to a mode jump  $\Delta M_{\text{jump}}$  is based on the equation for the resonance frequency of the resonator

$$\nu = \frac{Nc_0}{2nl_{\text{geom}}}, \quad (3.6)$$

with the geometrical length  $l_{\text{geom}}$  of the cavity, the speed of light in vacuum  $c_0$ , the refractive index of the medium between the mirrors  $n$ , and the  $N$ th longitudinal cavity mode. The master laser is always locked on the same Lamb dip, thus the frequency  $\nu_{\text{ML}}$  remains constant. From this follows that the optical length at the master laser wavelength  $l_{\text{opt,ML}} = n_{\text{ML}}l_{\text{geom}}$ , which depends on the refractive index  $n_{\text{ML}}$  at the actual wavelength, must change for a mode jump  $\Delta M_{\text{jump}}$  by

$$\begin{aligned} \nu_{\text{ML}} &= \frac{M_0 c_0}{2l_{\text{opt,ML}}} \text{ and} \\ \nu_{\text{ML}} &= \frac{(M_0 + \Delta M_{\text{jump}}) c_0}{2(l_{\text{opt,ML}} + \Delta l_{\text{opt,ML}})} \\ \Rightarrow \Delta l_{\text{opt,ML}} &= l_{\text{opt,ML}} \frac{\Delta M_{\text{jump}}}{M_0} = \frac{\lambda_{\text{ML}}}{2} \Delta M_{\text{jump}}, \end{aligned} \quad (3.7)$$

with the master laser wavelength  $\lambda_{\text{ML}}$  and the cavity mode  $M_0$  of the master laser wavelength. The optical length changes by half the master laser wavelength for one mode jump. For the small wavelength difference between master and spectroscopy laser, the spectroscopy laser wavelength also shifts one FSR ( $\Delta N_{\text{jump}} = 1$ ) plus a frequency offset  $\nu_{\text{jump,SL}}$ . For a single mode jump  $\Delta M_{\text{jump}} = 1$  this yields

$$\begin{aligned} \nu_{\text{jump,SL}} := \nu_{\text{jump}}(\nu_{\text{SL}}) &= \frac{(N_0 + 1)c_0}{2n_{\text{SL}} \left( \frac{l_{\text{opt,ML}} + \Delta l_{\text{opt,ML}}}{n_{\text{ML}}} \right)} - \frac{N_0 c_0}{2n_{\text{SL}} \frac{l_{\text{opt,ML}}}{n_{\text{ML}}}} \\ &= \frac{c_0}{2l_{\text{opt,ML}}} \frac{n_{\text{ML}}}{n_{\text{SL}}} \frac{M_0 - N_0}{M_0 + 1} \\ &\approx \frac{c_0}{2l_{\text{opt,ML}}} \left( \frac{n_{\text{ML}}}{n_{\text{SL}}} - \frac{\nu_{\text{SL}}}{\nu_{\text{ML}}} \right), \end{aligned} \quad (3.8)$$

with the spectroscopy laser frequency  $\nu_{\text{SL}}$ , the refractive index of air  $n_{\text{SL}}$  at  $\nu_{\text{SL}}$ , and the cavity mode  $N_0$  at  $\nu_{\text{SL}}$ . The result yields a frequency shift of  $\nu_{\text{jump,SL}} = -55.520(1)$  MHz for a master and spectroscopy laser wavelength of 452.756 nm and 441.156 nm and an optical length of  $l_{\text{opt,ML}} = 70.99$  mm (table 3.1 for more spectroscopy laser frequencies). Besides the length uncertainty, the uncertainty considers the frequency uncertainty of master and spectroscopy laser and also a change of the refractive index due to air temperature, pressure, and humidity drifts of 0.2 K, 1 hPa, and 10 %.

This technique allows for an increase of the frequency scan range (Fig. 3.1 c) and d)). With multiple jumps the complete FSR of the cavity can be covered. A remote control and sample-and-hold circuit of the spectroscopy laser PID-controller and the transfer cavity's PI-controller enables a fully automatized frequency scan.

---

### 3.2.1 High Resolution Frequency Scan over Several Gigahertz

---

To demonstrate the tunability of the laser system, a scan was made over a complete free spectral range of the transfer cavity (Fig. 3.3) around the calibration line at 441.156 nm (next to the relative cavity mode 474, see next sections for details). The measurement consists of small scans with the AOM, which shifts the spectroscopy laser wavelength over the spectrum. Each scan is frequency shifted with the cavity mode jump scheme presented in the last section. Additionally, a second measurement was made, which started one FSR towards lower frequencies (at the relative cavity mode 473). The assembled spectrum is shown in Fig. 3.3. The complete measurement consists of 185 scans. Each covers a range of 140 MHz and is shifted by  $\nu_{\text{jump,SL}} = -55.20(5)$  MHz. The offset is obtained by fits of dispersion signal of the Lamb dips and is smaller than the previously calculated values (table 3.1 on page 55) because of a different master laser wavelength. The two measurements from the different cavity resonances (relative cavity modes 473 and 474) are separated by the FSR of 2.111 GHz. The Fits to the dispersion signal of the Lamb dip at  $-1100$  MHz,

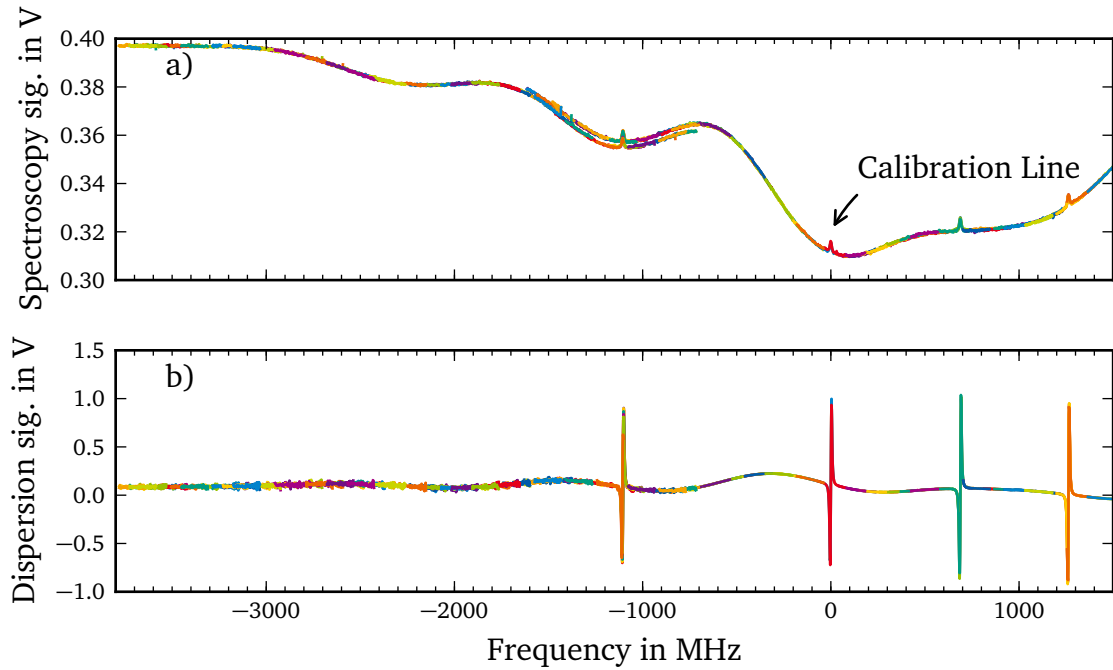


**Figure 3.3:** Frequency scan over several gigahertz of the tellurium spectrum. a) Photodiode signal of the spectroscopy. The Doppler-broadened spectrum with the Lamb dips can be seen. b) Dispersion signal derived using a lock-in amplifier. The Lamb dips produce strong signals, which can be used to determine the centre frequency. The frequency is given relative to the calibration line at the relative cavity mode 474 (Table 3.1) with the frequency  $\nu_{441.156}$ . Each frequency scan with the AOM over a range of 140 MHz is plotted in a separate colour. With the cavity mode jump method they are all frequency shifted relative to each other by  $\nu_{\text{jump,SL}} = -55.2$  MHz. The overall measurement consists of two runs starting at the relative cavity modes 473 and 474, respectively. The overlap can be seen in a) around the Lamb dip at  $-1104$  MHz. The two runs have a small signal offset, which is caused by small variations of the spectroscopy laser power and the  $\text{Te}_2$ -oven temperature.

---

which is included in both measurements, confirm this value. The signal between  $-3800$  MHz and  $-700$  MHz is noisier than the rest. This was caused by incorrect gain settings of the PID-controller of the spectroscopy laser, which led to a frequency oscillation. This issue only had a minor influence on the signals and the laser system. The small offset in the spectroscopy signal around  $-1000$  MHz has its origin in small variations of the laser power and varying pressure and absorption, which are caused by changes of temperature in the tellurium cell. The positions of the Lamb dips are at  $-1104(1)$  MHz,  $0.00(5)$  MHz,  $688.1(7)$  MHz, and  $1263(1)$  MHz.

The measurement covers a frequency range of 5.3 GHz. This is more than twice the FSR and demonstrates the ability to stabilize the laser system continuously on every wavelength within the range of the spectroscopy laser.

---

### 3.3 Frequency Determination of Important Lamb dips

---

The  $\text{Te}_2$ -spectroscopy can be used as an absolute frequency reference for the determination of the  $\text{Ar}^{13+}$ -transitions.  $\text{Te}_2$  has a lot of transitions in the region of interest and some were measured with a high accuracy of 1 MHz by Scholl et al. [77]. The high accuracy lines closest to the centre wavelength of the  $\text{Ar}^{13+}$ -transition at 441.256 nm are the  $\text{Te}_2$ -atlas lines 1855 at 441.807 nm and the two closely spaced lines 2082 and 2083 at 439.598 nm. This corresponds to a frequency range of 3.4 THz. The references can be used as the end points for a record of a high-resolution spectrum, but a scan of the stabilized laser system with the AOM and the cavity mode jump scheme would take several months. Thus, this method is not suitable and an alternative approach will be discussed.

To calibrate the  $\text{Te}_2$ -spectroscopy, the transfer resonator was stabilized to the master-laser frequency while the spectroscopy laser was free-running. The master-laser frequency was locked to a  $\text{Te}_2$ -line at 452.756 nm. This creates fixed equidistant frequency markers with a spacing of the FSR of the cavity. Frequency scans of the spectroscopy laser allow for recording the photodiode signal of the  $\text{Te}_2$ -spectroscopy and the cavity signal at the same time. Therefore, the laser scanned between 10 and 50 GHz several times per second over the spectrum (Fig. 3.4 a) and b)). The complete spectrum between the three reference lines 1855, 2082, and 2083 was recorded by taking a series of overlapping scans.

The processing of the recorded data consists of several steps: Normalizing each spectrum to multiples of the FSR instead of the scan voltage, combining the spectra, and absolute frequency calibration of the cavity modes.

Because of the non-linearity of the scan method using the piezoelectric ring actuator of the spectroscopy laser, an automatic routine was used to detect the cavity peaks and to linearly interpolate the abscissa in multiples of the FSR. The normalized spectra were combined manually to form a complete  $\text{Te}_2$ -spectrum. One issue of the wide scan range is the laser power. It drops with higher scan voltages, because of the current feed forward circuit in the laser. This leads to a decreasing spectroscopy signal. The linear and quadratic effects of this decrease are dominant and were cor-

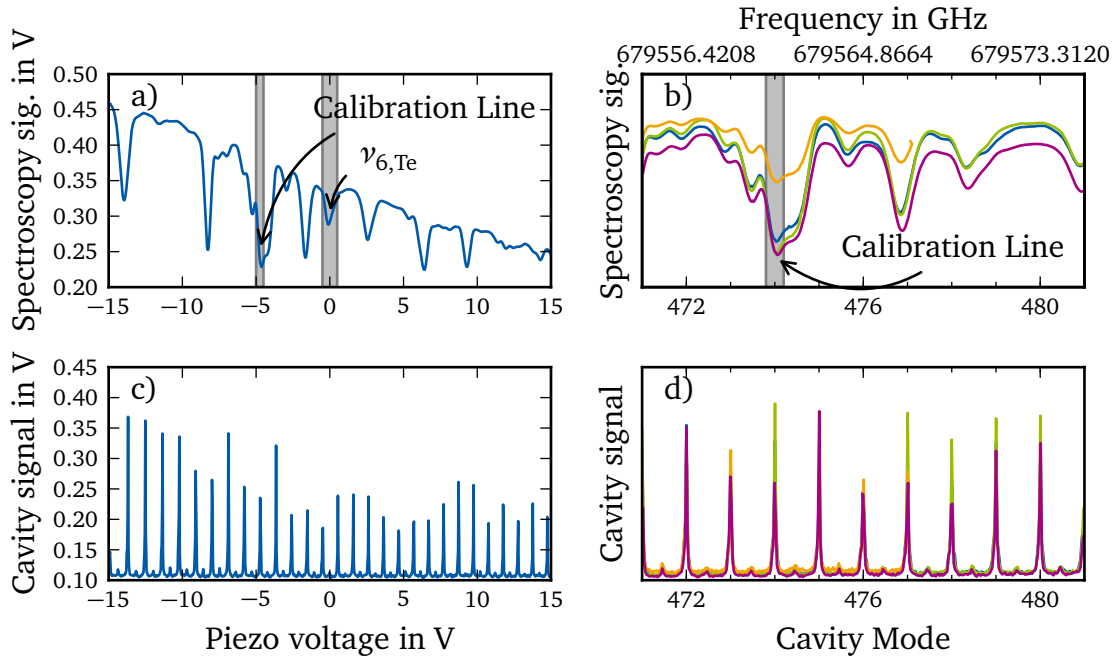


**Figure 3.4:** Scan over the  $\text{Te}_2$ -spectrum and the transfer resonator at 441.156 nm. a) and c) show the recorded raw data of the frequency scan. The piezo voltage is in this case a non-linear measure for the frequency. b) and d) depict the tellurium and cavity-scan data after processing. The signal strengths are normalized and the spectra are scaled such that the frequency axis is given in multiples of the FSR. The lines with different colours indicate the different overlapping and frequency-shifted scans. The different scans were stitched together manually.

rected with a fit (Fig. 3.4 c) and d) for a detailed view of the final spectrum). Because of the measurement setup and this evaluation method, the relative absorption of two largely separated Doppler-broadened lines is not comparable. In this case the  $\text{Te}_2$ -atlas [65] should be used. The complete spectrum revealed a distance of  $\approx 1615$  FSRs between reference line 1855 and 2082 and  $\approx 1616$  FSRs between 1855 and 2083. For the evaluation, the number of FSRs between one of the reference lines and a desired frequency (for example a tellurium Lamb dip or an  $\text{Ar}^{13+}$ -transition) is of importance. Therefore, the first cavity resonance next to line 1855 is defined as the origin and has the relative cavity mode  $\Delta N_{1855} = 0$ . This yields the relative modes  $\Delta N_{2082} = 1615$  and  $\Delta N_{2083} = 1616$  for the lines 2082 and 2083.

In the next step, the absolute frequencies must be calculated from the normalized spectrum, which is only given in relative FSRs. Therefore, the exact frequency position of the reference lines 1855, 2082, and 2083 relative to the cavity modes were determined: The spectroscopy laser was stabilized to the cavity and a high resolution frequency-scan with the AOM and the cavity mode jump method was done (Fig. 3.5). In addition to the absorption signals of the spectroscopy with the Lamb dips,

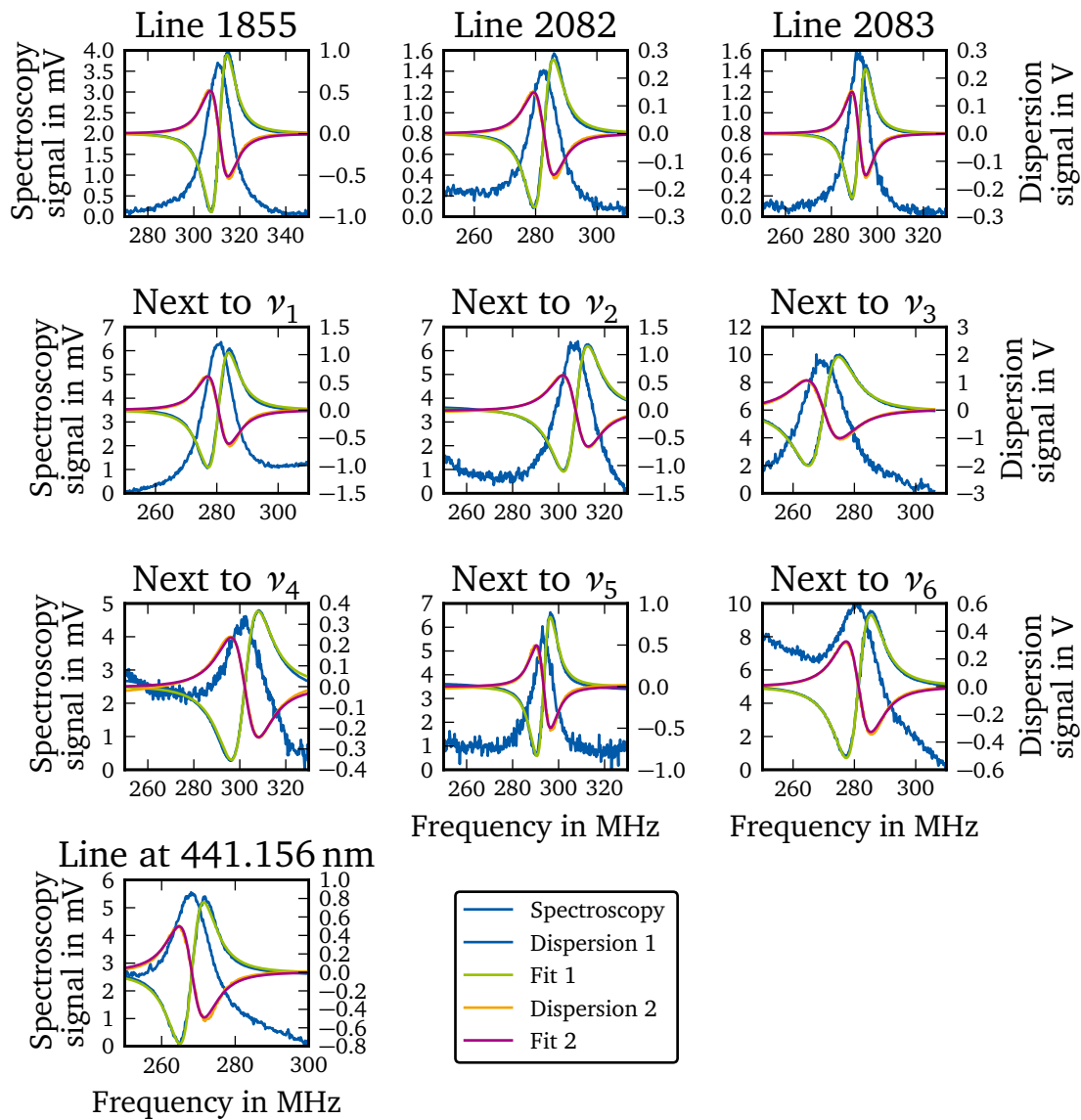


**Figure 3.5:** Frequency scan over different  $\text{Te}_2$ -transitions using the AOM. In addition to the Lamb dips, the dispersion signal of two lock-in amplifiers with a phase shift of  $\approx 90^\circ$  and corresponding fits are shown. The three tellurium lines 1855, 2082, and 2083 are known with high accuracy and are used as reference lines. The next six lines are Lamb dips next to the expected  $\text{Ar}^{13+}$ -transitions and the last one is used for several characterization and calibration measurements.

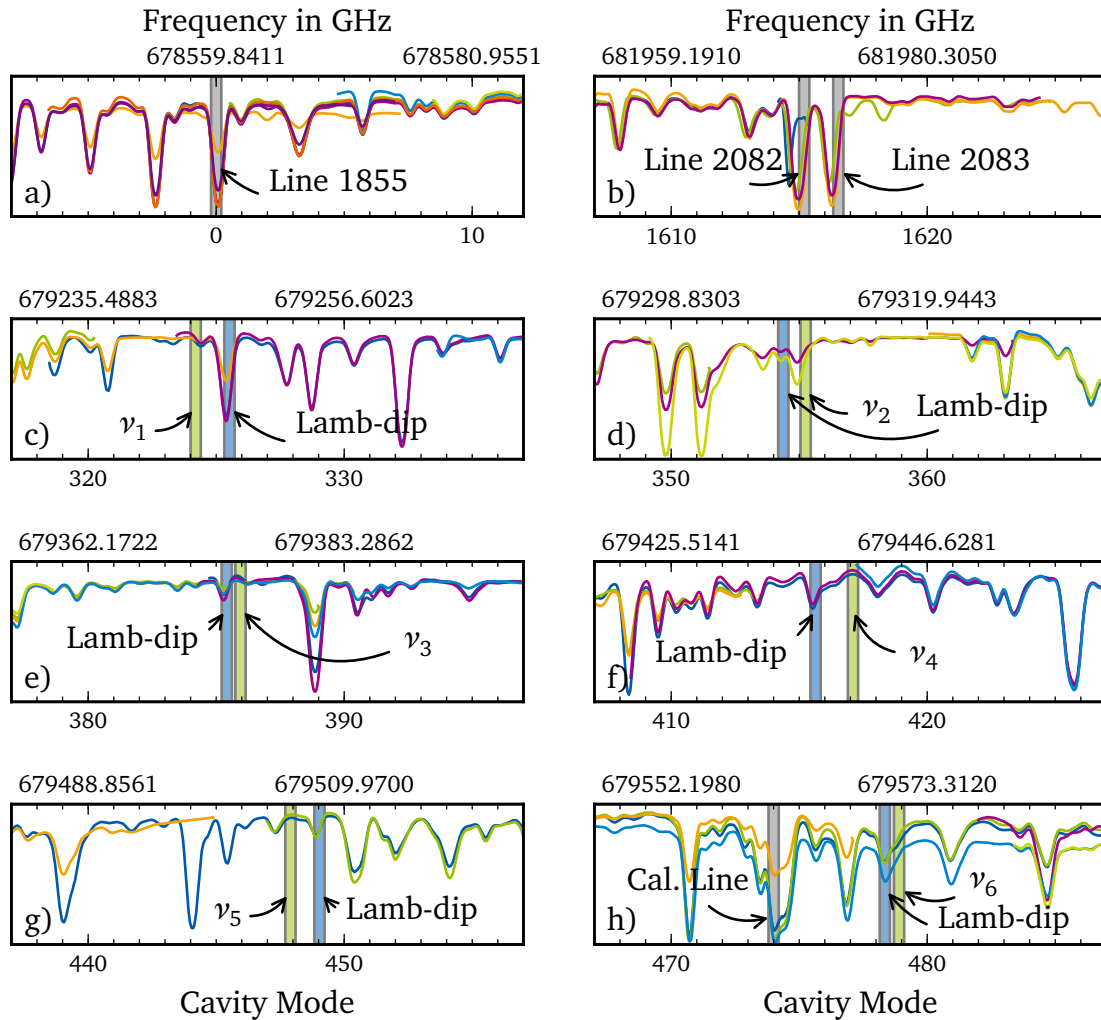


**Figure 3.6:** Important regions of the Te<sub>2</sub>-spectrum. a) and b) shows the reference lines measured by Scholl et al. [77]. d) to h) show the regions, where the Ar<sup>13+</sup>-transitions are expected for a magnetic field of 7.003 T. The closest available Te<sub>2</sub>-Lamb dips, which can be used as a reference are marked. The relative cavity modes are measured and the origin is set next to the Te<sub>2</sub>-reference line. The absolute frequencies are calculated from these modes and have an uncertainty of around 1.3 MHz.

the dispersive signal from a lock-in amplifier were recorded. The Lamb dips have a Lorentzian shape. Thus, the derivation of this function with an offset were fitted to the signals from the LI-amplifier in a small range around the centre (table 3.1). The uncertainty of the centre frequency of the fits of  $< 20$  kHz is negligible compared to the uncertainty of 1 MHz of the reference lines. For line 1855, the evaluation yields a frequency difference to the next resonance of 311.03(9) MHz. No cavity jumps of the master-laser lock were necessary to reach the Lamb dip. For line 2082 and 2083, -2 and -13 cavity mode jumps were necessary. The negative sign indicates a reduction of the cavity length. The frequency difference to the next cavity resonance of line 2082 yields  $282.69 \text{ MHz} + (-2)(-63.202 \text{ MHz}) = 409.09 \text{ MHz}$ . For line 2083 it yields  $291.94 \text{ MHz} + (-13)(-63.211 \text{ MHz}) = 1136.9 \text{ MHz}$ . The frequency change due to the jump is calculated with equation (3.8). With this results, the absolute frequencies  $\nu_{\Delta N,1855}$ ,  $\nu_{\Delta N,2082}$ , and  $\nu_{\Delta N,2083}$  of the three relative modes  $\Delta N_{1855}$ ,  $\Delta N_{2082}$ , and  $\Delta N_{2083}$  will now be calculated.

With the knowledge of the absolute frequency of three cavity resonances and the number of FSRs  $\Delta N$  between them, the length of the cavity and the absolute longitudinal cavity mode  $N_{1855}$ , which corresponds to the resonance next to line 1855, can be calculated. Due to the stabilization of the cavity to the master-laser frequency, the optical length at this wavelength  $l_{\text{opt,ML}} = l_{\text{geom}} n_{\text{ML}}$  is constant. The geometrical length changes with the air pressure due to the refractive index of air at the master-laser wavelength  $n_{\text{ML}}$ . Therefore, the cavity equation 3.6 for the frequency  $\nu$  can be modified to be

$$\nu = \frac{n_{\text{ML}}(N_{1855} + \Delta N)c_0}{2n_{\lambda}l_{\text{opt,ML}}}. \quad (3.9)$$

The geometrical length is substituted by the optical length  $l_{\text{opt,ML}}$  and the corresponding refractive index  $n_{\text{ML}}$ . The refractive index  $n_{\lambda}$  corresponds to the actual mode  $N_{1855} + \Delta N$  and can be calculated. The optical length  $l_{\text{opt,ML}}$  and the absolute mode  $N_{1855}$  can be obtained from a fit using the three known cavity resonances  $\nu_{\Delta N,1855}$ ,  $\nu_{\Delta N,2082}$ , and  $\nu_{\Delta N,2083}$ . It yields the length  $l_{\text{opt,ML}} = 70.992\,617(28) \text{ mm}$  and the absolute cavity mode for the resonance next to line 1855 of  $N_{1855} = 321\,374.05(13)$ . In this case, the FSR is 2111.4500(8) MHz for an air pressure of 1000 hPa and at a wavelength of 441.256 nm, but depends on the actual wavelength and the air pressure due to the refractivity of air. E.g. at a wavelength of 441.150 nm and 441.362 nm, the FSR is 17 kHz lower.

In principle, the frequency of an arbitrary mode can now be calculated with the length  $l_{\text{opt,ML}}$ , the absolute cavity mode  $N_{1855}$ , and the modified resonator equation (3.9). The calculation yields the right frequencies, but with a total uncertainty of 500 MHz due to the uncertainty of the cavity length and the absolute mode number. A

more realistic uncertainty can be estimated by substituting the absolute cavity mode  $N_{1855}$  in equation (3.9) by the measured frequency  $\nu_{\Delta N,1855}$ . This yields

$$\begin{aligned}
 \nu_{\Delta N} := \nu(\Delta N) &= \frac{n_{\text{ML},2} N_{1855} c_0}{2n_{\lambda,2} l_{\text{opt,ML}}} + \frac{n_{\text{ML},2} \Delta N c_0}{2n_{\lambda,2} l_{\text{opt,ML}}} \\
 &= \nu_{\Delta N,1855} \frac{n_{1855,1}}{n_{\lambda,2}} \frac{n_{\text{ML},2}}{n_{\text{ML},1}} + \frac{n_{\text{ML},2} \Delta N c_0}{2n_{\lambda,2} l_{\text{opt,ML}}} \\
 &= \frac{n_{\text{ML},2}}{n_{\lambda,2}} \left( \nu_{\Delta N,1855} \frac{n_{1855,1}}{n_{\text{ML},1}} + \frac{\Delta N c_0}{2l_{\text{opt,ML}}} \right).
 \end{aligned} \tag{3.10}$$

The refractive indices  $n_{\text{ML},2}$  and  $n_{\lambda,2}$  use the same environmental conditions, especially the air pressure, while  $n_{\text{ML},1}$  and  $n_{1855,1}$  correspond to the actual air pressure when the frequency  $\nu_{\Delta N,1855}$  was determined. The uncertainty of this equation is dominated by the uncertainty of  $\Delta \nu_{\Delta N,1855} = 1$  MHz. An advantage of this formula is the weaker dependence on the cavity-length uncertainty. If the transfer resonator for example is stabilized to another mode, this error source only scales with about  $\Delta \nu \propto \Delta N \times \Delta l_{\text{opt,ML}} \approx 4 \times 10^2 \times \Delta l_{\text{opt,ML}}$  instead of  $N_{1855} \times \Delta l_{\text{opt,ML}} \approx 3 \times 10^5 \times \Delta l_{\text{opt,ML}}$  for equation (3.9). One issue of the evaluation remains: The refractive index  $n_{\lambda,2}$  depends on the frequency  $\nu$ . It must be solved iteratively or by using a rough assumption, e.g. with a wavemeter.

Equation (3.10) is used to determine the absolute frequencies of the resonator modes in the large scan of the tellurium spectroscopy over 3.4 THz (Fig. 3.4 b), Fig. 3.6, and Appendix A). As the exact frequency depends on the environmental conditions, the frequencies were calculated assuming a mean pressure of 1000 hPa, a cavity temperature of 19.8 °C, and a humidity of 40 %.

---

### 3.4 Absolute Frequency Determination with the Te<sub>2</sub>-Spectrum

---

The evaluation presented in the previous section allows for the calculation of the absolute frequency for every desired transition in the blue region around 440 nm. The method will be demonstrated for six Te<sub>2</sub> Lamb dips next to the expected Ar<sup>13+</sup>-transitions and one Lamb dip around 441.156 nm, which was used for many calibration measurements.

The experimental setup is the same as in the previous section: The transfer resonator is stabilized at the master-laser wavelength, which is locked to a tellurium Lamb dip around 452.756 nm. With the spectroscopy laser the stabilization to the correct cavity mode can be tested: The tellurium line 1855 should be at  $2\nu_{\text{AOM}} \approx 311$  MHz (table 3.1). Otherwise, the cavity is set to the wrong longitudinal mode and does not have the correct length. After this check, the spectroscopy laser can be stabilized to arbitrary cavity modes next to the desired tellurium Lamb dips. The relative cavity mode  $\Delta N$  can be obtained by comparing the spectrum with the tellurium atlas from the last section (Fig. 3.6 or Appendix A).

Lamb dip	$\Delta N$	Cavity mode jumps $\Delta N_{\text{jump}}$	$\nu_{\text{jump,SL}}$ in MHz	$2\nu_{\text{AOM}}$ in MHz
Ref. line 1855	0	0	-52.329(1)	311.03(9)
Ref. line 2082	1615	-2	-63.202(1)	282.69(11)
Ref. line 2083	1616	-13	-63.211(1)	291.94(8)
$\nu_{1,\text{Te}}$	325	-15	-54.519(1)	280.51(12)
$\nu_{2,\text{Te}}$	354	-9	-54.714(1)	307.39(9)
$\nu_{3,\text{Te}}$	385	-11	-54.923(1)	269.89(12)
$\nu_{4,\text{Te}}$	415	-19	-55.126(1)	302.16(17)
$\nu_{5,\text{Te}}$	449	4	-55.351(1)	293.46(13)
$\nu_{6,\text{Te}}$	478	-8	-55.548(1)	281.32(10)
441.156 nm	474	0	-55.520(1)	268.19(12)

**Table 3.1:** Important experimental parameters for different tellurium Lamb dips.

Lamb dip	$\Delta N$	Frequency in GHz	$\Delta\nu(\text{Ar}^{13+})$ in GHz
$\nu_{1,\text{Te}}$	325	679 247.1424(11)	-3.0
$\nu_{2,\text{Te}}$	354	679 308.0745(11)	1.6
$\nu_{3,\text{Te}}$	385	679 373.6021(12)	1.1
$\nu_{4,\text{Te}}$	415	679 437.4195(12)	2.8
$\nu_{5,\text{Te}}$	449	679 507.9295(12)	-2.6
$\nu_{6,\text{Te}}$	478	679 569.8136(12)	1.0
Calibration line	474	679 560.9106(12)	(441.156 nm)

**Table 3.2:** Absolute frequencies  $\nu_{i,\text{Te}}$  of the tellurium Lamb dips closest to the expected  $\text{Ar}^{13+}$ -transitions  $\nu_i$ . Positive difference values  $\Delta\nu(\text{Ar}^{13+})$  yield a higher expected  $\text{Ar}^{13+}$ -transition frequency relative to the tellurium Lamb dip frequency.

Next, the spectroscopy laser is stabilized to the transfer resonator in order to scan over the Lamb dip with the double-pass AOM and the cavity mode jump method. A fit of the resonance gives the exact relative frequency of the Lamb dip. The frequency difference of the cavity mode jump method can be calculated with equation (3.8) (table 3.1 for all parameters of the new reference lines). This allows for the calculation of the absolute frequency of the desired transition

$$\nu_{\text{new}} = \nu_{\Delta N} + \Delta N_{\text{jump}} \times \nu_{\text{jump,SL}} + 2 \times \nu_{\text{AOM}}, \quad (3.11)$$

with the frequency  $\nu_{\Delta N}$  of the relative cavity mode  $\Delta N$  from equation 3.10,  $\Delta N_{\text{jump}}$  times the frequency offset  $\nu_{\text{jump,SL}}$  due to the cavity mode jump method, and the AOM driver frequency  $\nu_{\text{AOM}}$  on the transition resonance.

Uncertainty contribution	Uncertainty in kHz
$\Delta \nu_{\Delta N=1855} = 1 \text{ MHz}$	1000
$\Delta l_{\text{opt,ML}} = 28 \text{ nm}$	402
Air pressure $\Delta p_2 = 1 \text{ hPa}$	288
Air pressure $\Delta p_1 = 1 \text{ hPa}$	271
Temperature $\Delta T_2 = 0.2 \text{ K}$	189
Temperature $\Delta T_1 = 0.2 \text{ K}$	178
Fit Lamb dip $\Delta \nu = 10 \text{ kHz}$	10
Cavity mode jump method $\Delta \nu_{\text{jump,SL}} = 1.2 \text{ kHz}$	$\Delta N_{\text{jump}} \times 1.2 \approx 10$
Humidity $\Delta \varphi_1 = 0.1$	2
Humidity $\Delta \varphi_2 = 0.1$	2
$\Delta \nu_{\text{ML}} = 100 \text{ MHz}^{*)}$	0.002
$\Delta \nu_{\text{tot}}$	1177

**Table 3.3:** Contributions to the total uncertainty of the Lamb dip  $\nu_{6,\text{Te}}$  frequency. The uncertainties for the other frequencies are similar. The values with index 1 corresponds to the measurements of the frequency  $\Delta \nu_{\Delta N=1855}$  next to the tellurium line 1855 and 2 corresponds to  $\nu_{6,\text{Te}}$ . \*) Uncertainty of the absolute frequency determination of the transition. It is not the uncertainty of the frequency stabilization of the master laser.

The evaluation was done with six tellurium Lamb dips next to the expected  $\text{Ar}^{13+}$ -transitions and a calibration line. The results are summarized in table 3.2. The uncertainty of around 1.2 MHz is dominated by the uncertainty of the reference line 1855 of 1 MHz. Further contributions are the air pressure, the cavity temperature, the humidity, the uncertainty of the absolute master-laser frequency  $\Delta \nu_{\text{ML}}$ , the frequency shift due to the cavity mode jump method, and the fit of the Lamb dip (table 3.3). The uncertainty  $\Delta \nu_{\text{ML}}$  corresponds to the absolute frequency determination of the Lamb dip used for the stabilization. It should not be confused with the uncertainty of the frequency stabilization which is in the order of the Lamb-dip width.

A cross check of the calculated frequencies has been done with a similar measurement using only the reference lines 1855 and 2082 to calculate  $\nu_{6,\text{Te}}$  and the Lamb dip at 441.156 nm. The comparison yields only small deviations within the uncertainties. An independent proof was done with a high resolution wavemeter WSU12-17 from HighFinesse. It has an absolute accuracy of 10 MHz and a relative of 1 MHz, but displays values down to 0.1 MHz. The presented frequencies of the calculated lines are all within the absolute accuracy of the wavemeter.

---

## 3.5 Long Term Characterization of the Laser System

---

The measurement of the long-term behaviour is an important aspect for the characterization of the entire laser system. The knowledge of frequency drifts determine the accuracy of the Ar<sup>13+</sup>-transition measurement. It also allows for a check of the interaction of the single components of the system. As described in the previous sections, the laser system consists of the master laser, the tellurium spectroscopy, the transfer cavity, and the spectroscopy laser. Each element and each stabilization circuit can be a source for frequency drifts, e.g. a shift of the laser beams or an offset in the PI controller set point. A major influence on the long-term frequency stability is the transfer cavity. The air pressure, temperature, and humidity lead to a frequency shift due to the dispersion of the air, which has been shown in a similar stabilization system by S. Albrecht [76]. Therefore, the next section discusses these influences in detail. Finally, a long term measurement is discussed.

---

### 3.5.1 Air Pressure Dependence of the Spectroscopy-Laser Frequency

---

The influences of the environmental conditions in the laboratory on the frequency stabilization of the laser system already have been discussed in the previous sections. In this section an approximation for the dominant value, the air pressure, will be derived.

The most sensitive element in the laser system is the transfer resonator. The refractive index is, as pointed out earlier, most sensitive to air pressure and temperature and shows a smaller dependence on humidity. Due to the temperature stabilization of the cavity to 19.8 °C, the air pressure is the dominant influence which must be considered. Humidity is orders of magnitude smaller in influence on the frequency stability for typical environmental changes (table 3.3). It is also significantly more constant due to the sealed cavity housing with only small holes for the pressure compensation. This suppresses air convection which has a larger influence for the humidity compensation than diffusion.

The derivation of the frequency shift due to the air pressure assumes the standard setup of the laser system: The transfer cavity is stabilized to the wavelength of the master laser and the master laser is frequency stabilized to a molecular tellurium resonance at 452.756 nm. Thus, the optical length of the cavity is kept constant  $l_{\text{opt,ML}} = n_{\text{ML}} \times l_{\text{geom}}$  with the piezoelectric ring actuator. The frequency  $\nu_N$  of a given longitudinal mode  $N$  of the cavity can be calculated with equation (3.6). At the wave-

length  $\lambda_{\text{ML}}$  of the master laser a pressure change  $\Delta p$  leads to both a refractive index change and a geometrical length change, as the optical length  $l_{\text{opt,ML}}$  is stabilized,

$$\begin{aligned}
l_{\text{geom}} &= \frac{N_{\text{ML}}c_0}{2n_{\text{ML}}} \times \frac{1}{v_{\text{ML}}} \\
\frac{\partial}{\partial p} l_{\text{geom}} &= \frac{N_{\text{ML}}c_0}{2} \times \frac{1}{v_{\text{ML}}} \left( \frac{\partial}{\partial p} \frac{1}{n_{\text{ML}}} \right) \\
\Delta l_{\text{geom}} &\approx \frac{N_{\text{ML}}c_0}{2} \times \frac{1}{v_{\text{ML}}} \left( -\frac{1}{n_{\text{ML}}^2} \right) \Delta n_{\text{ML}} \\
&\approx \frac{N_{\text{ML}}c_0}{2n_{\text{ML}}l_{\text{geom}}} \times \frac{1}{v_{\text{ML}}} \left( -\frac{l_{\text{geom}}}{n_{\text{ML}}} \right) \Delta n_{\text{ML}} \\
&\approx -\left( \frac{l_{\text{geom}}}{n_{\text{ML}}} \right) \Delta n_{\text{ML}},
\end{aligned} \tag{3.12}$$

with the absolute longitudinal mode  $N_{\text{ML}}$  of the cavity at the master laser wavelength. The refractive index difference can be calculated with

$$\begin{aligned}
\Delta n_{\text{ML}} &= \frac{\partial n}{\partial p} \times \Delta p \\
&= \frac{n-1}{p} \times \Delta p,
\end{aligned} \tag{3.13}$$

using the pressure dependent refractive index given in equation (3.3). For the wavelength  $\lambda = 452.756 \text{ nm}$ , the temperature  $19.8^\circ\text{C}$ , and the cavity length  $l_{\text{geom}} = 70.977 \text{ mm}$ , a pressure change of  $1 \text{ hPa}$  around  $1013.25 \text{ hPa}$  leads to a change of the refractive index of  $\Delta n_{\text{ML}} = -2.74 \times 10^{-7}$ , which leads to a length change of  $\Delta l_{\text{geom}} = 19 \text{ nm}$ .

The wavelength of the spectroscopy laser is stabilized to the transfer cavity. A pressure change results here in a frequency shift because of the refractive index and the cavity length change

$$\begin{aligned}
\nu_{\text{SL}} &= \frac{N_{\text{SL}}c_0}{2n_{\text{SL}}l_{\text{geom}}} \\
\frac{\partial}{\partial p} \nu_{\text{SL}} &= \frac{\partial}{\partial p} \left( \frac{N_{\text{SL}}c_0}{2n_{\text{SL}}l_{\text{geom}}} \right) \\
\Delta \nu_{\text{SL}} &\approx \frac{N_{\text{SL}}c_0}{2} \left[ -\frac{1}{n_{\text{SL}}l_{\text{geom}}^2} \frac{\partial l_{\text{geom}}}{\partial p} - \frac{1}{n_{\text{SL}}^2 l_{\text{geom}}} \frac{\partial n_{\text{SL}}}{\partial p} \right] \\
&\approx -\nu_{\text{SL}} \left[ \frac{\Delta l_{\text{geom}}}{l_{\text{geom}}} + \frac{\Delta n_{\text{SL}}}{n_{\text{SL}}} \right],
\end{aligned} \tag{3.14}$$

with the absolute longitudinal cavity mode  $N_{\text{SL}}$  at the spectroscopy laser wavelength. The length change of the cavity shifts the spectroscopy laser frequency by

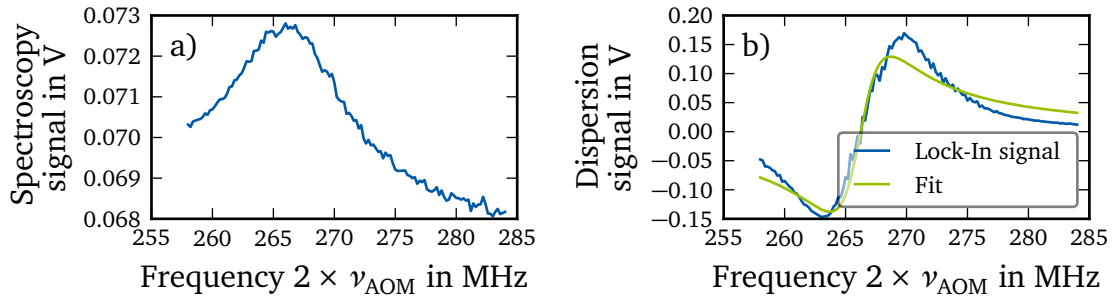


**Figure 3.7:** Scan of the spectroscopy laser over the reference line at 441.156 nm (Fig. 3.3 a) and 3.6 h)). a) Transmission signal of the tellurium Lamb dip. b) Lock-in signal of the Lamb dip and the corresponding fit function to determine the resonance frequency. The frequency is given in relative laser frequency since the double-pass AOM configuration shifts the laser twice.

−184.149 MHz/hPa and the refractive index change shifts it by +184.436 MHz/hPa. Because of the opposite sign, the total shift is only 287 kHz/hPa. Equation (3.14) for the frequency shift can be further simplified by inserting 3.13 and 3.12

$$\begin{aligned} \Delta \nu_{\text{SL}} &\approx -\nu_{\text{SL}} \left[ -\frac{\Delta n_{\text{ML}}}{n_{\text{ML}}} + \frac{\Delta n_{\text{SL}}}{n_{\text{SL}}} \right] \\ &\approx \nu_{\text{SL}} \left[ \frac{1}{n_{\text{SL}}} - \frac{1}{n_{\text{ML}}} \right] \frac{\Delta p}{p}. \end{aligned} \quad (3.15)$$

With this equation, the frequency shift of the spectroscopy laser due to the air pressure can be taken into account with good approximation.

### 3.5.2 Long Term Frequency Stability of the Laser System

A measurement over two days was performed to verify the long term stability of the stabilization chain. The master laser was frequency stabilized to a tellurium Lamb dip at 452.756 nm. The spectroscopy laser was stabilized to the transfer cavity, which was locked to the master laser. The spectroscopy laser scanned over a tellurium Lamb dip in a continuous loop with the double-pass AOM. The AOM frequency, the power of the probe beam in the spectroscopy, the lock-in signal, and the laboratory air pressure and humidity were recorded.

The transmission signal of the Lamb dip of each frequency scan has a Lorentzian shape and the lock-in signal is the derivative of this signal (Fig. 3.7). The centre frequency is determined by a fit to the lock-in signal. The fit function differs from the measured signal around the extrema. This is caused by the strong current modulation of the spectroscopy laser, which produces strong side bands. A smaller modulation strength would have led to a better matching with the fit function but also would have decreased the signal strength.

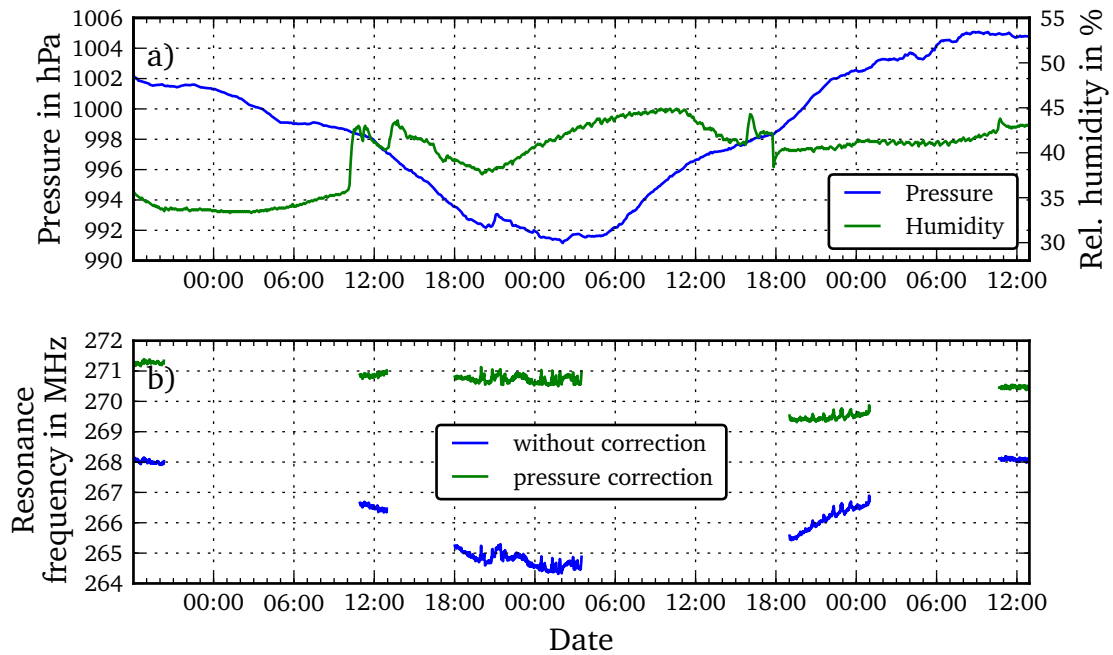


**Figure 3.8:** Long term stability of the complete frequency stabilization chain. a) Air pressure and humidity in the laboratory during the measurement. b) Measured resonance frequency of the reference line at 441.156 nm (Fig. 3.3 a) and 3.6 h)) over more than two days. In blue the unprocessed measured resonance frequency is shown. The green curve corrects drifts due to the change of air pressure. Without the correction a correlation between the frequency and the air pressure can be seen. Including the air pressure correction leads to a constant resonance frequency with an uncertainty of  $\nu_{\max} - \nu_{\min} = 2 \times 1.04 \text{ MHz}$ .

---

The air pressure during the long term measurement varied between 990 and 1006 hPa and the humidity between 30 and 55 % (Fig. 3.8 a)). The fit results of the centre frequency show a strong correlation with the air pressure (blue curve in Fig. 3.8 b)). The mean centre frequency is 266.0(13) MHz and the difference between the minimum and the maximum is  $\nu_{\max} - \nu_{\min} = 2 \times 2$  MHz (blue line). The measurement series was interrupted several times due to instabilities of the laser system or other measurements. Therefore, the complete measurement consists of five runs.

The air pressure correction using equation (3.15) leads to a smaller centre-frequency spread. Each of the five measurement runs is constant without large drifts during the run. The mean frequency is 270.46(62) MHz with a maximum difference of  $\nu_{\max} - \nu_{\min} = 2 \times 1.04$  MHz (green line). A varying offset between the runs can be still noticed, which is probably caused by the adjustment of the stabilization electronics. Since the detailed uncertainty statistics of the offset is unknown, only an upper boundary of the long-term stability can be estimated by half of the maximum occurred frequency difference of 1.04 MHz. If the offset between the runs is neglected, the weighted standard deviation yields 56 kHz. This can be seen as a lower limit and can only be reached by eliminating the source of the offset variation. Therefore, this value can be seen as a benchmark for further optimization of the laser system and the stabilization circuits.

The total accuracy of the laser system can be obtained now from the uncertainty of the absolute frequency determination of 1.2 MHz (Chap. 3.4) and the upper limit of the long-term stability of 1.04 MHz. For the safest assumption, both uncertainties are added to 2.2 MHz. This yields the upper limit of the total frequency uncertainty of the laser system.

---

### 3.6 Conclusion

---

The tellurium spectroscopy is a central element for the frequency stability of the spectroscopy laser. With the double-pass AOM and the cavity mode jump method, a continuous frequency locking scheme was demonstrated, which allows for a stabilization to arbitrary frequencies.

An absolute frequency determination of certain Lamb dips next to the expected  $\text{Ar}^{13+}$ -transitions was done. It was shown, that the achieved accuracy of 1.2 MHz is limited by the frequency accuracy of the reference lines of 1 MHz and not the system itself. The long-term stability with a deviation of 1.04 MHz is comparable to the uncertainty of the frequency determination and leads to an upper limit of the frequency uncertainty of 2.2 MHz, which can be achieved with the laser system.

The frequency stability of the laser system is more than sufficient for the spectroscopy of  $\text{Ar}^{13+}$ , as the uncertainties are noticeably smaller than the expected Doppler broadening of around 150 MHz at 4 K. However, if a higher stability is needed, some improvements could be done: The implementation of a 1f-3f- or 1f-5f-spectroscopy allows for a reduction of the frequency widths of the lock signals.

---

It also lowers the influence of the background signal. This technique modulates the laser frequency with a three or five times higher frequency to generate not the first but the third or fifth derivative with the lock-in amplifier. Another option would be a transfer resonator with a higher finesse. A further improvement would be the evacuation of the transfer cavity. The refractive index would be exactly one in this case, which means optical and geometrical length become the same and the uncertainty due to the environmental influences would vanish.

Independent from the improvement, a calibration measurement with an independent spectroscopy or a frequency comb would be useful to determine additional drifts. With the presented setup, it is not possible to measure systematic frequency shifts, e.g. pressure shifts due to temperature-variations of the tellurium cell.



---

## 4 Preparation and Detection of Laser Cooled Metastable Neon Atoms

The study of inelastic two-body collisions of cold metastable neon requires an experimental setup to prepare the metastable state, to capture the atoms, and to cool them to several hundreds of  $\mu\text{K}$  or below. This chapter gives a short overview of the preparation and the detection. A more presentation can be found in the theses of M. Zinner [85], P. Spoden [86], and J. Schütz [87]. Especially the descriptions in the latter one are still valid, as no major changes were done in this work.

The chapter starts with an overview of important properties of metastable neon and then presents the experimental setup.

---

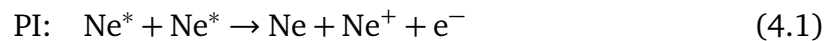
### 4.1 Properties of Metastable Neon

---

Neon (Ne) is the second rare gas in the periodic table and is one of the most common elements in the universe after hydrogen, helium, oxygen, carbon, and nitrogen [88]. The three stable isotopes  $^{20}\text{Ne}$ ,  $^{21}\text{Ne}$ , and  $^{22}\text{Ne}$  have a natural abundance in air in mole fraction of 90.48(3)%, 0.27(1)%, and 9.25(3)% [46]. While  $^{20}\text{Ne}$  and  $^{22}\text{Ne}$  are bosonic,  $^{21}\text{Ne}$  is a fermionic isotope with a nuclear spin of  $I = 3/2$ . Since neon is a rare gas, the ground electronic state is in LS-notation the state  $^1\text{S}_0$ .  $^3\text{P}_2$  is first excited state, wherefore a p-electron from the closed shell  $(2s)^2(2p)^6$  is excited into the  $(3s)$  state. Due to the spin-orbit interaction between the valence electron and the core electrons, the Racah-coupling is better suited to describe the atom states than the LS-coupling [86]. However, a transformation to LS-coupling is possible [87] and is used in the further discussion.

The metastable state  $^3\text{P}_2$  is a good choice for laser cooling and trapping in a magneto-optical trap, as it has a closed dipole-transition to  $^3\text{D}_3$  (Fig. 4.1) and a long lifetime of 14.73 s, which is sufficient for experimental studies. The state lies 16.6 eV above the ground state. This is more than half of the ionization energy of 21.6 eV.

The high internal energy of the metastable neon atom ( $\text{Ne}^*$ -atom) allows for ionizing collisions of two atoms. Two different processes, Penning-ionization (PI) and associative ionization (AI), may occur. In addition to a free electron, the collision products are a  $\text{Ne}^+$ -ion and a Ne-atom or a  $\text{Ne}_2^+$ -dimer:



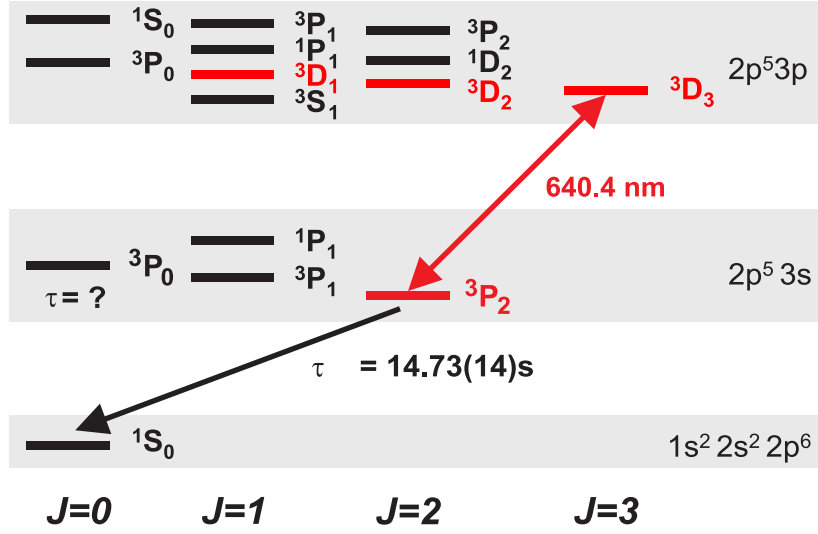


**Figure 4.1:** Partial energy level diagram of neon. The initial state used for experiments is  $^3P_2$ . The cooling transition to  $^3D_3$  has an excitation energy, which requires a red laser at 640.4 nm. The decay into the ground state creates a VUV photon.

In both reactions, two metastable atoms are lost and one ion is produced. The dominant loss process is the Penning-ionization [89, 90]. As it cannot be distinguished in the experiment between them, both processes will be summarised as Penning-ionization in the further discussion. With a micro-channel plate (MCP) (Sec. 4.3.2), the produced ions can be detected to determine the ionization rate.

In a cloud of  $\text{Ne}^*$ -atoms, the rate of PI can be described with the inelastic two-body loss coefficient  $\beta$ . It is defined by the decrease of the number of atoms  $N$  in the cloud with the time  $t$  by

$$\frac{d}{dt}N(t) = -\beta \int d^3r n^2(\vec{r}, t). \quad (4.3)$$

Here,  $n$  is the density of the  $\text{Ne}^*$ -cloud.

The PI and thus the  $\beta$  coefficient depends on the Zeeman sublevel of the colliding atoms. Especially a collision between atoms in the same stretched state  $m_J = +2$  or  $-2$  leads to a suppression. The reason is the conservation of the electron spin  $S$ , which is also known as Wigner's spin-conservation rule [91]. The total angular momentum  $\vec{J}$  is the sum of the orbital angular momentum  $\vec{L}$  and the spin  $\vec{S}$ ,  $\vec{J} = \vec{L} + \vec{S}$ . From this follows a total spin of  $S = 2$  for two  $\text{Ne}^*$ -atoms in  $m_J = +2$  ( $-2$  for  $m_J = -2$ ) before the collision. After the ionization, both the electron and the ion (single ion for PI or dimer for AI), have a spin of  $1/2$ , while the neutral neon atom has no spin in the case of PI. The total spin is therefore  $\leq 1$ . This violates the spin conservation and leads to a suppression of 38(16) for  $^{20}\text{Ne}$  and 7(5) for  $^{22}\text{Ne}$  [33]. In metastable helium, the suppression can be as large as four orders of magnitude [92, 93] compared to an unpolarized atom ensemble. The weaker

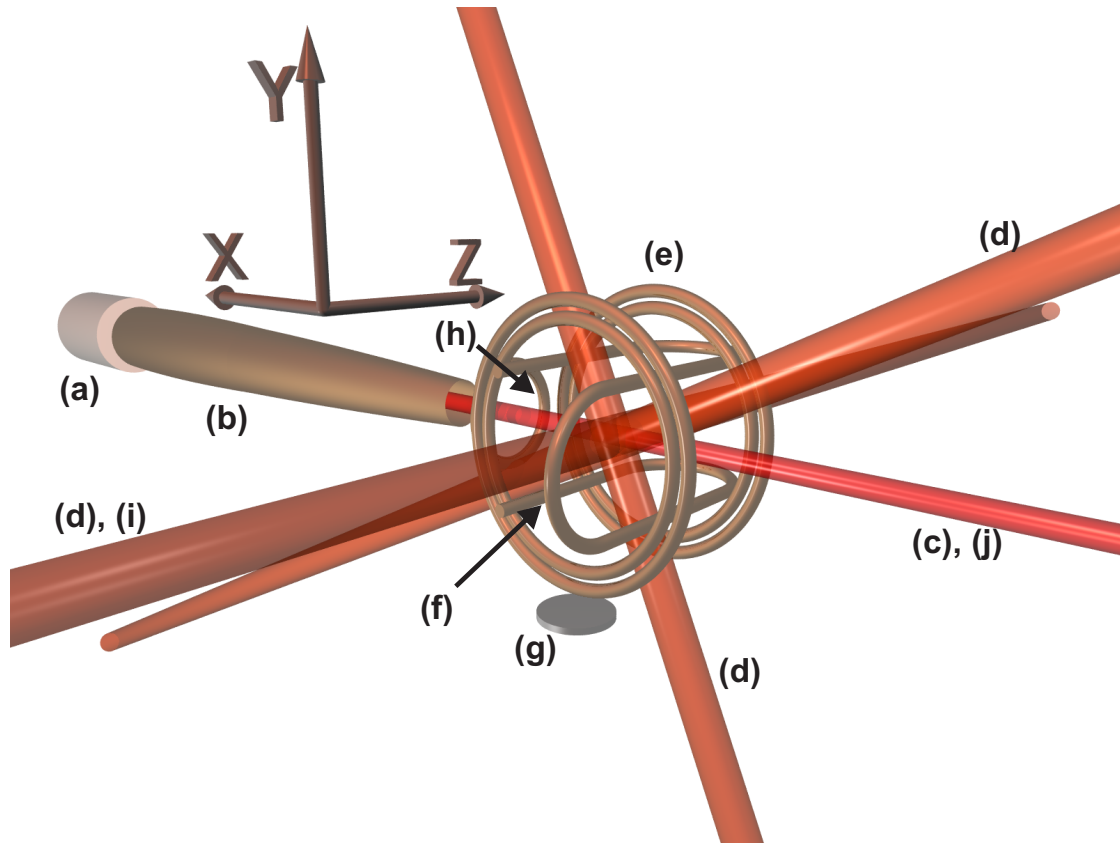


**Figure 4.2:** Experimental setup: (a)  $\text{Ne}^*$  source, (b) Zeeman slower, (c) Laser beam for Zeeman-slower, (d) MOT beams, (e) Inner: dipole coils, (e) Outer: Helmholtz coils, (f) Quadrupole bars, (g) Micro-channel plate, (h) RF antenna, (i) Laser beams for Doppler cooling and spin polarization, (j) Push-out laser beam.

suppression of neon is the result of a quadrupole-quadrupole interaction of the atoms as shown by Doery et al. [94]. For heavier rare gases such as argon, krypton, and xenon, the spin polarization has no influence on the ionization rate [95,96].

---

## 4.2 Measurement Setup

---

The neon experiment consists of a section for  $\text{Ne}^*$  creation and a experiment chamber where the preparation and the measurements are done. The separation is necessary due to the large pressure differences. The excitation of the neon atoms is done at about 1 mbar while the collision experiments requires pressures as low as possible to suppress atom losses due to collisions with the residual gas. A pressure of  $10^{-9}$  to below  $10^{-10}$  mbar can be reached in the experiment chamber.

---

### 4.2.1 Creation and Transport of Metastable Neon Atoms

---

The neon gas is stored in a pressure bottle. Through a pressure regulator and a copper tube, the gas is fed into the source chamber. Here, the atoms are excited to the metastable state with a gas discharge of an electron beam. The gas exits the chamber through a nozzle in an atom beam. The beam is collimated by a transversal optical molasses. A Zeeman slower leads the beam into the experiment chamber to the magneto-optical trap (MOT) and cools the beam in longitudinal direction (Fig. 4.2). The source chamber is divided into several parts, which allows for a differential pumping scheme with an oil diffusion pump for the high pumping speed and two turbomolecular pumps for lower gas pressures in front of the Zeeman slower. A mechanical shutter in front of the Zeeman slower blocks the geometrical view to the main chamber. It is only opened when the MOT is loaded.

---

### 4.2.2 Magneto-Optical and Magnetic Trap

---

The  $\text{Ne}^*$ -atoms from the beam are loaded into the magneto-optical trap (MOT) [11] in the main chamber (Fig. 4.2). The magnetic quadrupole field is generated by two dipole coils with opposing electric currents. One of the three orthogonal laser beam pairs of the MOT is aligned with the axial symmetry defined by the coils. The other two beam pairs are orthogonal to each other in radial direction. Each beam pair consists of two counter-propagating laser beams with properly chosen circular polarization for the MOT. Temperatures of typically 1 mK can be reached in the MOT with atom numbers of about  $6 \times 10^8$  for  $^{20}\text{Ne}$  or  $2 \times 10^8$  for  $^{22}\text{Ne}$ , respectively.

After the capture and cooling in the MOT, the  $\text{Ne}^*$  cloud is loaded into the magnetic trap. Since this trap forms only an attractive potential for atoms in the Zeeman-states  $m_j \geq 1$ , the cloud is pumped in the stretched state  $m_j = +2$  with a circular polarized beam in axial direction, while a magnetic offset field is applied by the dipole coils to define the quantisation axis. After the pumping, the ensemble is loaded into the magnetic trap. Further cooling is done with one-dimensional Doppler cooling in axial direction. The final temperature is typically 300  $\mu\text{K}$  with  $2 \times 10^8$   $^{20}\text{Ne}$ -atoms or  $8 \times 10^7$   $^{22}\text{Ne}$ -atoms, respectively.

The magnetic trap is realized in a Ioffe-Pritchard design which allows for a good optical access with laser beams. The design has four parallel bars in axial direction and symmetrically aligned in a square around the axis. The opposite current direction of adjacent bars leads to a linear quadrupole field for the radial confinement. Axial confinement is achieved by the dipole coils and the Helmholtz coils. The resulting magnetic field of the configuration can be derived in a multipole expansion [97] in cylindrical coordinates  $(\rho, \phi, z)$  which yields

$$\begin{aligned} B_\rho &= -B''z\rho/2 + B'\rho \cos(2\phi) \\ B_\phi &= -B'\rho \sin(2\phi) \\ B_z &= B_0 + B''(z^2 - \rho^2/2). \end{aligned} \tag{4.4}$$

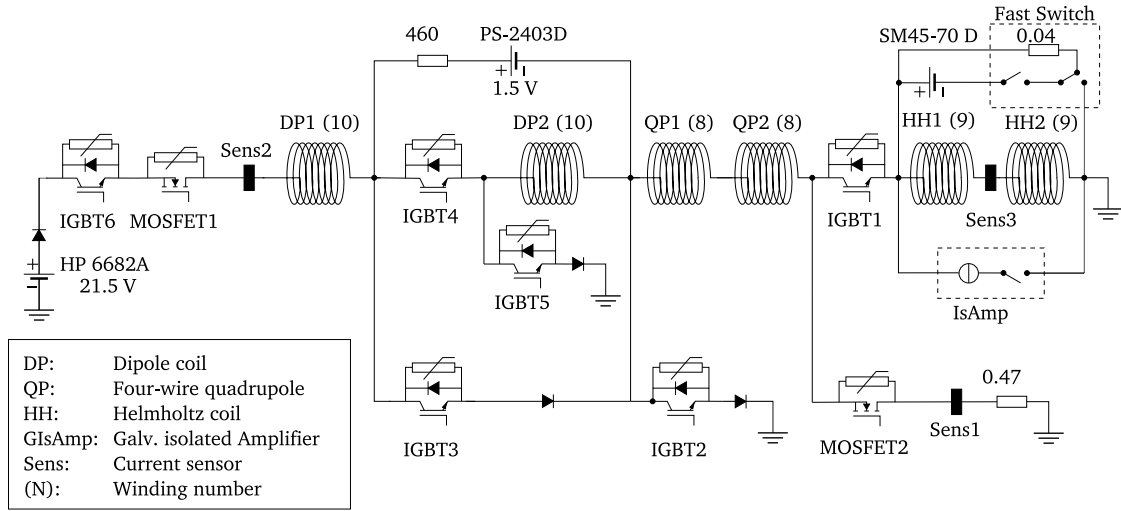


**Figure 4.3:** Circuit diagram of the trap coils in the vacuum chamber [98]. MOSFET1 controls the current from the power supply HP 6682A, while the current through the Helmholtz coils can be varied with MOSFET2. The different geometries of the magnetic field can be created with the IGBTs. The isolated amplifier (IsAmp) and the power supply SM45-70 D together with the fast switch allow for an adjustable current through the Helmholtz coils.

The offset field  $B_0$  is generated by the dipole and Helmholtz coils and can be tuned with the current ratio between them. The total field also depends on the radial gradient  $B'$  at  $z = 0$  and the radial curvature  $B''$ . The potential depth  $U$  can be obtained from the Zeeman-splitting  $U = m_J g_J \mu_B B$  with the Zeeman sublevel  $m_J$ , the Landé factor  $g_J$ , and the Bohr magneton  $\mu_B$ . The quadratic derivation of the distance to the trap centre leads to a potential of the form (Sec. 2.2.4 in [87])

$$U(\rho, z) = \frac{m}{2} \omega_{\text{rad}}^2 \rho^2 + \frac{m}{2} \omega_{\text{ax}}^2 z^2 \quad (4.5)$$

with the mass  $m$  of the atoms and the harmonic trap frequencies in radial and axial direction

$$\omega_{\text{rad}}^2 = \frac{m_J g_J \mu_B}{m} \left( \frac{B'^2}{B_0} - \frac{B''}{2} \right) \text{ and } \omega_{\text{ax}}^2 = \frac{m_J g_J \mu_B}{m} B'' \quad (4.6)$$

The harmonic approximation holds for  $\rho \lesssim B_0/B'$  in radial direction and  $z \lesssim (B'^2 - B_0 B''/2)/(B' B'')$  (Sec. 2.3.1 in [86]). Typical values in the experiment are  $B_0 = 26 \text{ G}$ ,  $B' = 212 \text{ G/cm}$ , and  $B'' = 306 \text{ G/cm}^2$  (Sec. 2.2.4 on page 15 in [87]). This yields a harmonic region with a radius around the trap centre of  $\approx 1 \text{ mm}$  in radial and  $\approx 6 \text{ mm}$  in axial direction. In radial direction, the potential gets linear for larger distances to the centre (Fig. 2.5 in [87]).

---

The currents for the trap coils can be switched with six insulated-gate bipolar transistors (IGBTs) and regulated with two metal–oxide–semiconductor field-effect transistors (MOSFETs) to change the magnetic field geometry (Fig. 4.3). For the current of up to 230 A the power supply HP 6682A by Hewlett Packard is used. The magnetic trap configuration is realized by closing IGBTs 1, 4, and 6 and MOSFET 1. With MOSFET 2 the current through the Helmholtz coils can be reduced to tune the offset field  $B_0$  and therefore the form of the magnetic trap. Further possible configurations are offset fields for the spin-polarization, strongly inhomogeneous fields for Stern-Gerlach experiments, and quadrupole fields for the MOT (table 5.2 in [85]).

All experiments in the next chapters are done with a free expanding cloud after release from the magnetic trap. Most of the experiments require a defined spin polarization. A small offset field of about 0.4 G after the switch-off is sufficient to maintain the polarization. This is realized with the Helmholtz coils and an isolating amplifier (IsAmp) [99]. The amplifier can be controlled from the experiment computer and allows for field strengths of up to 0.5 G parallel and anti-parallel to the offset field of the magnetic trap. Higher offset field strengths of up to 123 G can be applied with a 70 A current supply SM45-70 D from DELTA ELEKTRONIKA, which is attached in parallel to the IsAmp (Fig. 4.3).

An important detail for the release of the atoms from the trap must be considered: A simple switch-off of the magnetic trap by opening IGBT 6 and MOSFET 1 leads to a partial loss of spin polarization. Only around 80 % of the atoms remain in  $m_J = +2$  while the rest is distributed in  $m_J = +1$  and  $m_J = 0$  [87]. Therefore, a soft switch-off method with an intermediate step is used: Before the complete shut off, MOSFET 1 is closed except for a small current, IGBT 1 is closed completely, and IGBT 2 is opened for 300  $\mu$ s. This yields a remaining spin polarization of > 95 %.

An additionally issue are eddy currents in the walls of the vacuum chamber induced by the magnetic trap switch-off. They lead to exponential decaying magnetic fields over several milliseconds. They are highly reproducible and are treated with corresponding dynamic fields from external compensation coil-pairs. This allows for a stability of the offset field within 0.02 G during the observation time [100].

---

## 4.3 Detection

---

The study of the dynamics of  $\delta$ -kick cooling (Chap. 5) requires the measurement of spatial and velocity widths of the  $\text{Ne}^*$ -cloud, while the studies of the two-body collisions (Chap. 6 and 7) need the knowledge of the total atom number, the temperature, and the loss rate. All these properties can be measured with the optical and electrical detectors of this experiment.

---

### 4.3.1 Optical Detection

---

The optical detection uses the 12-bit CCD-camera Sensys 1400E by Photometrics to take images of the cloud. The camera is temperature stabilized and has a resolution

---

of  $1500 \times 1035$  pixels with a pixel size of  $6.8 \mu\text{m} \times 6.8 \mu\text{m}$ . The imaging lens is a MD Macro-Objective 100 mm by Minolta.

The camera is oriented towards the centre of the trap in radial direction. A collimated and linearly-polarized laser beam from the opposite direction shines through the atom cloud and produces a shadow image on the camera sensor. The laser beam is resonant to the cooling transition  $^3\text{P}_2 - ^3\text{D}_3$  so that the light is attenuated by the absorption of the atoms and with Beer-Lambert law, the atom density can be calculated in absolute numbers (Sec. 2.3.1 in [87]). Standard picture processing is used for this purpose: Besides the absorption image, an image without atoms, i.e. the white image, and an image without illumination, i.e. the dark image, is taken. The subtraction of the dark image from the absorption image eliminates the different dark currents of the CCD pixels and the division of the absorption image by the white image eliminates the vignetting of the lens and intensity fluctuations of the laser beam.

The Zeeman splitting due to the magnetic fields shifts the resonance. Therefore, the absorption images are recorded with the atoms released from the trap in absence of external fields. Because of this and the pumping between the states due to the laser light, the absorption images are a destructive measurement method.

The total atom number of the cloud can be obtained by numerically integrating the density over the complete image. Alternatively, the cloud shape can be fitted with a Gaussian function. The pixels of the image are projected to the axial and the radial axis of the trap. Since the camera takes pictures from the radial direction and the trap has a cylindrical symmetry, the radial and axial dimension are aligned with the vertical and horizontal axis of the image. Thus, the projection allows for one-dimensional fits in both trap dimensions. Since the atom distribution in a harmonic trap is Gaussian (Sec. 5.1.2) the resulting projection also has a Gaussian profile. The fits yield the spatial widths in both direction and also allow for the calculation of the atom number (Eq. (6.2)).

The velocity width and the temperature can be obtained from the expansion rate of the free expanding cloud after the release from the trap. For this purpose, the spatial widths of a series of time-of-flight images is measured. Fits of the equations (5.24) and (5.25) yield the temperatures and the initial widths.

The distribution of the Zeeman-sublevels population can also be measured with absorption images. If the free expanding atom cloud falls through a strongly inhomogeneous magnetic field which is produced by one of the dipole coils for 1.2 ms. Due to the Stern-Gerlach effect, the cloud splits in the axial direction (Fig. 2.8 in [87]).

An alternative method to measure the cloud properties is fluorescence imaging. Here, a laser resonantly excites the atoms and the camera detects the fluorescence light (Sec. 2.3.3 in [87]). This method requires a high intensity and frequency stability of the laser light and is therefore not used here.

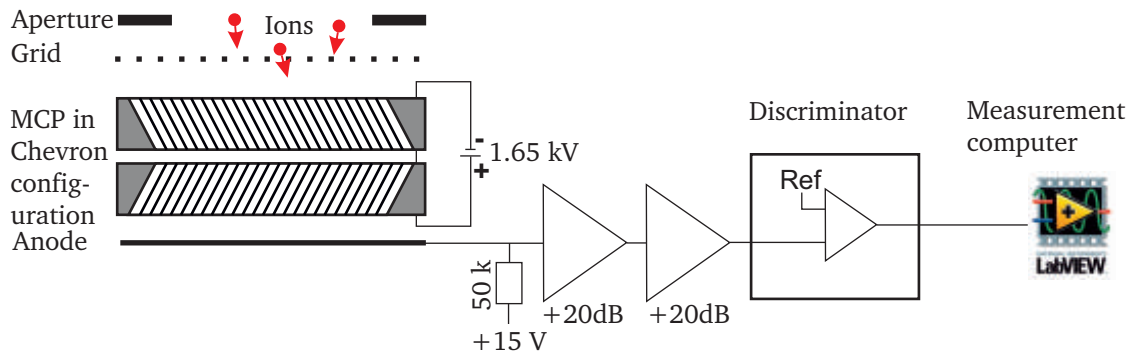


**Figure 4.4:** MCP detection system for single atom detection.

### 4.3.2 Single Atom Detection

For the electronic detection of the atoms, the experiment is equipped with a micro-channel plate (MCP) in Chevron configuration. The MCP is an electron multiplier which is sensitive to metastable neon atoms, vacuum ultra-violet (VUV) photons, and ions. It can be used in single particle counting mode and in integrating mode.

The MCP consists of a highly resistive plate with a grid of small tubes of several tens of micrometers in diameter, the micro-channels (Fig. 4.4). The channels are aligned in parallel with a small angle relative to the surface and form a continuous dynode by applying a high-voltage (HV) between the ends. The electric field from the HV accelerates electrons entering from the top towards the end of the tube. By collisions with the wall of the tube, secondary electrons are produced. Multiple collisions of all electrons lead to an electron avalanche. The primary electron is in general produced by the collision of a  $\text{Ne}^*$ -atom, ion, or VUV photon with the surface of the MCP. To increase the efficiency, a grid in front of the surface with an applied negative voltage of  $-2.2\text{ kV}$  accelerates the primary electrons towards the channel entrances.

The Chevron configuration used in the experiment consists of two MCPs in series, in such a way that the channels form a V-shape (Fig. 4.4). An electron bunch from the first MCP is multiplied in the second. After the second MCP, the bunch is accelerated with an electric field towards an anode to collect the charges. Due to saturation effects in the second MCP, the gain in Chevron configuration is Gaussian distributed, which allows for an effective particle detection. The total gain for the typical applied MCP HV of  $1.65\text{ kV}$  is  $2.5 \times 10^6$  (Fig. 4.5).

The charges can be detected with an electronic integrator and amplifier which allows for the measurement of slowly varying signals on the time scale of several ten milliseconds, like the atom cloud falling on the MCP. A more sensitive setup is shown in figure 4.4: The charges of the single bunches are converted over  $50\text{ k}\Omega$  resistor into a voltage. A voltage of  $15\text{ V}$  additionally applied at the resistor leads to an accelerating electric field for the electrons towards the anode, which increases the detection efficiency. The voltage signal of the electron bunch is amplified by  $40\text{ dB}$  with two amplifiers ZX60-3018G-S+ by Mini-Circuits. An electronic discriminator

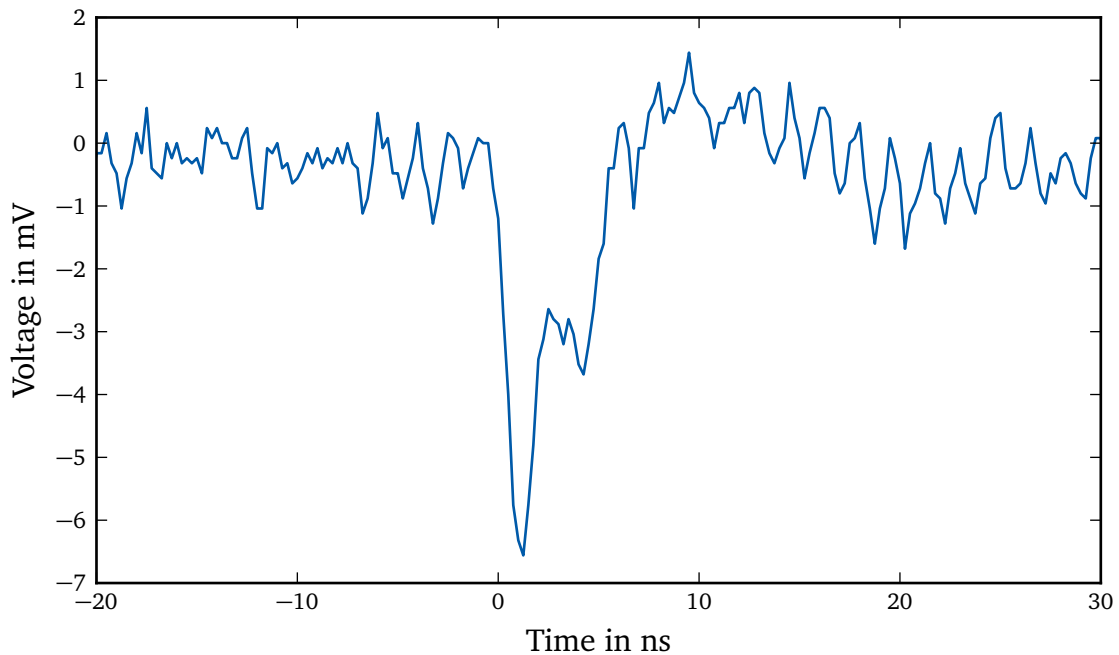


**Figure 4.5:** Signal of a single electron bunch from the MCP in Chevron configuration. The integrated pulse area corresponds to  $2.5 \times 10^6$  electrons. The double-peak structure is the result of reflections in the cable due to a mismatch of the impedance.

detects the amplified signal and converts it to a TTL-logic signal with a duration of 160 ns. The logic signals are recorded time-resolved on a fast counting board in the measurement computer.

The efficient detection of the  $\text{Ne}^*$  atoms is given by positioning of the MCP below the trap. Due to the gravitation the atoms fall onto the surface. The free view between the trap centre and the MCP allows for the additional detection of VUV photons. However, the ions require an electric field for an efficient transport to the MCP. Therefore, a HV between  $\pm 2.1$  kV can be applied to an aperture in front of the MCP to attract or repel  $\text{Ne}^+$  ions and  $2\text{Ne}^+$  molecules. As shown in [101], a successful ion detection is extremely sensitive to the electric potentials of the trap coils. They shield the electric field of the MCP aperture at the trap centre and field fluctuations lead to different ion trajectories. Therefore, small voltages of several volts are applied to the dipole coils and the Ioffe bars (Sec. 2.3.4 in [87]) to increase the transport efficiency to about 4%.



---

## 5 Dynamics of a Cold Atom Cloud

To determine the cross section and the two-body loss coefficient of  $\text{Ne}^*$  collisions, the relative kinetic energy of the colliding atoms and the density of the cloud are important. The calculation of these cloud parameters and their temporal dynamics will be discussed in this chapter. The results will be used to determine in chapter 6 the magnetic field dependence and in chapter 7 the temperature dependence of the collisions.

A focus of this chapter lies on  $\delta$ -kick cooling (DKC). Introduced by Ammann and Christensen [102] in 1997, it is a method for reducing the width of the momentum distribution of atoms. They proposed to apply a short pulsed attractive potential, the  $\delta$ -kick, with an optical trap to a freely expanding cloud of Cs or Na atoms. This squeezes the momentum distribution and results in temperatures below the recoil limit. However, DKC manipulates only the phase-space distribution of an atomic ensemble, but conserves its volume. Thus, it is not a true cooling mechanism. Since DKC is the conventional term in literature, the further discussion will use it too. One-dimensional DKC was first demonstrated in 1999 by Maréchal et al. [103] with a Cs cloud and in 2000 by Myrskog et al. [104] using Rb atoms. Both used a pulsed magnetic field for cooling. The first experiment in a Ioffe-Pritchard trap was done by Aoki et al. [105] with sodium. The technique is used in many experiments, e. g. in Bose-Einstein condensation [106] or in atom interferometry [107]. DKC was even been shown in an electrostatic ion-beam trap [108] and in molecular beams [109] has been shown. Currently, temperatures as low as 50 pK were achieved by Kovachy et al. [110] with  $^{87}\text{Rb}$ .

---

### 5.1 Density Distribution in a Harmonic Potential

---

Thermal atoms in a trap have a characteristic velocity and position distribution. This allows for the calculation of the dynamical behaviour in a trap and of the free expansion after release from the trap. In order to describe the expansion and the relative velocity of two-body collisions between atoms of the released cloud, the velocity distribution and the position distribution will be discussed first in general. With these results the dynamics of the cloud can be calculated.

---

### 5.1.1 Velocity Distribution

---

An ensemble of classical atoms in thermal equilibrium of temperature  $T$  can be described by a Maxwell-Boltzmann velocity distribution

$$\rho_{\vec{v}}(\vec{v}) = \left( \frac{m}{2\pi k_B T} \right)^{3/2} e^{-\frac{1}{2} \frac{m\vec{v}^2}{k_B T}}. \quad (5.1)$$

Here  $T$  is the temperature,  $k_B = 1.38 \times 10^{-23}$  J/K the Boltzmann constant,  $m$  the mass of the particles, and  $\vec{v}^2 = v_x^2 + v_y^2 + v_z^2$  the square velocity in the three spatial dimensions  $x, y, z$ . For simplicity, only the one-dimensional case in the  $x$ -direction with velocity  $v \equiv v_x$  will be considered in the following discussion, which is given by

$$\rho_v(v) = \frac{1}{\sqrt{2\pi k_B T/m}} e^{-\frac{1}{2} \frac{mv^2}{k_B T}}. \quad (5.2)$$

The three-dimensional distribution can be constructed from the one-dimensional case by means of

$$\rho_{\vec{v}}(\vec{v}) = \rho_v(v_x) \rho_v(v_y) \rho_v(v_z). \quad (5.3)$$

The distribution  $\rho_v(v)$  is larger for a higher temperature or a smaller mass. This can be seen directly from the width of the Gaussian distribution of equation (5.1)

$$\sigma_{\vec{v}} = (k_B T/m)^{3/2} \text{ (in 3D) or} \quad (5.4)$$

$$\sigma_{v_x} \equiv \sigma_v = \sqrt{\frac{k_B T}{m}} \text{ (in 1D)}. \quad (5.5)$$

The same result can be obtained by looking at the mean square velocity

$$\langle v_x^2 \rangle = \int v_x^2 \rho_v(v_x) dv_x = \frac{k_B T}{m} = \sigma_{v_x}^2. \quad (5.6)$$

With this result, the mean kinetic energy in one dimension can be calculated with

$$\bar{E}_{\text{kin}} = \frac{m}{2} \langle v_x^2 \rangle = \frac{1}{2} k_B T. \quad (5.7)$$

The result connects the velocity distribution with the temperature. In the further discussion and the next chapters the temperature will be given sometimes for a density distribution, which is not in thermal equilibrium. In these cases, the mean square velocity is given in units of the temperature.

Since  $\rho_{\vec{v}}(\vec{v})$  is a density distribution it is normalized through condition

$$\int \rho_{\vec{v}}(\vec{v}) dv_x dv_y dv_z = 1. \quad (5.8)$$

This relation is true for all classical density distributions. If quantum mechanical effects must be considered, the density distribution can be generalized to a quasi density distribution, the quantum mechanical Wigner distribution. It allows for negative quasi probabilities, which describes interference effects. In the special case of a harmonic potential, the interference terms in the equation of motion disappear, and the classical equation remains valid [111]. As only harmonic potentials are considered here, the quantum mechanical approach leads to the same results.

---

### 5.1.2 Position Distribution

---

After the discussion of the velocity distribution, the position distribution will be discussed in this section. The exponent of the Maxwell-Boltzmann distribution of the velocity consists of the ratio between kinetic energy and thermal energy,  $E_{\text{kin}}/(k_{\text{B}}T)$ . A similar assumption can be done for the position distribution with a given potential  $E_{\text{pot}} = V(\vec{r})$

$$\rho_{\vec{r}}(\vec{r}) \propto e^{-\frac{V(\vec{r})}{k_{\text{B}}T}}. \quad (5.9)$$

In general, the potential consists of an externally applied potential  $V_{\text{ext}}(\vec{r})$ , like gravitation or the trapping potential, and an interaction potential  $V_{\text{int}}(|\vec{r}_i - \vec{r}_j|)$ , which describes collisions between the atoms at the locations  $\vec{r}_i$  and  $\vec{r}_j$ . The total potential is then given by

$$V(\vec{r}) = \sum_{i=1}^N V_{\text{ext}}(\vec{r}_i) + \sum_{i=1}^N \sum_{j>i}^N V_{\text{int}}(|\vec{r}_i - \vec{r}_j|). \quad (5.10)$$

For a weakly interacting atom cloud, which is the case for the neon experiment, the interaction term can be neglected. This assumption allows for calculations of analytic expressions for the cloud dynamics.

The magnetic trap in this experiment can be approximated by a harmonic potential to a good degree. Again, considering only the one-dimensional case, it is given by

$$V(x) = \frac{m}{2} \omega_x^2 x^2, \quad (5.11)$$

with the angular frequency  $\omega_x$  of the harmonic oscillator. Inserting the harmonic potential into equation (5.9) gives the local probability distribution

$$\rho_x(x) = \frac{1}{\sqrt{2\pi k_{\text{B}}T/(m\omega^2)}} e^{-\frac{1}{2} \frac{m\omega_x^2 x^2}{k_{\text{B}}T}}. \quad (5.12)$$

This is, like in the case of the velocity, again a Maxwell-Boltzmann distribution. The integral is normalized to unity and the mean potential energy  $\bar{E}_{\text{pot}}$  can be calculated in the same way as equation (5.7) to

$$\bar{E}_{\text{pot}} = \frac{m\omega^2}{2} \langle x^2 \rangle = \frac{1}{2} k_{\text{B}}T. \quad (5.13)$$

Therefore, comparing to the mean kinetic energy  $\bar{E}_{\text{kin}}$  in equation (5.7), the total thermal energy  $E_{\text{tot}} = \bar{E}_{\text{kin}} + \bar{E}_{\text{pot}} = k_{\text{B}}T$  is equally distributed between the kinetic and the potential energy. The width of the distribution given in equation (5.12) is

$$\sigma_x = \sqrt{\langle x^2 \rangle} = \sqrt{\frac{k_{\text{B}}T}{m\omega_x^2}}. \quad (5.14)$$

This result looks similar to the velocity spread  $\sigma_v$  in equation (5.5) and is an important intermediate result: Considering a harmonic potential, the position and the velocity distribution in thermal equilibrium are connected via the potential frequency  $\omega_x$  as

$$\sigma_v = \omega_x \sigma_x. \quad (5.15)$$

For further considerations, the phase space density is an important tool. It is defined by the combination of the position and the velocity distribution to

$$\rho(x, v) = \rho_x(x) \rho_v(v). \quad (5.16)$$

Here no correlation is assumed between both densities. This is true for the cloud in thermal equilibrium. The phase space density can be rewritten using the Hamiltonian  $H = p_x^2/(2m) + V(x)$  and the momentum  $p_x = mv_x \equiv mv$ , resulting in:

$$\rho(x, v) \propto e^{-\frac{p_x^2/(2m)+V(x)}{k_{\text{B}}T}} = e^{-\frac{H(x,p_x)}{k_{\text{B}}T}}. \quad (5.17)$$

For the harmonic potential, this distribution is given by

$$\rho(x, v) = \frac{1}{2\pi k_{\text{B}}T / (m\omega_x)} e^{-\frac{m}{2} \frac{\omega_x^2 x^2 + v^2}{k_{\text{B}}T}}. \quad (5.18)$$

The phase space density contains all the necessary information to describe the system including both, the preparation and the time evolution. Therefore, it is the basis for all further discussions.

---

## 5.2 Free Expansion of an Atom Cloud and Reduction of Collision Energy

---

The phase space density  $\rho(x, v)$  given by equation (5.18) will be used in this section to describe the free expansion of a cloud released from the harmonic trap potential. This allows for the determination of the initial temperature and spatial width. Additionally due to the expansion, the relative collision energy is reduced. The technique is quite simple: An atom cloud is released from the trap. Due to the initial velocity, the cloud starts to expand and the volume increases. In the phase space, the initial thermal atom cloud (Fig. 5.1 a)) has a two-dimensional Gaussian shape. The free expansion shears the distribution in the spatial dimension (Fig. 5.1 b)), while the total

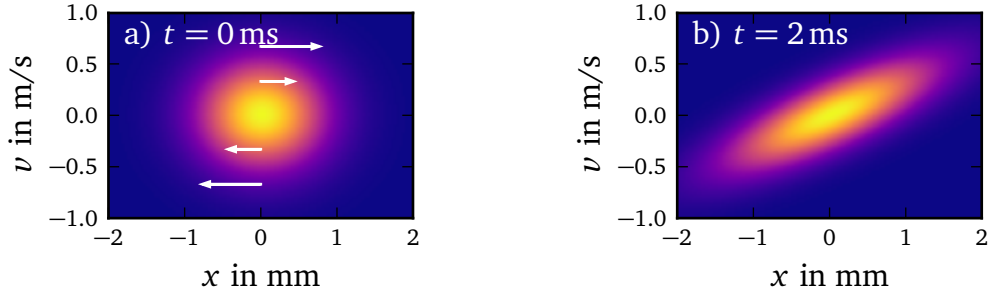


**Figure 5.1:** Phase space density plots of a  $\text{Ne}^*$  atom cloud with typical spatial and velocity widths. a) Immediately after release from the trap and b) after a free expansion time of  $t = 2$  ms. The density distribution shears with the expansion time, which is indicated by the arrows. The spatial width increases, while the velocity distribution over the whole cloud stays constant. However, the velocity distribution for a specific spatial region (e. g. vertical cut at  $x = 0$ ) decreases with time.

width in the velocity dimension remains constant. Collisions between the atoms are neglected in this discussion.

The detailed derivation starts with the initial position and velocity probability distribution in a harmonic trap potential (Fig. 5.1 a)), using equations (5.2) and (5.12) discussed earlier. At the start time  $t = 0$  the densities are given by

$$\rho_x(x) = \frac{1}{\sqrt{2\pi}\sigma_{x,0}} e^{-\frac{1}{2}\frac{x^2}{\sigma_{x,0}^2}}, \text{ and } \rho_v(v) = \frac{1}{\sqrt{2\pi}\sigma_{v,0}} e^{-\frac{1}{2}\frac{v^2}{\sigma_{v,0}^2}}, \quad (5.19)$$

with the initial widths  $\sigma_{x,0} = \sigma_x(t=0) = \sqrt{\frac{k_B T_0}{m\omega_x^2}}$  and  $\sigma_{v,0} = \sigma_v(t=0) = \sqrt{\frac{k_B T_0}{m}}$ , the initial temperature  $T_0 = T(t=0)$ , and the trap frequency  $\omega_x$ . After a free expansion of time  $t$ , an exemplary atom moves from  $x_0 = x(t=0)$  to  $x = x_0 + v_0 t$ , while the velocity remains constant  $v = v_0 = v(t=0)$ . This yields the shear in the spatial dimension of the phase space (Fig. 5.1 b)). For the atom cloud this leads to the density distribution

$$\begin{aligned} \rho(x, v, t) &= \iint \rho_x(x_0) \rho_v(v_0) \delta(x_0 + v_0 t - x) \delta(v_0 - v) dx_0 dv_0 \\ &= \frac{1}{\sqrt{2\pi}\sigma_{x,0}} e^{-\frac{1}{2}\frac{(x-vt)^2}{\sigma_{x,0}^2}} \times \frac{1}{\sqrt{2\pi}\sigma_{v,0}} e^{-\frac{1}{2}\frac{v^2}{\sigma_{v,0}^2}} \\ &= \rho_x(x - vt) \times \rho_v(v). \end{aligned} \quad (5.20)$$

The integrations over the delta-distributions lead to a simple substitution for  $x$  and  $v$ . They are only shown here to demonstrate the principal proceeding, as it occurs also in the discussion of the other preparation methods.

The integration over all velocities results in the time depending position distribution

$$\begin{aligned}\rho_x(x, t) &= \int \rho(x, v, t) dv \\ &= \frac{1}{\sqrt{2\pi}\sqrt{\sigma_{x,0}^2 + \sigma_{v,0}^2 t^2}} e^{-\frac{1}{2} \frac{x^2}{\sigma_{x,0}^2 + \sigma_{v,0}^2 t^2}}.\end{aligned}\quad (5.21)$$

The width of the cloud after the expansion time  $t$  is then

$$\sigma_x^2(t) = \langle x^2(t) \rangle = \int x^2 \rho_x(x, t) dx \quad (5.22)$$

$$= \sigma_{x,0}^2 + \sigma_{v,0}^2 t^2 \quad (5.23)$$

$$= \sigma_{x,0}^2 + \frac{k_B T_0}{m} t^2 \quad (5.24)$$

$$= \frac{k_B T_0}{m} \left( \frac{1}{\omega_x^2} + t^2 \right). \quad (5.25)$$

As can be seen, the expansion depends only on the initial temperature  $T_0$ , the trap frequency  $\omega_x$ , and the time  $t$ . The last two equations are used in chapter 6 and 7 to determine the initial temperature of the cloud. These parameters can be extracted using a series of absorption images with varying time of flight as discussed later.

Neglecting gravity, no other external forces are acting on the atom cloud during the free expansion, the velocity distribution is time independent. This can also be shown using the density distribution of the velocity

$$\begin{aligned}\rho_v(v, t) &= \int \rho(x, v, t) dx \\ &= \frac{1}{\sqrt{2\pi}\sigma_{v,0}} e^{-\frac{1}{2} \frac{v^2}{\sigma_{v,0}^2}} \\ &= \rho_v(v, 0) = \rho_v(v_0).\end{aligned}\quad (5.26)$$

Since the velocity distribution is constant, the velocity spread is a constant as well

$$\begin{aligned}\sigma_v^2(t) = \langle v^2(t) \rangle &= \iint v^2 \rho(x, v, t) dx dv \\ &= \int v^2 \rho_v(v, t) dv \\ &= \sigma_{v,0}^2.\end{aligned}\quad (5.27)$$

The gravitational force can be neglected in this derivation, because it only leads to an acceleration of the centre of mass motion and doesn't affect the other cloud properties.

---

## 5.2.1 Local Velocity Distribution

---

Two-body collision properties in general are temperature dependent. Therefore, the kinetic energy of the collisions is important, which can be determined from the relative velocity of the collision partners. Here, the relative velocity is a local property of the atom cloud and should not be confused with the global velocity distribution. As discussed in the previous section, the global velocity distribution of the cloud remains constant during free expansion, but the local velocity distribution is time-dependent. This can be easily understood: The initial position and velocity distributions in the trap are uncorrelated and have a Gaussian shape. This is illustrated in figure 5.1 a). The cloud is then released from the trap at time  $t = t_0 = 0$  and starts to expand. After a time of free expansion  $t > t_0$  only atoms with similar velocity remain next to each other. This is shown in the phase space density plot in figure 5.1 b). The width of the velocity at a certain point (e.g. at  $x_0 = 0$ ), which corresponds to a vertical cross section through the phase-space plot, is narrower after the free expansion than in the beginning. This means, the correlation between position and velocity increases with time and the relative velocity differences, an important parameter for the inter-atomic collisions, decreases. Thus, the velocities of adjacent atoms equalise with time. This can be described by introducing an effective temperature  $T_{\text{eff}}$  and the effective velocity spread  $v_{\text{eff}}$ .

Assuming the local velocity at the centre of the trap, which corresponds to a vertical cut in the phase space at  $x_0 = 0$  (Fig. 5.1), the velocity width can be calculated with the help of the Dirac delta function  $\delta(x - x_0)$

$$\sigma_{v_{\text{eff}}}^2 := \langle v_{\text{eff}}^2 \rangle = \frac{\iint dx dv v^2 \rho(x, v, t) \delta(x - x_0)}{\iint dx dv \rho(x, v, t) \delta(x - x_0)} \quad (5.28)$$

$$= \frac{\sigma_{v,0}^2}{1 + \frac{\sigma_{v,0}^2}{\sigma_{x,0}^2} t^2}, \text{ or}$$

$$\sigma_{v_{\text{eff}}} = \frac{\sigma_{v,0}}{\sqrt{1 + \frac{\sigma_{v,0}^2}{\sigma_{x,0}^2} t^2}}, \quad (5.29)$$

with the initial widths  $\sigma_{x,0}$  and  $\sigma_{v,0}$ .

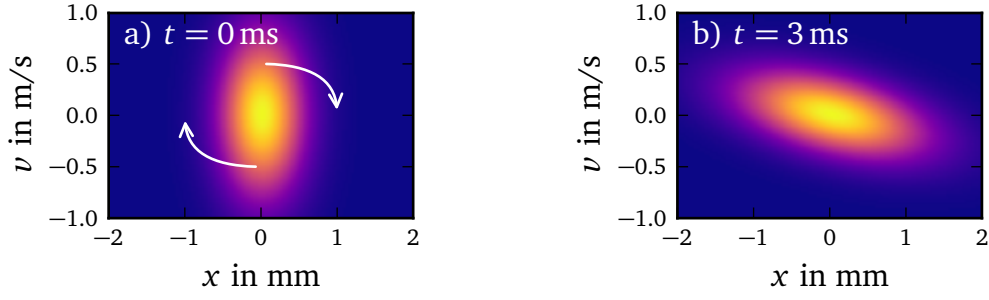


**Figure 5.2:** Phase space plots of a squeezed  $\text{Ne}^*$  atom cloud. a) The spatial width of the cloud is squeezed, which yields an elongated velocity width at  $t = 0$ . b) Cloud after evolution time  $t = 3$  ms in the trap. The distribution rotates clockwise in the phase space (indicated by the arrows) due to the harmonic potential.

The temperature of the cloud is proportional to the squared velocity:  $T \propto E_{\text{kin}} \propto v^2$  (Eq. (5.5)). Therefore, an effective time-dependent temperature for the collisions can be obtained from equation (5.29) with

$$T_{\text{eff, 1D}}(t) = \frac{T_0}{1 + \frac{\sigma_{v,0}^2}{\sigma_{x,0}^2} t^2} \quad (5.30)$$

$$= \frac{T_0}{1 + \frac{k_B T_0}{m \sigma_{x,0}^2} t^2}. \quad (5.31)$$

In the last step, the dependence between the initial velocity spread  $\sigma_{v,0}$  and the temperature  $T_0$  of the cloud in the trap given in equation (5.5) is used. The result shows, the effective temperature  $T_{\text{eff}}$  only depends on the expansion time  $t$  and the initial conditions, which can be measured using absorption images.

The real atom cloud in this experiment has different initial velocity and local widths for the axial and the radial dimensions. This can be considered by averaging over the dimensions in axial and radial direction

$$T_{\text{eff}}(t) = (2 \times T_{\text{eff, rad}}(t) + T_{\text{eff, ax}}(t)) / 3. \quad (5.32)$$

This equation together with (5.31) allows for the evaluation of the temperature dependence of ionizing collisions, which will be used in chapter 7 for further evaluation.

---

### 5.3 Dynamics of an Atom Cloud in a Harmonic Potential

---

The same approach as for the calculation of the dynamics of the free expanding cloud will be used now to determine the dynamics in a harmonic trap. The dynamics of

a single particle at position  $x$  and with velocity  $v$  in a harmonic potential can be described by the Hamiltonian

$$H = \frac{mv^2}{2} + V(x) \quad (5.33)$$

$$= \frac{mv^2}{2} + \frac{m\omega_x^2 x^2}{2}. \quad (5.34)$$

Here, the frequency  $\omega_x$  describes the strength of the harmonic potential. Inserting this into the canonical equations leads to the differential equation

$$\ddot{x} + \omega_x^2 x = 0. \quad (5.35)$$

The general solution of this equation for a particle with the mass  $m$ , which starts at  $x_0$  at the time  $t_0$  with velocity  $v_0 = p_0/m$  and momentum  $p_0$  is

$$x_0 = x \cos(\omega_x t) - \frac{v}{\omega_x} \sin(\omega_x t) \quad (5.36)$$

$$v_0 = v \cos(\omega_x t) + \omega_x x \sin(\omega_x t). \quad (5.37)$$

After time  $t$  the particle is at position  $x$  with the velocity  $v$ . The solution describes an elliptical path in phase space. As the equations are already solved for the initial conditions  $x_0$  and  $v_0$  they can be inserted into the previously discussed phase space density  $\rho(x, v)$  of equation (5.16)

$$\begin{aligned} \rho_{\text{harm}}(x, v, t) &= \iint \rho_x(\tilde{x}) \rho_v(\tilde{v}) \delta(\tilde{x} - x_0) \delta(\tilde{v} - v_0) d\tilde{x} d\tilde{v} \\ &= \rho\left(x \cos(\omega_x t) - \frac{v}{\omega_x} \sin(\omega_x t), v \cos(\omega_x t) + \omega_x x \sin(\omega_x t)\right). \end{aligned} \quad (5.38)$$

This solution also follows elliptical paths in phase space. The dynamics for a squeezed cloud is shown in figure 5.2 a) and b) at  $t_0 = 0$  and after evolution time  $t$ . All particles rotate clockwise in phase space and so does the density distribution. A cloud in thermal equilibrium does not show any dynamics of the density distribution  $\rho(x, v)$  in phase space. For a squeezed cloud, the relation between spatial width  $\sigma_x$  and velocity width  $\sigma_v$  given in equation (5.15) does not apply as  $\sigma_v \neq \omega_x \sigma_x$ . A complete rotation takes the time  $t = 1/\omega_x$ . Furthermore, the distribution after one half time is indistinguishable from a full cycle. After only a quarter cycle the aspect ratio of the squeezed cloud is inverted.

To illustrate this behaviour the time evolution of the widths in position and velocity can be calculated

$$\begin{aligned}\sigma_x^2(t) &= \langle x^2(t) \rangle = \iint x^2 \rho_{\text{harm}}(x, v, t) dx dv \\ &= \sigma_{x,0}^2 \cos^2(\omega_x t) + \frac{\sigma_{v,0}^2}{\omega_x^2} \sin^2(\omega_x t),\end{aligned}\tag{5.39}$$

$$\begin{aligned}\sigma_v^2(t) &= \langle v^2(t) \rangle = \iint v^2 \rho_{\text{harm}}(x, v, t) dx dv \\ &= \sigma_{v,0}^2 \cos^2(\omega_x t) + \omega_x^2 \sigma_{x,0}^2 \sin^2(\omega_x t).\end{aligned}\tag{5.40}$$

The dynamics only depend on the initial conditions of the widths  $\sigma_{x,0}$  and  $\sigma_{v,0}$ . For a cloud in thermal equilibrium both of these widths are connected through equation (5.15). Substituting into equations (5.39) and (5.40) eliminates the oscillatory terms and the equations get time-independent,  $\sigma_x^2(t) = \sigma_{x,0}^2$  and  $\sigma_v^2(t) = \sigma_{v,0}^2$ .

---

## 5.4 General Dynamics of an Atom Cloud after $\delta$ -Kick Cooling

---

$\delta$ -kick cooling is a combination of free expansion and oscillation in a trap. Therefore, the results of the previous sections will be used for the discussion.

The  $\delta$ -kick cooling method consists of several preparation steps:

1. An atom cloud is released from the trap.
2. After an expansion time  $t_{\text{pre}}$ , the trap potential is switched on again for a short time  $t_{\text{DKC}}$ .
3. The cloud expands again for  $t_{\text{post}}$ .

During the first expansion, the cloud size increases depending on the initial velocity. After a sufficient expansion time only such atoms are located next to each other, which have a similar velocity, while their initial position gets less important (Fig. 5.3 a) and b)). When the trap potential is switched on again, the atoms decelerate by converting kinetic into potential energy. At the turning point, that means, when all atoms are almost at rest, the potential is switched off (Fig. 5.3 c)). The atom cloud is now "cooler" at the cost of a lower density.

An alternative view at the problem can be given in the phase space (Fig. 5.4). The atom cloud has at the beginning a Gaussian position and velocity distribution with the widths  $\sigma_{x,0}$  and  $\sigma_{v,0}$ , which are uncorrelated. With increasing expansion time  $t_{\text{pre}}$  the correlation increases as shown in section 5.2. The phase space distribution shears, such that the velocity distribution width  $\sigma_v$  remains constant and the position width  $\sigma_x$  increases (Fig. 5.4 b)). The trap potential is then switched on again for  $\delta$ -kick cooling and the cloud starts to rotate clockwise in phase space. When the minimum

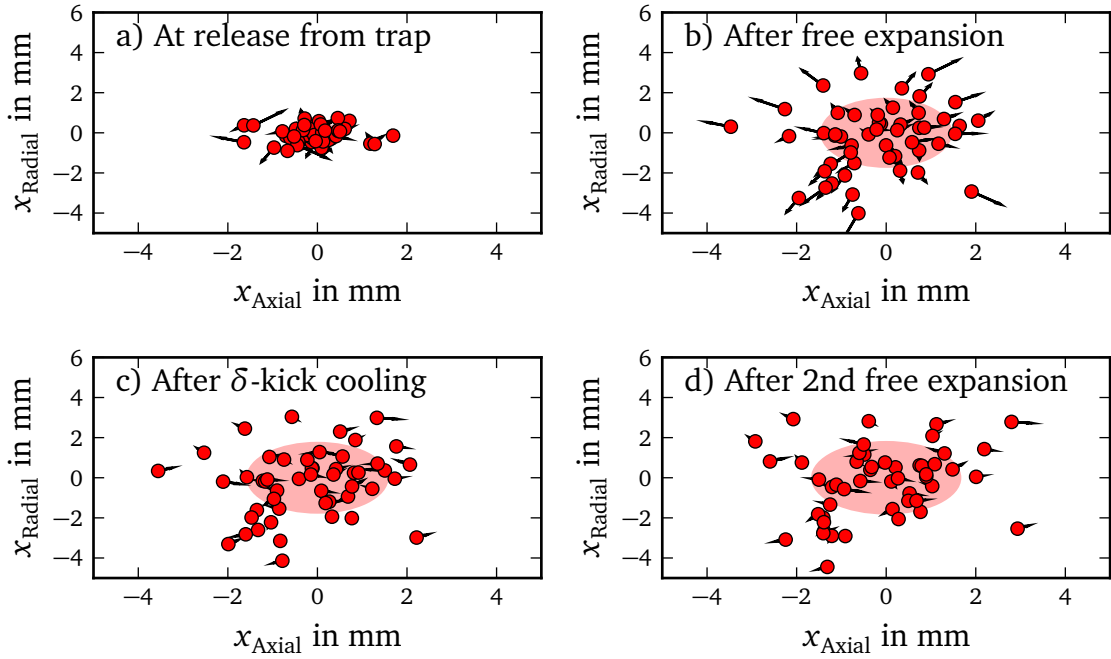


**Figure 5.3:** Two-dimensional schematic of the time evolution of cooled atoms released from a harmonic trap. The atoms are represented by red dots and their velocities by arrows. The red ellipses indicate the positional spreads of the ensemble. a) Atoms immediately after the release: The positions and the velocity are Gaussian distributed and uncorrelated. b) After a first free expansion: The distributions are still Gaussian, but now velocity and positions are (partially) correlated: Adjacent atoms have similar velocities and flight directions. c) After  $\delta$ -kick cooling: The velocities are much smaller, whereas the positions remain nearly unchanged. d) After a second free expansion: The positions of the atoms have changed less compared to the first expansion.

velocity width is reached (Fig. 5.4 c)), the trap is switched off again. Now, the cloud expands with a smaller velocity width and thus has a lower "temperature" (Fig. 5.4 d)).

This description can be used for a quantitative derivation. It starts in reversed temporal order with an exemplary particle at the position  $x_{\text{post}}$  and the velocity  $v_{\text{post}}$  after the primary free expansion, the  $\delta$ -kick cooling, and the secondary expansion. The aim now is to calculate the origin of this particle when it was released from the trap with  $(x_0, v_0)$ . Before the second expansion the atom was at  $(x_{\text{DKC}} = x_{\text{post}} - v_{\text{post}} t_{\text{post}}, v_{\text{DKC}} = v_{\text{post}})$ . During  $\delta$ -kick cooling it followed the trajectory for a harmonic potential, which is given by equation (5.37). This gives the phase space coordinates before the cooling  $(x_{\text{pre}}, v_{\text{pre}})$ . The origin  $(x_0, v_0)$

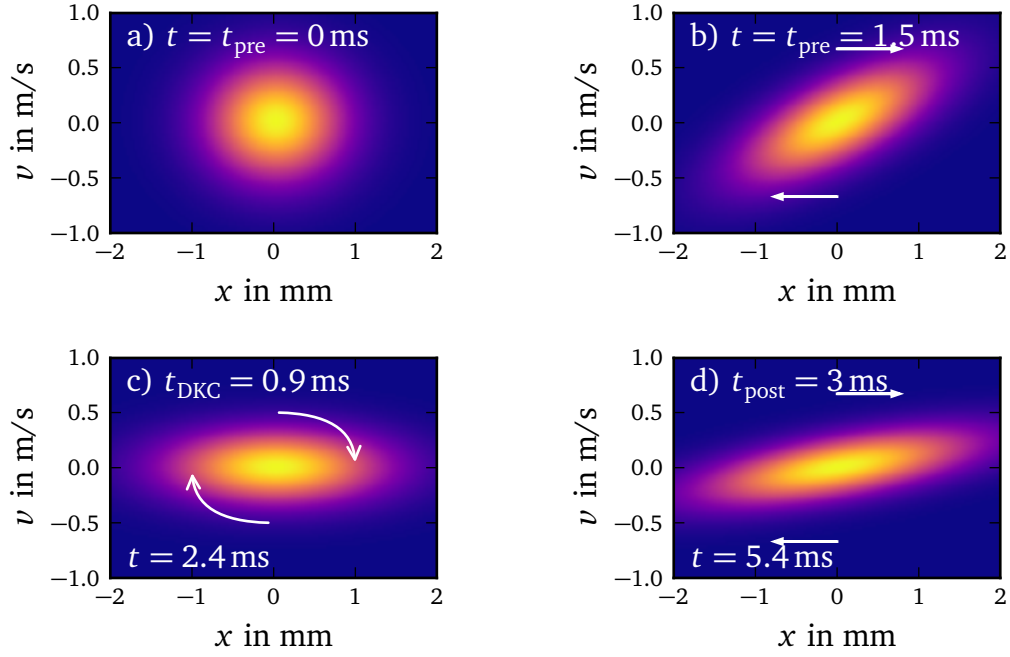


**Figure 5.4:** Sequential phase space density plots of a  $\text{Ne}^*$  atom cloud during  $\delta$ -kick cooling with typical spatial and velocity widths. a) Distribution immediately after switching off the trap, b) after a first free expansion, c) after applying  $\delta$ -kick cooling, and d) after a second free expansion. After the  $\delta$ -kick cooling the velocity spread is narrower than before.

can be calculated from these points under consideration of the first expansion ( $x_0 = x_{\text{pre}} - v_{\text{pre}} t_{\text{pre}}$ ,  $v_0 = v_{\text{pre}}$ ). Together this gives the full path

$$x_0 = (x_{\text{post}} - v_{\text{post}} t_{\text{post}}) \cos(\omega_x t_{\text{DKC}}) - \frac{v_{\text{post}}}{\omega_x} \sin(\omega_x t_{\text{DKC}}) \quad (5.41)$$

$$- (\omega_x (x_{\text{post}} - v_{\text{post}} t_{\text{post}}) \sin(\omega_x t_{\text{DKC}}) + v_{\text{post}} \cos(\omega_x t_{\text{DKC}})) t_{\text{pre}} \text{ and} \quad (5.42)$$

$$v_0 = \omega_x (x_{\text{post}} - v_{\text{post}} t_{\text{post}}) \sin(\omega_x t_{\text{DKC}}) + v_{\text{post}} \cos(\omega_x t_{\text{DKC}}).$$

This allows for a calculation of the phase space distribution from the initial Gaussian probability distributions given by equations (5.2) and (5.12)

$$\rho_{\text{post}}(x_{\text{post}}, v_{\text{post}}, t_{\text{pre}}, t_{\text{DKC}}, t_{\text{post}}) = \iint \rho_x(x) \rho_v(v) \delta(x - x_0) \delta(v - v_0) dx dv. \quad (5.43)$$

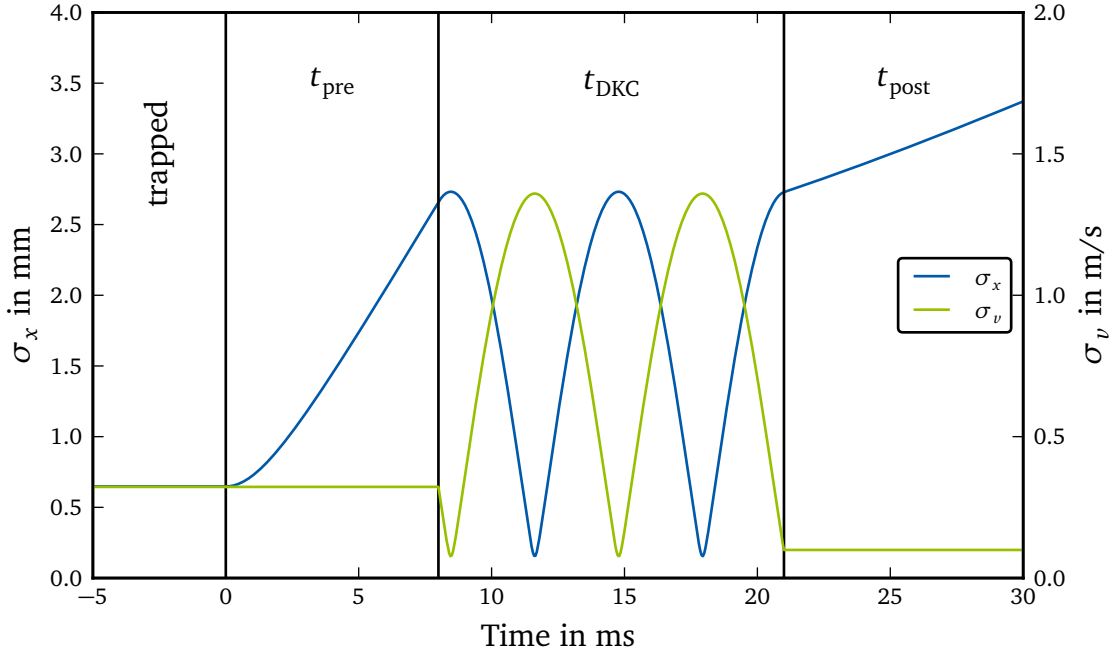


**Figure 5.5:** Time evolution of the spatial and velocity width during the  $\delta$ -kick cooling cycle.

The solution of the integral results in a large equation. Nevertheless, the time-dependent widths can still be determined analytically as

$$\begin{aligned}
\sigma_x^2(t_{\text{pre}}, t_{\text{DKC}}, t_{\text{post}}) &= \iint x^2 \rho_{\text{post}}(x, v, t_{\text{pre}}, t_{\text{DKC}}, t_{\text{post}}) dx dv \\
&= \sigma_{x,0}^2 \left( \cos(\omega_x t_{\text{DKC}}) - \omega_x t_{\text{post}} \sin(\omega_x t_{\text{DKC}}) \right)^2 \\
&\quad + \frac{\sigma_{v,0}^2}{\omega_x^2} \left( \omega_x (t_{\text{pre}} + t_{\text{post}}) \cos(\omega_x t_{\text{DKC}}) \right. \\
&\quad \left. + (1 - \omega_x^2 t_{\text{pre}} t_{\text{post}}) \sin(\omega_x t_{\text{DKC}}) \right)^2, \text{ and}
\end{aligned} \tag{5.44}$$

$$\begin{aligned}
\sigma_v^2(t_{\text{pre}}, t_{\text{DKC}}) &= \iint v^2 \rho_{\text{post}}(x, v, t_{\text{pre}}, t_{\text{DKC}}, t_{\text{post}}) dx dv \\
&= \omega_x^2 \sigma_{x,0}^2 \sin^2(\omega_x t_{\text{DKC}}) \\
&\quad + \sigma_{v,0}^2 \left( \cos(\omega_x t_{\text{DKC}}) - \omega_x t_{\text{pre}} \sin(\omega_x t_{\text{DKC}}) \right)^2.
\end{aligned} \tag{5.45}$$

These equations describe the complete dynamics of the atom cloud for the  $\delta$ -kick cooling cycle (Fig. 5.5). After the release from the trap at  $t = 0$  the cloud starts to expand while the velocity distribution remains constant. When the harmonic potential is switched on again, the cloud starts to oscillate. The oscillation of the position width and velocity width is phase-shifted by  $\pi/2$ . After the potential is switched off

the cloud expands again and the velocity is constant, but as can be seen at a much lower level. This can also be seen in equation (5.45), in which  $\sigma_v^2(t_{\text{pre}}, t_{\text{DKC}})$  is independent from  $t_{\text{post}}$ .

For  $t_{\text{DKC}} = 0$  and  $t_{\text{post}} = 0$  the equations for the spatial (5.44) and velocity width (5.45) reduce to the solutions for free expansion (5.24) and (5.27), while for  $t_{\text{pre}} = 0$  and  $t_{\text{post}} = 0$ , they reduce to the solutions in a harmonic potential (5.39) and (5.40).

The solution of the dynamics has an interesting property. If the condition

$$\omega_x t_{\text{pre}} = \frac{1}{\tan(\omega_x t_{\text{DKC}})} \quad (5.46)$$

is chosen, the velocity width  $\sigma_v^2(t_{\text{pre}}, t_{\text{DKC}})$  of equation (5.45) has a solution, which is independent of the initial velocity spread  $\sigma_{v,0}$ . Inserting this condition into equation (5.45) results in

$$\sigma_v^2(t_{\text{pre}}, \arctan(1/(\omega_x t_{\text{pre}}))/\omega_x) = \frac{\omega_x^2 \sigma_{x,0}^2}{1 + \omega_x^2 t_{\text{pre}}^2}. \quad (5.47)$$

As pointed out by Maréchal et al. [103], this allows for a production of arbitrary low velocity spreads by manipulating the initial spatial width  $\sigma_{x,0}^2$  and the expansion time  $t_{\text{pre}}$  only. In contrast to the example shown in figure 5.4 c), this solution will not yield the smallest achievable velocity width, but it is a good approximation for large expansion times where the initial width is less important  $\sigma_{x,0}^2 \ll \sigma_{v,0}^2 t_{\text{pre}}^2$ . In general, a cloud created with this solution is slightly tilted and the exact minimum velocity width must be derived numerically.

The initial width  $\sigma_{x,0}^2$  in equation (5.47) can be substituted for the initial temperature from equation (5.14). This yields an approximation for the temperature after applying the  $\delta$ -kick

$$T_{\text{post}}(t_{\text{pre}}) = \frac{\omega_{\text{DKC}}^2 T_0}{\omega_x^2 (1 + \omega_{\text{DKC}}^2 t_{\text{pre}}^2)}. \quad (5.48)$$

Here  $T_0$  is the initial temperature,  $\omega_x$  the trap oscillation frequency, and  $\omega_{\text{DKC}}$  the oscillation frequency during the  $\delta$ -kick. In general, these frequencies are different. As can be seen, in order to prepare low temperature clouds long primary expansion times or weaker  $\delta$ -kick potentials are required.

A common analogy to the  $\delta$ -kick cooling is the imaging of a thin lens. Here, the initial spatial width  $\sigma_{x,0}$  is treated as the object and the minimum width after the  $\delta$ -kick is the image. The  $\delta$ -kick resembles the thin lens and the strength of the kick corresponds to the inverse of the focal length. To qualify as a thin lens the  $\delta$ -kick has to be much shorter than the expansion times,  $t_{\text{DKC}} \ll t_{\text{pre}}, t_{\text{post}}$ . In this experiment, these conditions are not fully satisfied. A more detailed description can be found in reference [103].

---

### 5.4.1 Phase Space Density Discussion

---

An important property of cooling is the ability to change the phase space density. This is the case for laser cooling. However, the phase space density remains constant for  $\delta$ -kick cooling. This is discussed in this section.

The Liouville's theorem describes the time evolution of the density operator [11]

$$\frac{d\rho}{dt} = \frac{\partial \rho}{\partial t} + \frac{\partial \rho}{\partial x} \frac{\partial x}{\partial t} + \frac{\partial \rho}{\partial p} \frac{\partial p}{\partial t} = 0, \quad (5.49)$$

with the canonical momentum  $p$ . If this equation is fulfilled, the phase space density remains constant. The shape of the density distribution can still change with time in this case.

The canonical momentum for free expansion is  $p = mv$ . The use of the momentum and the density distribution  $\rho(x, v, t)$  of the free expansion given in equation (5.20) in Liouville's theorem yield a true assertion. The same applies for the dynamics of the density distribution  $\rho_{\text{harm}}(x, v, t)$  in a harmonic potential from equation (5.38). As  $\delta$ -kick cooling is a combination of free expansion and motion in a trap, Liouville's theorem is also true for this case. Thus, the phase space density is conserved, which means, that this preparation technique is not a true cooling method. A decrease in the velocity spread  $\sigma_v$  yields always an increase in spatial width  $\sigma_x$  as a direct result of the theorem.

In contrast to  $\delta$ -kick cooling, Doppler cooling of atoms with laser-light is a true cooling method: The total time derivative of the phase space density is larger than zero, which means, the phase space density increases [11].

However,  $\delta$ -kick **cooling** is a common term for this preparation technique and shall be used in this thesis as well.

---

## 5.5 Implementation of $\delta$ -Kick Cooling with Ne\* atoms

---

The method of  $\delta$ -kick cooling is an interesting tool facilitating the measurement of the collision properties of cold atoms, such as Ne\*-atoms. It allows for a full control over the temperature versus the density of the Ne\*-cloud. Thus, it is possible to prepare a hot cloud of several millikelvin or a cold one of some ten microkelvin. A further advantage is the slower expansion after the  $\delta$ -kick cooling. This increases the observation time available and thus the statistics of the collision measurement, which cuts down the number of required measurement cycles. It leads to a significant reduction of total experiment time.

The technique will be analysed in detail in the next sections. A focus lies on the understanding and optimization of the control parameters to prepare the desired cloud parameters.

---

### 5.5.1 Preparation and Measurement

---

The experiment starts with a cold cloud of  $\text{Ne}^*$  atoms in a magnetic trap. The cloud is laser cooled axially by one-dimensional Doppler cooling. This results in a non-equilibrium state of the cloud. Nevertheless, it can be described by the independent temperatures  $T_{\text{ax}}$  in axial and  $T_{\text{rad}}$  in radial direction of the trap. Thermal equilibrium is reached due to elastic collisions, which lead to cross-dimensional relaxations [33, 112] for relaxation time longer than applied here. In this experiment, the non-equilibrium is the initial state for all investigations. Thus, the thermal energy of the cloud is described by the mean temperature  $\bar{T} = (T_{\text{ax}} + 2T_{\text{rad}})/3$ . The experimental procedure is as follows: First the atom cloud is released from the trap and starts to expand for the time  $t_{\text{pre}}$ . Next, the trap potential is switched on again for the  $\delta$ -kick for time  $t_{\text{DKC}}$ . Afterwards, the cloud re-expands freely for the time  $t_{\text{post}}$ . With absorption images the cloud widths in axial and radial dimensions were measured (Fig. 5.9 b) and c)). From repeated measurements for different expansion times  $t_{\text{pre}}$  the initial temperature  $T_{0,\text{ax/rad}}$  and the initial velocity distribution  $\sigma_{v,0,\text{ax/rad}}$  can be fitted using equation (5.25) in axial and radial direction. Due to the orthogonal directions of the trap (radial and axial) and the slow thermalisation rate due to elastic collisions compared to the observation time, both directions can be treated independently.

The initial spatial width  $\sigma_{x,0,\text{ax/rad}}$  is calculated from equation (5.14) using the temperature from the previous fit and the corresponding trap frequency in axial and radial direction  $\omega_{\text{ax}}$  and  $\omega_{\text{rad}}$ . The trap frequencies are known from the electric current through the trap coils and equation (4.6). Typical values are  $\omega_{\text{ax}} = 2\pi \times 80$  Hz and  $\omega_{\text{rad}} = 2\pi \times 160$  Hz. In contrast, a reconstruction of  $\sigma_{x,0,\text{ax/rad}}$  from the expansion series using (5.24) is not recommend, because the influence of the initial width on the measured width decreases with  $t_{\text{pre}}$  and the images cannot be taken shortly after switching-off the trap due to temporal B-field gradients, which distort the images and influence the expansion dynamics. Because of this, the initial width  $\sigma_{x,0,\text{ax/rad}}$  is determined by using the temperature and the trap frequency.

For the characterization of the  $\delta$ -kick cooling process, a second series of  $t_{\text{post}}$ -dependent absorption images is recorded. The dynamics of the second expansion  $\sigma_x^2(t_{\text{pre}}, t_{\text{DKC}}, t_{\text{post}})$  and  $\sigma_v^2(t_{\text{pre}}, t_{\text{DKC}})$  can then be described by equations (5.44) and (5.45).

---

### 5.5.2 Influence of the Primary Expansion Time $t_{\text{pre}}$

---

In order to tune the temperature after  $\delta$ -kick cooling it is possible to change the expansion time  $t_{\text{pre}}$  before the kick. This section will now discuss the influence of this parameter on the final temperature. The achieved temperatures will be compared with the theoretically expected values obtained by the approximation  $T_{\text{DKC}}(t_{\text{pre}})$  from equation (5.48), which depends on the primary expansion time  $t_{\text{pre}}$ .

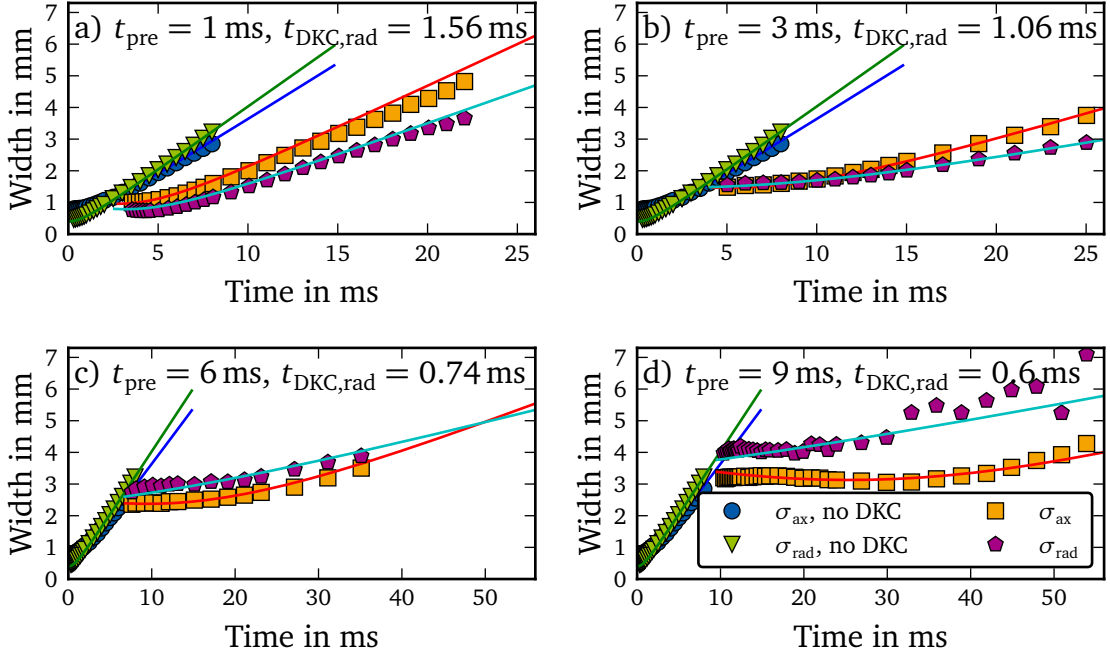


**Figure 5.6:** Atom cloud dynamics with  $\delta$ -kick cooling after different expansion times  $t_{\text{pre}}$ . The blue circles and the green triangles denote the cloud expansion after the release from the trap in axial and radial direction without  $\delta$ -kick cooling. The red squares and the cyan pentagons indicate the spatial width in axial and radial direction after the delta kick cooling. The solid lines present fits to the experimental data based on equation (5.44).

The initial temperatures were measured from an absorption image series and are  $T_{\text{ax},0} = T_{\text{ax}}(t=0) = 306(3) \mu\text{K}$  in axial and  $T_{\text{rad},0} = T_{\text{rad}}(t=0) = 387(3) \mu\text{K}$  in radial direction. From these temperatures the initial width can be calculated to  $\sigma_{x,0,\text{ax}} = 717(13) \mu\text{m}$  and  $\sigma_{x,0,\text{rad}} = 397(8) \mu\text{m}$  respectively. The initial velocity spreads are  $\sigma_{v,0,\text{ax}} = 357(2) \text{mm/s}$  and  $\sigma_{v,0,\text{rad}} = 401(2) \text{mm/s}$ . The  $\delta$ -kick lengths  $t_{\text{DKC}}$  were optimized to always give the minimum temperature for a chosen expansion time  $t_{\text{pre}}$ . For the kick at  $t_{\text{pre}} = 1 \text{ ms}$  ( $3 \text{ ms}$ ,  $6 \text{ ms}$ ,  $9 \text{ ms}$ ) the pulse had a length of  $t_{\text{DKC,rad}} = 1.56 \text{ ms}$  ( $1.06 \text{ ms}$ ,  $0.74 \text{ ms}$ ,  $0.60 \text{ ms}$ ). The kick duration decreases with the primary expansion time. Due to the anisotropic potential in axial and radial direction, the pulse length in axial direction was up to  $300 \mu\text{s}$  longer with  $t_{\text{DKC,ax}} = 1.76 \text{ ms}$  ( $1.22 \text{ ms}$ ,  $0.82 \text{ ms}$ ,  $0.60 \text{ ms}$ ). This was done by switching off the trap potential in radial direction earlier (closing IGBT 1 and MOSFET 2, opening IGBT 2, Fig. 4.3). Afterwards, the trap was switched off with the soft procedure for another  $300 \mu\text{s}$  (Sec. 4.2.2).

The final results for  $\delta$ -kick cooling are presented in figure 5.6. The blue circles and the green triangles indicate the width of the cloud in axial and radial direction for several exemplary expansion times  $t_{\text{pre}}$  without  $\delta$ -kick cooling. The faster expansion in the radial dimension is a result of the higher initial temperature. The lines in the cor-

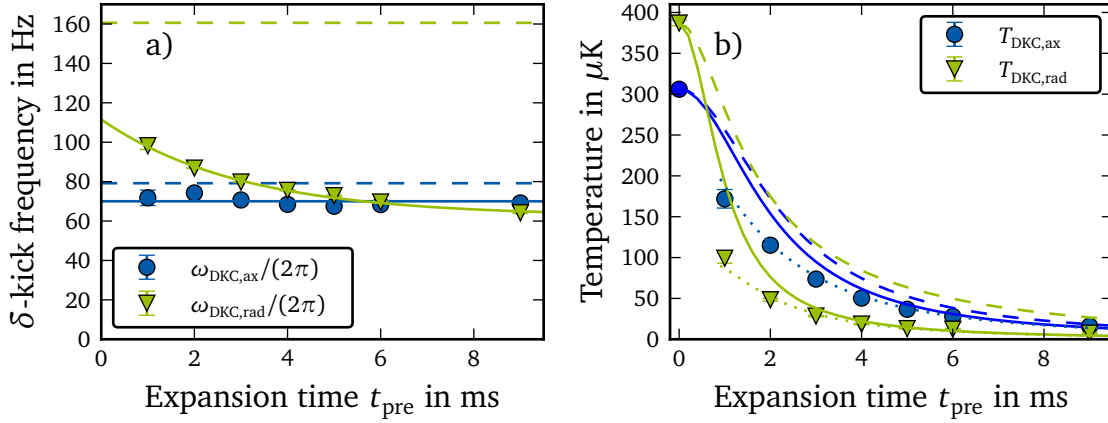


**Figure 5.7:** a) Fit results of the potential frequencies of the  $\delta$ -kick pulse in axial and radial direction for different expansion times  $t_{\text{pre}}$ . The solid lines are fits to the data and the dashed lines indicate the respective frequencies of the magnetic trap in harmonic approximation. b) The calculated temperatures of the cloud in both directions. The solid lines indicate the minimum temperature for  $\delta$ -kick cooling using the fitted potential frequencies from a). The dashed lines show the temperature for a  $\delta$ -kick with the higher frequencies of the magnetic trap in harmonic approximation and the dotted lines show the minimum temperature obtained by a numerical solution.

responding colours represent the fit results of the initial conditions. The red squares for the axial dimension and the cyan pentagons for the radial show the widths of the cloud after the  $\delta$ -kick. The expansion rate after  $\delta$ -kick cooling is always lower compared to the case without it. Additionally, the velocity spread of the cloud decreases for  $\delta$ -kicks at later times  $t_{\text{pre}}$ : The axial dimension for a  $\delta$ -kick at  $t_{\text{pre}} = 1$  ms after  $t_{\text{post}} = 14$  ms is around 3.6 mm, whereas for a kick at  $t_{\text{pre}} = 3$  ms it is only 2.9 mm. The solid lines in red and cyan show fits of  $\sigma_{x,\text{ax/rad}}(t_{\text{pre}}, t_{\text{DKC}}, t_{\text{post}})$  based on equation (5.44). The only free fit parameter, the potential frequency  $\omega_{\text{DKC,ax/rad}}$ , is used to determine the  $\delta$ -kick strength, whereas the timings  $t_{\text{pre}}$ ,  $t_{\text{DKC,ax/rad}}$ , and  $t_{\text{post}}$  are determined by the measurement. The soft switch-off time is included in the second expansion time  $t_{\text{post}}$ . For  $t_{\text{pre}} = 1$  ms, the fit slope overestimates the expansion which results in a too high temperature. In the  $t_{\text{pre}} = 9$  ms measurement it can be seen that the radial dimension is distorted for  $t_{\text{post}} > 20$  ms (at  $t \approx 30$  ms in Fig. 5.6 d)). In this case, the absolute dimension of the cloud is larger than the imaging region of the camera. Therefore, only the data points from shorter expansion times  $t_{\text{post}} < 20$  ms were used for the fit.

The potential frequencies  $\omega_{\text{DKC,ax}}$  and  $\omega_{\text{DKC,rad}}$  of the  $\delta$ -kick obtained from the fits are expected to be equal to the corresponding frequencies of the magnetic trap. However, the fits yield systematic lower frequencies (Fig. 5.7 a) and b)): The axial frequency  $\omega_{\text{DKC,ax}} = 2\pi \times 70$  Hz is nearly constant and is approximately 11 % smaller

than the magnetic trap frequency ( $2\pi \times 80$  Hz). The radial frequency is much smaller than in the trap. For  $t_{\text{pre}} = 1$  ms with  $\omega_{\text{DKC,rad}} = 2\pi \times 98$  Hz it is only 61 % of the strength of the magnetic trap ( $2\pi \times 160$  Hz) and it further decreases to 40 % for  $t_{\text{pre}} = 9$  ms. A phenomenological obtained exponential decay of the form  $\omega_{\text{DKC,rad}}(t_{\text{pre}}) = \omega_{\text{rad,amp}} \exp(-t_{\text{pre}}/\tau) + \omega_{\text{rad,offset}}$  can be fitted to the radial frequency. It yields a decay time of  $\tau = 3.0(3)$  ms with an amplitude of  $\omega_{\text{rad,amp}} = 2\pi \times 49(2)$  Hz and converges to  $\omega_{\text{rad,offset}} = 2\pi \times 63(2)$  Hz for long expansion times.

An exponential fit in radial direction for the  $\delta$ -kick-duration-depending frequency  $\omega_{\text{DKC,rad}}$  gives a time constant of  $\tau_{\text{DKC,rad}} = 0.74(9)$  ms and an offset of  $2\pi \times 109(6)$  Hz (Fig. 5.7 b)).

The probable reason for the radial variation of the  $\delta$ -kick potential frequency is the geometry of the trap potential. In radial direction the harmonic region is much smaller than in axial direction. The potential becomes linear with increasing distance. E.g. the true potential at a distance of 3 mm from the centre is 20 % smaller than the harmonic approximation [87]. In axial direction no difference can be seen up to 4 mm. This means, the force on the atoms towards the centre is no longer linear with the distance, but constant resulting in a lower oscillation frequency for atoms in the outer region of the trap. Thus, the radial  $\delta$ -kick potential frequency  $\omega_{\text{DKC,rad}}$  decreases for longer primary expansion times  $t_{\text{pre}}$ , because of the larger atom clouds.

The known timings and the fitted potential frequencies of the  $\delta$ -kick allow for a calculation of the velocity spread  $\sigma_v(t_{\text{pre}}, t_{\text{DKC}})$  after the preparation from equation (5.45). From that, the temperatures  $T_{\text{DKC,ax}}$  and  $T_{\text{DKC,rad}}$  in axial and radial direction can be obtained with equation (5.5) (Fig. 5.7 c) and table 5.1). The results yield a lower final temperature with larger expansion times  $t_{\text{pre}}$ . The lowest temperatures were achieved after  $t_{\text{pre}} = 9$  ms with  $T_{\text{DKC,ax}} = 16$   $\mu$ K and  $T_{\text{DKC,rad}} = 7$   $\mu$ K. This is only 5 % and 2 % of the initial temperatures  $T_{0,\text{ax}} = 306$   $\mu$ K in axial and  $T_{0,\text{rad}} = 387$   $\mu$ K radial direction, respectively. The initial temperatures of the cloud are also plotted in figure 5.7 c) for  $t_{\text{pre}} = 0$  ms to visualize the start temperature.

An approximation for the minimum temperature after the cooling can be calculated by using  $T_{\text{post}}(t_{\text{pre}})$  from equation (5.48) using the initial spatial and velocity distribution of the cloud. The calculated temperatures in axial and radial direction are shown in figure 5.7 c), in one case as dashed lines assuming the frequencies of the steady-state magnetic trap for the  $\delta$ -kick potential and in a second case as solid lines using the fits of the measured frequencies, which are shown in 5.7 a). In axial direction, the mean value of the measured frequencies is used, whereas in radial direction the exponential decay is assumed. The calculated temperatures  $T_{\text{post}}(t_{\text{pre}})$  using the frequencies of the steady-state magnetic trap overestimates the measured temperatures, but converges for long primary expansion times. The temperature curves using the fitted measured frequencies (Fig. 5.7 a)) of the  $\delta$ -kick potential reproduce the measurements better, especially in radial direction. Nevertheless, the deviations for small expansion times  $t_{\text{pre}} < 5$  ms are still apparent. The explanation of the deviations can be found in the derivation of the equation for the temperature  $T_{\text{post}}(t_{\text{pre}})$  (Eq. (5.48)). The equation is the solution of the  $\delta$ -kick dynamics which is

independent from the initial velocity distribution  $\sigma_{v,0}$ . The solution converges only for long primary expansion times  $t_{\text{pre}}$  or for arbitrary small initial spatial distributions  $\sigma_{x,0} \rightarrow 0$  towards the minimum temperature. For a real cloud and small times  $t_{\text{pre}}$ , it yields an analytical approximation for the upper limit of the lowest temperature. In contrast, the numerical solution for the minimum temperature reproduces the measured temperatures (dotted line in Fig. 5.7 c)). It uses the initial temperatures, the initial spatial widths, the used  $\delta$ -kick durations, and the fitted  $\delta$ -kick strengths (lines in Fig. 5.7 a)). Even for short times  $t_{\text{pre}} = 1$  ms, the temperatures match. For shorter times, no extrapolation of the numerical-obtained minimum temperature is done. The experimental uncertainties of the magnetic-field gradients due to the switch-off of the magnetic trap and the unknown exact switching characteristics of the IGBTs leads to an unpredictable dynamics of the potential frequency  $\omega_{\text{DKC}}$  for these short times. The exponential behaviour in radial direction probably underestimates the actual potential frequency in the experiment.

$t_{\text{pre}}$ in ms	Axial temperature in $\mu\text{K}$	Radial temperature in $\mu\text{K}$
no $\delta$ -kick cooling	$306.05 \pm 3.47$	$387.04 \pm 3.29$
1	$171.91 \pm 11.32$	$99.20 \pm 6.13$
2	$115.11 \pm 3.99$	$48.37 \pm 1.65$
3	$73.64 \pm 2.29$	$28.39 \pm 0.97$
4	$50.36 \pm 1.56$	$18.58 \pm 0.65$
5	$36.68 \pm 1.08$	$13.00 \pm 0.49$
6	$27.89 \pm 0.95$	$12.28 \pm 0.93$
9	$16.07 \pm 0.61$	$7.47 \pm 0.80$

**Table 5.1:** Temperatures of the cloud after  $\delta$ -kick cooling from figure 5.7 c). The initial temperatures without  $\delta$ -kick cooling are also shown.

### 5.5.3 Influence of the $\delta$ -Kick Cooling Length

After the discussion of different primary expansion times  $t_{\text{pre}}$ , the influence of the pulse duration  $t_{\text{DKC}}$  of the  $\delta$ -kick cooling on the resulting atom cloud will be discussed.

The preparation is similar to the previous section, but with the first expansion time fixed at  $t_{\text{pre}} = 1.5$  ms, while the pulse length  $t_{\text{DKC}}$  is varied. The kick has the same duration in axial and radial dimension and the current is switched off hard. The initial temperatures were measured with a time-of-flight series of absorption images, from which the axial and radial widths are used to fit  $\sigma_{x,\text{ax},\text{rad}}(t_{\text{pre}})$  from equation (5.25) (blue dots in Fig. 5.8 a) and green triangles in Fig. 5.8 b)). As the absorption images are distorted for small times after the switch-off of the trap due to B-field gradients, only the measurement points at  $t_{\text{pre}} > 0.6$  ms are used. The distortion results in a deviation of the measured widths from the fit for small times and is

ignored in the evaluation. The resulting temperatures are  $T_{0,\text{ax}} = 247(2) \mu\text{K}$  in axial and  $T_{0,\text{rad}} = 392(3) \mu\text{K}$  in radial direction, respectively.

The expansion after the  $\delta$ -kick cooling pulse was measured for  $t_{\text{DKC}} = 0.5 \text{ ms}$ ,  $1 \text{ ms}$ , and  $2 \text{ ms}$ . Equation (5.46) resolved to  $t_{\text{DKC}}$  provides for the radial dimension an optimal pulse length of  $t_{\text{DKC,rad}} = 1.4 \text{ ms}$  and in axial dimension  $t_{\text{DKC,ax}} = 1.9 \text{ ms}$ , assuming the magnetic-trap frequencies. Therefore, the measured  $\delta$ -kick durations of up to  $2 \text{ ms}$  covers the case of the minimum temperature in both directions.

The measurement data for different  $\delta$ -kick durations are shown in figures 5.8 a) and b) in addition to the free expansion measures without  $\delta$ -kick cooling. The time is given relative to the trap switch-off time  $t = 0$ . Fits for  $\sigma_x(t_{\text{pre}}, t_{\text{DKC}}, t_{\text{post}})$  of equation (5.44) are used to describe the data with the  $\delta$ -kick potential frequency as the free fit parameter. The temperature in axial direction, which corresponds to the expansion velocity, decreases with increasing  $\delta$ -kick duration (Fig. 5.8 a)). A minimum temperature cannot be determined from the graph and will be evaluated in the discussion below. In radial direction, the minimum temperature is achieved between  $t_{\text{DKC}} = 1 \text{ ms}$  and  $2 \text{ ms}$  (Fig. 5.8 b)). The  $2 \text{ ms}$  pulse length is already too long and yields an increased temperature. Additionally, the  $\delta$ -kick leads to a decreasing spatial width immediately after the  $\delta$ -kick. After the minimum has been reached, the expansion is faster than for the other measurements.

The results for the fits of the  $\delta$ -kick-potential frequency are plotted in figure 5.9 a). The axial frequency is constant, like in the previous section, with a mean of  $\omega_{\text{DKC,ax}} = 2\pi \times 52 \text{ Hz}$ . This is only 65 % of the steady-state frequency of the magnetic trap of  $2\pi \times 80 \text{ Hz}$ . The frequency-results in radial direction are not constant, as can be seen in the graph, but can be described with an exponential fit with the rise time of  $\tau = 1.26(11) \text{ ms}$ . A convergence to the frequency of the steady-state magnetic trap for long pulse times is assumed for the fit. Therefore, the asymptotic frequency of  $\omega_{\text{rad}} = 2\pi \times 160.6 \text{ Hz}$  is a fixed value. The temporal variation of the radial frequency can be expressed as

$$\omega_{\text{DKC,rad}}(t_{\text{DKC}}) = 2\pi \times 160.6 \text{ Hz} \times (1 - e^{-t_{\text{DKC}}/1.26 \text{ ms}}). \quad (5.50)$$

The reason for the varying frequency could be again the deviation from the harmonic potential. With increasing  $\delta$ -kick duration the spatial width of the cloud shrinks. Since the potential is at the centre is more harmonic, this yields frequencies  $\omega_{\text{DKC,rad}}$  more closely to the frequencies of the steady-state magnetic trap.

With the  $\delta$ -kick-potential frequencies and the initial cloud parameters, the temperatures in axial and radial direction after the cooling can be calculated with equation (5.45) for the velocity spread  $\sigma_v(t_{\text{pre}}, t_{\text{DKC}})$  and relation (5.5) between temperature and velocity  $T_{\text{ax,rad}} = \sigma_{v_{\text{ax,rad}}}^2 m/k_B$ . Figure 5.9 b) and c) show the measured temperatures from the absorption image series and the calculations. They are in good agreement. Only the temperature in radial direction for  $t_{\text{DKC}} = 2 \text{ ms}$  is lower than calculated. The minimum temperature in the axial dimension is  $78 \mu\text{K}$  for a pulse length of  $t_{\text{DKC}} = 2.9 \text{ ms}$ . In the radial dimension, a temperature of  $70 \mu\text{K}$  can be reached for  $t_{\text{DKC}} = 1.2 \text{ ms}$ . The difference of the measured and the estimated pulse

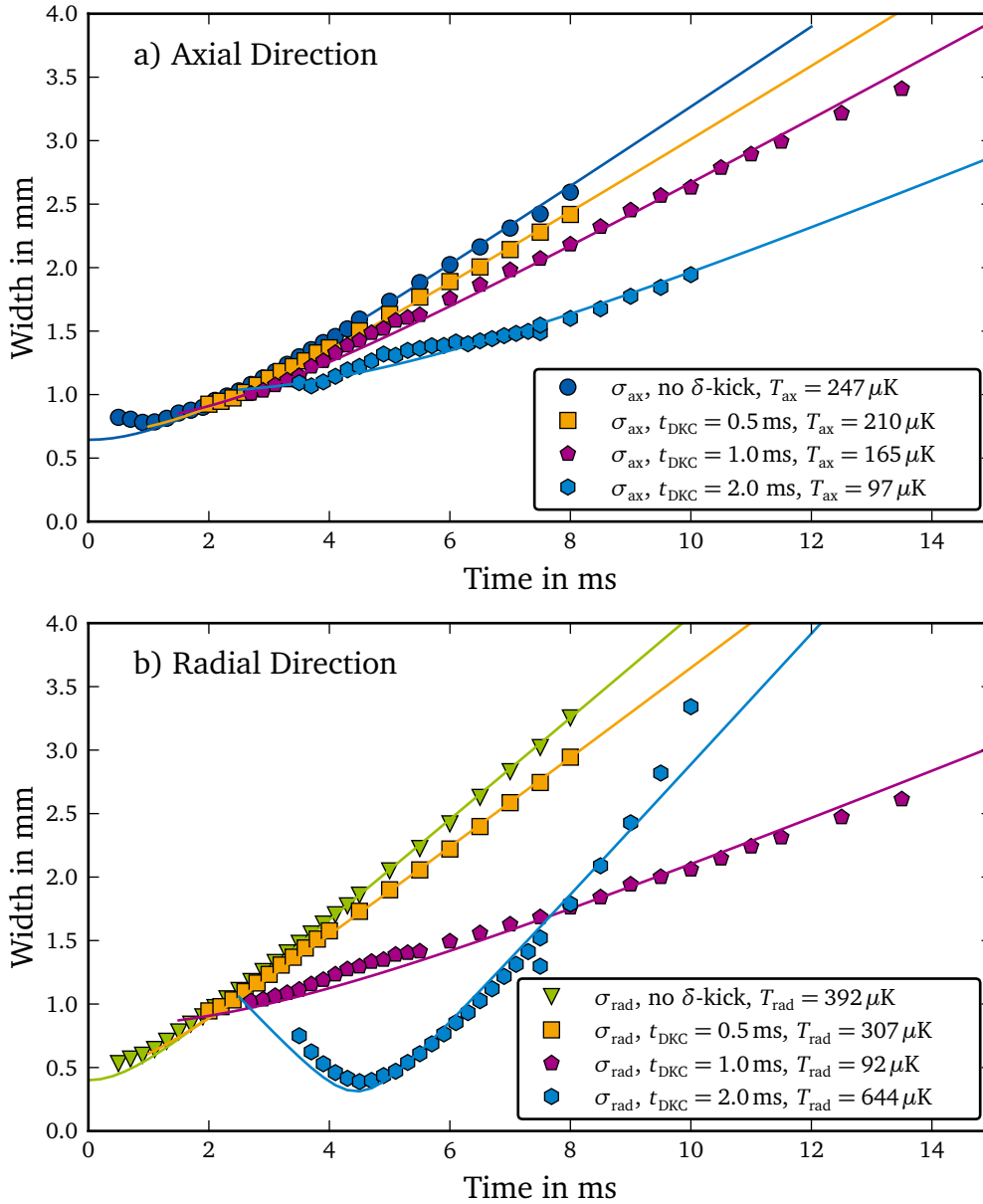


**Figure 5.8:** Expansion of the atom cloud widths before and after the  $\delta$ -kick cooling in the axial a) and in the radial b) dimension. The time is relative to the trap switch-off time  $t = 0$ . The solid lines indicate fit functions. The blue dots and green triangles show the measurements without  $\delta$ -kick cooling. The other polygons are the measured widths for the given  $\delta$ -kick pulse lengths.

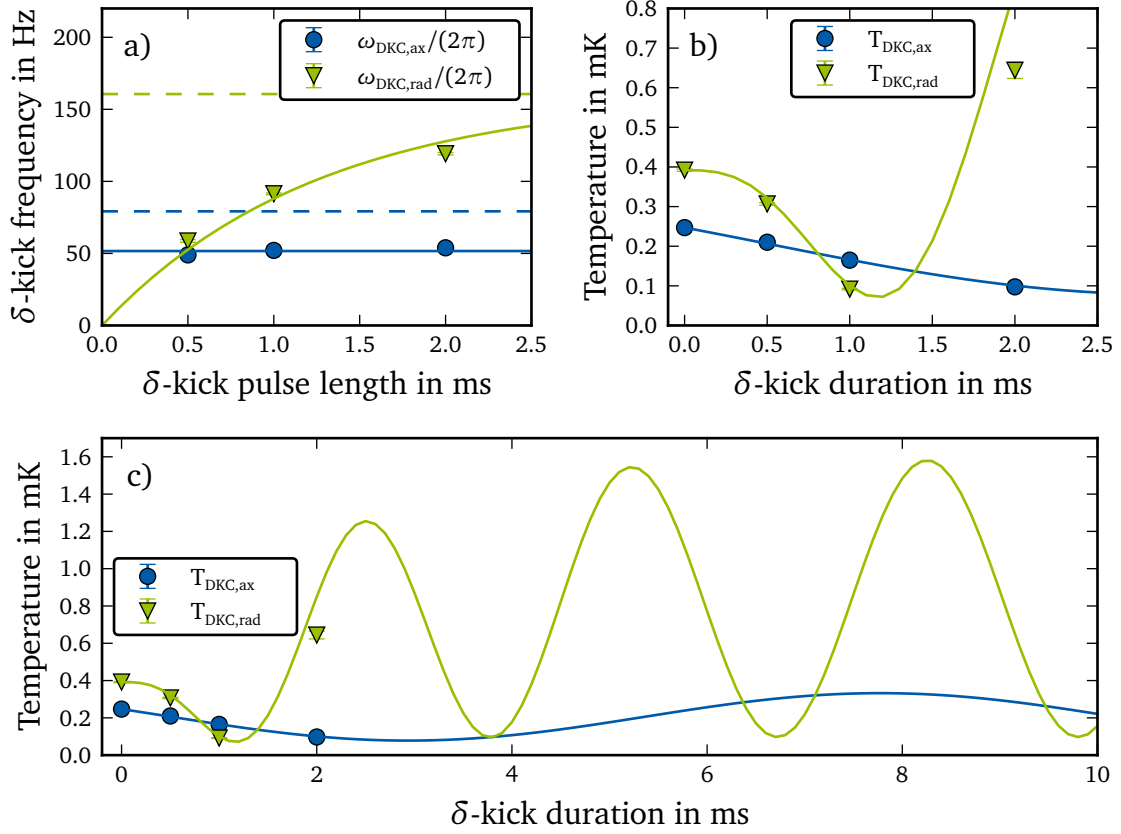


**Figure 5.9:** a)  $\delta$ -kick-potential frequency for different pulse length in axial and radial direction. The solid lines are fits to the data points and the dashed lines are the steady-state harmonic magnetic trap frequencies. b) Temperature after  $\delta$ -kick cooling. The solid lines are the calculated temperatures, which use the fitted  $\delta$ -kick-potential frequencies from a). c) Longer time evolution version of b).

length of 2.9 ms and 1.9 ms in axial direction can be explained with the different assumed ( $2\pi \times 80$  Hz) and measured ( $2\pi \times 52$  Hz) axial  $\delta$ -kick frequency: The ratio of the pulse lengths and the frequencies are the same  $2.9 \text{ ms}/1.9 \text{ ms} \approx 80 \text{ Hz}/52 \text{ Hz}$ . The duration in radial dimension is close to the estimated optimal kick length 1.4 ms.

The calculated temperatures from  $\sigma_\nu(t_{\text{pre}}, t_{\text{DKC}})$  in figure 5.9 b) are extrapolated to pulse length of 10 ms in figure 5.9 c) to illustrate the oscillatory character of the  $\delta$ -kick cooling method. Further data to support this will be shown in the next measurement series discussed below in this section. The amplitude of the temperature oscillation in axial direction is constant, while it grows in radial direction. The reason is the exponentially converging frequency  $\omega_{\text{DKC,Rad}}$ . Also noticeable is the slower oscillation in axial direction due to the lower trap frequency during the  $\delta$ -kick. Additionally, the amplitude of the temperature oscillation is much smaller than in radial direction. This is also the result of the lower trap frequency and can be understood

with the approximation (5.48) for the minimum temperature after cooling. It leads for  $1 \ll \omega_{\text{DKC}}^2 t_{\text{pre}}^2$  to

$$\frac{T_{0,\text{ax/rad}}}{T_{\text{DKC}}(t_{\text{pre}})} \approx \omega_{\text{ax/rad}}^2 t_{\text{pre}}^2, \quad (5.51)$$

with the ratio of the initial temperature and the temperature after the  $\delta$ -kick,  $T_0/T_{\text{DKC}}(t_{\text{pre}})$ , which can be seen as a measure for the amplitude, and the potential frequency  $\omega_{\text{ax/rad}}$  of the steady-state magnetic trap. This approximation yields a quadratic amplitude dependence from the steady-state trap frequency. Also notable is the independence of the amplitude from the  $\delta$ -kick potential frequency.

Another experimental investigation was performed with a smaller step size of the  $\delta$ -kick cooling length and larger final kick duration. This allows for an observation of the oscillatory behaviour of the cloud during the  $\delta$ -kick, which is shown in the calculated extrapolation in figure 5.9 c).

The kick duration was increased in 0.1 ms steps up to a total of 3.5 ms after a constant primary expansion time of  $t_{\text{pre}} = 1.5$  ms. At a fixed time  $t_{\text{post}} = 4$  ms of the secondary expansion, the absorption images were taken. The images for long  $\delta$ -kick duration show a crescent shape deformation of the atom cloud (Fig. 5.10 d)). This deviation from the expected two-dimensional Gaussian shape (Fig. 5.10 b)) leads to an incorrect estimation of the width in radial direction. Therefore, an one-dimensional Gaussian fit of the cross section through the centre of the cloud is used in this direction instead of a fit of the image's row-sum (Fig. 5.10 c) and e) for cuts in axial and radial direction). The result of the conventional row-sum fit are used to determine the centre for the cut. For a comparison, this evaluation method is also done for the axial direction, but no significant deviation from the Gaussian shape can be observed compared to the conventional image evaluation. Both methods, sum and cut, yield therefore the same widths in axial dimension, whereas the radial distribution shows distortions for long  $\delta$ -kick lengths (Fig. 5.10 e)). The sum fit, which is not shown, overestimates the radial width in this case. Because of this, the discussion uses in radial direction the result of the one-dimensional Gaussian fit of the cut through the centre and in axial direction the result of the standard sum fit from the absorption images.

A possible reason for the distorted form of the cloud could be its size compared to the harmonic trap dimension. A large cloud can have a non-negligible part in the outer region of the trap volume, where the deviation from a harmonic potential increases. This leads to non-Gaussian deformation of the cloud distribution in phase space which yields a distorted cloud shape at  $t_{\text{DKC}} = 2.8$  ms (Fig. 5.10 d)) with its crescent-shape instead of the expected Gaussian shape. The crescent shape could be an indication for an additional mixing of the axial and radial motion of the cloud. For shorter  $\delta$ -kick duration is the influence smaller and therefore the distortions are less.

The evaluation of the  $\delta$ -kick time variation shows a complete oscillation in the radial and a half oscillation in the axial dimension (Fig. 5.10 a)). Additionally, an

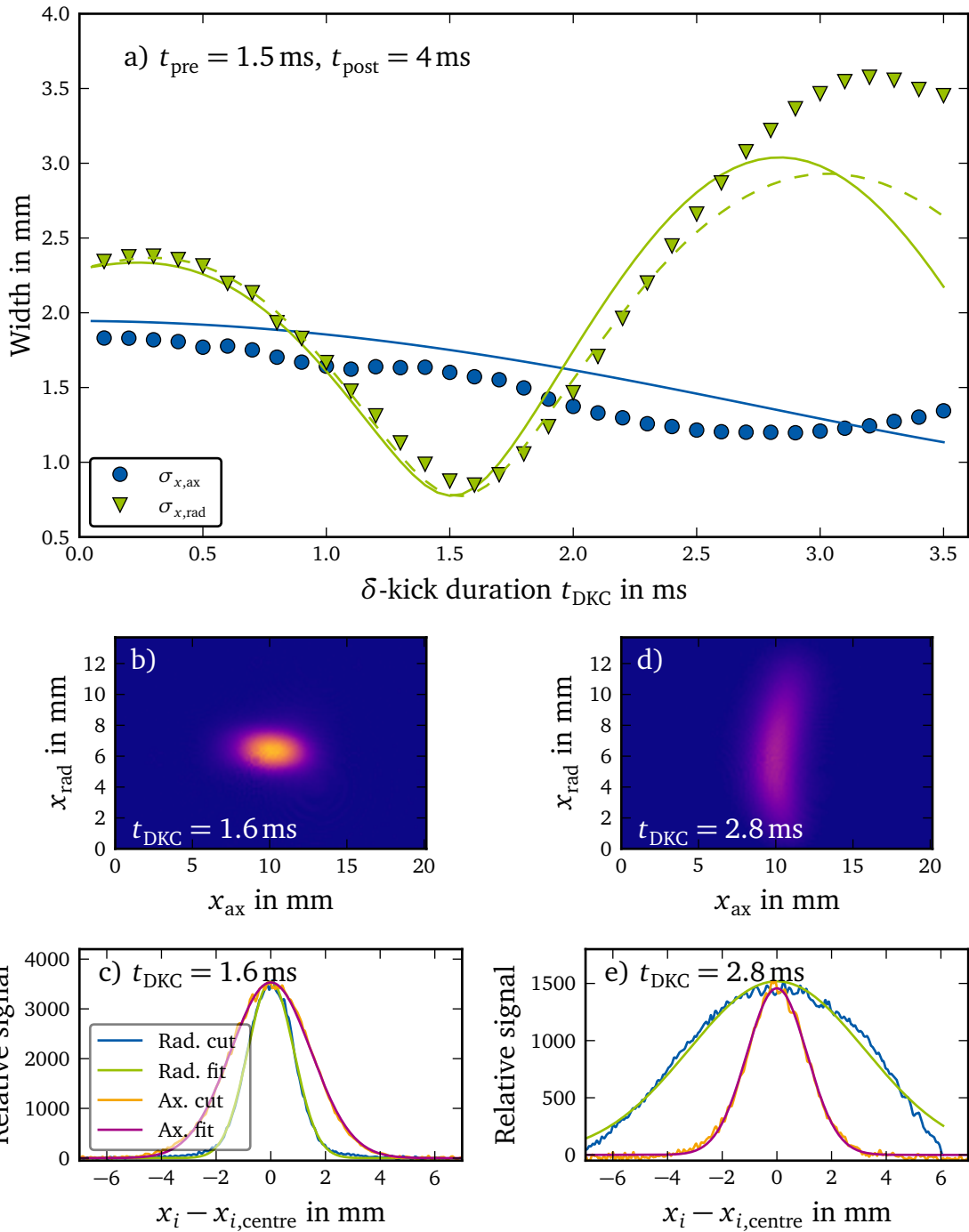


**Figure 5.10:** a) Axial and radial width of the atom cloud for varying  $\delta$ -kick duration. The times  $t_{pre} = 1.5$  ms and  $t_{post} = 4$  ms are constant. The solid green line uses the exponential decaying radial frequency with the time constant  $\tau = 1.26$  ms from the previous measurement, while the dashed curve is the result of a exponential fit to this measurement. b) and d) Shape of the cloud after a  $\delta$ -kick length of  $t_{DKC} = 1.6$  ms and 2.8 ms. c) and e) Cross sections through the centre of the cloud in  $i = \text{axial/radial}$  direction of the absorption images in b) and d).

increase of the oscillation amplitude in radial direction, similar to the predicted increase of the temperature oscillation (Fig. 5.9 c)), can be seen. The measured widths can be compared with the calculated dynamics of the widths  $\sigma_{x,\text{ax/rad}}(t_{\text{pre}}, t_{\text{DKC}}, t_{\text{post}})$  from equation (5.44). The previous results for the  $\delta$ -kick potential frequencies  $\omega_{\text{DKC,ax/rad}}$  (Fig. 5.9 a)) are used for this: The frequency in axial direction is constant  $\omega_{\text{DKC,ax}} = 2\pi \times 52 \text{ Hz}$  with time, whereas it exponentially converges in radial direction. For the initial temperatures, which are needed for the calculation, the values of the previous experiment of this section are used. The calculated width in axial direction has a lower oscillation frequency than the measured one and it overestimates the width up to a  $\delta$ -kick duration of 3.1 ms (solid blue line in Fig. 5.10 a)). In contrast, the width in radial direction matches the measured data up to a  $\delta$ -kick duration of around 1.5 ms (see solid green line in Fig. 5.10 a)). With a new fit of the exponential time constant and asymptotic  $\delta$ -kick frequency of the duration depending  $\delta$ -kick potential frequency, the experimental data in radial direction can be reproduced better. The fit yields  $\tau = 1.02(18) \text{ ms}$  which is 20% smaller time constant than from the previous evaluation for equation (5.50) and an asymptotic frequency of  $2\pi \times 137(7) \text{ Hz}$  instead of  $\omega_{\text{rad}} = 2\pi \times 160.6 \text{ Hz}$ . The position of the minimum and maximum width can be reproduced better (dashed green line in Fig. 5.10 a)). The amplitude of the maximum at 3 ms is in this case also underestimated, but the increase of the oscillation amplitude of the width occurs in both calculations of the radial width. The increase is a result of the exponential time-dependence of the  $\delta$ -kick potential frequency  $\omega_{\text{DKC,rad}}$ .

The measurement confirms the extrapolated oscillatory behaviour of the cloud for an increasing  $\delta$ -kick duration. Similar to the calculated temperature oscillation shown in figure 5.9 c) an increasing oscillation amplitude of the width can be seen in this evaluation. The larger deviations between the measurements and the calculation compared to the previous temperature evaluation are mainly the result of the missing absorption image series for the primary and the secondary expansions. This leads to large uncertainties of the temperatures before and after the  $\delta$ -kick.

---

#### 5.5.4 Cloud Dynamic during $\delta$ -Kick Cooling

---

In the previous sections, the dynamics of the atom cloud were analysed using absorption time-of-flight images. In this section, a detection scheme utilizing the two-body collision rate will be discussed. Regarding only a single measurement, the dynamics can be recorded continuously. The drawback of the method is, that the axial and the radial dimension can no longer be analysed separately.

The collision rate can be measured with a micro-channel plate (MCP) and a discriminator electronics, which detects time-resolved single ions. Each two-body collision leads to the production of a  $\text{Ne}^+$ -ion or a  $2\text{Ne}^+$ -dimer due to Penning or associative ionization. A high electric field accelerates the ions toward the MCP. To obtain a continuous signal-rate from those single events, a histogram with a bin width of  $10 \mu\text{s}$  is calculated. The ion rate of two-body collisions is proportional to  $R_{\text{I}} \propto N^2/V_{\text{eff}}(t)$ .

Thus, it is anti-proportional to the effective cloud volume  $V_{\text{eff}}(t)$ , which can be calculated from the cloud widths in axial  $\sigma_{x,\text{ax}}$  and radial  $\sigma_{x,\text{rad}}$  direction using

$$V_{\text{eff}}(t) = (4\pi)^{3/2} \sigma_{x,\text{ax}}(t) \sigma_{x,\text{rad}}^2(t). \quad (5.52)$$

The time depending widths  $\sigma_{x,\text{ax/rad}}(t_{\text{pre}}, t_{\text{DKC}}, t_{\text{post}})$  can be calculated with equation (5.44) and the initial cloud parameters. The latter are estimated using the values from the measurement shown in figure 5.9 in the previous section. This can safely be done, because the setup was not significantly altered, between the experiments.

The signal seen from one-body collisions, for example with background gases, is typically two orders of magnitude weaker than the two-body collisions of the cloud in the trap before the release. Therefore, they will be neglected here. A more detailed discussion of the measurement of inelastic collisions can be found in section 6.1 and [87].

The result of the measurement is shown in figure 5.11 a). The  $\text{Ne}^*$  cloud is released from the trap at  $t = 0$ . Before the release, a constant ion signal from the two-body collisions in the trap can be seen. The release from the trap with a soft switch-off procedure discussed earlier is indicated by two strong pulse signals at  $t = 0$  and  $0.3$  ms which are electronic noise due to switching of the trap current. During this period the ion signal can therefore not be measured. Then, the cloud freely expands for  $1.5$  ms until the trap potential ( $= \delta$ -kick potential) is switched on again at  $t = 1.5$  ms. Again the switching pulse can be clearly seen. Because of the free expansion the cloud density and consequently the ion signal decrease. The re-trapped cloud at  $t = 1.5$  ms expands further for about  $1.5$  ms until the minimum density and collision rate is reached at the reversal point and the density increases again. The oscillation process is a superposition of the axial and the radial density oscillation. Therefore, the ion rate shows a complex oscillatory behaviour with no obvious period. The signal shape also indicates the presence of damping. This brings the cloud back to equilibrium.

The oscillation can be described by a fit to the inverse effective volume  $V_{\text{eff}}(t)^{-1}$ . It is proportional to the ion signal and can therefore be used as the basis for the fit function. The fit function also includes an additional damping term. From the results of the previous sections especially the asymptotic increase of the radial trap frequency  $\omega_{\text{DKC, Rad}}(t_{\text{DKC}})$  with the  $\delta$ -kick duration must be considered. The axial trap frequency is assumed to be constant. Using the width  $\sigma_{x,\text{ax/rad}}(t_{\text{pre}} = 1.5 \text{ ms}, t_{\text{DKC}}, t_{\text{post}} = 0 \text{ ms})$  from calculated equation (5.44), this leads to the time dependent width in one dimension

$$\begin{aligned} \sigma_{x,\text{ax/rad}}(t_{\text{DKC}}) = & e^{-t_{\text{DKC}}/\tau} \sigma_{x,\text{ax/rad}}(t_{\text{pre}} = 1.5 \text{ ms}, t_{\text{DKC}}, t_{\text{post}} = 0 \text{ ms}) \\ & + (1 - e^{-t_{\text{DKC}}/\tau}) \sigma_{x,\text{offset,ax/rad}}, \end{aligned} \quad (5.53)$$

with the asymptotic width for long  $\delta$ -kick times  $\sigma_{x,\text{offset}}$ , the trapping time  $t_{\text{DKC}}$  and the damping constant  $\tau$ . The potential frequency  $\omega$  is not explicitly indicated but is

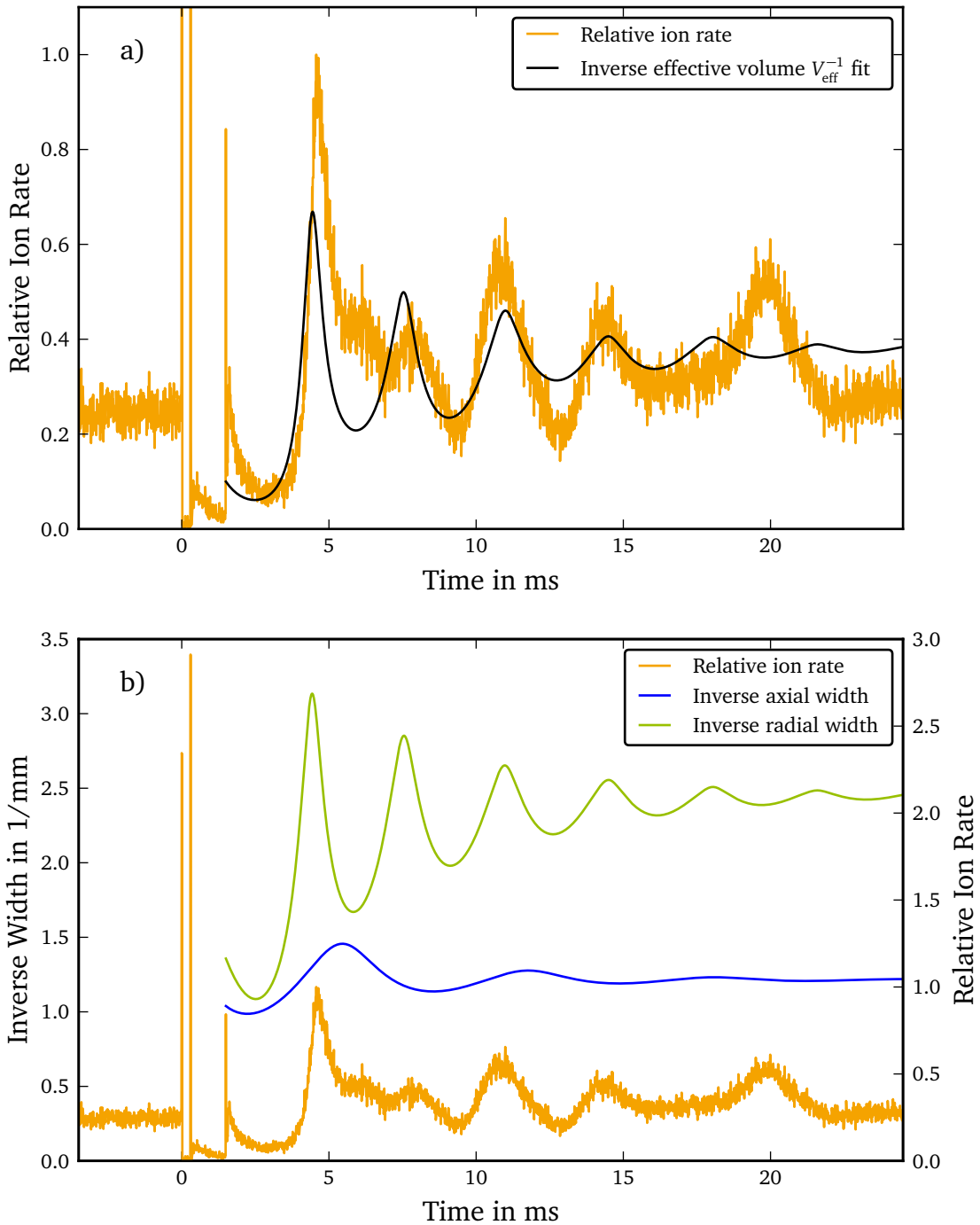


**Figure 5.11:** Relative ion signal of the atom cloud. The cloud is released at  $t = -1.5$  ms from the trap and recaptured at  $t = 0$  ms. a) Relative ion signal and fit. The fit function is the scaled inverse volume of the atom cloud. b) Fit of the inverse axial and radial width of the atom cloud. The cloud volume is calculated from these widths. The ion signal is shown again for better comparison.

contained in  $\sigma_{x,\text{ax}/\text{rad}}(1.5 \text{ ms}, t_{\text{DKC}}, 0 \text{ ms})$ . This is important, since the frequency in radial direction  $\omega_{\text{DKC},\text{rad}}(t_{\text{DKC}})$  is time dependent with the decay time  $\tau = 1.26 \text{ ms}$  (Eq. (5.50)). For the fit, the asymptotic radial trap frequency  $\omega_{\text{DKC},\text{offset},\text{rad}}$  in  $\sigma_{x,\text{offset},\text{rad}}$  is a free fit parameter. The axial frequency  $\omega_{\text{DKC},\text{ax}} = 2 \times 80 \text{ Hz}$  is constant during the  $\delta$ -kick cooling and therefore not free. The damping constant  $\tau$  is also a free parameter and assumed to be equal in both axial and radial direction. Together with a scaling factor  $\alpha$  to match the inverse volume to the ion signal the fit function (based on Eq. (5.52)) then consists of three fit parameters: the damping constant  $\tau$ , the asymptotic radial trap frequency  $\omega_{\text{DKC},\text{offset},\text{rad}}$ , and the scaling factor  $\alpha$ .

The asymptotic radial trap frequency obtained by the fit is with  $\omega_{\text{DKC},\text{rad},\text{offset}} = 2\pi \times 140.9(2) \text{ Hz}$  12% smaller. The damping constant was found to be  $\tau = 5.2(1) \text{ ms}$ . A plot with these results is shown figure 5.11 a). The oscillations are described very well and only the position of the first maximum is slightly shifted with the plateau at  $t = 6 \text{ ms}$  in the ion signal not being reproduced in the simulation. Also the maximum at  $t = 20 \text{ ms}$  is not reproduced. Figure 5.11 b) shows the corresponding inverse cloud-widths of the fit in both directions. Here, the reason for the large first maximum compared to the rest can be seen: Both, axial and radial, density at this point are almost in phase. The same applies for the minima at  $t = 3 \text{ ms}$  and  $t = 13 \text{ ms}$ . Overall is the influence in radial direction stronger because of the squared dependency in the volume  $V_{\text{eff}}(t)$  (Eq. (5.52)).

There are several explanations for the deviations of the fit results. An option to reproduce the first extrema would be a temporal offset. A fit function with a temporal offset can reproduce the positions of the extrema more accurately, but the resulting delay in radial direction of more than half a millisecond was not indicated by the previous results in section 5.5.3. The only measurement that also showed deviations in the oscillation amplitude was in section 5.5.3 with variable  $\delta$ -kick durations  $t_{\text{DKC}}$  (shown in Fig. 5.9) with kick length longer than 2 ms. A possible reason for both the deviations in section 5.5.3 and the position shifts in the ion signal could be the shape of the trap potential, which changes from a harmonic into a linear form for larger distances from the centre. The harmonic region causes a linear force ( $U(x) \propto x^2$  and  $F \propto \partial U(x)/\partial x \propto 2x$ ) towards the centre, while the linear region causes a constant force ( $U(x) \propto x$  and  $F \propto \text{const.}$ ). Atoms with higher energies are longer in the linear region. This results in a lower oscillation period, which leads to a broadening of the potential frequencies. Another explanation could be an oscillation of the centre of mass of the atom cloud. A displacement of the cloud from the trap centre, for example due to a momentum kick during the switch-off and switch-on sequence of the trap, could lead to such an oscillation. This would lead to an additional oscillation in the ion signal.

Given these uncertainties, the applied fit model does not make further assumption. The only new assumption compared to the previous measurements for the  $\delta$ -kick cooling is the damping of the cloud dynamics. A more detailed understanding would

---

also require longer absorption image series after  $\delta$ -kick times of up to several tens of milliseconds.

---

## 5.6 Conclusion

---

This chapter discussed the dynamics of a cold atom cloud, released from a harmonic trap.  $\delta$ -kick cooling was introduced and described with the classical density distribution formalism in details. This technique allows for the full control of the velocity distribution, which can be expressed in units of the temperature. A temperature reduction of almost two orders could be shown using  $\delta$ -kick cooling. Temperatures of  $16\ \mu\text{K}$  in axial and  $7.5\ \mu\text{K}$  in radial direction could be reached. This is far below the Doppler limit of  $200\ \mu\text{K}$  and almost comparable of the recoil limit of  $2.3\ \mu\text{K}$ . This allows for a significant increase in measurement time for the investigation of the collisional properties of metastable neon. A temperature increase of 60 %, to  $644\ \mu\text{K}$ , using the  $\delta$ -kick method could also be realized in axial direction, while the temperature in radial direction was more than 6 times smaller. In principle, temperatures above one millikelvin are accessible. These region is of interest, as collisions with higher angular momentum occur, which influences the inelastic two-body collision rate.

The ion rate measurement of the recaptured cloud in the magnetic trap revealed an additional option for the temperature measurement of the collision properties of spin polarized atoms, complementing the technique presented in chapter 7.

---

## 6 Magnetic Field Dependence of Ionizing Collisions of Ne\*

The collision properties of metastable neon can be influenced by external fields. For example Glover et al. [113] demonstrated an increase of a factor of four in the ionization rate by using a red detuned control laser driving the cooling transition  $^3P_2$  to  $^3D_3$ , and a factor of five decrease for blue-detuned laser light. Several calculations were made for metastable earth-alkaline atoms by Derevianko et al. and Kokkoouline et al. [114, 115], which predict an influence on the elastic and inelastic collision properties due to magnetic fields in the region of several 100 G. Measurements with metastable calcium by Hansen et al. [116] indicated higher inelastic collision cross sections than theoretical predicted at fields of a few Gauss. Griesmaier et al. generated a quantum degenerated chromium gas by applying a magnetic field. This lead for chromium atoms prepared in the lowest Zeeman sub-level to a suppression of two-body losses which prevented an efficient cooling [25]. Therefore, the energy splitting of the Zeeman sublevels had to overcome the kinetic energy of the collisions.

W. J. van Drunen [117] measured the two-body loss rate for  $^{22}\text{Ne}$  in magnetic fields between 2 and 47 G in a magnetic trap. He found a minimum for the two-body loss rate between 15 and 45 G. The maximum achievable field strength was limited by the magnetic trap.

Higher field strengths are obtained in this work with free expanding Ne\* atoms in an offset field using the Helmholtz coils of the magnetic trap. This allows for a measurement of the two-body loss rate up to field strengths of 122.5 G. A comparison of both stretched spin states  $m_J = +2$  and  $m_J = -2$  is of interest, since the high fields lead to larger energy splitting ( $\Delta E = g_J \mu_B B = h \times 250 \text{ MHz}$ ) than the thermal collision energy ( $E \approx k_B \times 400 \mu\text{K} = h \times 8 \text{ MHz}$ ).

---

### 6.1 Measurement Evaluation

---

To measure the ionization properties of Ne\*, a freely expanding atom cloud was used. After loading the Ne\* atoms from the magneto-optical trap into the magnetic trap and laser cooling, the trap is switched-off and the atoms can expand freely. In the intermediate step of the magnetic trap, only for atoms in  $m_J \geq +1$  an attractive trap potential is formed. Thus, most atoms that remain are spin polarized in  $m_J = +2$ . A small offset field of  $B = 0.35 \text{ G}$ , which is generated by a current of 0.2 A through the Helmholtz coils, preserves this polarization. The atoms have a typical mean temperature of  $\bar{T} = (2T_{\text{rad}} + T_{\text{ax}})/3 = 350 \mu\text{K}$  with  $T_{\text{rad}} = 400 \mu\text{K}$  and  $T_{\text{ax}} = 250 \mu\text{K}$  after they are released, as explained in section 5.5.1.

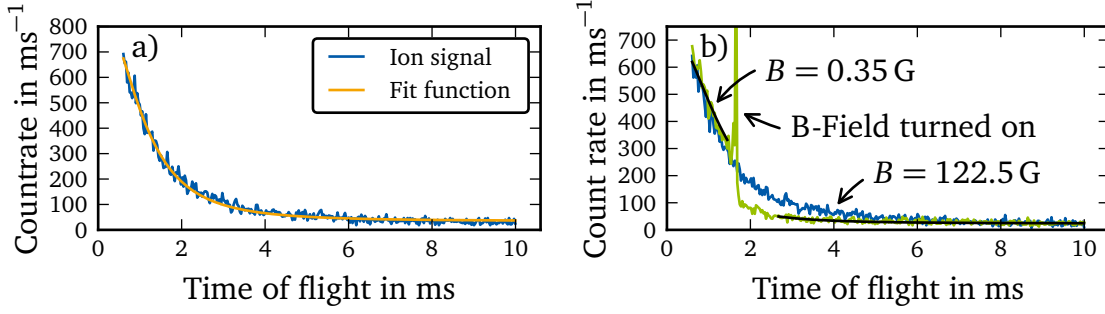


**Figure 6.1:** a) Ion signal of the  $\text{Ne}^*$  cloud after release from the magnetic trap. Due to the expansion the count rate decays to a constant level after 7 ms, which is induced by collisions with the residual gas. b) Same as a), but with applied magnetic field at  $t = 1.5$  ms. The magnetic field takes 1.7 to 2.6 ms until it reaches a stable point at full strength. This can be seen in the count rate. The black lines correspond to fits before and after the magnetic fields were applied.

The ionization rate  $R_I(t)$  depends both on the single atom collisions with residual gas and two-body collisions, which can lead to Penning or associative ionization. The first effect only depends on the atom number  $N$  and is described by the rate  $\alpha N$ , while the second depends on the atom density  $n(\vec{r}, t)$  and scales with the two-body loss parameter  $\beta$ . As the total number  $N$  doesn't change much during the measurement time, it can be assumed to be constant. This leads to the ionization rate

$$R_I(t) = \alpha N + \frac{1}{2}\beta \int d^3r n^2(\vec{r}, t) = \alpha N + \frac{1}{2}\beta \frac{N^2}{V_{\text{eff}}(t)}, \quad (6.1)$$

with the effective volume  $V_{\text{eff}}$ . The two-body losses are scaled by 1/2 because only one ion is generated by a collision, while two atoms are lost. For the expansion of the effective volume  $V_{\text{eff}}(t)$ , a Gaussian position and momentum distribution in the magnetic trap are assumed, as discussed in chapter 5 and in [87]. This leads to

$$V_{\text{eff}}(t) = (4\pi)^{3/2} \sigma_{x,\text{ax}}(t) \sigma_{x,\text{rad}}^2(t), \quad (6.2)$$

and

$$\sigma_{x,\text{ax/rad}}^2(t) = \sigma_{x,0,\text{ax/rad}}^2 + \frac{k_B T_{0,\text{ax/rad}}}{m} t^2, \quad (6.3)$$

with the initial cloud width  $\sigma_{x,0,\text{ax/rad}} = \sigma_{x,\text{ax/rad}}(t = 0)$  and temperature  $T_{0,\text{ax/rad}}$  in axial and radial direction at time  $t = 0$ .

The ion rate is measured with a micro-channel plate (MCP). For the detection, a negative high voltage is applied to the MCP aperture while the trap coils are set to a small positive voltage (Ch. 7 in [87]). The detected signal rate must be corrected by

the overall detection efficiency  $\epsilon$ . All further evaluations are based on the detected signal rate  $R(t) = \epsilon R_I(t)$ .

The MCP detection system supplies a timestamp for every ion event. From these timestamps, a histogram is calculated to obtain the signal rate  $R(t)$  (Fig. 6.1 a)). The histogram is typically generated from 20 measurement cycles with a bin width of  $30 \mu\text{s}$ . The ion rate  $R(t)$  is fitted with the signal rate of background gas collisions  $\epsilon\alpha$  and two-body collisions  $\epsilon\beta$  as fit parameter, while the initial temperatures  $T_{0,\text{ax}}$  and  $T_{0,\text{rad}}$  and the cloud widths  $\sigma_{x,0,\text{ax}}$  and  $\sigma_{x,0,\text{rad}}$  are obtained from fits of the cloud expansion  $\sigma_{x,\text{ax/rad}}(t)$  from equation (6.3) using the absorption images of the free expansion of the cloud.

A direct measurement of the absolute two-body collision rate  $\beta$  cannot be realized due to the large uncertainty in the detection efficiency  $\epsilon$ , which is typically under 50% and strongly depending on the applied fields of the Ioffe-Pritchard bars and the dipole coils as shown in [101]. Therefore, the magnetic field dependency of the two-body collision rate is determined by comparing the rate  $\epsilon\beta_{\text{mag}}$  for a certain strong field with the rate  $\epsilon\beta_{\text{ref}}$  using a low offset field of 0.35 G (Fig. 6.1 b)). The field was switched at  $t = 1.5 \text{ ms}$ . This yields the collision factor  $\epsilon\beta_{\text{mag}}/\epsilon\beta_{\text{ref}}$ , which allows for the elimination of the unknown efficiency  $\epsilon$  and the calculation of absolute collision rates by using the known rates  $\beta_{\text{ref}} = \beta_{+2,+2}$  for spin polarized  $^{20}\text{Ne}$  and  $^{22}\text{Ne}$  from [33]. The histograms always show a strong peak at 1.7 ms, an electronic artefact. The switching of the high current induces electronic interferences in the detection electronics, which are interpreted as a signal. As a side-effect, it can be used as a marker, since it occurs always at the same moment. The magnetic field takes up to 1 ms after switching-on to reach the target value. During this time, the ion signal cannot be used for the evaluation. Therefore, the fits of the ion signal uses the time interval from 0.6 to 1.45 ms and from 2.65 to 10 ms to determine the two collision rates  $\epsilon\beta_{\text{ref}}$  and  $\epsilon\beta_{\text{mag}}$  respectively.

The Helmholtz coils of the magnetic trap are used to generate the homogeneous magnetic field for these measurements. The IsAmp is used for the weak magnetic offset field of about 0.4 G. For the strong field, a SM45-70 D power supply by DELTA ELEKTRONIKA is used, which can supply up to 70 A. The current can be controlled with a current switch which consists of two MOSFETs and a bypass resistor (Fig. 4.3). The first MOSFET is a change-over switch between the Helmholtz coils and the high-power resistor, which is matched to the series resistance of the coils. This allows for a fast magnetic field switch (on and off) within a millisecond without any load change on the power supply. Without this method, the power supply would take several 10 to 100 ms to establish a stable operation for each current change. The second MOSFET is in series with the power supply and disconnects it from the rest of the electric circuit. It switches-off the current in-between the measurements. For a measurement, it is closed several hundred milliseconds before the atom cloud is released from the trap to establish a stable current operation. The current  $I$  through the Helmholtz coils generates a magnetic field  $B_0(I) = I \times 1.75 \text{ G/A}$  [117], resulting in a maximum of 122.5 G for a current of 70 A.

## 6.2 Ionizing Collisions for spin polarized Ne\* in $^3P_2, m_J = +2$

Using the setup discussed in the last section the following procedure can be used to measure the magnetic field dependence of ionizing collisions of spin polarized Ne\*. The atom cloud is spin polarized in  $m_J = +2$  after releasing it from the magnetic trap. The offset field applied initially keeps them in this Zeeman state. The strong field applied after 1.5 ms points into the same direction, thus doesn't change the state of the atoms. This allows for a comparison of the two-body collision rates for high fields up to 122.5 G with the known ones at low field strength. These are  $\beta_{+2,+2} = 6.5(18) \times 10^{-12} \text{ cm}^3/\text{s}$  for  $^{20}\text{Ne}$  and  $\beta_{+2,+2} = 1.2(3) \times 10^{-11} \text{ cm}^3/\text{s}$  for  $^{22}\text{Ne}$  and have been measured at a field of 25 G [33].

The evaluation is based on two measurement series for each isotope (Fig. 6.2 b), c), d), and e)). The magnetic field strengths 0.35 G, 3.5 G, 17.5 G, 70 G, and 122.5 G were measured in both series, while the rest were only recorded in one of them. The signal rate for different magnetic field strengths for  $^{20}\text{Ne}$  and  $^{22}\text{Ne}$  varies in all measurement series for  $t < 1.5 \text{ ms}$ . This demonstrates the importance to compare the two-body collision rates before  $\epsilon\beta_{\text{ref}}$  and after  $\epsilon\beta_{\text{mag}}$  applying the strong field. Additional for  $^{22}\text{Ne}$ , a clear drop in the count rate can be seen for high magnetic fields, whereas  $^{20}\text{Ne}$  is unaffected except for the measurements at 70 G and 122.5 G. In these histograms, an increase can be noticed. The two-body collision rates are obtained from fits of equation (6.1). Mean values are calculated from the rates for magnetic fields which were recorded in both measurement series by using

$$\overline{(\beta_{\text{mag}}/\beta_{\text{ref}})} = ((\beta_{\text{mag},1}/\beta_{\text{ref},1}) + (\beta_{\text{mag},2}/\beta_{\text{ref},2}))/2$$

where  $i$  in  $\beta_{\text{mag}/\text{ref},i}$  denotes measurements from the same series. The two series are also used to determine the measurement uncertainty  $\Delta(\overline{\beta_{\text{mag}}/\beta_{\text{ref}}})$ . Therefore, the mean of the differences is calculated by

$$\Delta(\overline{\beta_{\text{mag}}/\beta_{\text{ref}}}) = \sum_n \frac{(\beta_{\text{mag},1}/\beta_{\text{ref},1}) - (\beta_{\text{mag},2}/\beta_{\text{ref},2})}{n}$$

over all  $n = 5$  double-measured ratios. The evaluation yields a mean uncertainty of  $\Delta(\overline{\beta_{\text{mag}}/\beta_{\text{ref}}}) = 0.71$  for  $^{20}\text{Ne}$  and  $\Delta(\overline{\beta_{\text{mag}}/\beta_{\text{ref}}}) = 0.08$  for  $^{22}\text{Ne}$ . This mean uncertainty is used for each ratio. Furthermore, the uncertainties obtained from the fit of the ion signal additionally increases the error bars. They are in a range between 0.04 to 0.10 for  $^{20}\text{Ne}$  and 0.03 to 0.07 for  $^{22}\text{Ne}$ .

The reference measurement without a field change (only offset field of 0.35 G) yields an increase of the two-body loss coefficient of around 25 % for  $^{20}\text{Ne}$  and a decrease of around 2 % for  $^{22}\text{Ne}$  for the first measurement series (Fig. 6.2 c) and d)) and similar results for the other series. These increases are probably caused by a mixing of the Zeeman sublevels due to the preparation. Assuming the magnetic-field

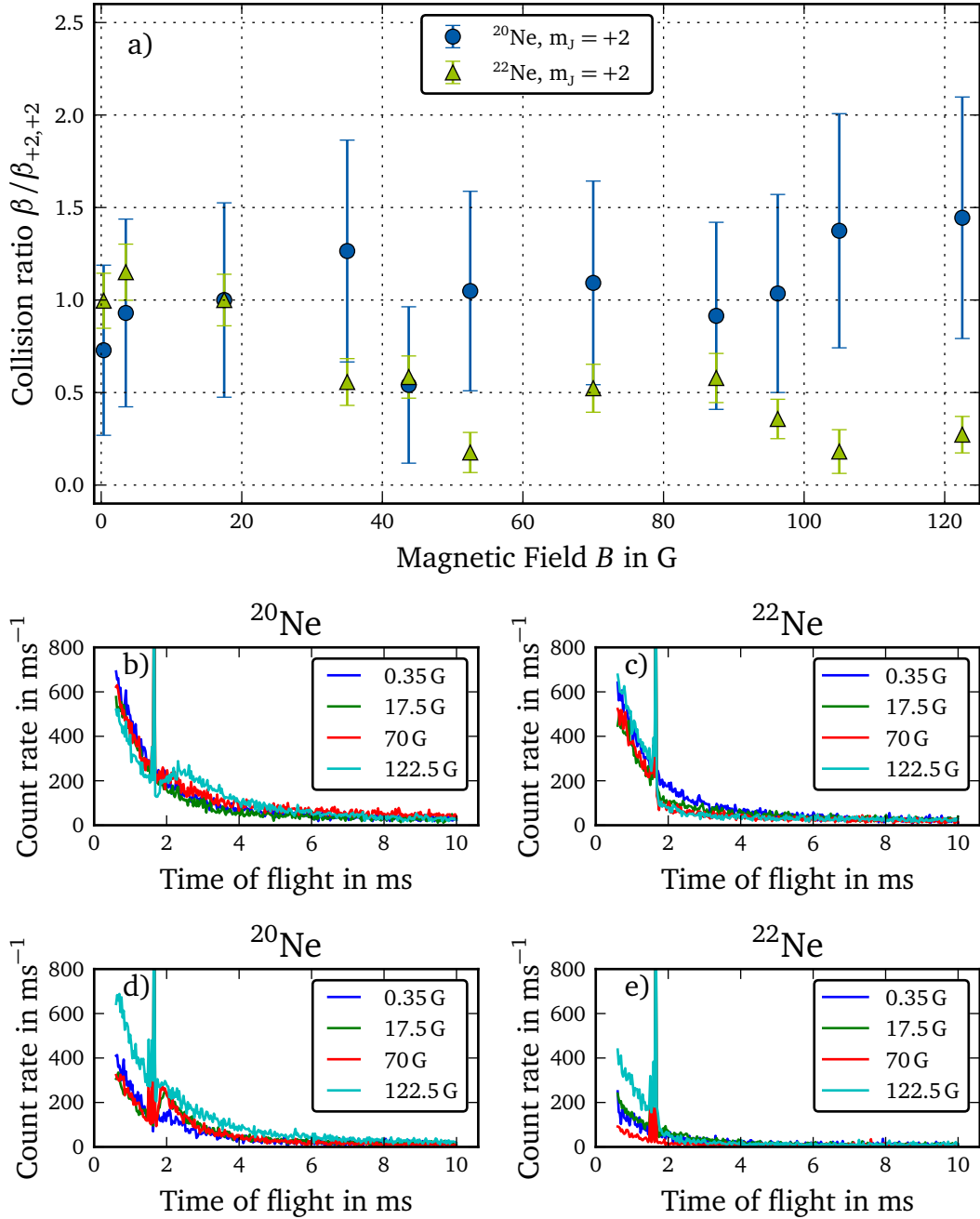


**Figure 6.2:** a) Relative  $\beta$  coefficients for spin polarized  $^{20}\text{Ne}$  and  $^{22}\text{Ne}$  in  $m_J = +2$  for different magnetic field strengths. The coefficients are normalized to the value at the field strength of 17.5 G. b) and c) Ion signal of  $\text{Ne}^{20}$  and  $\text{Ne}^{22}$  before and after the target magnetic field is applied of the first measurement series. d) and e) Ion signal of the second series. For a better overview, only signals of selected magnetic field strengths are shown.

increase only pumps from  $m_J = +2$  to  $+1$ , the population transfer can be calculated using the total collision rate for arbitrary spin mixtures  $\beta$  from equation (7.8) and the coefficients  $\beta_{+2,+1}$  and  $\beta_{+1,+1}$  given in [87]. This yields a population transfer of less than 5% for both isotopes. This collision increase due to mixing is considered by normalizing all measurements by the rate-increase of the measurement with an applied field of 17.5 G:

$$\beta/\beta_{+2,+2} := \overline{(\beta_{\text{mag}}/\beta_{\text{ref}})}_{\text{norm}} = \frac{\overline{(\beta_{\text{mag}}/\beta_{\text{ref}})}}{\overline{(\beta_{\text{mag}}(B = 17.5 \text{ G})/\beta_{\text{ref}}(B = 17.5 \text{ G}))}},$$

with the collision ratio  $\overline{(\beta_{\text{mag}}(B = 17.5 \text{ G})/\beta_{\text{ref}}(B = 17.5 \text{ G}))}$  at 17.5 G. The measurement at  $B = 17.5 \text{ G}$  is chosen since it is close to the field of 25 G for which the absolute two-body collision rate  $\beta_{+2,+2}$  has been measured [33]. Additionally, the 17.5 G is large enough to force the increase due to the mixing of spin states.

The result of the evaluation yields the magnetic field dependence of the two-body collision rate (Fig. 6.2 a) and table 6.1). The two-body coefficient ratio for  $^{22}\text{Ne}$  decreases with increasing magnetic fields. The lowest collision rates of only 18% compared to the rate at 17.5 G are obtained for 52.5 and 105 G. A scattering of the ratios can be seen, but with an overall decreasing trend. In contrast, the two-body collision ratio for  $^{20}\text{Ne}$  stays between 0.54 and 1.44. Due to the large uncertainties, no significant deviation of the collision factor from unity can be seen and the weighted mean of all data points yield 0.97(16).

By comparing the collision ratio of  $^{20}\text{Ne}$  and  $^{22}\text{Ne}$ , the different behaviour is obvious: The magnetic field suppresses the collision rate for  $^{22}\text{Ne}$  and has no influence on the rate for  $^{20}\text{Ne}$  up to around 100 G.

---

### 6.3 Comparison of Ionizing Collisions between spin polarized $\text{Ne}^*$ in $m_J = +2$ and $m_J = -2$

---

This chapter deals with the analysis of spin polarized  $\text{Ne}^*$  in  $m_J = \pm 2$ . The opposite spin-stretched Zeeman sublevel  $m_J = -2$  can be prepared in various ways: One option is to change the orientation of the magnetic field by inverting the current through the Helmholtz coils. A disadvantage of this method is, that the offset field is zero for a small amount of time, when the counter field gets ramped up. During this moment, the polarization state can get lost. Or in case that the residual fields in the radial axes are not completely compensated, the field vector may rotate and flip. If this rotation is slow, the atoms can follow the field vector adiabatically. Another option would be a STIRAP process, as proposed in [87]. In this section, a coherent population transport using Rabi oscillations is used. The magnetic offset field  $B$  leads to a Zeeman splitting of  $\Delta E = g_J \mu_B B$ , with a typical used energy splitting in the range of  $\Delta E = h \times 100 \text{ kHz}$  to  $h \times 1 \text{ MHz}$  in these measurements. Resonant radio frequency (RF) from an antenna perpendicular to the field axis can drive the

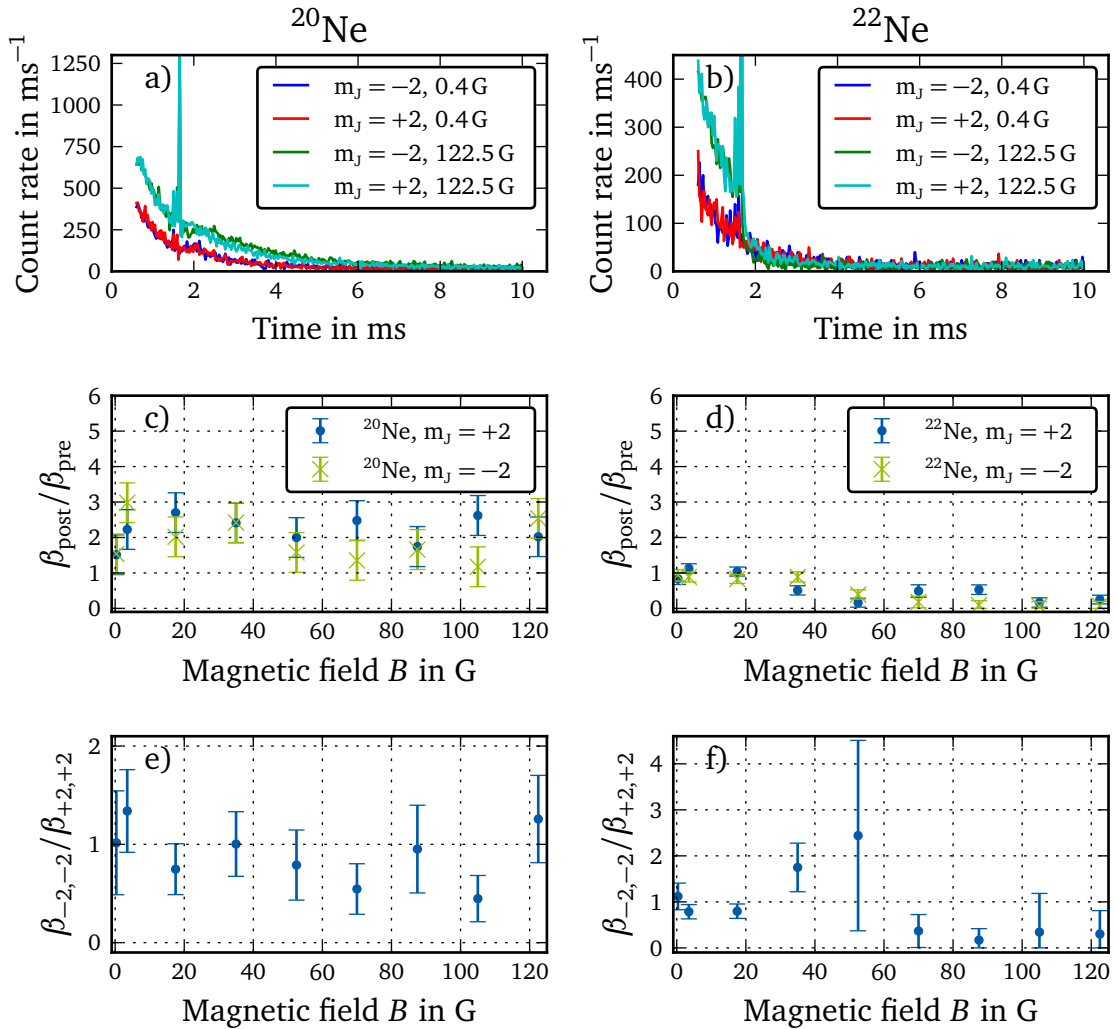


**Figure 6.3:** a) and b) Exemplary ion signals prepared in  $m_J = +2$  and  $m_J = -2$  at different field strength. c) and d) Relative  $\beta$  coefficients for spin polarized  $^{20}\text{Ne}$  and  $^{22}\text{Ne}$  with  $m_J = +2$  and  $m_J = -2$  for different magnetic field strengths. In contrast to the previous evaluation are the coefficients not normalized to the value at a certain B-field. e) and f) Comparison of  $\beta$  coefficients of spin polarized  $^{20}\text{Ne}$  and  $^{22}\text{Ne}$  for  $m_J = +2$  and  $m_J = -2$ .

B-Field in G	relative		absolute	
	$^{20}\text{Ne}$	$^{22}\text{Ne}$	$^{20}\text{Ne}$	$^{22}\text{Ne}$
	$\beta/\beta_{+2,+2}$	$\beta/\beta_{+2,+2}$	$\beta$ in ( $10^{-11}$ cm <sup>3</sup> /s)	$\beta$ in ( $10^{-11}$ cm <sup>3</sup> /s)
0.35	$0.73 \pm 0.46$	$1.00 \pm 0.15$	$0.47 \pm 0.35$	$1.20 \pm 0.35$
3.5	$0.93 \pm 0.51$	$1.15 \pm 0.15$	$0.60 \pm 0.38$	$1.38 \pm 0.35$
17.5	$1.00 \pm 0.53$	$1.00 \pm 0.14$	$0.65 \pm 0.39$	$1.20 \pm 0.34$
35	$1.26 \pm 0.60$	$0.56 \pm 0.13$	$0.82 \pm 0.43$	$0.67 \pm 0.34$
43.75	$0.54 \pm 0.42$	$0.58 \pm 0.11$	$0.35 \pm 0.33$	$0.70 \pm 0.33$
52.5	$1.05 \pm 0.54$	$0.18 \pm 0.11$	$0.68 \pm 0.39$	$0.21 \pm \begin{smallmatrix} +0.33 \\ -0.21 \end{smallmatrix}$
70	$1.09 \pm 0.55$	$0.52 \pm 0.13$	$0.71 \pm 0.40$	$0.63 \pm 0.34$
87.5	$0.91 \pm 0.51$	$0.58 \pm 0.13$	$0.59 \pm 0.37$	$0.69 \pm 0.34$
96.25	$1.04 \pm 0.54$	$0.36 \pm 0.11$	$0.67 \pm 0.39$	$0.43 \pm 0.33$
105	$1.37 \pm 0.63$	$0.18 \pm 0.12$	$0.89 \pm 0.45$	$0.22 \pm \begin{smallmatrix} +0.33 \\ -0.22 \end{smallmatrix}$
122.5	$1.44 \pm 0.65$	$0.27 \pm 0.10$	$0.94 \pm 0.46$	$0.33 \pm 0.32$

**Table 6.1:** Overview of the relative and absolute collision coefficients  $\beta/\beta_{+2,+2}$  for  $^{20}\text{Ne}$  and  $^{22}\text{Ne}$ . The values are normalized to the coefficient at a field strength of 17.5 G.

Rabi oscillations [87]. A  $\pi$ -pulse is used to transfer the complete population from  $m_J = +2$  to  $m_J = -2$ .

A full measurement cycle is like the previous section, with a  $\text{Ne}^*$  cloud being released from the magnetic trap. Additionally, during the 1.5 ms TOF sequence, 10  $\mu\text{s}$  before the magnetic field will be ramped up, the  $\pi$ -pulse is applied. Absorption images from a Stern-Gerlach experiment yield the resonance frequency  $\nu_{\text{Rabi}} = 833(2)$  kHz and a pulse length of  $\tau = 5.7 \mu\text{s}$ . This resonance frequency corresponds to a magnetic field of 0.4 G. An arbitrary waveform generator 33220A by HP was programmed to generate the resonance frequency in a rectangular pulse window. The signal rate was measured for different magnetic field strengths, both with and without the Rabi  $\pi$ -pulse. This allows for a comparison of the two-body loss rate of the the states  $m_J = +2$  and  $m_J = -2$ .

Histograms with a bin width of 30  $\mu\text{s}$  are calculated for evaluation. The signal rate for  $^{20}\text{Ne}$  and no field increase (0.4 G) shows an increase after the preparation of  $t = 1.5$  ms, although the magnetic field was not changed (Fig. 6.3 a)). This is caused by a mixing of the population with other Zeeman sublevels. Since both measurements  $m_J = +2$  and  $m_J = -2$  yield an increase but only the comparison of the collision ratios is of interest, no normalization is needed here. This is in contrast to the previous section. Moreover, the signal rates of both isotopes show a strong variation in the signal amplitudes before the preparation for  $t < 1.5$  ms (Fig. 6.3 a) and b)). This is caused by a decrease of the atom number in the cloud during the measurement.

The fit of the signal rate  $R(t) = \epsilon R_I(t)$  (eqn. (6.1)) yields the two-body loss coefficient before and after the preparation,  $\beta_{\text{ref}}$  and  $\beta_{\text{mag}}$ . The ratio  $\beta_{\text{mag}}/\beta_{\text{ref}}$  for  $^{20}\text{Ne}$  is varying around 2 over the magnetic field range, besides the ratio of 1.5 measured with the offset field of 0.35 G (Fig. 6.3 c)). The missing normalization compared to the previous evaluation yields this high ratio. With the normalization, the ratio is around one as on the last section. Again, only the ratio the two-body collisions between the sublevels  $m_J = +2$  and  $m_J = -2$  is of interest now. The collision ratio  $\beta_{\text{mag}}/\beta_{\text{ref}}$  for  $^{22}\text{Ne}$  and both Zeeman sublevels,  $m_J = +2$  and  $m_J = -2$  decreases with higher fields (Fig. 6.3 d)).

For the uncertainties of the ratios, the results from the last section are used again. These are  $\Delta(\beta_{\text{mag}}/\beta_{\text{ref}}) = 0.43$  for  $^{20}\text{Ne}$  and  $\Delta(\beta_{\text{mag}}/\beta_{\text{ref}}) = 0.14$  for  $^{22}\text{Ne}$ . To these uncertainties, the uncertainties from the fits are added. For  $^{22}\text{Ne}$ , the lower error bars are limited to zero to remove non-physical uncertainties (Fig. 6.3 d)).

The comparison between  $m_J = +2$  and  $-2$  is performed by dividing the relative rates by each other to get the collision factor

$$\beta_{-2,-2}/\beta_{+2,+2} = \frac{\beta_{-2,-2,\text{mag}}/\beta_{+2,+2,\text{ref}}}{\beta_{+2,+2,\text{mag}}/\beta_{+2,+2,\text{ref}}} = \beta_{-2,-2,\text{mag}}/\beta_{+2,+2,\text{mag}}, \quad (6.4)$$

with the coefficient for all population in  $m_J = +2$  before the preparation  $\beta_{+2,+2,\text{ref}}$ , and the rates after the preparation in  $m_J = +2$  and  $-2$ ,  $\beta_{+2,+2,\text{mag}}$  and  $\beta_{-2,-2,\text{mag}}$ .

The collision ratio  $\beta_{-2,-2}/\beta_{+2,+2}$  for  $^{20}\text{Ne}$  is between 0.5 and 1.3 with a mean of 0.9 (Fig. 6.3 e)). By considering the error-bars and the scattering of the values, no change of the two-body collision rate between both sublevels can be concluded. The same applies to  $^{22}\text{Ne}$ . Here, the ratio  $\beta_{-2,-2}/\beta_{+2,+2}$  scatters between 0.2 and 2.4 with a mean of 0.9 (Fig. 6.3 f)).

---

## 6.4 Conclusion

---

The  $\beta$  coefficient for inelastic two-body collisions was measured in a range from 0.35 G to 122.5 G. A different behaviour for  $^{20}\text{Ne}$  and  $^{22}\text{Ne}$  could be observed:  $^{20}\text{Ne}$  shows a constant rate up to 110 G. A slight tendency for an increase for high fields above 100 G can be noticed, but this could also be a statistical anomaly. The collision rate of  $^{22}\text{Ne}$  decreases with stronger magnetic fields. A suppression by a factor of 3 to 5.6 could be observed. The comparison of the collision rate in the Zeeman sublevels  $m_J = -2$  with  $+2$  revealed no difference for  $^{20}\text{Ne}$  and  $^{22}\text{Ne}$ . This is in contrast to the results of the investigations with chromium [25].

The results add a new facet to the investigation of the collisional properties of  $\text{Ne}^*$  and can be used for theoretical calculations. The suppression found with  $^{22}\text{Ne}$  are also a hint how to reach quantum degeneracy. Calculations by W. J. van Drunen [117] indicated, that a 5 to 7-fold suppression would be sufficient. Therefore, measurements with higher fields would be interesting, especially for  $^{22}\text{Ne}$ . Also, a comparison of collision rates of different spin mixtures, as they were performed for

---

low fields by J. Schütz [87], could be useful to verify and complete the magnetic field measurements.

---

## 7 Temperature Dependence of Ionizing Collisions of Ne\*

The temperature dependence of inelastic two-body collisions for Ne\* has been calculated theoretically with different models. Doery et al. [94] used a common coupled-channels calculation [118] of the scattering matrix. They predicted a constant inelastic scattering rate below one millikelvin and a maximum between 1 and 10 mK. J. Schütz simulated the collision interaction of bosonic ( $^{20}\text{Ne}$  and  $^{22}\text{Ne}$ ) and fermionic ( $^{21}\text{Ne}$ ) Neon isotopes by using a quantum barrier model [87]. It showed a similar behaviour like Doery for the bosonic isotopes. More recent calculations were done by C. Cop using coupled-channels [119] simulations based on the results of this neon experiment [33, 86, 87].

For a systematic analysis of the temperature dependence of ionizing collision rates, measurements over a wide temperature range of several orders of magnitude are necessary. With Ne\* atoms in a trap, a lot of effort is necessary to realize this. Especially the preparation of temperatures below  $100\ \mu\text{K}$  must be done with evaporative cooling, which leads to a strong atom loss and thus, to an experimental signal loss. An alternative approach was suggested by Orzel et al. [96] using metastable xenon atoms. The authors measured the collision rate time dependent in a free expanding atom cloud. Due to the increase of phase-space correlations the effective collision temperature drops with the expansion time. This technique will be used in this chapter to measure the collision properties over one order of magnitude variation in temperature.

---

### 7.1 Measurement Evaluation

---

The necessary experimental setup is the same as used in chapter 6: An atom cloud is released from the magnetic trap and expands freely in space. The effective collision temperature decreases, as discussed in section 5.2.1, with the expansion time. The initial temperatures in radial and axial directions of the cloud were obtained from a time-of-flight absorption image series. Instead of fitting the initial temperature and the width of the cloud with equation (6.3), only the temperature is used as a free fit parameter. The required initial widths  $\sigma_{x,0,\text{ax/rad}}^2$  were calculated from the trap frequencies  $\omega_{\text{rad}} = 2\pi \times 160.6\text{ Hz}$  and  $\omega_{\text{ax}} = 2\pi \times 79.2\text{ Hz}$  with

$$\sigma_{x,0,\text{ax/rad}}^2 = \frac{k_{\text{B}} T_{\text{ax/rad}}}{m \omega_{\text{ax/rad}}^2}. \quad (7.1)$$

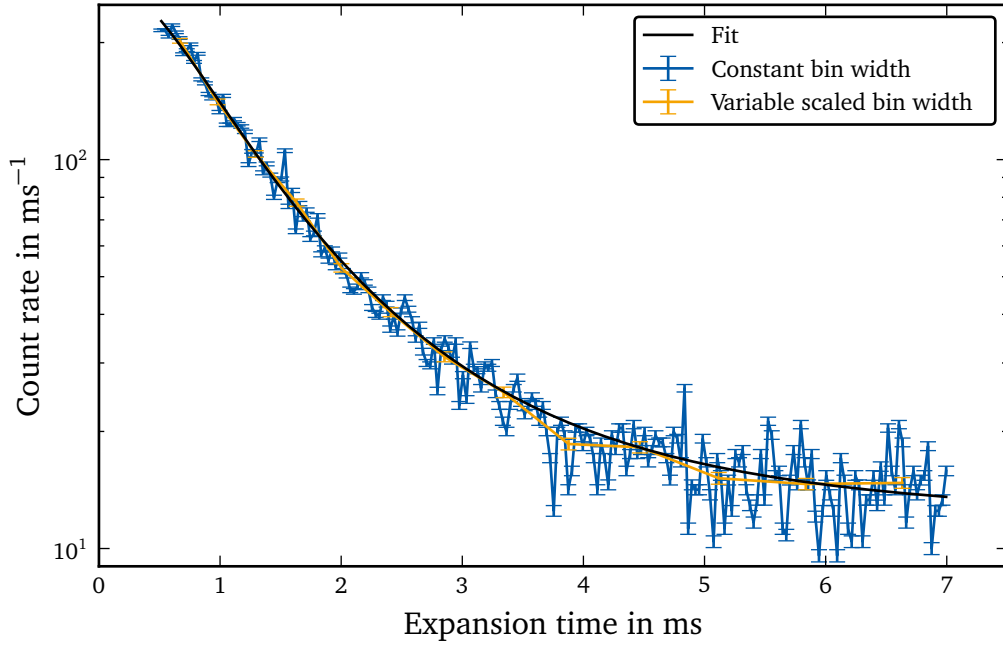


**Figure 7.1:** Logarithmic histogram plot of the ion signal of an atom cloud released from the magnetic trap at time  $t = 0$ . A histogram with a constant bin width of  $30 \mu\text{s}$  is plotted in blue, while a variable scaled one is shown in red. The variable width corresponds to a logarithmically scaled effective temperature. The error bars are calculated assuming Poisson distributed uncertainties, which is the square root of the total counts per bin. The error bars of the constant bin width histogram vary much stronger than the uncertainties of the scaled bins. The fit functions are based on the ion rate equation (6.1) assuming a constant two-body collision rate  $\bar{\beta}$  over the measurement time.

Using this in equation (6.3) yields the squared width

$$\sigma_{x,\text{ax/rad}}^2(t) = \frac{k_B T_{\text{ax/rad}}}{m} \left( \frac{1}{\omega_{\text{ax/rad}}^2} + t^2 \right). \quad (7.2)$$

The trap frequencies can be determined from the magnetic field in the trap, which depend on the current flowing through the trap coils. As this current is regulated by the power supply, the frequencies can be assumed constant for all measurements. Furthermore, the single parameter fit circumvents the issue of determining the initial cloud width  $\sigma_{x,0}$  with high precision. The first images cannot be taken directly after switching off the trap, but only after  $0.5 \text{ ms}$  time-of-flight due to the residual magnetic fields of eddy currents. This leads to an uncertainty of the initial width in the two parameter fit, which also influences the resulting temperature.

The collisions are detected time resolved with the MCP. From this, histograms are calculated (Fig. 7.1). This gives the time-dependent signal rate  $R(t)$ . With the depen-

dence between expansion time and effective temperature  $T_{\text{eff}}(t)$  taken from equation (5.32), the temperature dependent signal rate  $R(T_{\text{eff}})$  can be calculated.

The constant bin width of the standard histograms leads to small temperature windows with time passing, resulting in only a few events per bin. To circumvent this problem a histogram with increasing bin width is used. As the temperature dependence should be evaluated over an order of magnitude, a logarithmic temperature scale is favourable. This requires the inverted function of  $T_{\text{eff}, 1\text{-dim}}(t)$  of equation (5.31), which is given by

$$t(T_{\text{eff}, 1\text{-dim}}) = \sqrt{\frac{T_0 - T_{\text{eff}, 1\text{-dim}} \frac{\sigma_{x,0}}{\sigma_{v,0}}}{T_{\text{eff}, 1\text{-dim}} \frac{\sigma_{x,0}}{\sigma_{v,0}}}} \quad (7.3)$$

$$= \sqrt{\frac{m(T_0 - T_{\text{eff}, 1\text{-dim}})}{k_B T_0 T_{\text{eff}, 1\text{-dim}}} \sigma_{x,0}}. \quad (7.4)$$

This result can only be used for atom clouds with equal properties in all dimensions. For the  $\text{Ne}^*$  cloud in the experiment with different temperatures in axial and radial directions, the inverted function of equation (5.32) must be calculated. This leads to

$$t(T_{\text{eff}}) = \sqrt{\frac{a + \sqrt{4T_{\text{eff}}(T_{0,\text{ax}} + 2T_{0,\text{rad}} - T_{\text{eff}}) \sigma_{x,0,\text{ax}}^2 \sigma_{x,0,\text{rad}}^2 \sigma_{v,0,\text{ax}}^2 \sigma_{v,0,\text{rad}}^2 + a^2}}{2T_{\text{eff}} \sigma_{v,0,\text{ax}}^2 \sigma_{v,0,\text{rad}}^2}}, \quad (7.5)$$

with

$$a = (T_{0,\text{ax}} - T_{\text{eff}}) \sigma_{x,0,\text{ax}}^2 \sigma_{v,0,\text{rad}}^2 + (2T_{0,\text{rad}} - T_{\text{eff}}) \sigma_{x,0,\text{rad}}^2 \sigma_{v,0,\text{ax}}^2. \quad (7.6)$$

The inverted function allows for a calculation of the expansion time for a given effective temperature. It is also used to adjust the bin width of the histograms for a logarithmic scaled temperature range (Fig. 7.1 for a comparison of a histogram with a constant bin width of  $30 \mu\text{s}$  and the one with increasing bin widths). The advantage of the variable bins is the smaller spread of the uncertainties over the expansion time compared to the constant widths. The bin edges are distributed in such a way, that each temperature decade is divided in 10 parts, e. g. 100, 79, 63, ...,  $10 \mu\text{K}$ . This leads to larger bins for longer times, which increases the total counts per bin compared to constant bin widths. Therefore it reduces the statistical uncertainty, which increases the evaluable range towards lower temperatures.

---

## 7.2 Temperature Depending Ionizing Collisions of Spin Polarized Neon

---

The temperature dependence of the two-body collision coefficient  $\beta_{+2,+2}(T_{\text{eff}})$  of spin polarized  $^{20}\text{Ne}$  and  $^{22}\text{Ne}$  is measured with an atom cloud, which is released from the magnetic trap and is expanding with time. A small magnetic offset field of about

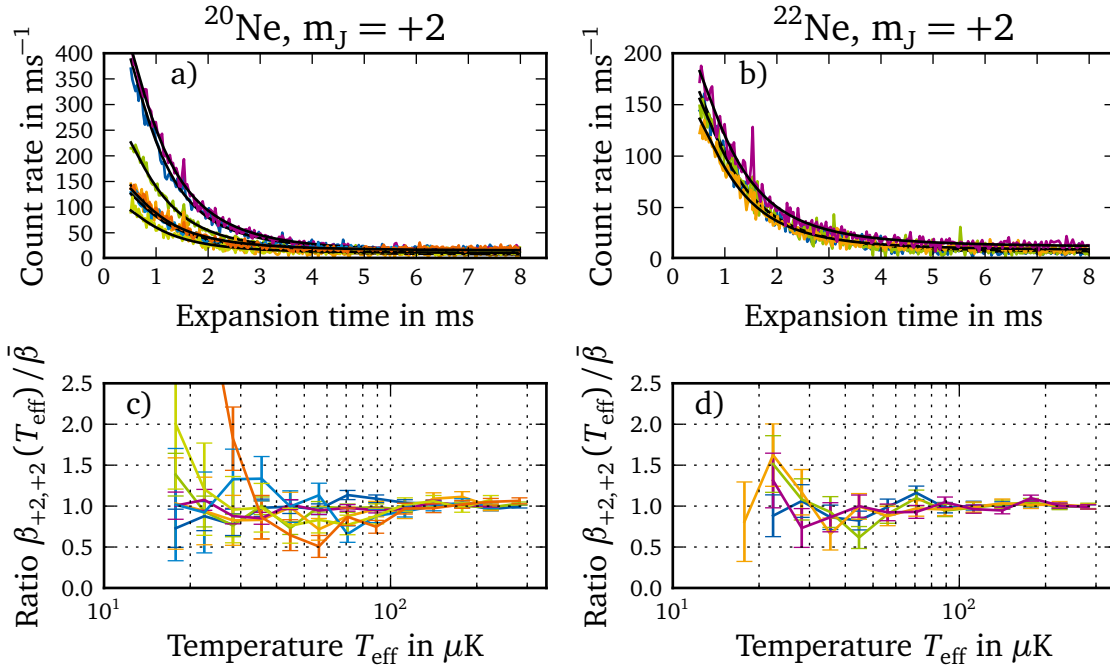


**Figure 7.2:** Temperature dependent two-body collisions. The ion signals and the corresponding fits of free expanding atom clouds of  $^{20}\text{Ne}$  and  $^{22}\text{Ne}$  are shown in a) and b). The fits assume a mean two-body coefficient  $\bar{\beta}$ . c) and d) The relative  $\beta$  coefficients plotted as a function of temperature.

0.4 G, produced by the Helmholtz coils, keeps the  $\text{Ne}^*$  atoms spin polarized in  $m_J = +2$ . Typical parameters of the cloud are a mean temperature of  $\bar{T}_0 = 300 \mu\text{K}$  and an initial width of  $\bar{\sigma}_{x,0} = 500 \mu\text{m}$ . The evaluation uses data from several measurement series to reduce the uncertainty. Some of the measurements were already used in [87] and are re-evaluated in this section.

The measured ion rate  $R_{\text{meas}}(t)$  of the time-of-flight experiment can be fitted with the signal rate  $R_{\text{fit}}(t)$  given by equations (6.1) to (6.3) for the free expansion of an atom cloud (Fig. 7.2 a) and b)). For the fits, the initial temperatures are taken from the absorption image series. The two-body collision parameter  $\bar{\beta}$  in this case is the mean value over the full measurement time, or temperature, respectively. Measurement series from different days are used to reduce the uncertainty and to decrease the influences of day by day variations. The bin width of the linear histogram is  $30 \mu\text{s}$ . Some measurements show a sharp peak at 1.5 ms. It is induced by electronic noise of switching signals. The free expansion functions were fitted in the time range between 0.45 and 8 ms. For shorter times, the ion signal is disturbed by noise from switching-off the trap, while for longer times, the ion rate rises slightly due to collisions of  $\text{Ne}^*$  with the trap coils and the trap mounting structure.

The time-dependent relative collision ratio  $\beta(t)/\bar{\beta}$  (more precise  $\epsilon\beta(t)/\epsilon\bar{\beta}$ ) is calculated by dividing the measured ion signal by the fitted collision coefficient, after

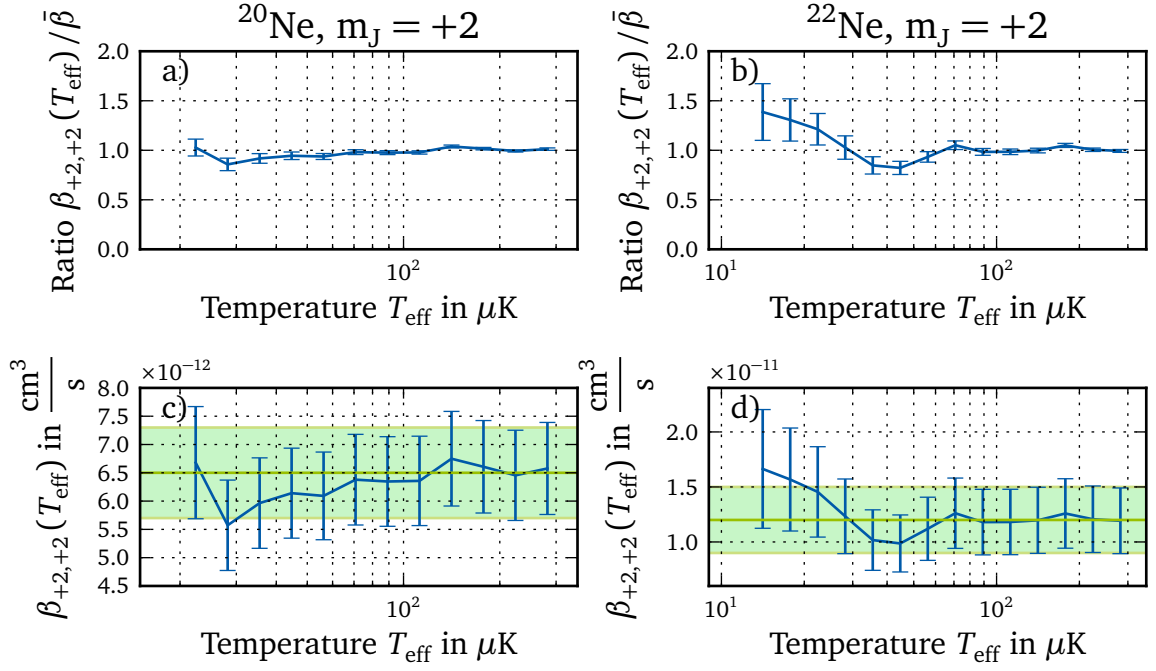


**Figure 7.3:** a) and b) Temperature dependence of the two-body collision coefficient  $\beta_{+2,+2}(T_{\text{eff}})$  for collisions of spin polarized  $^{20}\text{Ne}$  and  $^{22}\text{Ne}$ . The values are relative to the temperature independent coefficient  $\bar{\beta}$ . c) and d) Temperature dependence of the absolute two-body collision coefficient  $\beta_{+2,+2}(T_{\text{eff}})$ . The green horizontal line and band indicate the temperature independent literature values and uncertainties for  $\beta_{+2,+2}$ .

the fitted single neon atom collision coefficient  $\epsilon\alpha_{\text{fit}}$  is subtracted from both. This leads to the temperature-dependent two-body collision ratio

$$\beta(t)/\bar{\beta} = \frac{R_{\text{meas}}(t) - \epsilon\alpha_{\text{fit}}N}{R_{\text{fit}}(t) - \epsilon\alpha_{\text{fit}}N}, \quad (7.7)$$

with the ion signals  $R_{\text{meas/fit}}(t) = \epsilon R_{I,\text{meas/fit}}(t)$ , the detection efficiency  $\epsilon$ , the number  $N$  of atoms in the cloud, and the total ionization rate  $R_{I,\text{meas/fit}}(t)$  of equation (6.1). To obtain the temperature dependent collision ratio  $\beta_{+2,+2}(T_{\text{eff}})/\bar{\beta}$ ,  $T_{\text{eff},1\text{D}}(t)$  from equation (5.31) and  $T_{\text{eff}}(t)$  from (5.32) are used.

The two-body collision ratio is found to be nearly constant  $\beta_{+2,+2}(T_{\text{eff}})/\bar{\beta} = 1$  for both isotopes for temperatures between 30 and 300  $\mu\text{K}$  (Fig. 7.2 c) and d)). The uncertainties increase for lower temperatures, which makes an assertion difficult, but down to 20  $\mu\text{K}$  the error bars still include the value 1 for the relative collision ratio. The reason for the larger uncertainties at lower temperatures is the lower collision rate due to the expanding atom cloud, which results a poorer statistics for the ion signals (Fig. 7.1).

To reduce the relative uncertainty, weighted means are calculated from the different measurements with  $^{20}\text{Ne}$  and  $^{22}\text{Ne}$  (Fig. 7.3 a) and b)). The uncertainties

are much smaller than for the single measurements shown in figures 7.2 c) and d). The absolute temperature dependent two-body collision coefficients  $\beta_{+2,+2}(T_{\text{eff}})$  are derived from the relative ones by multiplying with the absolute values of  $\beta_{+2,+2} = 6.5(18) \times 10^{-12} \text{ cm}^3/\text{s}$  for  $^{20}\text{Ne}$  and  $\beta_{+2,+2} = 1.2(3) \times 10^{-11} \text{ cm}^3/\text{s}$  for  $^{22}\text{Ne}$  (Fig. 7.3 c) and d)). Here, the measurement uncertainties are dominated by the error bars of the absolute values. The uncertainty of the temperature evaluation is negligible especially for temperatures above  $100 \mu\text{K}$ .

---

### 7.3 Temperature Dependent Ionizing Collisions of Neon Spin Mixtures

---

The temperature dependence of inelastic collisions of spin polarized  $\text{Ne}^*$  in the previous section revealed no variation between 30 and  $300 \mu\text{K}$ . To analyze this behaviour for spin mixtures, a part of the measurements by J. Schütz (chapter seven in [87]) is re-evaluated. Therefore, a two level system, in which only the Zeeman sublevels  $m_J = +2$  and  $m_J = +1$  are populated, is used to determine the temperature dependence  $\beta_{+2,+1}(T_{\text{eff}})$  of the collisions between  $m_J = +2$  and  $m_J = +1$  and  $\beta_{+1,+1}(T_{\text{eff}})$  between  $m_J = +1$  and  $m_J = +1$ .

The preparation of this system uses the AC Stark shift and radio frequency (RF) induced Rabi oscillations. A strong circular polarized laser at 622 nm couples the metastable state  $^3\text{P}_2$  with the short lived state  $^3\text{D}_1$ . The excited state can decay into the metastable state  $^3\text{P}_0$  or into the ground state  $^1\text{S}_0$  by emitting a vacuum ultra violet (VUV) photon. The laser beam is aligned with the magnetic field axis and propagates in the opposite direction of the field vector. The left circularly polarized beam drives only  $\sigma^+$  transitions. The frequency is red-detuned by  $\Delta = -2\pi \times 130 \text{ MHz} = 129 \Gamma_{622}$ . This leads to an AC Stark shift for the Zeeman sublevels  $^3\text{P}_2$   $m_J = 0, -1$  and  $-2$ .

The magnetic offset field preserves the spin polarization of the  $\text{Ne}^*$  atoms after the release from the magnetic trap and leads to an energy splitting of the sublevels due to the Zeeman effect. The typical energy splitting is around  $\Delta E = h \times 500 \text{ kHz}$ . Resonant RF drives Rabi oscillations of the population between the Zeeman sublevels. A Rabi pulse with a pulse area of  $\pi$  leads to a population inversion from  $m_J = +2$  to  $-2$  in a 5-level system.

Applying the 622 nm laser during the Rabi preparation reduces the 5-level to a 2-level system. The AC Stark shift increases the energy splitting between  $m_J = +1$  and 0 and the RF is no longer resonant. The population oscillates now between  $m_J = +2$  and  $+1$ , while population in  $m_J = 0$  gets lost due to laser excitation and spontaneous emission. Therefore, a strong enough AC Stark shift is important to suppress non-resonant Rabi oscillation in this state. Measurements by J. Schütz (section 6.3 in [87]) show atom losses of less than 3 % for typical irradiation times of  $100 \mu\text{s}$  due to non-resonant population transfer.

The two-body collision coefficient  $\beta$  for an arbitrary, incoherent mixture can be calculated using

$$\beta = \sum_{m_i=-2}^2 p_{m_i}^2 \beta_{i,i} + \sum_{m_i=-2}^2 \sum_{m_j \neq m_i}^2 p_{m_i} p_{m_j} \beta_{m_i, m_j}, \quad (7.8)$$

with the relative population  $p_{m_i}$  in the sublevel  $m_J = m_i$ . For the 2-level system, this reduces to

$$\beta = p_2^2 \beta_{+2,+2} + p_1^2 \beta_{+1,+1} + 2p_2 p_1 \beta_{+1,+2}. \quad (7.9)$$

The experimental cycle starts with an atom cloud released from the magnetic trap. As described in the previous sections a magnetic field of  $B = 0.38$  G parallel to the axial direction of the trap preserves the spin polarization and provides the Zeeman splitting. 1.5 ms after the release the preparation using the laser and the RF is started. A  $2\pi$  Rabi pulse requires around 11  $\mu$ s. To obtain different spin mixtures a series with varying pulse lengths was recorded (Fig. 7.4 i) and j)). The population distribution was measured with absorption images of a Stern-Gerlach experiment after the preparation. The collision rate was measured with the time-resolved MCP system and the cloud temperature using absorption images of a time-of-flight series.

The ion signals are shown in figures 7.5 a) and b) for  $^{20}\text{Ne}$  and  $^{22}\text{Ne}$  with a constant bin width of 30  $\mu$ s and in c) and d) with a variable bin width. For a better overview, only a selection is plotted. The preparation creates a strong and sharp peak at 1.5 ms, which can be seen in a) and b). It is caused by VUV photons from Neon atoms decaying in the ground state, for which the MCP is also sensitive. The variable bin widths shown in c) and d) are calculated for each measurement separately to get a logarithmic scaled temperature histogram. The temperature decade is divided into ten parts for a sufficient temperature resolution. For the error bars a Poissonian uncertainty with  $\Delta N_i = \sqrt{N_i}$  for the number of events  $N_i$  in each bin  $i$  is assumed. The final error bars are smaller than the Poisson statistics would suggest. The reason is the normalization procedure: Each ion signal measurement was repeated several times to obtain more events. For a better comparison, all histograms are normalized to a single run by dividing through the number of repetitions.

The histograms with the scaled bin width are used for the evaluation. The linear histograms are only plotted to show the structure of the signal with a higher time resolution. The fit of the ion signal  $R_{\text{fit}}(t)$  with equation (6.1) before and after the preparation gives the relative two-body loss rate ratio  $\beta_{\text{eff}}/\beta_{+2,+2}$  with the coefficient after the preparation  $\beta_{\text{eff}}$  and the spin polarized coefficient before the preparation  $\beta_{\text{ref}} = \beta_{+2,+2}$ . Equation (7.7) is modified to obtain the relative time-dependent collision coefficient as

$$\beta_{\text{eff}}(t)/\beta_{+2,+2} = \frac{R_{\text{meas}}(t) - \epsilon \alpha_{\text{fit}} N}{\tilde{R}_{\text{fit}}(t) - \epsilon \alpha_{\text{fit}} N}. \quad (7.10)$$

The background signal  $\epsilon \alpha_{\text{fit}} N$  is obtained from the ion signal fit  $R_{\text{fit}}(t)$ . And the modified fitted ion signal  $\tilde{R}_{\text{fit}}(t)$  is an assumed signal rate without any preparation

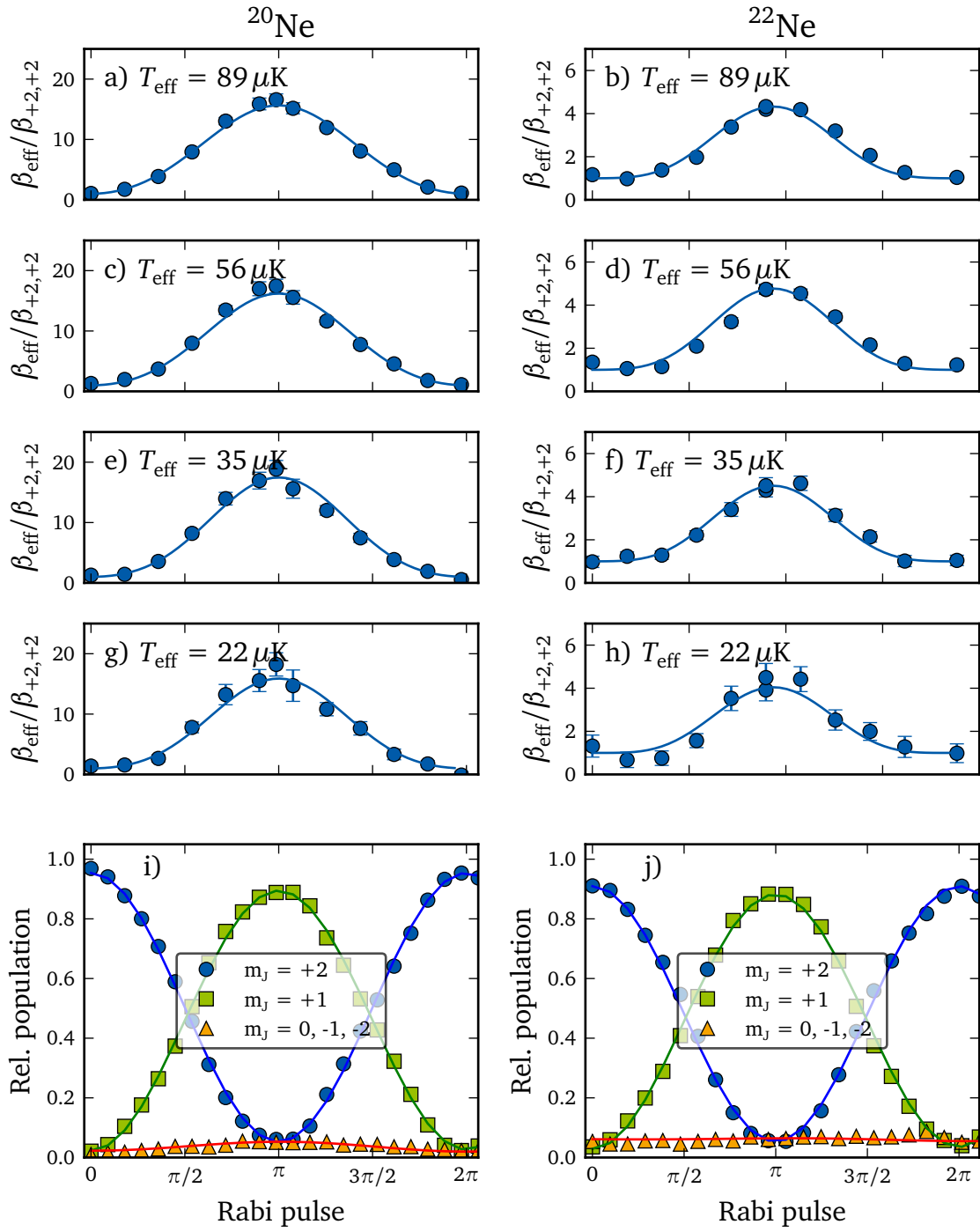


**Figure 7.4:** a) to h) Increase of the two-body collision rate after population transfer with a Rabi pulse for  $^{20}\text{Ne}$  and  $^{22}\text{Ne}$  for different temperatures. i) and j) Population distribution after the Rabi pulse.

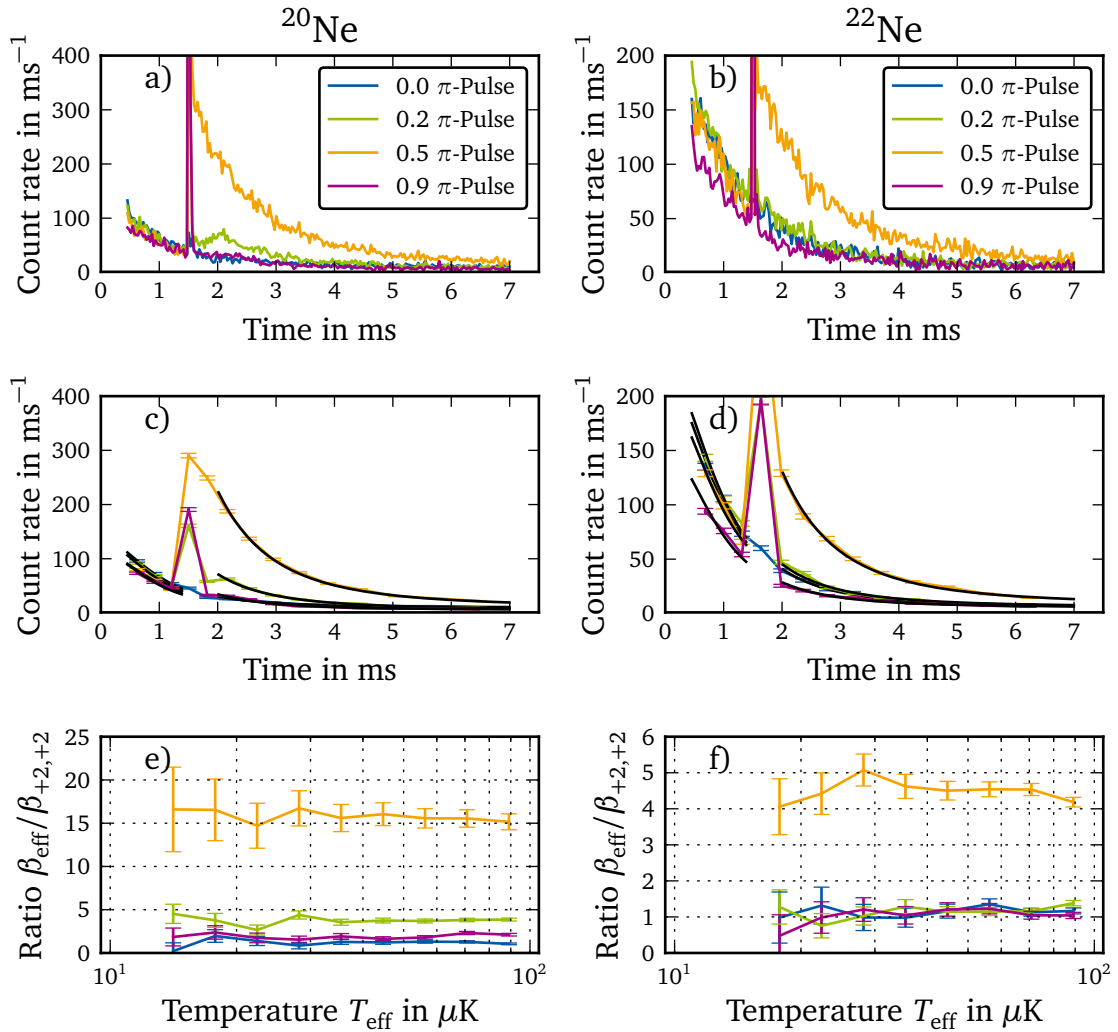


**Figure 7.5:** a) and b) Histograms of the ion signal of an expanding atom cloud after release from the magnetic trap for  $^{20}\text{Ne}$  and  $^{22}\text{Ne}$ . The bin width is  $30 \mu\text{s}$ . The RF pulse preparation starts at  $1.5$  ms. After the preparation, the collision rate increases. c) and d) The same signal as a) and b) but with histograms using a scaled bin width. The fits to determine the two-body collision coefficients before and after the preparation at  $t = 1.5$  ms are shown in black. e) and f) Relative two-body collision rate due to the preparation of spin mixtures. The two-body collision rates after the preparation are compared to the spin polarized coefficient before the preparation. The temperature is calculated from the width and temperature of the cloud. Only a selection of the data is shown. The colours in a), c), and e) and b), d), and f) correspond to the same measurements.

at 1.5 ms. Therefore, the fitted two-body collision coefficient after the preparation  $\beta_{\text{temp}}$  is replaced by the coefficient before the preparation  $\beta_{\text{ref}}$  in  $R_{\text{fit}}(t)$ . This is the same as the coefficient for spin-polarized  $\text{Ne}^*$ :  $\beta_{+2,+2} = \beta_{\text{ref}}$ .

The collision ratio  $\beta_{\text{eff}}/\beta_{+2,+2}$  for different Rabi pulse lengths is highest for the  $\pi/2$  pulse with  $\approx 15$  for  $^{20}\text{Ne}$  and  $\approx 4.5$  for  $^{22}\text{Ne}$  (Fig. 7.5 e) and f)). The  $0\pi$  pulse without RF preparation corresponds to the spin-polarized case with  $\beta_{+2,+2}$ . As expected, here the ratio  $\beta_{\text{eff}}/\beta_{+2,+2}$  for both isotopes is approximately unity. The uncertainties for the increase are not obtained with the reduced chi-squared statistics, like in the previous measurements. This method using the Poissonian uncertainties  $\Delta N_i$  yields a much smaller, unrealistic, uncertainty for the collision increase in this case. Instead, a method called Bootstrap [120–123] is used. This Monte Carlo based algorithm uses the optimal fit function, which is found by a least square fit, and the residuals to generate new artificial data points  $\tilde{N}_i$ , which are normal distributed around the fit function. The width of the normal distribution in this case is given by the uncertainty of the data point  $\Delta N_i$  and the residuals from the least square fit. Then, another least square fit finds the optimal fit parameters of this new dataset, which are saved in a list. The algorithm produces not only one dataset, but 100 and saves the fit values in a list. The standard deviation of the list yields the uncertainty of the fit parameters. The bootstrap method is often used in the case, that the underlying uncertainty is not known [121]. For the evaluation, this method yields uncertainties larger by several ten percent than with the reduced chi-squared method.

From the collision ratio and the population distribution the two-body collision coefficients  $\beta_{+1,+1}(T_{\text{eff}})$  and  $\beta_{+1,+2}(T_{\text{eff}})$  can be determined by using the total  $\beta$  coefficient from equation (7.9). The distribution is measured with the Stern-Gerlach method (Fig. 7.4 i) and j)) for both isotopes. The population starts in  $m_J = +2$  and transfers into  $+1$  with increasing pulse length. For the  $\pi$  pulse, almost the complete population is transferred. Only a small part remains in  $+2$ , and even less are in the sublevels  $0$ ,  $-1$  and  $-2$ . For longer pulse lengths, the population transfers back into  $m_J = +2$ . With damped sine function fits, the population distribution is determined for every pulse length (Fig. 7.4 i) and j)).

The results of the collision rate ratios  $\beta_{\text{eff}}/\beta_{+2,+2}$  (Fig. 7.5 e) and f)) can be rearranged in separate temperature slices. The increase in this case depends only on the Rabi pulse length. This allows for the calculation of the spin mixture dependent increase for different temperatures (Fig. 7.4 a) to h)). The collision rate has a minimum for all population in  $m_J = +2$  and increases with increasing population in  $m_J = +1$ . With the population distribution and equation (7.9) for the total two-body collision coefficient  $\beta$ , the two-body collision coefficients  $\beta_{+1,+1}(T_{\text{eff}})$  and  $\beta_{+1,+2}(T_{\text{eff}})$  can be fitted to the data (Fig. 7.4 a) to h)). The resulting coefficients are shown in figure 7.6 a) and b) for  $^{20}\text{Ne}$  and  $^{22}\text{Ne}$ . For a better comparison, the results and the uncertainties from J. Schütz [87] are included in the figure by horizontal lines and bands.

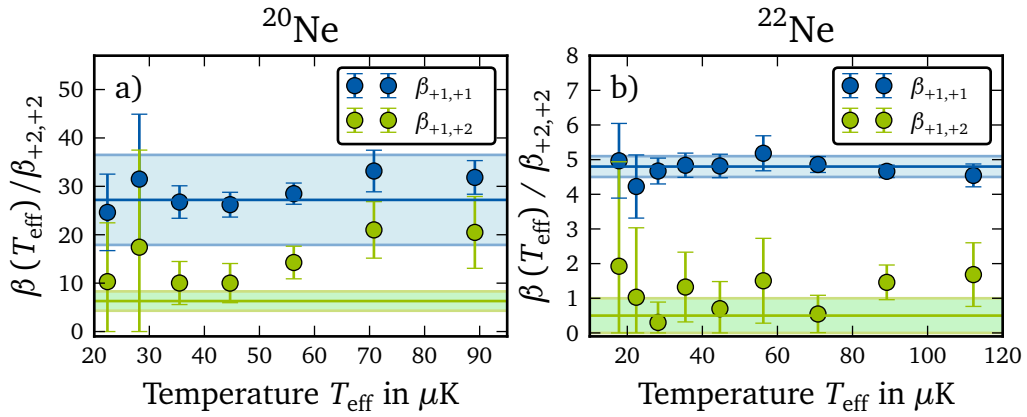


**Figure 7.6:** a) and b) Temperature dependence of the two-body collision coefficients  $\beta_{+1,+2}(T_{\text{eff}})$  and  $\beta_{+1,+1}(T_{\text{eff}})$  for collisions in the two-level system  $m_j = +2$  and  $+1$  for  $^{20}\text{Ne}$  and  $^{22}\text{Ne}$ . The coefficients are given relative to the spin polarized collision rate  $\beta_{+2,+2}$ . The horizontal lines with the bands indicate the coefficients and uncertainties determined by J. Schütz at a temperature of  $\bar{T} \approx 350 \mu\text{K}$ .

The coefficient  $\beta_{+1,+1}(T_{\text{eff}})$  for both isotopes are in good agreement with the results by J. Schütz, but the temperature dependent results for  $\beta_{+1,+2}(T_{\text{eff}})$  are in part significantly higher. While for  $^{22}\text{Ne}$  the results are still at the upper end of the uncertainty range with  $\beta_{+1,+2}(T_{\text{eff}}) \approx 1$ , for  $^{20}\text{Ne}$  and especially for temperatures  $T_{\text{eff}} > 50 \mu\text{K}$  they are nearly twice as big. Additionally, an increase with temperature is noticeable for  $^{20}\text{Ne}$  for  $\beta_{+1,+2}(T_{\text{eff}})$ . The other values are constant given their uncertainties in the range between 20 and 90  $\mu\text{K}$  for  $^{20}\text{Ne}$  and 15 and 120  $\mu\text{K}$  for  $^{22}\text{Ne}$ .

## 7.4 Conclusion

The temperature dependence of the two-body collision coefficient  $\beta$  was measured for spin polarized  $^{20}\text{Ne}$  and  $^{22}\text{Ne}$  over one decade in temperature between 20 and 300  $\mu\text{K}$ . For spin mixtures the dependence was measured between 20 and 90  $\mu\text{K}$  for  $^{20}\text{Ne}$  and between 15 and 120  $\mu\text{K}$  for  $^{22}\text{Ne}$ . The results for the spin-polarized measurements confirm the theoretical predicted constant behaviour for temperatures below one millikelvin. Also the spin mixture evaluation of  $^{22}\text{Ne}$  confirmed a constant dependence. Only  $^{20}\text{Ne}$  spin mixtures give some indications for a variation of  $\beta_{+1,+2}$  with temperature. Considering the uncertainties, this decrease does not contradict the constant  $\beta$ -coefficient from the theory for this temperature range.

For higher temperatures above one millikelvin, the theories predict a clear temperature dependence of the collisions, because collisions with higher angular momentum can occur. Thus, measurements in this region are of interest. For the measurement setup, the free expansion of the cloud released from the magnetic trap is preferable, as it allows the spin mixture preparation and produces reproducible cloud properties.

---

The disadvantage of the low temperatures in the magnetic trap could be overcome using the  $\delta$ -kick method, which allows for the preparation of temperatures above one millikelvin using the correct parameter set.

---

## 8 Summary and Outlook

This work was concerned with two exotic states of noble gases, boron-like argon ( $\text{Ar}^{13+}$ ) and metastable neon ( $\text{Ne}^*$ ), which allow on the one hand for high precision measurements for proves of quantum electrodynamics and otherwise for investigations on collision interactions of ultra-cold atoms. The discussion of these different questions starts with the results towards the spectroscopy of the fine-structure of  $\text{Ar}^{13+}$  and proceed with the results of the inelastic two-body collisions in  $\text{Ne}^*$ .

Within this thesis, a frequency stabilized laser system for the spectroscopy of  $\text{Ar}^{13+}$  has been developed. An absolute frequency determination of six tellurium transitions close to the energy splitting of the  $\text{Ar}^{13+}$  transitions was performed with an uncertainty of 1.4 MHz. For the determination, the laser system scanned over a frequency region of 3.4 THz. A long-term measurement yielded the absolute frequency accuracy of 2.2 MHz. The setup for the fluorescence spectroscopy was built, characterized, and optimized. The system allows for single photon detection by exciting the ion cloud for about 50 ms with laser light and afterwards recording the fluorescence light for 150 ms with a temporal resolution of 12.5 ns. A decrease of the background signal by three orders of magnitude was realized. Currently, the fine-structure splitting of  $\text{Ar}^{13+}$  is known within an uncertainty of 260 MHz [49]. This fluorescence spectroscopy system promises an improvement of at least one order of magnitude. Additionally, the absolute frequency accuracy of the laser system is high enough to resolve the second-order Zeeman shift of several MHz.

For a better signal-to-noise ratio of the fluorescence spectroscopy, further improvements can be envisioned: Since the implementation of filters in front of the single-photon detector led to a suppression of the background of around  $10^3$  an even narrower filter would be useful. Alternatively, the currently implemented line filter could be tilted. An angle of  $\approx 8^\circ$  would shift the filters edge close to the expected transition wavelengths. Another option would be to reduce the source of the background. The results of the fluorescence characterization indicated the glass materials of the optics used, such as the vacuum windows and the lenses, as the most probable remaining source. These critical materials could be replaced by lower fluoresce materials. Suitable materials are listed in [81]. The implementation of an electron multiplying CCD camera, which is already available, into the fluorescence spectroscopy setup replacing the single-photon multiplier is planned. The spatial resolution of the camera would allow for an additional discrimination of  $\text{Ar}^{13+}$  fluorescence signal from background signal and would therefore improve the signal-to-noise ratio with standard image processing methods such as dark images, white images, and offset images. Especially the white image, which is simply an image of the complete fluorescence signal without ions, would eliminate the influence of the background signal. The

---

drawback of the camera is the loss of the temporal information due to the longer exposure time of the camera. However, the temporal information could be regained by a time-shifting trigger point. Images of the fluorescence signal would additionally allow for the observation of the spatial distribution of the ion-cloud, which would yield information about the cloud dynamics in the trap. For example, the application of the rotating wall technique [52, 124, 125], which allows for manipulations of the ion-cloud form from cigar to oblate shape, is envisaged. This technique can be useful to optimize the fluorescence spectroscopy by compressing the ion cloud in radial direction.

After a successful spectroscopy of the two closed Zeeman sublevel transitions of the  $\text{Ar}^{13+}$  fine-structure, the other two axial excitable transitions should be determined. Since this leads to a transfer of population into the dark state, a repump laser is necessary. Therefore, a second laser at a wavelength of 441 nm should be built. The experience gained during the set up of the master laser can be helpful. Since the possibility of tuning the feedback to find the optimal value is no longer needed, the new setup should be based on the design of Baillard et al. [56]. This reduces the complexity of the setup and leads to a higher output power. Further improvements of the mechanical setup are already under way, such as an optimized mechanical mounting of the lenses for later adjustment and a new mounting of the laser diode for a better access and temperature stabilization. The modular setup of the laser system allows for an easy frequency stabilization of an additional laser: laser light of a third laser could be coupled into the transfer cavity, by overlapping the beam with light of one of the existing lasers using a dichroic mirror. The combination of wavelength selection by dichroic mirrors and polarization selection by polarizing beam splitters in the transfer cavity setup allows for a frequency stabilization of up to three lasers to a master laser frequency. The semi-transparent silver-coated mirrors of the transfer cavity are suitable for wavelength covering more than the complete visible wavelength regime.

After the optical spectroscopy of  $\text{Ar}^{13+}$ , the microwave spectroscopy is planned. The electronic setup for 65 GHz, which corresponds to the splitting of the  $^2P_{1/2}$  ground state in the Penning trap, is already implemented. As discussed in this thesis, the detection is planned to be realized optically by measuring the fluorescence signal in a cycling scheme. Therefore, the ions are irradiated by the microwaves and then the laser probes the population of the sub-levels. By probing an open transition with the laser, this leads to a dark signal due to pumping until the microwaves are in resonance with the energy splitting of the sub-level. A similar approach could be done to probe the energy splitting of the excited state after the implementation of the microwaves at 130 GHz [23].

Presently, only neutral gases can be injected and ionized in the Artemis experiment, which limits the available ion species for spectroscopy. To resolve this limitation, it is planned to connect the Artemis Penning trap to the accelerator facility at the GSI Helmholtzzentrum für Schwerionenforschung and FAIR. This allows for the spec-

---

troscopy of ions from multiple sources, such as an electron beam ion source or the accelerator beamline.

Concerning the second part of this thesis, during the work with metastable neon, the so called  $\delta$ -kick cooling method was implemented which allows for controlling the phase-space distribution of the cold  $\text{Ne}^*$  cloud. To realize the  $\delta$ -kick, the magnetic trap of this experiment was used to form the necessary potential. The geometry of the trap potential leads to different  $\delta$ -kick strengths in axial and radial direction, which were studied separately. The axial and radial velocity distributions were changed in a range which corresponds to a mean temperature between  $10\ \mu\text{K}$  and  $460\ \mu\text{K}$ . The distribution in radial direction was examined even over a broader range between  $7.5\ \mu\text{K}$  and  $640\ \mu\text{K}$  and a simulation yielded possible temperature increases over a millikelvin with the parameter used in the experiment. The investigations of the temperature dependent two-body collisions of  $\text{Ne}^*$  atoms were done in a temperature range between  $15\ \mu\text{K}$  and  $300\ \mu\text{K}$ . For the two-body collision coefficient  $\beta$ , the expected constant behaviour was confirmed for  $^{20}\text{Ne}^*$  and  $^{22}\text{Ne}^*$ . The measurements were performed with spin-polarized ensembles prepared in the Zeeman sublevel  $m_J = +2$  and for spin mixtures of  $m_J = +2$  and  $m_J = +1$  for both isotopes. In addition, the investigations of the two-body collisions of  $\text{Ne}^*$  atoms in magnetic fields covered a range from  $0.35\ \text{G}$  to  $122.5\ \text{G}$ . It was shown that the external magnetic field leads to a suppression of the two-body collision rate for  $^{22}\text{Ne}^*$  by a factor of 5.6, whereas the rate for  $^{20}\text{Ne}^*$  remains constant up to fields of  $122.5\ \text{G}$ . A comparison of the collision rate between the opposite stretched states  $m_J = +2$  and  $m_J = -2$  indicated no difference for both isotopes. The obtained data add a new facet to the collision properties of  $\text{Ne}^*$  and can be used for improvements of theoretical models. Especially the complementary collision properties of  $^{20}\text{Ne}$  and  $^{22}\text{Ne}$  in magnetic fields are of interest.

The promising results of the  $\delta$ -kick cooling method offer the possibility for further characterization of the temperature dependence of the inelastic and elastic collisions: With the appropriate parameters, the temperature can be increased to a few kelvins, where a collision variation due to the influence of higher partial waves are expected [87, 94, 119]. The advantage of  $\delta$ -kick cooling compared to a hotter cloud is the more precise control of the cloud properties. It is, for example, possible to prepare a “high temperature” in radial direction and a “low temperature” but high spatial density in axial direction. This allows for fine-tuning of the compromise between cloud density and temperature. For measurements with higher kinetic collision energies, a comparison of polarized and unpolarized ensembles of the bosonic isotopes  $^{20}\text{Ne}^*$  and  $^{22}\text{Ne}^*$  with the fermionic  $^{21}\text{Ne}^*$  are of interest, for which a completely different behaviour is predicted [87, 96]. Additionally, the large difference of thermal energies in axial and radial direction could be utilized for direction-dependent investigations. Since the two-body collision rate is a function of the atom density, a detailed knowledge of the phase-space distribution is required. Therefore, the anharmonicity of the  $\delta$ -kick potential, which is generated by the field geometry of the magnetic trap, must be considered. The anharmonicity leads to the observed damp-

---

ing and can be handled in calculations [126]. A possible increase of measurement efficiency is inspired by  $\delta$ -kick cooling: Since the collisional investigations are done with free-expanding atoms, the cloud could be recaptured after the observation and used for another measurement run. This recycling could be repeated and would multiply the amount of data per measurement cycle, which leads to more statistics. The recapturing could even be done with ensembles of arbitrary spin mixtures by spin-polarizing them before re-trapping. Additionally, for non-temperature dependent measurements, the observation time could be increased by reducing the temperature using  $\delta$ -kick cooling.

An interesting aspect for further investigations is the suppression of inelastic collisions for  $^{22}\text{Ne}$  in external magnetic fields. If the inelastic two-body collision rate can be further decreased, the creation of a Bose-Einstein condensate could get into reach. Calculation by W. J. van Drunen [117] yield a 7-fold suppression would be sufficient, which has almost been achieved here with a suppression of 5.6. Additionally, an extension to collision rate measurements with the fermionic  $^{21}\text{Ne}^*$  would complete the image of the magnetic field dependence and the results could help to understand the different behaviour of  $^{20}\text{Ne}^*$  and  $^{22}\text{Ne}^*$ .

Another auspicious investigation would be the coherent collision control as proposed by Arango et al. [127, 128]. They proposed a phase dependent behaviour of the collision rate for mixtures of Ar with a superposition of  $\text{Ne}^*$  in different Zeeman sublevels. The composition of the superposition and the phase tunes the inelastic collision rate over 4 orders of magnitude. A superposition of  $\text{Ne}^*$  in different Zeeman sublevels can be created with various techniques [87], such as radio frequency induced Rabi oscillations or stimulated Raman adiabatic passage techniques [129]. The phase of this superposition oscillates with a rate proportional to the energy-splitting of the sublevels, which in the experiment is about 100 kHz. With a sufficient temporal resolution of the collision-rate detection system, the collision control could also be measured in a superposition of  $\text{Ne}^*$  in different  $m_j$ -sublevels.

The presented studies on boron-like argon and metastable neon demonstrates the manifold of interesting investigations which are possible with laser spectroscopy of exotic states in noble gases.

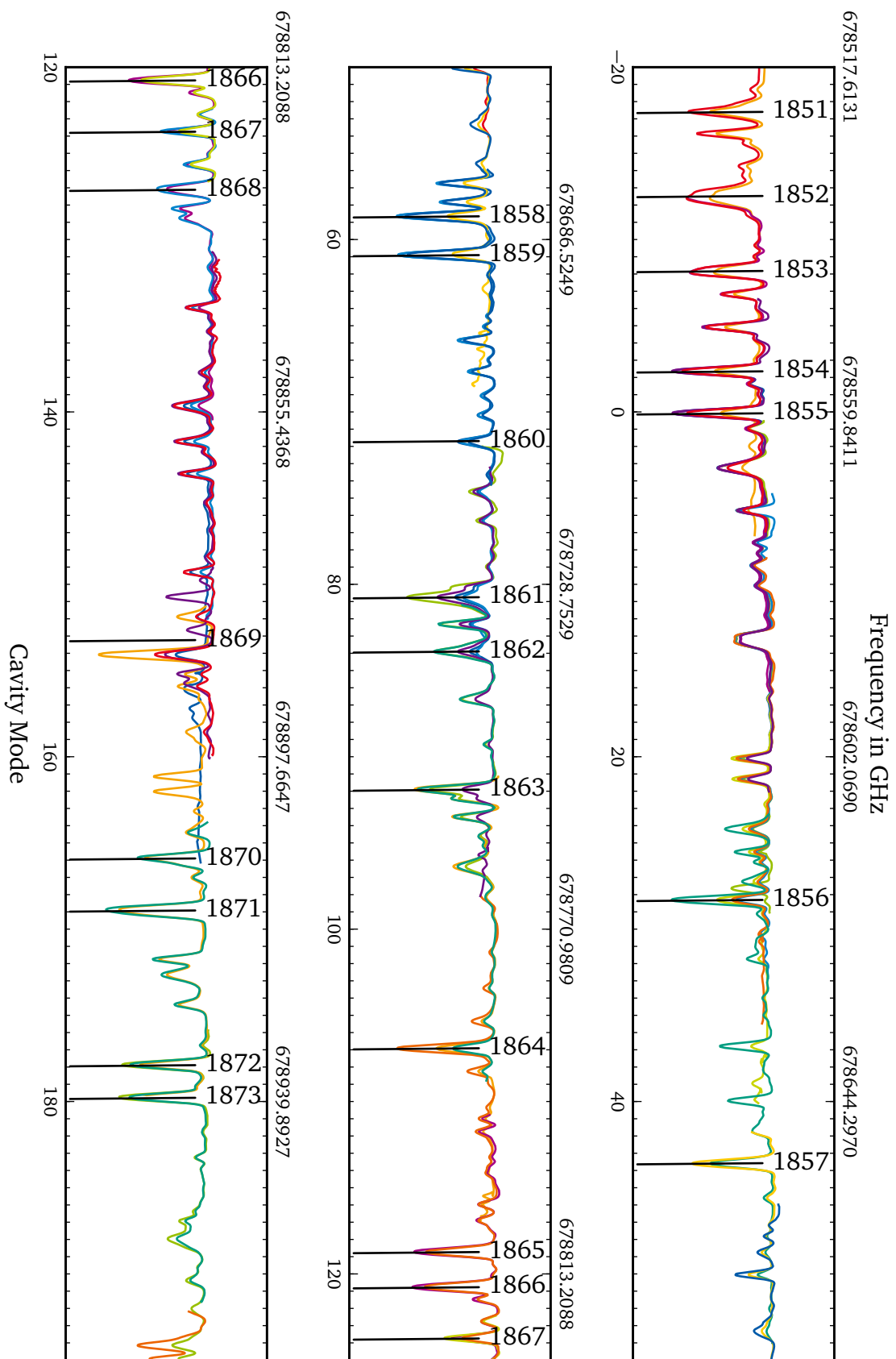
# A Tellurium Spectrum

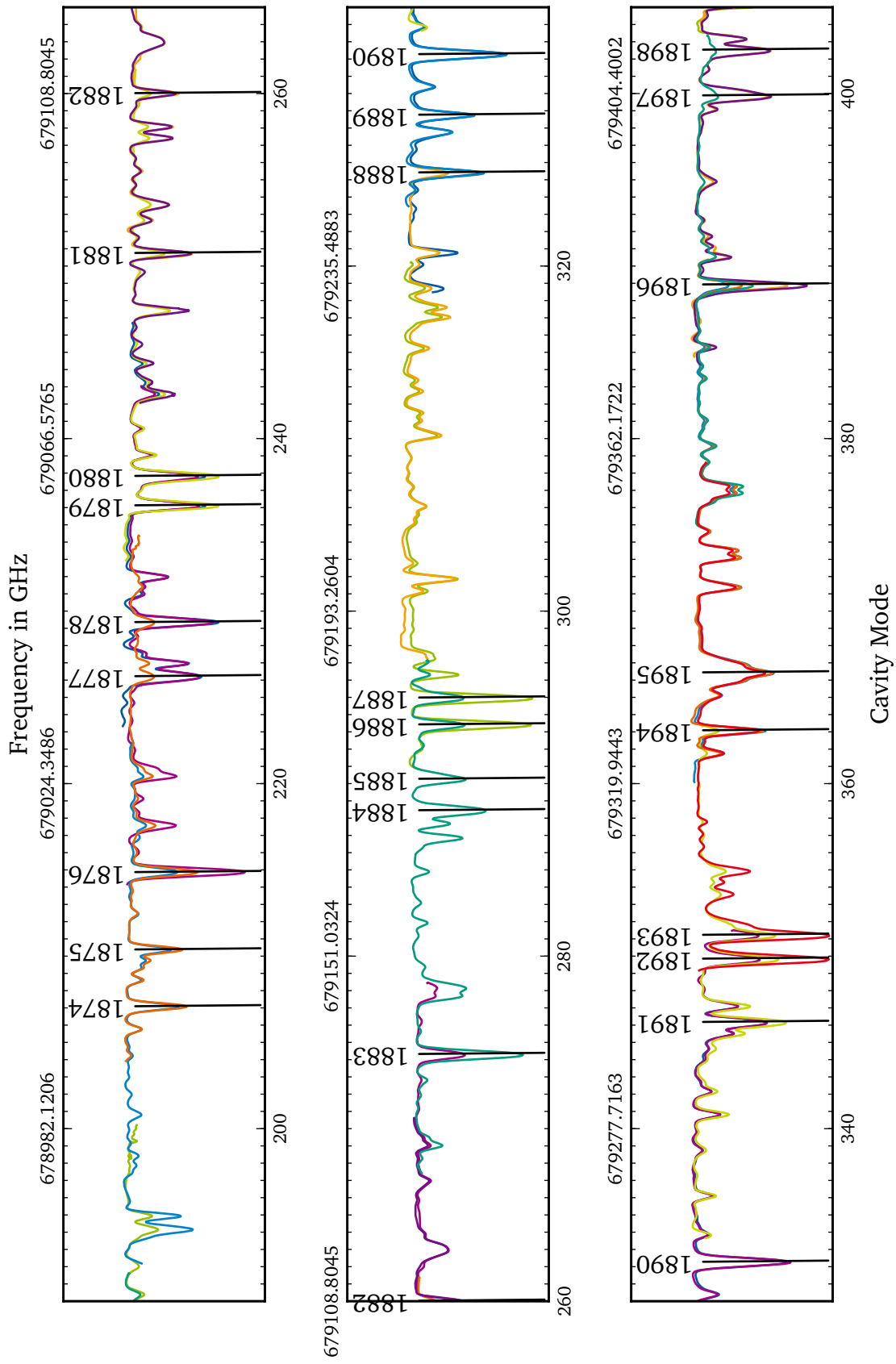
The determination of the absolute frequencies of six tellurium lines close to the fine-structure transitions of  $\text{Ar}^{13+}$  in the magnetic field of  $B \approx 7\text{ T}$  of the Penning trap are presented in chapter 3. The evaluation is based on a measurement of the tellurium spectrum in a range of about 3.4 THz between the reference lines 1855, 2082, and 2083 of the tellurium atlas [65]. The complete recorded spectrum is shown in this section. It can be used for frequency determinations of further tellurium lines by following the evaluation given in chapter 3. Therefore, the spectrum is given in multiples of the relative longitudinal cavity modes. The given frequency is calculated from the relative modes. The frequency position of the modes is not fix, since the length of the cavity depends on the refractive index of air, which again depends on the current air pressure.

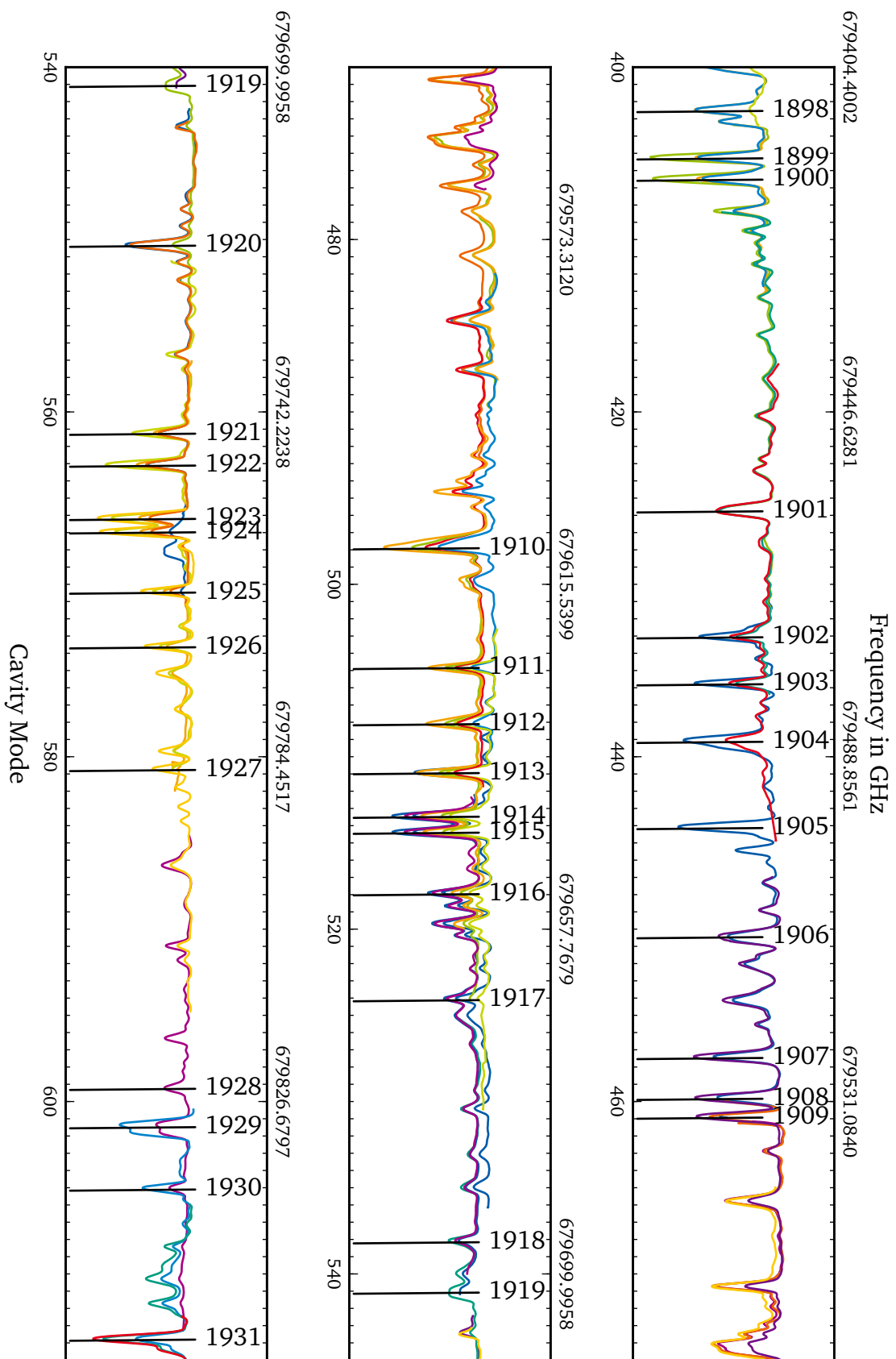
Additionally, the absolute frequencies of the six determined tellurium lines close to the  $\text{Ar}^{13+}$  transitions are shown in table A.1. The total frequency uncertainty of about 2.2 MHz is given by adding the uncertainty of the frequency determination of about 1.2 MHz and the deviation of the long-term measurement of 1.04 MHz.

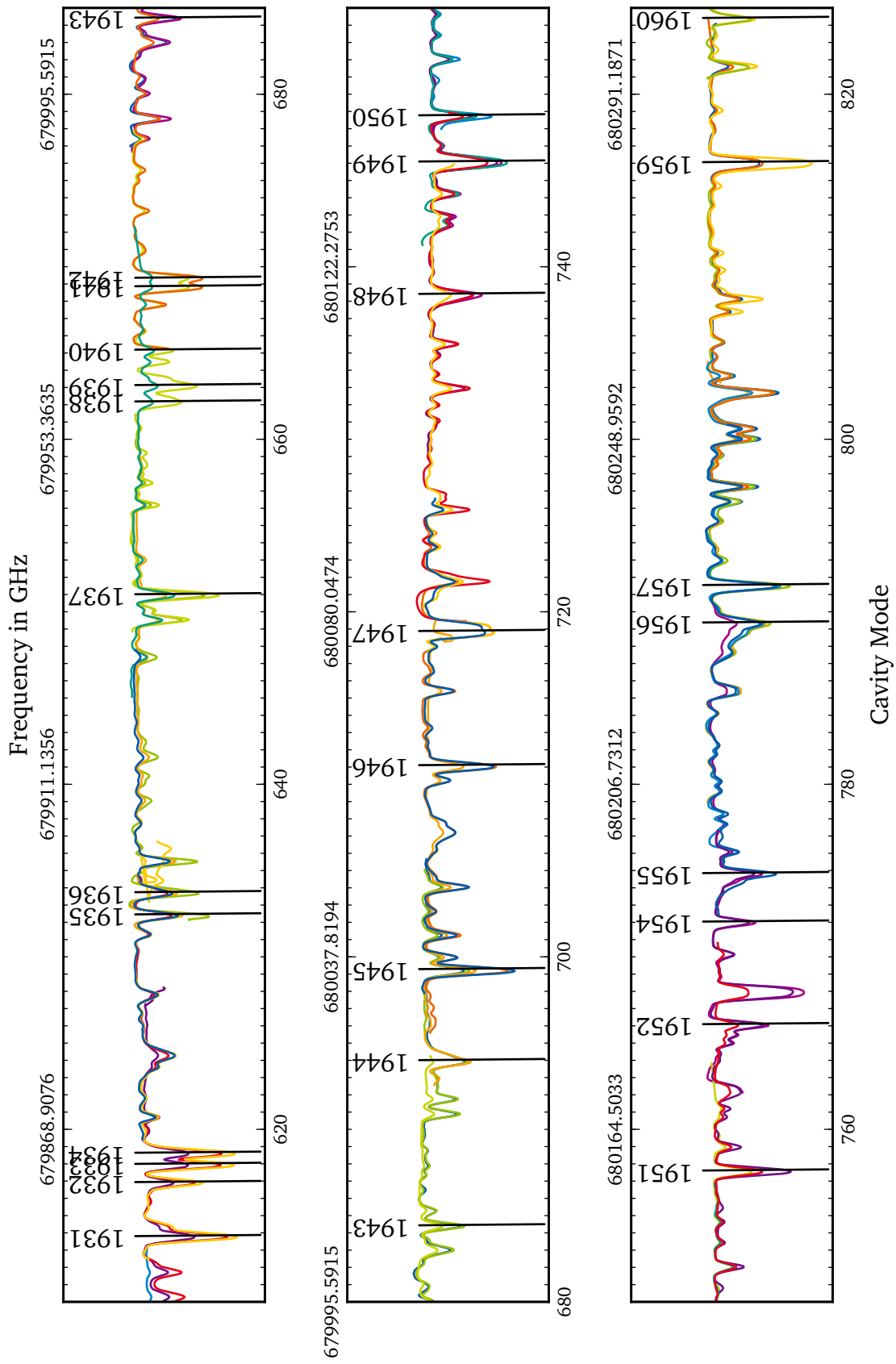
Lamb dip	$\Delta N$	Frequency in GHz	$\Delta \nu(\text{Ar}^{13+})$ in GHz
$\nu_{1,\text{Te}}$	325	679247.1424(11)(10)	-3.0
$\nu_{2,\text{Te}}$	354	679308.0745(11)(10)	1.6
$\nu_{3,\text{Te}}$	385	679373.6021(12)(10)	1.1
$\nu_{4,\text{Te}}$	415	679437.4195(12)(10)	2.8
$\nu_{5,\text{Te}}$	449	679507.9295(12)(10)	-2.6
$\nu_{6,\text{Te}}$	478	679569.8136(12)(10)	1.0
Calibration line	474	679560.9106(12)(10)	(441.156 nm)

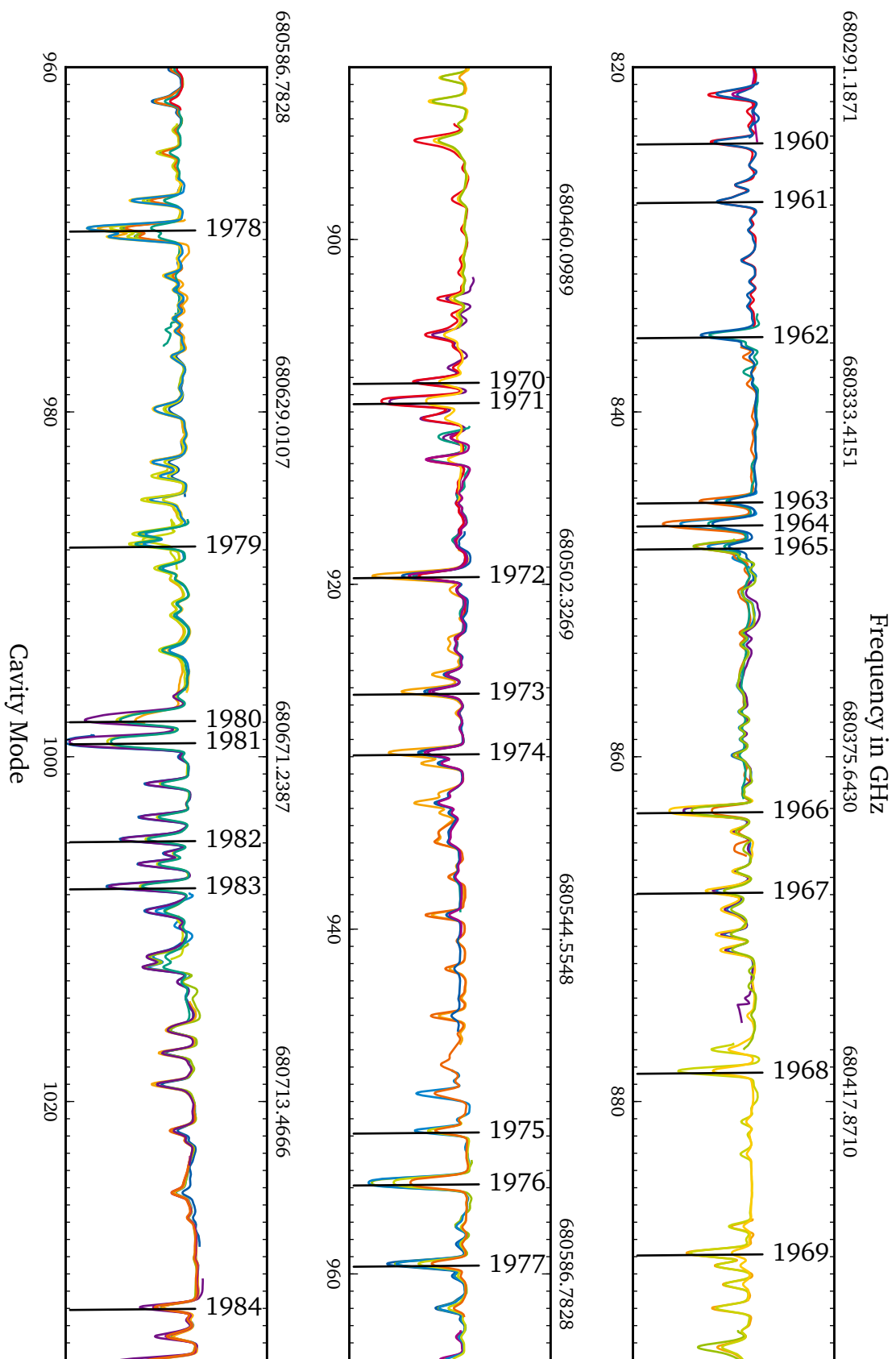
**Table A.1:** Absolute frequencies  $\nu_{i,\text{Te}}$  of the tellurium Lamb dips closest to the expected  $\text{Ar}^{13+}$ -transitions  $\nu_i$ . Positive difference values  $\Delta \nu(\text{Ar}^{13+})$  yield a higher expected  $\text{Ar}^{13+}$ -transition frequency relative to the tellurium Lamb dip frequency. The systematic uncertainty of the frequency determination, including the uncertainty of the reference transitions used or the uncertainty of the cavity length, is given first. Whereas the deviation of the long-term measurement is presented in the second bracket. The absolute frequency accuracy can be obtained by adding both uncertainties and yields 2.2 MHz.

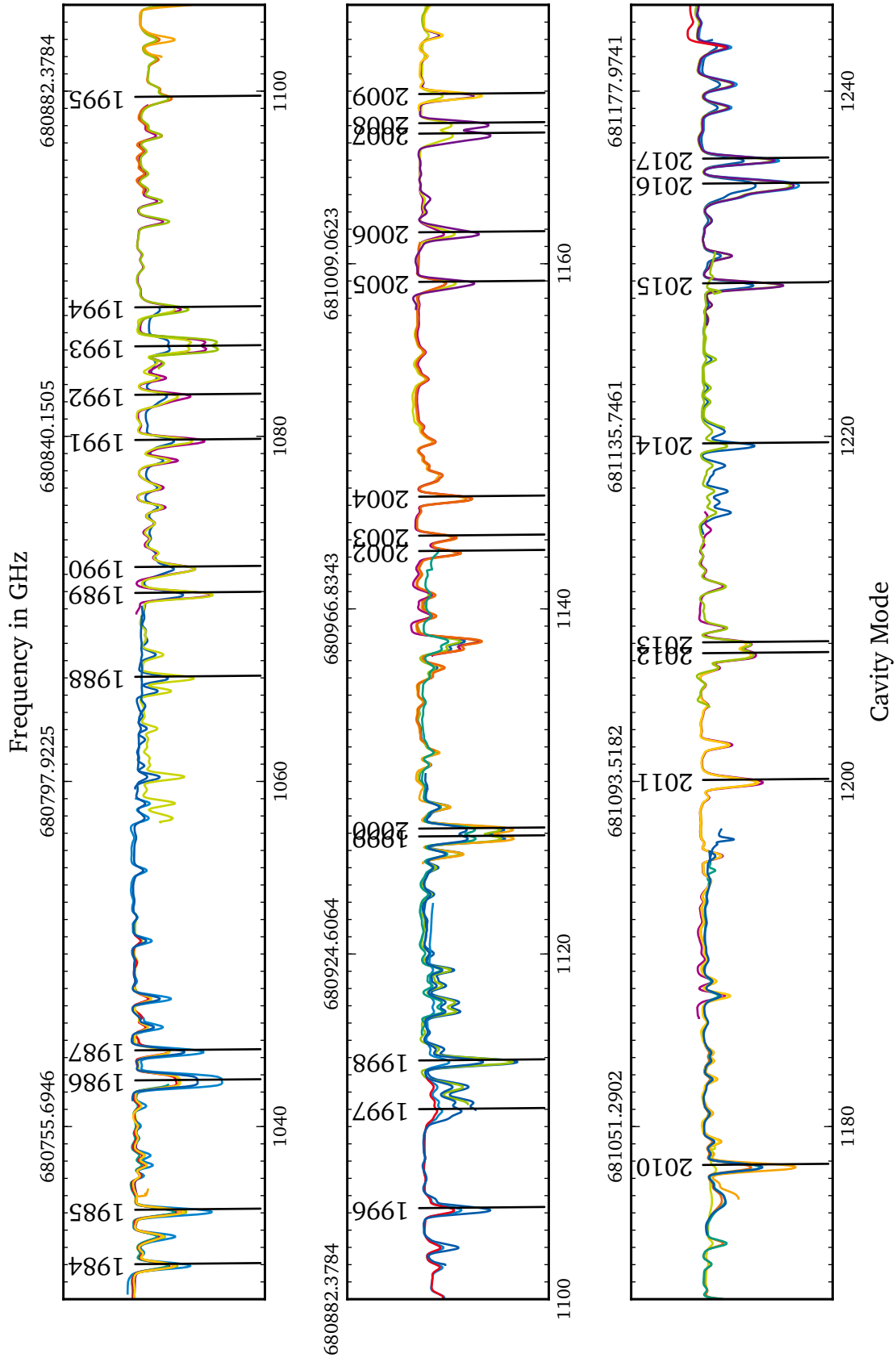


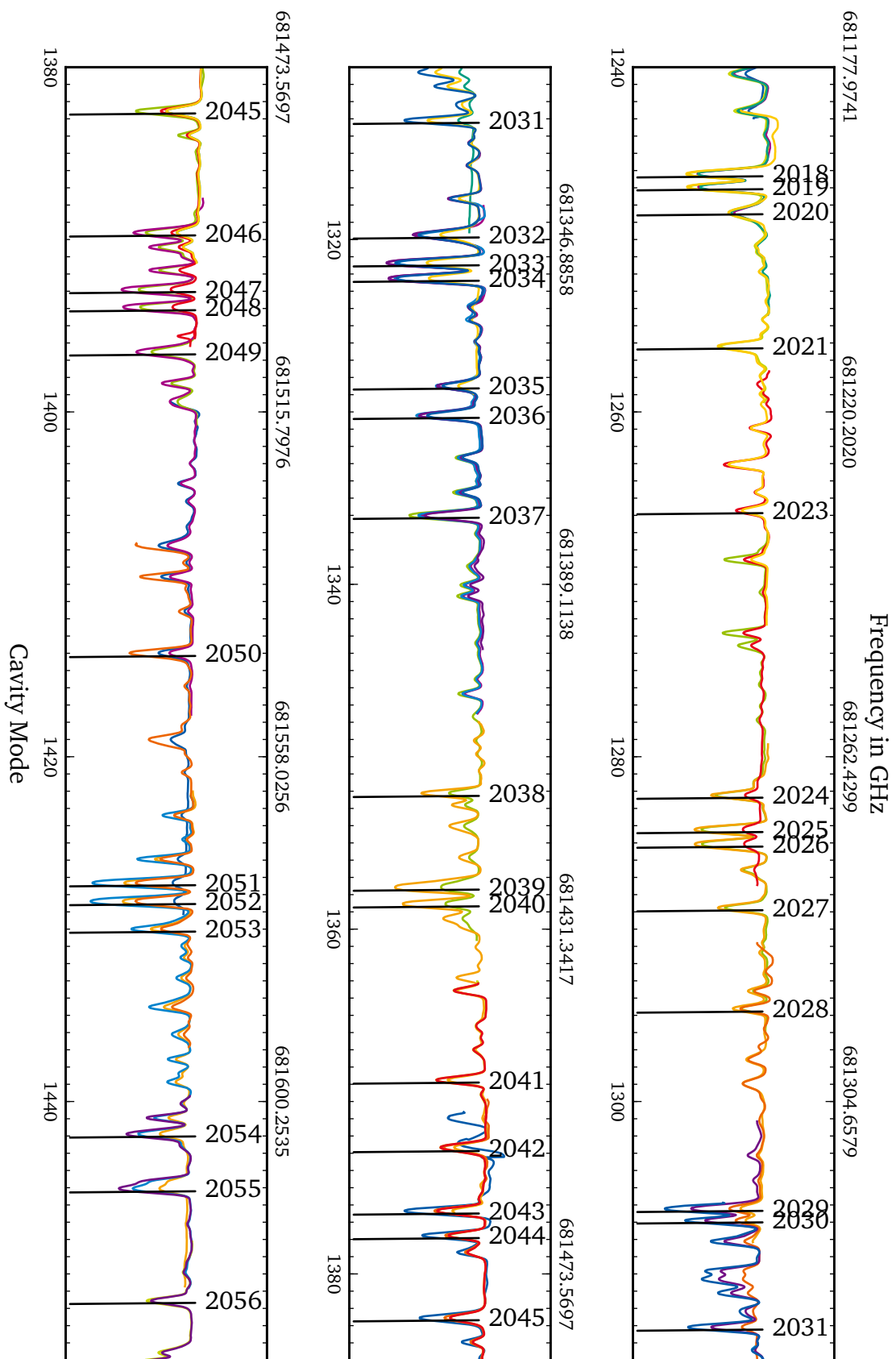


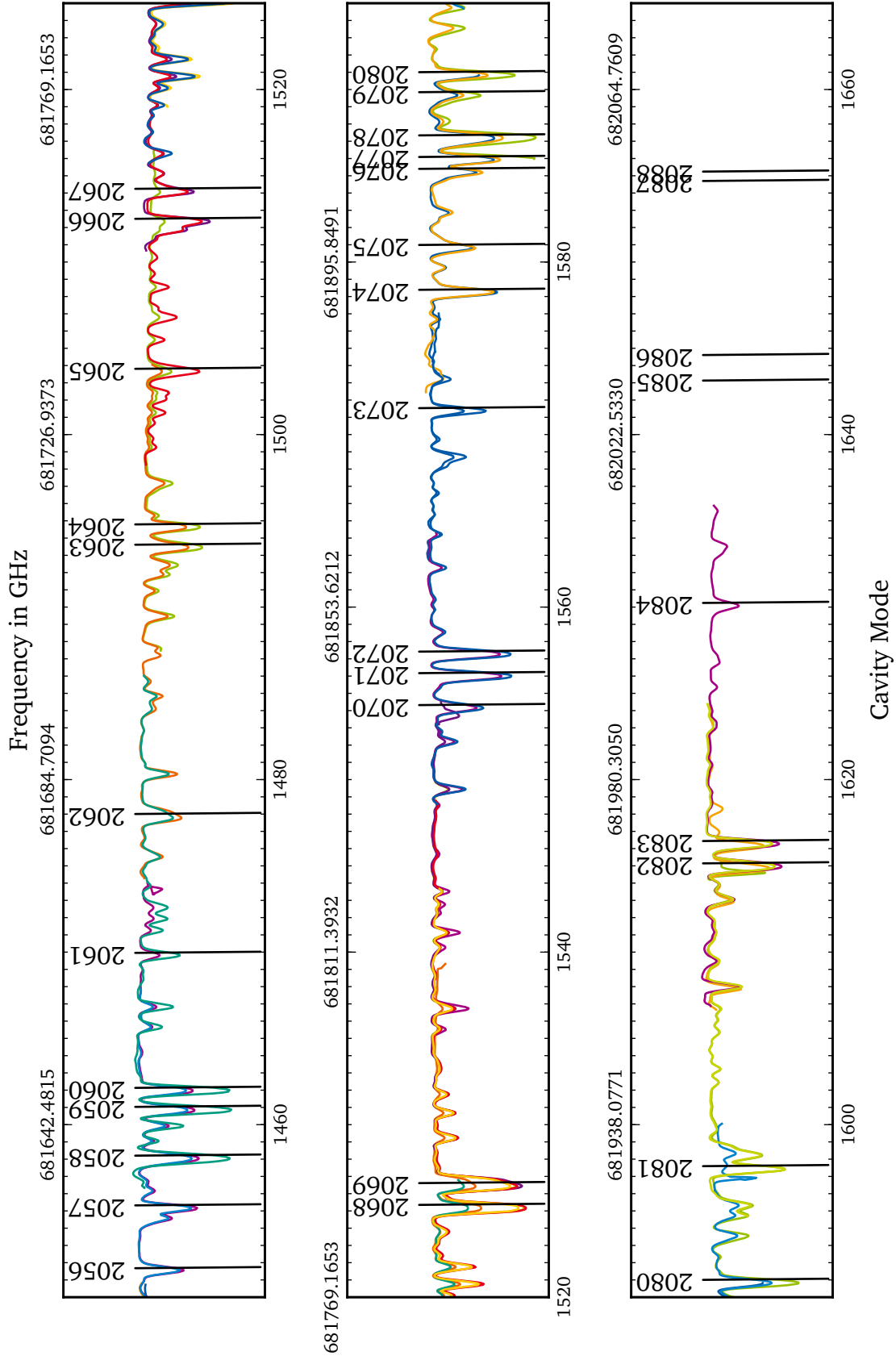














---

## B List of Publications

---

---

### Publications in Peer-Review Journals

---

A. Martin, P. Baus, and G. Birkl, *External cavity diode laser setup with two interference filters*, Appl. Phys. B **122**, 298 (2016)

M. S. Ebrahimi, N. Stallkamp, W. Quint, M. Wiesel, M. Vogel, A. Martin, and G. Birkl, *Superconducting radio-frequency resonator in magnetic fields up to 6 T*, Rev. Sci. Instr. **87**, 075110 (2016)

D. von Lindenfels, M. Wiesel, D. A. Glazov, A. V. Volotka, M. M. Sokolow, V. M. Shabaev, G. Plunien, W. Quint, G. Birkl, A. Martin, and M. Vogel, *Experimental access to higher-order Zeeman effects by precision spectroscopy of highly charged ions in a Penning trap*, Phys. Rev. A **87**, 023412 (2013)

C. Cop, A. Martin, G. Birkl, and R. Walser, *Penning ionization and elastic scattering in cold collisions of metastable neon atoms*, to be published

J. Schütz, A. Martin, S. Altenburg, and G. Birkl, *Zeeman state dependence of ionizing collision rates in metastable neon*, to be published

J. Schütz, A. Martin, S. Altenburg, and G. Birkl, *Preparation of Zeeman states and controlled superpositions in a five-level system using metastable neon atoms*, to be published

---

### Conference Contributions

---

M. Vogel, Z. Andelkovic, G. Birkl, S. Ebrahimi, V. Hannen, D. von Lindenfels, A. Martin, T. Murböck, W. Nörtershäuser, W. Quint, S. Schmidt, D. M. Segal, R. C. Thompson, J. Vollbrecht, Ch. Weinheimer, and M. Wiesel, *Penning-trap experiments for spectroscopy of highly-charged ions at HITRAP*, Phys. Scr. **2015**, 014066 (2015)

M. Vogel, G. Birkl, M.S. Ebrahimi, D. von Lindenfels, A. Martin, G.G. Paulus, W. Quint, S. Ringleb, Th. Stöhlker, and M. Wiesel, *Extreme-field physics in Penning traps - The ARTEMIS and HILITE experiments*, Hyp. Int. **236**, 65 - 71 (2015)



---

# Bibliography

- [1] W. H. Wollaston, *A Method of Examining Refractive and Dispersive Powers, by Prismatic Reflection*, Philosophical Transactions of the Royal Society of London **92**, 365 (1802).
- [2] J. Fraunhofer, *Bestimmung des Brechungs- und des Farbenzerstreungs-Vermögens verschiedener Glasarten, in Bezug auf die Vervollkommnung achromatischer Fernröhre*, Annalen der Physik **56**, 264 (1817).
- [3] T. H. Maiman, *Stimulated Optical Radiation in Ruby*, Nature **187**, 493 (1960).
- [4] A. L. Schawlow, and C. H. Townes, *Infrared and Optical Masers*, Phys. Rev. **112**, 1940 (1958).
- [5] A. Javan, *Possibility of Production of Negative Temperature in Gas Discharges*, Phys. Rev. Lett. **3**, 87 (1959).
- [6] *Optical Spectrum Analyzers - User Guide*, Thorlabs, 2016.
- [7] T. Schneider, E. Peik, and C. Tamm, *Sub-Hertz Optical Frequency Comparisons between Two Trapped  $^{171}\text{Yb}^+$  Ions*, Phys. Rev. Lett. **94**, 230801 (2005).
- [8] D. J. Wineland, R. E. Drullinger, and F. L. Walls, *Radiation-Pressure Cooling of Bound Resonant Absorbers*, Phys. Rev. Lett. **40**, 1639 (1978).
- [9] W. Neuhauser, M. Hohenstatt, P. E. Toschek, and H. Dehmelt, *Localized visible  $\text{Ba}^+$  mono-ion oscillator*, Phys. Rev. A **22**, 1137 (1980).
- [10] A. L. Migdall, J. V. Prodan, W. D. Phillips, T. H. Bergeman, and H. J. Metcalf, *First Observation of Magnetically Trapped Neutral Atoms*, Phys. Rev. Lett. **54**, 2596 (1985).
- [11] H. J. Metcalf, and P. van der Straten, *Laser Cooling and Trapping* (Springer New York, 1999).
- [12] T. Hänsch, and A. Schawlow, *Cooling of gases by laser radiation*, Optics Communications **13**, 68 (1975).
- [13] W. D. Phillips, and H. Metcalf, *Laser Deceleration of an Atomic Beam*, Phys. Rev. Lett. **48**, 596 (1982).
- [14] E. L. Raab, M. Prentiss, A. Cable, S. Chu, and D. E. Pritchard, *Trapping of Neutral Sodium Atoms with Radiation Pressure*, Phys. Rev. Lett. **59**, 2631 (1987).

- 
- [15] S.-I. Tomonaga, *Nobel Lecture: Development of Quantum Electrodynamics*, Physics 1963-1970 (1966).
- [16] J. Schwinger, *Nobel Lecture: Relativistic Quantum Field Theory*, Physics 1963-1970 (1965).
- [17] R. P. Feynman, *Nobel Lecture: The Development of the Space-Time View of Quantum Electrodynamics*, Physics 1963-1970 (1965).
- [18] J. Ullmann *et al.*, *An improved value for the hyperfine splitting of hydrogen-like  $^{209}\text{Bi } 82+$* , Journal of Physics B: Atomic, Molecular and Optical Physics **48**, 144022 (2015).
- [19] D. J. Berkeland, E. A. Hinds, and M. G. Boshier, *Precise Optical Measurement of Lamb Shifts in Atomic Hydrogen*, Phys. Rev. Lett. **75**, 2470 (1995).
- [20] S. Sturm, F. Kohler, J. Zatorski, A. Wagner, Z. Harman, G. Werth, W. Quint, C. H. Keitel, and K. Blaum, *High-precision measurement of the atomic mass of the electron*, Nature **506**, 467 (2014).
- [21] S. J. Brodsky, and G. W. Erickson, *Radiative Level Shifts. III. Hyperfine Structure in Hydrogenic Atoms*, Phys. Rev. **148**, 26 (1966).
- [22] T. Beier, *The  $g_j$  factor of a bound electron and the hyperfine structure splitting in hydrogenlike ions*, Physics Reports **339**, 79 (2000).
- [23] D. von Lindenfels *et al.*, *Experimental access to higher-order Zeeman effects by precision spectroscopy of highly charged ions in a Penning trap*, Phys. Rev. A **87**, 023412 (2013).
- [24] S. Chu, J. E. Bjorkholm, A. Ashkin, and A. Cable, *Experimental Observation of Optically Trapped Atoms*, Phys. Rev. Lett. **57**, 314 (1986).
- [25] A. Griesmaier, J. Werner, S. Hensler, J. Stuhler, and T. Pfau, *Bose-Einstein Condensation of Chromium*, Phys. Rev. Lett. **94**, 160401 (2005).
- [26] H. Hachisu, K. Miyagishi, S. G. Porsev, A. Derevianko, V. D. Ovsiannikov, V. G. Pal'chikov, M. Takamoto, and H. Katori, *Trapping of Neutral Mercury Atoms and Prospects for Optical Lattice Clocks*, Phys. Rev. Lett. **100**, 053001 (2008).
- [27] M. Lu, S. H. Youn, and B. L. Lev, *Trapping Ultracold Dysprosium: A Highly Magnetic Gas for Dipolar Physics*, Phys. Rev. Lett. **104**, 063001 (2010).
- [28] D. Sukachev, K. Chebakov, A. Sokolov, A. Akimov, N. Kolachevsky, and V. Sorokin, *Laser cooling of thulium atoms*, Optics and Spectroscopy **111**, 633 (2011).
- [29] J. F. Barry, D. J. McCarron, E. B. Norrgard, M. H. Steinecker, and D. DeMille, *Magneto-optical trapping of a diatomic molecule*, Nature **512**, 286 (2014).

- 
- [30] F. Pereira Dos Santos, J. Léonard, J. Wang, C. J. Barrelet, F. Perales, E. Rasel, C. S. Unnikrishnan, M. Leduc, and C. Cohen-Tannoudji, *Bose-Einstein Condensation of Metastable Helium*, Phys. Rev. Lett. **86**, 3459 (2001).
- [31] G. V. Shlyapnikov, J. T. M. Walraven, U. M. Rahmanov, and M. W. Reynolds, *Decay Kinetics and Bose Condensation in a Gas of Spin-Polarized Triplet Helium*, Phys. Rev. Lett. **73**, 3247 (1994).
- [32] P. O. Fedichev, M. W. Reynolds, U. M. Rahmanov, and G. V. Shlyapnikov, *Inelastic decay processes in a gas of spin-polarized triplet helium*, Phys. Rev. A **53**, 1447 (1996).
- [33] P. Spoden, M. Zinner, N. Herschbach, W. J. van Drunen, W. Ertmer, and G. Birkl, *Collisional Properties of Cold Spin-Polarized Metastable Neon Atoms*, Phys. Rev. Lett. **94**, 223201 (2005).
- [34] I. Klaft *et al.*, *Precision Laser Spectroscopy of the Ground State Hyperfine Splitting of Hydrogenlike  $^{209}\text{Bi}^{82+}$* , Phys. Rev. Lett. **73**, 2425 (1994).
- [35] M. Lochmann *et al.*, *Observation of the hyperfine transition in lithium-like bismuth  $^{209}\text{Bi}^{80+}$  : Towards a test of QED in strong magnetic fields*, Phys. Rev. A **90**, 030501 (2014).
- [36] A. Lapiere *et al.*, *Relativistic Electron Correlation, Quantum Electrodynamics, and the Lifetime of the  $1s^2 2s^2 2p^2 P_{3/2}^o$  Level in Boronlike Argon*, Phys. Rev. Lett. **95**, 183001 (2005).
- [37] T. Murböck, S. Schmidt, G. Birkl, W. Nörtershäuser, R. C. Thompson, and M. Vogel, *Rapid crystallization of externally produced ions in a Penning trap*, Phys. Rev. A **94**, 043410 (2016).
- [38] M. Vogel *et al.*, *Penning-trap experiments for spectroscopy of highly-charged ions at HITRAP*, Physica Scripta **2015**, 014066 (2015).
- [39] A. Mooser, S. Ulmer, K. Blaum, K. Franke, H. Kracke, C. Leiteritz, W. Quint, C. C. Rodegheri, C. Smorra, and J. Walz, *Direct high-precision measurement of the magnetic moment of the proton*, Nature **509**, 596 (2014).
- [40] R. E. Marrs, S. R. Elliott, and D. A. Knapp, *Production and Trapping of Hydrogenlike and Bare Uranium Ions in an Electron Beam Ion Trap*, Phys. Rev. Lett. **72**, 4082 (1994).
- [41] D. von Lindenfels, M. Vogel, W. Quint, G. Birkl, and M. Wiesel, *Half-open Penning trap with efficient light collection for precision laser spectroscopy of highly charged ions*, Hyperfine Interactions **227**, 197 (2014).
- [42] H. Amano, *Nobel Lecture: Growth of GaN on sapphire via low-temperature deposited buffer layer and realization of p-type GaN by Mg doping followed by low-energy electron beam irradiation*, Rev. Mod. Phys. **87**, 1133 (2015).

- 
- [43] S. Nakamura, *Nobel Lecture: Background story of the invention of efficient blue InGaN light emitting diodes*, Rev. Mod. Phys. **87**, 1139 (2015).
- [44] I. Akasaki, *Nobel Lecture: Fascinated journeys into blue light*, Rev. Mod. Phys. **87**, 1119 (2015).
- [45] D. von Lindenfels, *Experimental Studies of Highly Charged Ions in a Penning Trap for the Measurement of Electron Magnetic Moments by Double-Resonance Spectroscopy*, type, Ruperto-Carola University of Heidelberg, (2015).
- [46] M. Berglund, and M. E. Wieser, *Isotopic compositions of the elements 2009 (IUPAC Technical Report)*, Pure and Applied Chemistry **83**, 397 (2011).
- [47] K. Siegbahn, *Introduction to the Physics of Highly Charged Ions*, Nuclear Instruments and Methods in Physics Research Section A: Accelerators, Spectrometers, Detectors and Associated Equipment **500**, 446 (2003).
- [48] H. Beyer, and V. P. Shevelko, *Atomic Physics with Heavy Ions*, Vol. 26 of Springer Series on Atoms and Plasmas (Springer, 1999).
- [49] V. Mäckel, R. Klawitter, G. Brenner, J. R. C. López-Urrutia, and J. Ullrich, *Laser spectroscopy of highly charged argon at the Heidelberg electron beam ion trap*, Physica Scripta **2013**, 014004 (2013).
- [50] D. A. Glazov, A. V. Volotka, A. A. Schepetnov, M. M. Sokolov, V. M. Shabaev, I. I. Tupitsyn, and G. Plunien, *g factor of boron-like ions: ground and excited states*, Physica Scripta **2013**, 014014 (2013).
- [51] L. S. Brown, and G. Gabrielse, *Geonium theory: Physics of a single electron or ion in a Penning trap*, Rev. Mod. Phys. **58**, 233 (1986).
- [52] S. Bharadia, M. Vogel, D. M. Segal, and R. C. Thompson, *Dynamics of laser-cooled Ca<sup>+</sup> ions in a Penning trap with a rotating wall*, Applied Physics B **107**, 1105 (2012).
- [53] G. Gabrielse, and F. Mackintosh, *Cylindrical Penning traps with orthogonalized anharmonicity compensation*, International Journal of Mass Spectrometry and Ion Processes **57**, 1 (1984).
- [54] P. Baus, *Characterization of a Wide Tunable, Robust, Multi Application Diode Laser for Spectroscopy*, Masterthesis, TU Darmstadt, (2014).
- [55] A. Martin, P. Baus, and G. Birkl, *External cavity diode laser setup with two interference filters*, Applied Physics B **122** (2016).
- [56] X. Baillard, A. Gauguet, S. Bize, P. Lemonde, P. Laurent, A. Clairon, and P. Rosenbusch, *Interference-filter-stabilized external-cavity diode lasers*, Optics Communications **266**, 609 (2006).

- 
- [57] D. J. Thompson, and R. E. Scholten, *Narrow linewidth tunable external cavity diode laser using wide bandwidth filter*, Review of Scientific Instruments **83** (2012).
- [58] T. Hänsch, and B. Couillaud, *Laser frequency stabilization by polarization spectroscopy of a reflecting reference cavity*, Optics Communications **35**, 441 (1980).
- [59] T. Führer, D. Stang, and T. Walther, *Actively Controlled Tuning of an External Cavity Diode Laser by Polarization Spectroscopy*, Opt. Express **17**, 4991 (2009).
- [60] *Blue Laser Diode in TO38 ICut Package*, OSRAM Opto Semiconductors, 2013.
- [61] W. T. Silfvast, *Laser Fundamentals*, 2 ed. (Cambridge University Press, 2004).
- [62] S. Nakamura, and S. F. Chichibu, *Introduction to Nitride Semiconductor Blue Lasers and Light Emitting Diodes* (Taylor & Francis, 2000).
- [63] S. Lutgen, and M. Schmitt, *Blue Laser diodes*, Optik & Photonik **4**, 37 (2009).
- [64] C. J. Erickson, M. Van Zijll, G. Doermann, and D. S. Durfee, *An ultrahigh stability, low-noise laser current driver with digital control*, Review of Scientific Instruments **79** (2008).
- [65] J. Cariou, and P. Luc, *Atlas du Spectre d’Absorption de la Molécule de Tellure, 21100 cm<sup>-1</sup> – 23800 cm<sup>-1</sup>*, No. Bd. 5 in *Atlas du Spectre d’Absorption de la Molécule de Tellure* (Laboratoire Aime-Cotton, 1980).
- [66] C. Siegel, *Aufbau eines UV-Lasersystems für die Laserspektroskopie an gespeicherten hochgeladenen Ionen*, 2008.
- [67] N. Hodgson, and H. Weber, *Laser Resonators and Beam Propagation*, 2 ed. (Springer-Verlag, 2005).
- [68] J. Cariou, and P. Luc, *Atlas du Spectre d’Absorption de la Molécule de Tellure, 20300 cm<sup>-1</sup> – 21195 cm<sup>-1</sup>*, *Atlas du spectre d’absorption de la molécule de tellure* (Laboratoire Aime-Cotton, 1980).
- [69] J. Cariou, and P. Luc, *Atlas du Spectre d’Absorption de la Molécule de Tellure entre 18 500–23 800 cm<sup>-1</sup>* CNRS, 1980.
- [70] J. D. Gillaspay, and C. J. Sansonetti, *Absolute wavelength determinations in molecular tellurium: new reference lines for precision laser spectroscopy*, J. Opt. Soc. Am. B **8**, 2414 (1991).
- [71] D. H. McIntyre, and T. W. Hänsch, *Interferometric frequency measurement of a <sup>130</sup>Te<sub>2</sub> reference line for muonium 1S – 2S spectroscopy*, Phys. Rev. A **36**, 4115 (1987).

- 
- [72] G. P. Barwood, W. R. C. Rowley, P. Gill, J. L. Flowers, and B. W. Petley, *Interferometric measurements of  $^{130}\text{Te}_2$  reference frequencies for  $1\text{S} - 2\text{S}$  transitions in hydrogenlike atoms*, Phys. Rev. A **43**, 4783 (1991).
- [73] P. Cancio, and D. Bermejo, *Absolute wavelengths in  $^{130}\text{Te}_2$ : new reference lines for laser spectroscopy coinciding with emissions of the Ar+ laser*, J. Opt. Soc. Am. B **14**, 1305 (1997).
- [74] D. H. McIntyre, and T. W. Hänsch, *Absolute calibration of the  $^{130}\text{Te}_2$  reference line for positronium  $1^3\text{S}_1 - 2^3\text{S}_1$  spectroscopy*, Phys. Rev. A **34**, 4504 (1986).
- [75] S. Albrecht, S. Altenburg, C. Siegel, N. Herschbach, and G. Birkl, *A laser system for the spectroscopy of highly charged bismuth ions*, Applied Physics B **107**, 1069 (2011).
- [76] S. Albrecht, *Ein Lasersystem zur Spektroskopie von hochgeladenen Ionen, Tellurmolekülen und Rubidium-Rydberg-Zuständen*, Phd, TU Darmstadt, (2014).
- [77] T. J. Scholl, S. J. Rehse, R. A. Holt, and S. D. Rosner, *Absolute wave-number measurements in  $^{130}\text{Te}_2$ : reference lines spanning the 420.9 – 464.6 nm region*, J. Opt. Soc. Am. B **22**, 1128 (2005).
- [78] W. Demtröder, *Laserspektroskopie* (Springer Nature, 2000).
- [79] *standard cell for isotopic tellurium 130*, <http://www.e-o-phos.com/>, 2016.
- [80] R. E. Machol, and E. F. W. Jr., *Vapor Pressure of Liquid Tellurium*, Journal of the American Chemical Society **80**, 2950 (1958).
- [81] SCHOTT, *TIE-36: Fluorescence of optical glass*, 2004.
- [82] B. Edlén, *The Refractive Index of Air*, Metrologia **2**, 71 (1966).
- [83] K. P. Birch, and M. J. Downs, *An Updated Edlén Equation for the Refractive Index of Air*, Metrologia **30**, 155 (1993).
- [84] F. Vollrath, *Characterization of a Wide Tunable, Robust, Multi Application Diode Laser for Spectroscopy*, Masterthesis, TU Darmstadt, (2014).
- [85] M. Zinner, *Untersuchungen an lasergekühlten und gespeicherten metastabilen Neon-Atomen*, type, Universität Hannover, (2002).
- [86] P. Spoden, *Stoßwechselwirkungen in einem kalten Gas metastabiler Neonatome*, type, Universität Hannover, (2004).
- [87] J. Schütz, *Stoßwechselwirkungen in Isotopen- und Spinmischungen lasergekühlter metastabiler Neonatome*, type, TU Darmstadt, (2013).
- [88] H. Binder, *Lexikon der chemischen Elemente: das Periodensystem in Fakten, Zahlen und Daten* (Hirzel, 1999).

- 
- [89] W. Vassen, C. Cohen-Tannoudji, M. Leduc, D. Boiron, C. I. Westbrook, A. Truscott, K. Baldwin, G. Birkl, P. Cancio, and M. Trippenbach, *Cold and trapped metastable noble gases*, Rev. Mod. Phys. **84**, 175 (2012).
- [90] H. C. W. Beijerinck, E. J. D. Vredenburg, R. J. W. Stas, M. R. Doery, and J. G. C. Tempelaars, *Prospects for Bose-Einstein condensation of metastable neon atoms*, Phys. Rev. A **61**, 023607 (2000).
- [91] H. S. W. Massey, E. H. S. Burhop, and H. B. Gilbody, *Electronic and Ionic Impact Phenomena* (Oxford University Press, 1971), Vol. 3.
- [92] A. S. Tychkov, T. Jelte, J. M. McNamara, P. J. J. Tol, N. Herschbach, W. Hogervorst, and W. Vassen, *Metastable helium Bose-Einstein condensate with a large number of atoms*, Phys. Rev. A **73**, 031603 (2006).
- [93] R. J. W. Stas, J. M. McNamara, W. Hogervorst, and W. Vassen, *Homonuclear ionizing collisions of laser-cooled metastable helium atoms*, Phys. Rev. A **73**, 032713 (2006).
- [94] M. R. Doery, E. J. D. Vredenburg, S. S. Op de Beek, H. C. W. Beijerinck, and B. J. Verhaar, *Limit on suppression of ionization in metastable neon traps due to long-range anisotropy*, Phys. Rev. A **58**, 3673 (1998).
- [95] H. Katori, H. Kunugita, and T. Ido, *Quantum statistical effect on ionizing collisions of ultracold metastable Kr isotopes*, Phys. Rev. A **52**, R4324 (1995).
- [96] C. Orzel, M. Walhout, U. Sterr, P. S. Julienne, and S. L. Rolston, *Spin polarization and quantum-statistical effects in ultracold ionizing collisions*, Phys. Rev. A **59**, 1926 (1999).
- [97] T. Bergeman, G. Erez, and H. J. Metcalf, *Magnetostatic trapping fields for neutral atoms*, Phys. Rev. A **35**, 1535 (1987).
- [98] J. Keller, *Kohärente Manipulation von lasergekühlten metastabilen Neon-Atomen mittels Stimulated Raman Adiabatic Passage*, 2009.
- [99] R. Hertwig, *Aufbau eines galvanisch getrennten Verstärkers*, 2012.
- [100] A. Martin, *Zeitaufgelöste Untersuchung der Stoßwechselwirkung metastabiler Neonatome*, 2011.
- [101] S. Altenburg, *Zustandsabhängige Stoßwechselwirkungen lasergekühlter, metastabiler Neonatome*, 2012.
- [102] H. Ammann, and N. Christensen, *Delta Kick Cooling: A New Method for Cooling Atoms*, Phys. Rev. Lett. **78**, 2088 (1997).
- [103] E. Maréchal, S. Guibal, J.-L. Bossennec, R. Barbé, J.-C. Keller, and O. Gorceix, *Longitudinal focusing of an atomic cloud using pulsed magnetic forces*, Phys. Rev. A **59**, 4636 (1999).

- 
- [104] S. H. Myrskog, J. K. Fox, H. S. Moon, J. B. Kim, and A. M. Steinberg, *Modified “ $\delta$ -kick cooling” using magnetic field gradients*, Phys. Rev. A **61**, 053412 (2000).
- [105] T. Aoki, T. Kato, Y. Tanami, and H. Nakamatsu,  *$\delta$ -kick cooling using the Ioffe-Pritchard potential*, Phys. Rev. A **73**, 063603 (2006).
- [106] F. Dalfovo, S. Giorgini, L. P. Pitaevskii, and S. Stringari, *Theory of Bose-Einstein condensation in trapped gases*, Rev. Mod. Phys. **71**, 463 (1999).
- [107] M. Kasevich, and S. Chu, *Measurement of the gravitational acceleration of an atom with a light-pulse atom interferometer*, Applied Physics B **54**, 321 (1992).
- [108] S. Goldberg, D. Strasser, O. Heber, M. L. Rappaport, A. Diner, and D. Zajfman, *Phase-space manipulation of stored ions using the  $\delta$ -kick method*, Phys. Rev. A **68**, 043410 (2003).
- [109] F. M. H. Crompvoets, R. T. Jongma, H. L. Bethlem, A. J. A. van Roij, and G. Meijer, *Longitudinal Focusing and Cooling of a Molecular Beam*, Phys. Rev. Lett. **89**, 093004 (2002).
- [110] T. Kovachy, J. M. Hogan, A. Sugarbaker, S. M. Dickerson, C. A. Donnelly, C. Overstreet, and M. A. Kasevich, *Matter Wave Lensing to Picokelvin Temperatures*, Phys. Rev. Lett. **114**, 143004 (2015).
- [111] W. B. Case, *Wigner functions and Weyl transforms for pedestrians*, American Journal of Physics **76**, 937 (2008).
- [112] G. M. Kavoulakis, C. J. Pethick, and H. Smith, *Collisional relaxation in diffuse clouds of trapped bosons*, Phys. Rev. A **61**, 053603 (2000).
- [113] R. D. Glover, J. E. Calvert, D. E. Laban, and R. T. Sang, *Optical control of collision dynamics in a metastable neon magneto-optical trap*, Journal of Physics B: Atomic, Molecular and Optical Physics **44**, 245202 (2011).
- [114] A. Derevianko, S. G. Porsev, S. Kotochigova, E. Tiesinga, and P. S. Julienne, *Ultracold Collision Properties of Metastable Alkaline-Earth Atoms*, Phys. Rev. Lett. **90**, 063002 (2003).
- [115] V. Kokoouline, R. Santra, and C. H. Greene, *Multichannel Cold Collisions between Metastable Sr Atoms*, Phys. Rev. Lett. **90**, 253201 (2003).
- [116] D. Hansen, and A. Hemmerich, *Observation of Multichannel Collisions of Cold Metastable Calcium Atoms*, Phys. Rev. Lett. **96**, 073003 (2006).
- [117] W. J. van Drunen, *Collisional interaction between metastable neon atoms*, type, TU Darmstadt, (2008).
- [118] N. F. Mott, and H. S. W. Massey, *The Theory of Atomic Collisions*, 3 ed. (Oxford University Press, 1971).

- 
- [119] C. Cop (to be published).
- [120] B. Efron, and R. T. Tibshirani, *An Introduction to the Bootstrap* (Chapman & Hall, 1993).
- [121] J. Yung, *Confidence Intervals on the Estimated Parameters: The Bootstrap*, <http://phe.rockefeller.edu/LogletLab/whitepaper/node17.html>, accessed: 2016-09-14.
- [122] P. M. Duarte, *Getting standard errors on fitted parameters using the optimize.leastsq method in python*, <http://stackoverflow.com/questions/14581358/getting-standard-errors-on-fitted-parameters-using-the-optimize-leastsq-method-i>, accessed: 2016-09-14.
- [123] *Perform a Bootstrap Analysis*, <https://reference.wolfram.com/language/howto/PerformABootstrapAnalysis.html>, accessed: 2016-09-14.
- [124] X.-P. Huang, F. Anderegg, E. M. Hollmann, C. F. Driscoll, and T. M. O’Neil, *Steady-State Confinement of Non-neutral Plasmas by Rotating Electric Fields*, Phys. Rev. Lett. **78**, 875 (1997).
- [125] X.-P. Huang, J. J. Bollinger, T. B. Mitchell, and W. M. Itano, *Phase-Locked Rotation of Crystallized Non-neutral Plasmas by Rotating Electric Fields*, Phys. Rev. Lett. **80**, 73 (1998).
- [126] M. Morinaga, I. Bouchoule, J.-C. Karam, and C. Salomon, *Manipulation of Motional Quantum States of Neutral Atoms*, Phys. Rev. Lett. **83**, 4037 (1999).
- [127] C. A. Arango, M. Shapiro, and P. Brumer, *Cold Atomic Collisions: Coherent Control of Penning and Associative Ionization*, Phys. Rev. Lett. **97**, 193202 (2006).
- [128] C. A. Arango, M. Shapiro, and P. Brumer, *Coherent control of collision processes: Penning versus associative ionization*, The Journal of Chemical Physics **125**, 094315 (2006).
- [129] R. Unanyan, M. Fleischhauer, B. Shore, and K. Bergmann, *Robust creation and phase-sensitive probing of superposition states via stimulated Raman adiabatic passage (STIRAP) with degenerate dark states*, Optics Communications **155**, 144 (1998).



---

# Curriculum Vitae

## Graduation

08/2011–04/2017 Graduation in the group of Prof. Dr. Gerhard Birkl, Institut für Angewandte Physik, Technische Universität Darmstadt  
Thesis title: *Laser Spectroscopic Investigation of Exotic States in Noble Gases*

## Academic education

04/2006–04/2011 Studies of physics, Technische Universität Darmstadt

04/2011 Master of Science

04/2010–04/2011 Master thesis in the group of Prof. Dr. Gerhard Birkl, Institut für Angewandte Physik, Technische Universität Darmstadt  
Thesis title: *Zeitaufgelöste Untersuchung der Stoßwechselwirkung metastabiler Neonatome*

03/2009–06/2009 Bachelor thesis in the group of Prof. Dr. Gerhard Birkl, Institut für Angewandte Physik, Technische Universität Darmstadt  
Thesis title: *Aufbau eines Diodenlasersystems bei 640 nm*



---

# Erklärung zur Dissertation

Hiermit versichere ich, die vorliegende Dissertation ohne Hilfe Dritter nur mit den angegebenen Quellen und Hilfsmitteln angefertigt zu haben. Alle Stellen, die aus Quellen entnommen wurden, sind als solche kenntlich gemacht. Diese Arbeit hat in gleicher oder ähnlicher Form noch keiner Prüfungsbehörde vorgelegen.

Darmstadt, den 07.02.2017

---

(Alexander Martin)